Title

Receptivity of Straight Blunt Cones to Broadband Freestream Pulse Disturbances for Transition Prediction in Hypersonic Flow

Author

He, Simon

Publication Date

2022

UNIVERSITY OF CALIFORNIA
Los Angeles

Receptivity of Straight Blunt Cones to Broadband Freestream Pulse Disturbances for Transition Prediction in Hypersonic Flow

A dissertation submitted in partial satisfaction
of the requirements for the degree
Doctor of Philosophy in Aerospace Engineering

by

Simon He

2022

ABSTRACT OF THE DISSERTATION

Receptivity of Straight Blunt Cones to Broadband Freestream Pulse Disturbances for Transition Prediction in Hypersonic Flow

by

Simon He
Doctor of Philosophy in Aerospace Engineering
University of California, Los Angeles, 2022
Professor Xiaolin Zhong, Chair

Traditional stability analysis for hypersonic flows has focused on the development and relative amplification of a dominant disturbance mode, namely Mack's second mode. However, conventional e^N method transition estimates based purely on the relative amplification of the second mode ignore the receptivity mechanisms which govern the response of a flow to different environmental disturbances. These receptivity mechanisms are now known to play a much more significant role in the laminar-to-turbulent transition of hypersonic flows, and numerous theoretical, computational, and experimental studies have been made to characterize them. Computational studies in particular are useful due to the large amount of high precision data they can generate with a relatively low cost, while experimental receptivity studies face difficulties due to the high noise environments present in conventional hypersonic windtunnels, as well as the general expense of hypersonic experiments. While computational receptivity studies have been prominent in the literature, most of these prior studies have focused on discrete frequency disturbances and have neglected to consider the more continuous and broadband disturbance spectra that can be found in experiments and in flight.

This work aims to expand the prior body of receptivity research by studying the response to broadband disturbances that are more reflective of realistic environmental forcing. This process involves simulating the receptivity to axisymmetric disturbances as well as some preliminary investigations of the receptivity to 3-D pulse disturbances which excite azimuthal wave modes. The axisymmetric receptivity coefficients are also used to explore further applications of the amplitude method for transition prediction. This work uses perfect gas linear stability theory (LST) and direct numerical simulation (DNS) to simulate the Mach 10 flow over 9.525 mm (Case B), 5.080 mm (Case I), and 1 mm (Case S) nose radius axisymmetric straight cones with 7-degree half-angles. Case B and Case I utilized approximately the same freestream conditions, while the unit Reynolds number for Case S is 60% lower. The 2-D receptivity of Case B and Case I are studied using finite spherical and planar pulse disturbances in the freestream. These include freestream fast acoustic, slow acoustic, temperature, and vorticity disturbances in order to generate receptivity coefficient spectra for a wide variety of possible freestream noise sources. LST analysis predicted significant second mode growth for both Case B and Case I, with mode F being unstable for Case B and mode S being unstable for Case I. Case I was found to be more destabilizing to the second mode, as expected from the reduced nose radius. These LST results are used to validate the unsteady DNS, and to extract receptivity coefficients for the dominant second mode disturbance. The sharpest Case S is also studied using both axisymmetric planar acoustic pulses as well as azimuthally varying, 3-D acoustic pulse disturbances.

Unsteady DNS for Case B and Case I show that all of the disturbances excite second mode growth and generally follow the amplification profile predicted by LST. The results for the blunter Case B show much stronger freestream noise effects than for Case I, while Case I seems to be more sensitive to extremely low frequency boundary layer modes associated with upstream disturbances originating in the entropy layer. Additionally, the blunter Case B is observed to have a much stronger supersonic mode, which is qualitiatively observed in acoustic radiation from the boundary layer disturbance wavepacket. This is attributed to the destabilized discrete mode F in Case B which is more capable than the discrete mode S of slowing and becoming supersonic relative to the meanflow. DNS and LST data are used to extract second mode receptivity coefficients and phase spectra for Case B and Case I for application to an iterative transition prediction method. The receptivity coefficients are decomposed from the total surface disturbance by renormalizing the unsteady DNS data with the LST-derived amplifcation rate. Most pulse cases saw the same spectral receptivity

coefficient behavior, with peak amplitudes being at the most amplified downstream frequencies. However, the planar fast acoustic pulse in both Case I and Case B was found to excite a much more broadband disturbance profile associated with continuous mode instabilities. This likely necessitates more advanced modal decomposition methods, like the bi-orthogonal decomposition, to cleanly resolve the modes of interest. Additionally, Case I was found to be much more receptive to the temperature and vorticity pulses than Case B while the acoustic responses were fairly similar. This may be due to stronger low frequency upstream forcing that was found in Case I that is associated with entropy layer modes, and indicates differing receptivity mechanisms between the two nose bluntnesses.

The receptivity cofficients for Case B and Case I are applied to a simplified 2-D implementation of Mack's amplitude method in an attempt to better approximate the transition location for those cases. Unlike the conventional e^N method, the amplitude method directly estimates disturbance amplitudes in the boundary layer. This requires the use of receptivity data and freestream noise profiles along with other correlations for threshold breakdown amplitudes. The correlations for freestream noise and breakdown amplitude are taken from Marineau(AIAA Journal, 2017). While some improvement is seen over the base accuracy of standard e^N method predictions, the estimated transition locations using the receptivity data from this study are found to still be significantly overpredicted. The Case I results, however, match much more closely with experimental measurements likely due to the stronger second mode. The disagreement with experiment and Marineau's results can be attributed to imprecise correlations of freestream noise and oversimplifications of the original amplitude method relations.

True flight conditions will inevitably contain oblique disturbances, whether through local geometry or from the nature of freestream noise. Therefore, while the 2-D second mode disturbance has found to dominate in a large selection of hypersonic flows, consideration of 3-D disturbances is necessary to complete our view of the transition process. To accomplish this a preliminary analysis of both planar 2-D and 3-D azimuthally varying pulse simulations were also run on the small bluntness (1 mm nose radius) Case S. LST analysis of this new case shows an upstream shift in the destabilized second mode positions, as well as higher

destabilized frequencies that match expectations for the smaller nose radius. While the peak growthrates were highest for Case S the reduced freestream unit Reynolds number compared to Case B and Case I led to a weaker overall amplification of the second mode in the streamwise direction, as measured by peak N-factor. Freestream fast and slow acoustic pulses were modelled using gaussian distributions in both the streamwise and azimuthal directions. Results for the 2-D pulses demonstrate strong similarities to prior results for Case B and Case I, with the planar fast acoustic pulse inducing strong broadband continuous mode variation while the slow acoustic pulse induced only second mode disturbances. The 3-D azimuthally varying pulses followed a similar pattern, as downstream excitations were primarily isolated to low wavenumber modes in the slow acoustic case. The 3-D fast acoustic pulse is found to also excite a wide range of disturbance frequencies, though excited frequency bands outside of the second mode are generally confined to lower wavenumbers. Disturbances at the second mode frequencies, however, saw little to no decay at higher wavenumbers compared to the 3-D slow acoustic case. This indicates that fast acoustic disturbances are highly capable of exciting both a broad range of disturbance wavenumbers as well as a broad range of disturbance frequencies.

The dissertation of Simon He is approved.

Raymond M. Spearrin

Jeffrey D. Eldredge

Ann R. Karagozian

Xiaolin Zhong, Committee Chair

University of California, Los Angeles

2022

TABLE OF CONTENTS

LIST OF FIGURES

LIST OF TABLES

Nomenclature

$()_0$	Stagnation Value
$()_\infty$	Freestream Value
$()_i$	Imaginary Component
$()_r$	Real Component
$()_T$	Parameter Value at Transition Location
α	Spatial Wavenumber
ϵM_∞	Peak Freestream Disturbance Amplitude
γ	Ratio of Specific Heats
γ_0	Freestream Pitot Noise Component
μ	Viscosity Coefficient
ω	Circular Frequency
ϕ	Phase Angle
ρ	Density
σ	Gaussian Frequency Shape Parameter
σ_k	Gaussian Azimuthal Shape Parameter
τ	Shear stress
A	Disturbance Amplitude
c_∞	Freestream Disturbance Velocity
C_p	Constant Pressure Specific Heat Coefficient

c_r	Non-dimensional phase speed
C_v	Constant Volume Specific Heat Coefficient
C_{rec}	Receptivity Coefficient
$d() or ()'$	Perturbation variable
f	Frequency
k, β	Azimuthal Wavenumber
L^*	Boundary Layer Thickness Parameter
M	Mach Number
N	N-factor
P	Pressure
Pr	Prandtl Number
q	Heat Transfer
R	Gas Constant
Re	Reynolds Number
S	Entropy
s^*	Streamwise position along body surface
T	Temperature
X	Cartesian Streamwise Coordinate
Y	Wall Normal Coordinate

ACKNOWLEDGMENTS

I would like to express my gratitude to my advisor, Dr. Zhong, for his encouragement and patience throughout my time at UCLA. His guidance has been invaluable in interpreting the results of my research and improving my scientific writing. I would also like to thank my committee: Dr. Karagozian, Dr. Eldredge, and Dr. Spearrin for their time and insights while serving on my committee. I would also like to thank my family for their unwaivering support throughout my time in the graduate program at UCLA. Finally, I would also like to thank my labmates, the other students in the MAE department, and everyone else I have had the pleasure of meeting in my time here.

This research was supported by the Air Force Office of Scientific Research (AFOSR) under AFOSR Grant #FA9550-19-1-0206, previously monitored by Dr. Ivett Leyva and Dr. Sarah H. Popkin. This work was also partially supported by Office of Naval Research (ONR) Grant #N00014-17-1-2343, monitored by Dr. Eric Marineau. Primary computational resources were provided by the Extreme Science and Engineering Discovery Environment (XSEDE) through the Texas Advanced Computing Center (TACC) and the San Diego Supercomputer Center (SDSC) under grant number TG-ASC090076, supported in part by the National Science Foundation (NSF). Additional computational resources were provided by the Department of Defense High Performance Computing Modernization Program (DoD HPCMP) through project AFOSR40702004. The views and conclusions contained herein are those of the authors and should not be interpreted as necessarily representing the official policies or endorsements, either expressed or implied, of the U.S. Air Force Office of Scientific Research, Office of Naval Research, XSEDE, or the U.S. Government.

VITA

2012–2016	B.S. with Honors in Aerospace Engineering, University of California Los Angeles.
2016–2017	M.S. in Aerospace Engineering, University of California Los Angeles.
2016–2022	Teaching Assistant/Reader, Mechanical and Aerospace Engineering Department, UCLA. Worked as a TA/Reader for MAE 82, MAE 150B, MAE 154A, and MAE 250D.
2016–2022	Graduate Student Researcher, Mechanical and Aerospace Engineering Department, UCLA.

PUBLICATIONS

S. He and X. Zhong, “The Effects of Nose Bluntness on Broadband Disturbance Receptivity in Hypersonic Flow,” *Physics of Fluids* 34, 054104, p. 1-25, 2022.

S. He and X. Zhong, “Hypersonic Boundary Layer Receptivity over a Blunt Cone to Freestream Pulse Disturbances,” *AIAA Journal* Vol. 59, Number 9, p. 3546-3565, 2021.

S. He and X. Zhong, “Numerical Study of the Receptivity of a Blunt Cone to Freestream Pulse Disturbances in Hypersonic Flow,” AIAA Aviation Paper 2021-2887, August 2021.

S. He and X. Zhong, “Numerical Study of the Receptivity of a Blunt Cone to Hypersonic Freestream Pulse Disturbances,” AIAA Scitech Paper 2021-0742, January 2021.

S. He and X. Zhong, “Numerical Study of Hypersonic Boundary Layer Receptivity over a Blunt Cone to Freestream Pulse Disturbances,” AIAA Aviation Paper 2020-2996, June 2020.

S. He and X. Zhong, “Hypersonic Boundary Layer Receptivity over a Blunt Cone to Freestream Pulse Disturbances,” AIAA Scitech Paper 2020-2057, January 2020.

CHAPTER 1

Introduction

1.1 Background

The accurate prediction of laminar to turbulent transition in hypersonic flows is a major concern when using computational fluid dynamics (CFD) to aid in the design of high-speed vehicles and projectiles. The design of these vehicles is critical to national security, the development of orbital vehicles for future space missions, and to further advance commercial aviation capabilities.

The transition to turbulence is marked by the onset of many adverse conditions for a high-speed vehicle including: increased drag, increased surface heating, and loss of control [1, 9, 10]. At hypersonic speeds, the extreme increase in surface heating rates in particular provides challenging structural and material design constraints. In particular, these extreme loads necessitate the deployment of thermal protection systems (TPS). Delaying transition and accurately predicting its behavior in hypersonic vehicles will allow for greater specificity in the design of TPS's and minimize the weight impact of these systems. Doing so would have a substantial payoff, enabling better flight performance and expanded payload capacities for potential hypersonic vehicles. However, transition itself is a multi-faceted system composed of numerous mechanisms which are yet to be fully understood[11]. The further characterization of these underlying mechanisms and their interactions is necessary in order to understand hypersonic transition phenomena and to improve the accuracy of transition predictions.

1.2 Boundary Layer Transition

Transition in a hypersonic boundary layer is governed by several mechanisms, and in the case of weak environmental forcing can be broken down into three primary stages: (i) boundary layer receptivity, (ii) linear growth of small amplitude instabilities, and (iii) non-linear breakdown at finite disturbance amplitudes[12]. Though, under certain conditions these steps may be circumvented in a process called bypass transition[13]. A diagram documenting these stages to transition is shown in Fig. 1.1, adapted from Zhong and Wang[1]. In stage (i) environmental disturbances such as freestream acoustic noise, surface imperfections on the geometry, or impinging particulates perturb the flow to generate the initial boundary layer disturbances. The amplitudes and spectral content of these initial disturbances are dictated by the receptivity mechanism. For weak forcing, these initial perturbations experience linear eigenmode growth in stage (ii). Afterwards in stage (iii), after sufficient amplification, the finite amplitude perturbations experience intense non-linear interactions which gradually cause the breakdown to turbulence. This process is depicted in path A in Fig. 1.1 and is the most classical path to turbulence. The transient growth stage in Paths B, C, and D is caused when initial disturbance modes are not perfectly orthogonal, as originally assumed in Path A[14, 13]. This leads to interactions between the disturbance modes which generate small algebraic amplification of perturbations before they experience linear eigenmode growth. In the cases of sufficiently strong environmental forcing or transient growth effects, this linear eigenmode growth step can be skipped entirely as seen in Paths C, D, and E. In this finite amplitude disturbance case, non-linearities in the disturbance interactions immediately become significant and begin to generate complex flow structures that eventually lead to full turbulent breakdown. While many paths to turbulence exist, it is well known that environmental forcing in atmospheric flight conditions is generally very weak[15, 16]. As such, this work focuses on the receptivity mechanisms of low amplitude forcing depicted in Path A.

Early work in transition can be traced back to Rayleigh and Tollmien and Schlichting, after whom the eponymous Tollmien-Schlichting (T-S) waves in hydrodynamic stability theory are named. Rayleigh[17] first derived the generalized inflection point criterion for inviscid

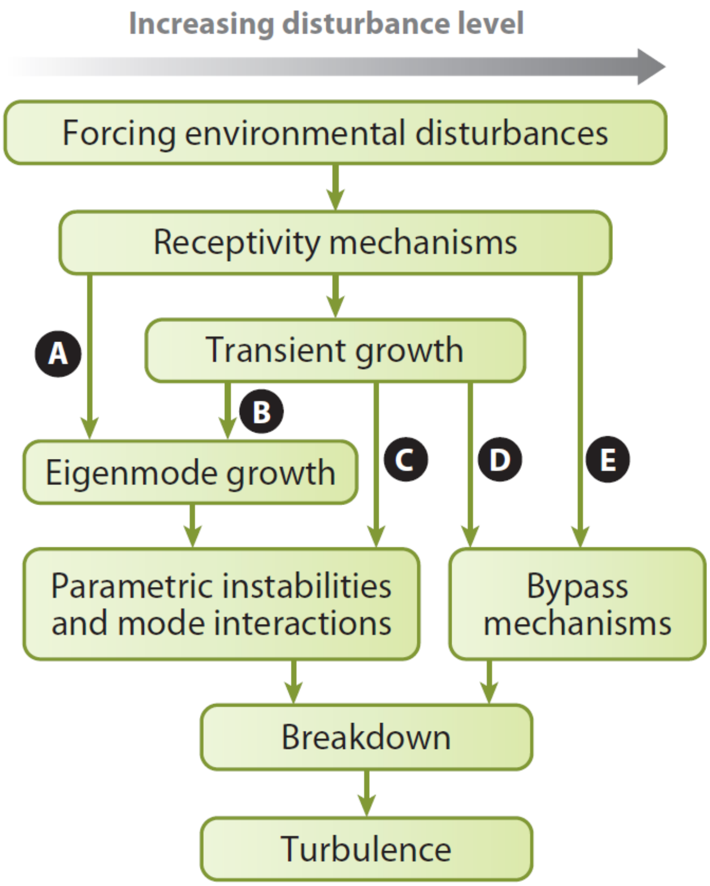

Figure 1.1: Pathways to turbulence, adapted from [1].

instabilities in incompressible flows. Tollmien and Schlichting[18, 19] similarly studied instability waves by solving the fully viscous linearized Navier-Stokes equations for incompressible flows, continuing to lay the groundwork for modern Linear Stability Theory (LST). Their solutions of the stability system, known as the Orr-Sommerfeld equations, predicted the evolution of exponentially growing viscous instabilities which propagated downstream parallel to the body. The amplification of these T-S waves could eventually trip transition to turbulence. While complex flows experience many different mechanisms that govern their transition, Rayleigh's as well as Tollmien and Schlichting's work introduced and further characterized the concepts of both inviscid and viscous wave-like instabilities to hydrodynamics.

This concept of propagating wave-like disturbances was later expanded to compressible flows by Lees and Lin[20] and Dunn and Lin[21]. Mack[22] also later noted that the primary disturbance in low speed compressible flows, what is now called the first mode, is a compressible equivalent to the T-S waves observed by Tollmien and Schlichting originally for incompressible fluids. Furthermore, he also found that as the Mach number of the flow increased, the disturbance gradually became inviscid in nature and observed a compressible equivalent to the generalized inflection point theory first derived by Rayleigh. Mack also identified additional instability modes present in high speed boundary layers which he referred to as the multiple-viscous solutions[23]. For a bounded flow these multiple-viscous solutions contain an infinite number of disturbance modes which are isolated to the boundary layer, though for hypersonic flows the second mode instability is found to experience the highest degree of amplification and to have the largest overall disturbance amplitude. Thus, a majority of transition studies for hypersonic flows have historically been focused on the generation and development of the second mode instability.

A wide range of instabilities exist in hypersonic boundary layers, and in hypersonic flows in general. The aforementioned multiple-viscous solutions, more commonly referred to now as the Mack modes, are known in literature as discrete mode instabilities. These discrete mode instabilities are primarily confined to the boundary layer and rapidly decay in the freestream. Fig. 1.2 depicts an example flat plate case from Ma and Zhong[2] which depicts a large number of discrete modes. The multiple-viscous solutions discussed previously refer in this case to the Mode I, Mode II, Mode III, and Mode IV instabilities which emerge from the continuous fast acoustic spectrum which is demarcated at a non-dimensional phase speed of $1 + 1/M_\infty$. While each of these fast acoustic discrete modes is capable of synchronizing with the continuous modes or the discrete slow acoustic mode and causing instability, in a hypersonic flow only small selection of these modes is significant[23]. The strongest of these discrete modes, the first and the second mode, have been described as acoustic rays physically trapped between the wall and the local sonic line [24, 25, 9]. This is visualized in Fig. 1.3.

While these discrete modes generate the dominant instabilities in boundary layers, they are not the only disturbances present in the flow. Additional fast acoustic, slow acoustic, entropy, and vorticity waves also exist simultaneously with the discrete modes in the boundary

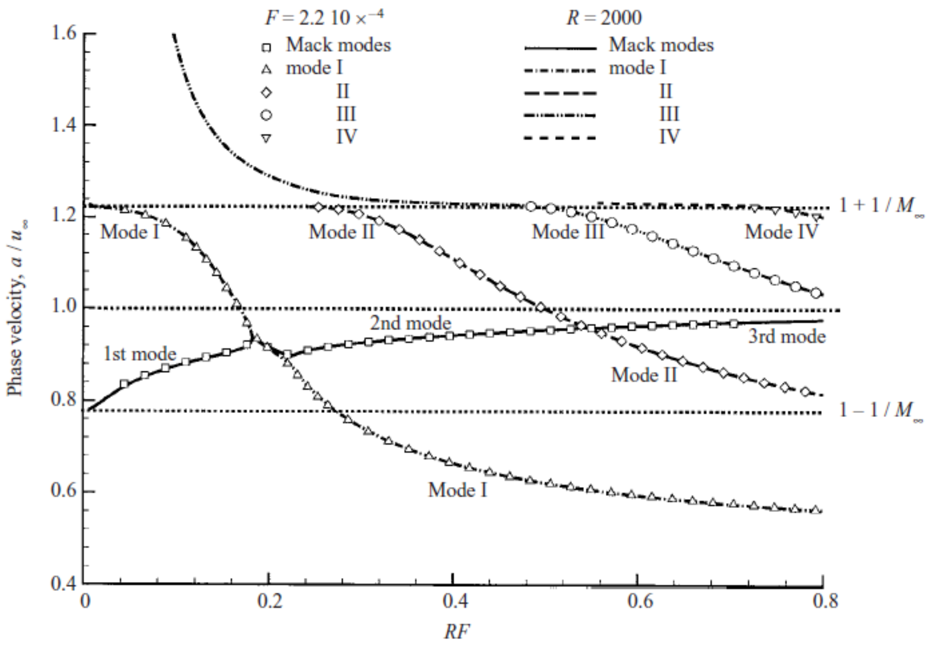

Figure 1.2: Example depicting predicted existence of additional higher order discrete modes emerging from the fast acoustic spectrum. Adapted from Ma and Zhong[2].

layer and are known as the continuous modes. Furthermore, these continuous modes are not confined to the boundary layer like the discrete modes and are instead present throughout the freestream as well. These continuous mode instabilities are commonly identified by their non-dimensional phase speeds. The continuous fast acoustic waves propagate through the flow at a relative phase speed of $(1+1/M)$ while continuous slow acoustic waves propagate at $(1-1/M)$. The continuous entropy and vorticity waves propagte at the same speed as the local meanflow. These continuous modes for the cone flows are a result of the bounded nature of modelled disturbances in the unbounded flow domains about aerodynamic bodies[26].

New terminology has been recently coined by Fedorov and Tumin[27] to more directly reflect the asymptotic behavior of the discrete modes. The discrete mode F refers to a disturbance emerging from the continuous fast acoustic spectrum and correspond to the previous Mode I, Mode II, etc. found in Fig. 1.2. Additionally, mode S emerges from the continuous slow acoustic spectrum and corresponds to the 1st mode, 2nd mode, and 3rd mode lines marked in Fig. 1.2. This more recent terminology also accounts for the fact that for cone geometries the discrete fast acoustic modes have also been found to be capable of

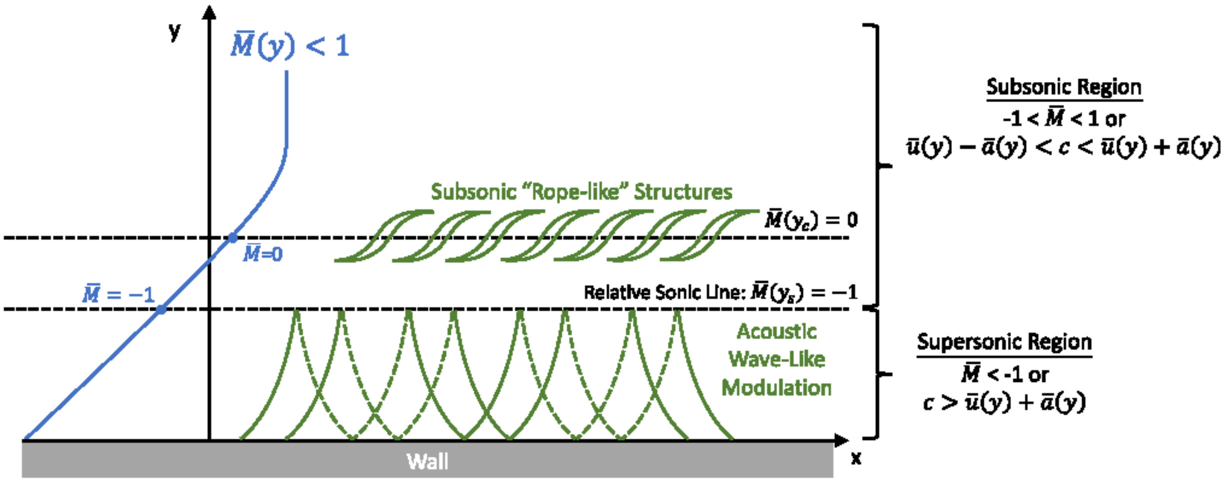

Figure 1.3: Visualization of second mode, adapted from [3].

destabilizing into the second mode. An example of the continuous mode spectra and their associated discrete modes can be seen in Fedorov[9]. While the continuous modes themselves typically do not experience growth in the boundary layer, their interactions with and generation of the primary discrete mode instabilities greatly complicate the stability behaviors of hypersonic flows. The discrete modes can experience a phenomenon called synchronization in which they interact with each other or with the continuous modes, exchanging energy. This synchronization is observed when the phase speeds of two or more disturbance modes intersect, which can be seen at the intersections of the discrete mode disturbances with each other in Fig. 1.2. Synchronization between discrete modes in particular can cause rapid destabilization as energy is transferred between the modes. In hypersonic flows this is typically indicative of the primary second mode disturbance. While the discrete modes can be classified into mode F and mode S based on their asymptotic behavior, the second mode itself is identified by the rapid destabilization caused by the initial synchronization between the discrete modes. Therefore while the second mode refers to mode S in many classical cases, mode F can also become the unstable second mode under certain conditions[9, 28].

Boundary layer stability for hypersonic flows has also been rigorously tested in experiment. While direct flight testing is possible and has been performed, the prohibitive cost of doing so usually restricts experimental studies to high-speed windtunnels. Early studies by Softley et al.[29] and Stetson et al.[30, 31, 32] provided early experimental proof of the development of second mode disturbances. These studies have confirmed theoretical results governing the development of primary instabilities, though they have also illuminated some phenomena that have yet to be fully explained. Most prominent is the phenomenon of transition reversal that occurs in geometries with highly blunted leading edges. Experiments, theory, and computation all show that small to intermediate levels of nose bluntness have stabilizing effects on the flow field, effectively delaying transition. In blunt cones this is largely attributed to the effects of the more extensive entropy layer pushing back the development of boundary layer disturbance modes[33]. Large nose bluntnesses, however, have been demonstrated in experiments to cause significant upstream shifting of transition locations. Conventional stability theory has failed to accurately capture this phenomena, and instead predicts continued modal stabilization, even at the high nose bluntnesses that are observed in experiment to experience the reversal phenomenon[34]. Current theories posit increased sensitivity to local surface roughness and non-modal disturbance growth as possible explanations[35, 8, 36] though consensus has yet to be reached on the exact cause of this phenomenon. Experiments continue to this day in the work of Jewell et al.[37] and Marineau et al.[7, 38, 39] who have continued to record data detailing the development of modal instabilities and the process of transition for a variety of sharp and blunt cones. Studies such as Juliano et al's[40] have also been made using quiet tunnels developed to reduce the freestream noise that the model is exposed to in an attempt to replicate the low amplitude perturbation environment expected in true flight[41, 15]. While low noise experiments like are useful in investigating the transition behavior of flight vehicles, more direct investigation of receptivity mechanisms are necessary to link the results of the numerous studies in both quiet and noisy windtunnels. Additionally, computational receptivity models can be validated against these experimental studies and eventually used to more easily develop high fidelity receptivity databases for further application in transition prediction models and further investigations of the physical breakdown mechanisms involved in the transition to turbulence.

1.3 Receptivity

Traditionally, studies on laminar to turbulent transition at hypersonic speeds and zero angle of attack have been focused on the linear growth of Mack modes, for which the second mode instability has been found to dominate [22]. However receptivity mechanisms dictate the initial disturbance amplitudes of flow instabilities, like the second mode, in response to external forcing. Depending on the freestream disturbance environments present, the receptivity process can result in drastically different disturbance amplitude profiles in flows that otherwise have the same mean conditions. This variation can cause significant differences in the threshold amplification factors that are most commonly used to predict transition[41]. Therefore, the characterization of receptivity behaviors is critical to developing more accurate hypersonic transition prediction tools.

External forcing can come in a variety of forms such as: freestream acoustic disturbances[42, 43], surface disturbances on the geometry itself, freestream entropy or vorticity disturbances[44, 45, 4], and impinging particulate disturbances[46]. Potential surface disturbances include surface blowing/suction actuation[47], surface chemistry[48], or surface roughness[49, 50, 51]. A schematic diagram for receptivity over a blunt body at hypersonic speeds is presented in Fig. 1.4. Studies of receptivity commonly focus on the disturbance response to freestream noise which, for compressible flows, can be categorized into three distinct types: acoustic, entropy, and vorticity disturbances[52]. In hypersonic flows, the interaction of these freestream disturbances with a bow shock generates disturbance waves of all three types behind the shock that can then perturb the boundary layer[53]. However, the mechanisms of the shock-disturbance interactions for each of these freestream disturbances differs. This can cause differences in the resulting disturbance wave content, both in terms of wave amplitude and phase[4]. Thus, a wideranging consideration of all the disturbance types is needed to fully characterize the receptivity of a hypersonic flow.

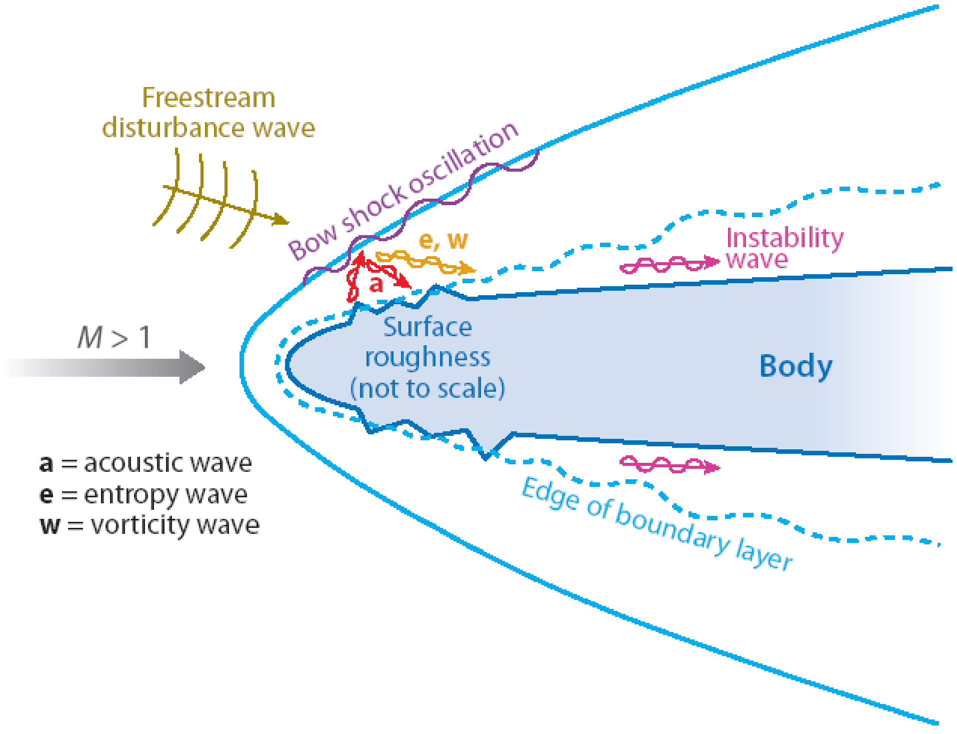

Figure 1.4: Schematic diagram of general receptivity over a blunt body at hypersonic speeds, adapted from Zhong and Wang[1].

1.3.1 Receptivity of Flat Plates

The receptivity of hypersonic boundary layers to freestream disturbances in particular has been extensively studied in flows over both flat plate[54, 2, 55, 56, 12, 57, 58, 59] and cone[60, 61, 44, 4, 62, 33, 63, 64, 65] geometries. For a flat plate case it was found that freestream acoustic disturbances generate initially stable modes near the leading edge, which then become unstable after synchronization [2, 55, 12]. This synchronization point is where the discrete modes originating from the continuous freestream fast and slow acoustic spectra interact and exchange energy, potentially destabilizing and causing a Mack mode instability. Studies have found that freestream acoustic, vorticity, and entropy waves modelled as discrete Fourier modes could all excite discrete mode disturbances in flat plate boundary layers, though the receptivity mechanisms differed greatly between the disturbance types. In particular, while all of these fundamental disturbance types could induce modal disturbances in the boundary layer, acoustic waves generally induced the most amplified second modes[2, 55, 12, 56]. Ma and Zhong[12] showed that a freestream entropy disturbance excited strong stable mode I (F1) disturbances upstream on the flat plate. These waves would then be converted into mode II (F2) mode instabilities after synchronization, though the oscillations indicative of multimodal interactions were found to be relatively weak near synchronization. The freestream fast acoustic disturbance excited similar disturbances. However, stronger oscillations apeared signalling much stronger coupling between the disturbance modes present in the boundary layer while not inducing a significant second mode response. The slow acoustic disturbance, on the other hand, was found to successfully excite an unstable second mode. In this case the second mode corresponded to the discrete mode S.

Fedorov et al.[58] also studied the receptivity to a flat plate, though they focused on the response to a temperature disturbance imposed either upstream of or downstream of the shock. When the temperature disturbance was imposed directly on the boundary layer they found that a discrete mode F was generated. After experiencing intermodal exchanges, these initial mode F disturbances excited the unstable mode S. They further found that significant acoustic waves were also excited behind the shock when the disturbance was imposed in the freestream. These then propagated through the boundary layer to excite the unstable mode S disturbance. This shock-disturbance interaction generated perturbation amplitudes that were an order of magnitude higher than those associated with the pure boundary layer disturbance. The results of these studies indicate diffierent receptivity paths for different disturbance types, and further necessitate a wide parameter space of studied disturbances in order to fully characterize the receptivity response of a flow.

1.3.2 Receptivity of Cones and Prior Investigations of Incident Broadband Disturbances

Numerous studies have also been made on the receptivity of cone geometries to freestream disturbances. Zhong and Ma[60] investigated the receptivity of a blunt cone with discrete freestream fast acoustic waves at Mach 7.99. They found through LST that the unstable

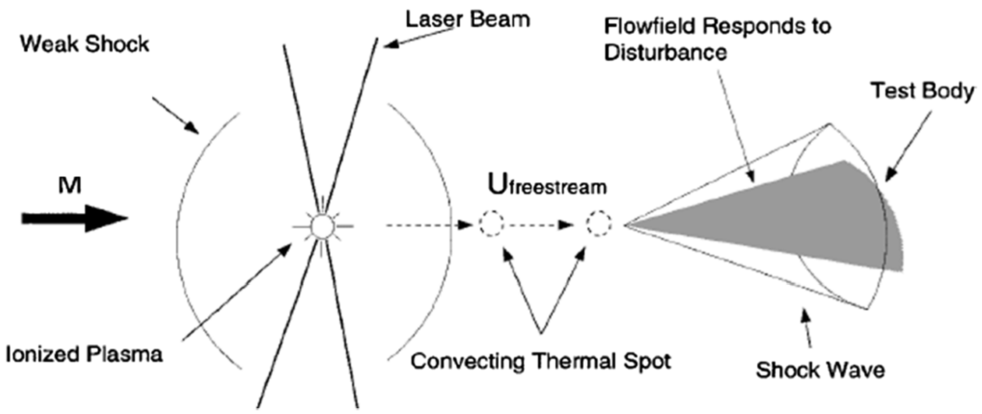

Figure 1.5: Schematic diagram of laser pulse experiment and resulting temperature spot, adapted from [4].

second mode for this case was mode S, similar to their previous flat plate case [12]. However, contrary to their previous flat plate result the freestream fast acoustic disturbance was was found to also excite the second mode instability in the boundary layer for the cone. This indicates strong differences in the receptivity process between the cone and flat plate geometries. This can be attributed to flow features such as bow shock interactions, nose bluntness, and potential entropy layer instabilities. Similarly, Balakumar and Kegerise [44] found that both vortical and acoustic disturbances could excite second mode instabilities in cone flows, and that the receptivity response was stronger for acoustic disturbance waves. They also reported that wave incidence had some effect on the receptivity response, indicating a need to account for more complex disturbance conditions to fully approximate the envelope of conditions found in flight. Kara et al.[33] used receptivity simulations for slow acoustic waves to investigate the effects of nose bluntness on transition. They found that while freestream acoustic waves readily generated second mode instabilities downstream on the cone, second mode amplification was unable to accurately predict the transition behavior observed in large nose bluntness cones as discussed previously for the transition reversal phenomena. Possible explanations for this include non-modal disturbance growth from sources like transient growth[14, 8], or a failure to accurately capture the effects of freestream environmental noise in the disturbance model[34, 66]. Wan, Su, and Chen[64] as well as Chen, et al.[67] further investigated the receptivity mechanism of planar slow acoustic waves over blunt cones and wedges to further characterize the development of instability modes. They found that acoustic waves excited fast acoustic boundary layer modes along with entropy layer modes upstream on the geometry. The fast acoustic modes were found to dampen significantly while the entropy layer disturbances grew to dominate and force more amplified downstream instabilities, including the primary second mode.

Many of these past receptivity studies utilized planar freestream disturbances modelled as discrete frequency Fourier modes[12, 44]. Environmental perturbations in experimental and flight conditions, however, are generally broadband in nature[41, 68]. This has motivated recent receptivity studies to begin incorporating more multi-frequency and broadband freestream disturbance models. Zhong[69] as well as Balakumar and Chou[62] attempted to approximate these broadband frequency disturbances through carefully chosen combinations of discrete frequency, continuously radiating two-dimensional planar slow acoustic waves. Zhong chose an arbitrary set of frequencies that were predicted by LST to be the most amplified for his blunt cone cases. Zhong attempted to track transition reversal effects using the broadband disturbance, but was unable to observe it in his test cases. Balakumar and Chou, on the other hand, determined the amplitudes of each of the waves in the disturbance packet by equating the energy of each discrete wave with a chosen frequency in the freestream pitot noise spectrum for the tunnel conditions of the experimental case they were simulating. They found that doing so allowed the transition location to predicted with reasonable accuracy for the sharp nose cases, though the accuracy of the threshold criterion they used decreased significantly for blunter cones.

Motivated by laser perturbation experiments from Purdue by Wheaton, et al.[70] and Chou, et al.[45, 71], Huang and Zhong[4, 72] simulated hotspot disturbances using freestream finite Gaussian pulses. Their studies investigated the receptivity of axisymmetric freestream hotspots over a selection of straight cones and compression cones, and showed that this hotspot was effective in exciting second mode instabilities in the boundary layer. A schematic of this disturbance configuration based on the Purdue experiments is shown in Fig. 1.5. They found that the resulting disturbance growth rate and phase speed compared well to LST, and corroborated the results from experiment. The receptivity mechanism for the entropy spot over a compression cone was also found to be very similar to that of discrete acoustic waves over a blunt cone, but different from entropy spot disturbances for flat plates. This further reinforces the significance of geometry on the receptivity mechanism. Using high accuracy receptivity simulations such as this, it is possible to to use a combination of the unsteady DNS and the LST disturbance data to extract both spectral receptivity coefficients for the second mode, and the phase angle spectra of the disturbance. With this data, the full response to this particular temperature disturbance as well as other arbitrary axisymmetric temperature disturbances can be reconstructed[63, 4]. While this study showed that Gaussian pulses could successfully approximate continuous frequency spectrum disturbances and excite significant modal instabilities in hypersonic flows over cones, it was very limited in terms of the disturbances it considered. Additional investigation into the receptivity of broadband acoustic waves must also be made as experimental environments are often dominated by acoustic noise[73]. This study aims to further expand on this and produce a more complete receptivity database which includes freestream acoustic, entropy, and vorticity disturbances. While purely axisymmetric disturbances can approximate idealized experimental conditions well, more complex three-dimensional disturbances will also need to be studied in the future in order to fully capture the receptivity response of hypersonic flows to true flight conditions.

Similar impulsive acoustic disturbances have also previously been studied experimentally using spark-inducers[74]. Chuvakhov, Fedorov, and Obraz[46] simulated the receptivity to small particulates in supersonic flows to investigate the potential effects of atmospheric or experimental dust particulates. In flight these particulates may be from free-floating dust or ice particles, partially ablated sections of TPS systems, or other debris present in the environment. Such particulate impingement can induce strong localized disturbances outside of the primary acoustic, entropy, or vorticity waves otherwise present in the noise environment. Chuvakhov, Fedorov, and Obraz demonstrated broadband excitation of both continuous and discrete instability modes, and showed that particulates could significantly excite wavepackets of amplified modal instabilities. Browne, Hasnine, and Brehm[75] used similar methodologies and investigated the receptivity over a wedge and flat plate to different particle impingement locations. While these models also offer sources of broadband excitation, they do not encompass the wide range of other potential freestream disturbance types that may be present in experimental or flight conditions. The many faceted responses of these hypersonic flows further emphasizes the importance of considering broadband incident disturbances to fully capture all of the flow features that may be present in an experimental environment.

1.3.3 Disturbance Coherence and Nose Bluntness Effects

Recent investigations of stochastic freestream perturbations have also been made to more closely match the nature of disturbances found in actual flight[76], as well as to account for the limited availability of environmental disturbance data[77, 59] for some configurations. Egorov, et al.[76] investigated the impact of phase coherence in freestream disturbances to determine the potential impact on receptivity coefficients. In this case, coherence refers to consistent phase relations in the disturbance spectra of the incident perturbation. Incoherent disturbances introduce forcing with randomized phase into the flow. Egorov, et al.[76] asserts that incoherent disturbances, such as from random incident acoustic waves or distributed surface roughness, are more capable of inducing instability than coherent disturbances. The fixed phase relations in an incident coherent disturbance can cause constructive and destructive interference in the resulting wavepackets. This is due to the dispersive nature of the excited waves. However, the total impact of phase coherence on broadband disturbances and the potential mechanistic differences in their receptivity responses has not been widely studied at this point in time.

Hader and Fasel[5] presented randomized pressure perturbations over cones as a means to simulate downstream non-linear breakdown for flows with unknown freestream noise profiles. They showed that these arbitrary disturbances induce similar breakdown mechanisms to their previous results using controlled disturbances. Goparaju, Unnikrishnan, and Gaitonde[59] expanded on this and investigated the receptivity of flat plates of different bluntnesses to stochastic pressure disturbances in an attempt to explain the transition reversal phenomenon observed in geometries with large leading-edge bluntness. They observed significant excitation in the entropy layer of their flat plate case along with a reversal in the growth rate. Further investigations on the effects of phase coherence will be necessary to further refine our understanding of receptivity in hypersonic flows, particularly in how this coherence of the initial disturbance may affect induced disturbance amplitudes in the boundary layer.

Most practical designs for hypersonic vehicles also include some form of nose bluntness, which greatly complicates the stability profile of the flow due to the introduction of features such as distinct entropy layers and increased sensitivity to local surface roughness. As stated previously, small to moderate nose bluntness has been shown experimentally and numerically to slow second mode growth and delay transition. Due to the prominence of nose bluntness in actual vehicle designs, several receptivity studies have attempted to investigate the coupled effects of bluntness and freestream receptivity. This includes the aforementioned works by Kara, et al.[33] who investigated the receptivity of different blunt and sharp cones to freestream discrete frequency waves, Goparaju, et al. [59] who investigated the receptivity of blunt cones to stochastic freestream acoustic disturbances, and Huang[4, 72] who investigated the receptivity of various straight and compression cones of different nose bluntnesses to freestream temperature spots. These studies have helped to elucidate the coupled effects of bluntness and freestream receptivity, however whether it is through limitations in the freestream disturbance model or differences caused by the geometry of the simulated body they each offer a somewhat incomplete view of these effects. This work aims to further expand on this line of research and more fully investigate the effects of bluntness on broadband receptivity.

Extremely large nose bluntnesses have also been observed to result in a reversal in the stabilization phenomenon, causing transition much earlier than expected[29, 32, 78]. Studies have shown that the second mode is unlikely to be the primary driver of this early transition, as stability theory predicts that large nose bluntnesses are consistently stabilizing to this mode, and the true cause of the reversal phenomenon remains an open question. Several potential factors such as entropy layer instabilities, increased sensitivity to local surface roughness, and non-modal disturbance growth have been proposed as potential causes of this behavior[33, 34]. However, this reversal phenomenon has not been definitively characterized and remains an area of active interest. Recent efforts have focused on investigating the impact of non-modal disturbance growth on the transition reversal phenomenon observed at large bluntnesses, as well as on the reduced stabilizing effect of intermediate nose bluntness. Reshotko and Tumin[36, 79, 14, 13] proposed that transient growth of locally stable, non-orthogonal instability modes could lead to algebraically amplified disturbances that can induce early transition through the bypass mechanism mentioned previously. Paredes, et al. [8, 35, 80] continued in this line of research and investigated the non-modal growth of disturbances near the frustum of blunt cones to attempt to explain the reversal phenomenon. Similarly to Goparaju, Unnikrishnan and Gaitonde[59] they found that traveling disturbances in the entropy layer experienced non-modal excitation and could, under certain circumstances, replicate the reversal observed in experiment though it is still unclear whether this is the universal cause of the reversal phenomenon.

1.3.4 Multimode Decomposition

The direct numerical simulation of hypersonic flows provides several prominent advantages over experiments in terms of investigating the stability and receptivity characteristics of a flow of interest. In terms of overall costs simulations allow for much more rapid testing and analysis, and do not have the extreme costs associated with constructing, validating, and maintaining a flight facility capable of running at hypersonic flow conditions. Additionally, limits on instrumentation often cause the flow field data measured in hypersonic experiments to be incomplete either in the scope of their measured flow variables or in the limited number of sampling points available. On the other hand, advanced simulations can be performed relatively easily with available high performance computing resources. These simulations can provide complete information of all of the pertinent variables in the flow field to a high degree of precision.

While this complete information is highly useful to characterizing the stability characteristics of the flow field, the disturbance profile can be greatly complicated by the presence of many unique continuous and discrete instability modes that are present in unbounded hypersonic flows[81]. The complex interactions between modal components of the boundary layer disturbances in combination with non-modal noise can muddle the signal of the primary modes of interest throughout the domain[82]. As such, methodologies to separate out and isolate modes of particular interest are also useful to studies of receptivity. This current work uses a simple modal decomposition method originally utilized by Huang and Zhong[4, 72] and proposed by Schneider[73] in which the unsteady DNS signal is sampled at a point at which the second mode is predicted through LST to be dominant. This value is then re-normalized by the LST-calculated amplification factor in order to backtrace the initial amplitude of the second mode disturbance for a given frequency. When repeated, this allows for a receptivity coefficient spectrum to be extracted from the simulations. Though this method can successfully extract the second mode receptivity coefficients in many cases, it cannot isolate other modal disturbances that may be of interest. For this, a more rigorous multimode decomposition method is necessary.

Tumin [79, 83] developed a multimode decomposition framework recently which has seen further development by Miselis [84]. The fundamental concept of this multimode decomposition is based on solving the linearized compressible Navier-Stokes equations using a combination of Fourier and Laplace transforms. Using orthogonality relationships, the discrete and continuous spectrum of disturbance modes can be isolated in a given flow field. The resulting differential equations differ from the traditional LST system and are solved using an asymptotic method in which the solutions are found at the freestream and integrated back towards the wall. While the general toolset has been developed, multimode decomposition has yet to see widespread application. However, it's ability to extract the behaviors of multiple continuous and discrete boundary layer disturbance modes may help further clarify the many complex mechanisms governing receptivity and hypersonic boundary layer transition in general.

1.4 Applications of Spectral Receptivity Data

1.4.1 non-linear Breakdown

Receptivity data has potential applications in several areas. For instance, the initial disturbance amplitudes derived from receptivity studies can be used to provide initial forcing conditions to non-linear breakdown studies such as Sivasubramanian's and Fasel's[85] or Hader and Fasel's[5]. In particular, common receptivity data for the second mode is useful to identify and characterize the fundamental breakdown mechanisms associated with the second mode and the transition to turbulence that it causes. The breakdown mechanisms preceding turbulence are characterized by large amplitude disturbances which experience strong non-linear interactions, generating the structures that cause the flow to fully transition into turbulence. These finite amplitude disturbances arise when the initial disturbances induced by the receptivity mechanisms of the flow to external forcing experience sufficient linear amplification, as shown in Fig. 1.6. By directly simulating these non-linear disturbance interactions insight can be gleaned into the mechanisms and structures that cause the eventual breakdown into turbulence.

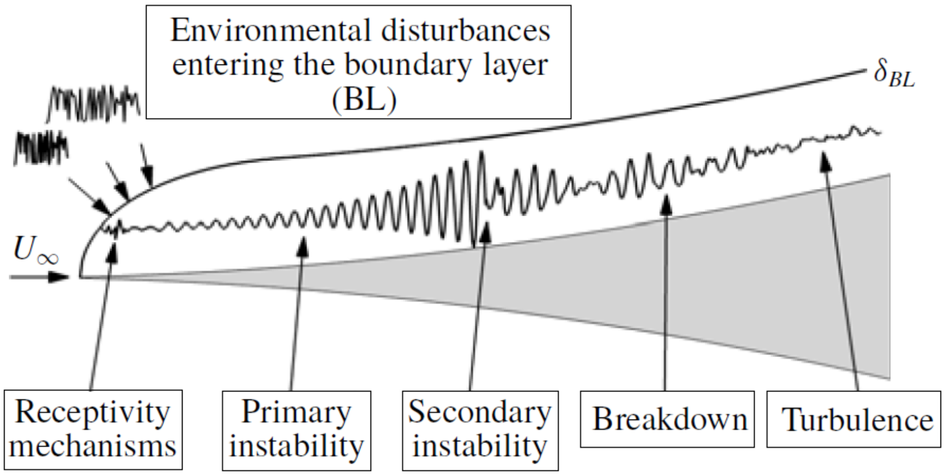

Figure 1.6: Schematic diagram of a linear path to turbulence including breakdown, adapted from Hader and Fasel[5].

For the low-noise transition path with which this work is focused, the fundamental breakdown mechanisms occur only when boundary layer disturbances are sufficiently amplified as to generate non-linear interactions. Due to the weak nature of the initial disturbances in this case, the perturbations only become sufficiently amplified at locations far downstream of the leading edge on a given geometry. Thus, in order to simulate non-linear breakdown, sufficient upstream disturbance data is required. This can be derived from directly simulating the receptivity mechanisms and disturbance amplification upstream on the geometry. However, this can become prohibitively expensive due to the large domain size and strict requirements on spatial resolution in order to capture the disturbance modes of interest. Receptivity results can instead be used to reconstruct disturbance inlet conditions, which allows simulations to begin at downstream regions along the domain. This can dramatically reduce both the necessary computational cost and time of these downstream simulations[63, 86].

1.4.2 Transition Prediction

The most direct application of receptivity data is to the development of improved transition estimation methods. Due to past constraints on computational power, simplified stability theory models have traditionally been utilized to track the development of instabilities in hypersonic flows. Linear stability theory (LST) which linearizes the Navier-Stokes system and tracks the development of modal instabilities has seen the most widespread historical application[23], though parabolized stability equations (PSE) have also risen in prominence to account for non-parallel and non-linear effects[87]. Both methods simplify the compressible Navier-Stokes equations, resulting in significantly cheaper computations which may be used to track the development of boundary layer disturbance modes. LST, as mentioned previously, assumes small amplitude disturbances. This allows the Navier-Stokes system to be linearized, into which a normal mode wave-like disturbance form is assumed to further reduce the system into a set of ordinary differential equations that can be resolved using a standard eigenvalue solver. The PSE system follows a similar derivation, though the assumption of a quasi-parallel (non-growing) boundary layer is relaxed in this case. This no longer allows the system to be reduced into a set of ODE's, and requires the application of streamwise marching schemes. Using either method the local growth rate of a given disturbance mode can be calculated, which when integrated becomes the amplification ratio or N-factor. Both methodologies have seen success and have been applied to transition prediction schemes, though by themselves they neglect the contribution of receptivity mechanisms to a flow's disturbance profile.

Current transition prediction procedures, such as the e^N method, rely on using growth rates for these modal instabilities derived from LST or PSE to determine the relative amplification of boundary layer disturbances. Empirically determined amplification threshold values are then used to predict the onset of turbulent transition[88, 43, 62]. This prediction approach assumes that this relative amplification is the most critical factor in determining transition and often ignores the receptivity mechanisms which govern the initial amplitudes of the disturbances themselves. While this assumption can provide good internal consistency in a given experimental environment, transition thresholds based on this methodology can vary significantly between different experiments. For instance, Schneider[41] described experiments with similar nominal freestream conditions that had threshold N-factors of 5 and 8. This difference is attributed to the high-degree of variabilitiy in freestream noise profiles between different experimental environments. Many older hypersonic windtunnel facilities operate with freestream noise levels far in excess of what is expected in atmospheric flight and which has not been rigorously quantified. Only recently have more advanced ”quiet” windtunnel facilities been constructed[73] and more focus been made to characterize the noise profile present in experimental setups[89, 68, 38]. Variability of this degree prevents the widespread application of uncorrected prediction results between experiments. The freestream noise in these experimental facilities comes primarily in the form of acoustic waves radiated from turbulent boundary layers on the tunnel walls[73, 89], though freestream turbulence and laser excitation can generate vorticity and entropy disturbances as well. Thus, it can be seen that neglecting the receptivity mechanisms which govern the amplitudes of the initial boundary layer disturbances can cause significant discrepancies in conventional transition prediction methodologies. While the standard e^N method is still widely used, the threshold criterion that are utilized cannot be easily generalized between cases that have significantly different freestream noise environments.

A number of improved transition prediction methodologies have seen increased interest recently to overcome some of the limitations of the traditional e^N method. Crouch and Ng[88] proposed a variable N-factor method that corrects the traditional e^N method through fitting a variation of the N-factor with a simplified model of the freestream response. This has the advantage of requiring no additional computations after the disturbance response and linear growth (N-factor) data are first obtained. Other improved transition prediction models are based on the amplitude method proposed by Mack[90]. Conventional estimation methods generally focus on the single most amplified disturbance frequency, and use the relative amplification of that single frequency to gauge the instability of a given flow. However, this does not adequately represent the highly broadband nature of disturbances that are present in a hypersonic boundary layer[90, 62]. Mack's proposed amplitude method suggested integrating across both the spanwise wavenumber and frequency spectra, centered about the most unstable wavenumber and frequency, in order to directly estimate the disturbance amplitude level in the boundary layer at a given position. These could then be used to better gauge the actual disturbance level in a flow and potentially predict transition more accurately. Ustinov[91] extended this amplitude method to investigate laminar-turbulent transition on a swept wing using a combined amplitude criterion for steady state and time dependent perturbations in the flow. They found that this method successfully reproduced experimentally observed dependencies on Reynolds number, local surface roughness, and freestream turbulence.

The amplitude method as originally proposed by Mack is simple at a glance, but requires specific instances of data that may either be difficult to obtain or efficiently calculate. For instance, while the method requires the disturbance to be integrated across it's frequency and wavenumber spectra, for a highly amplified discrete mode only a finite band of disturbances actually contributes in any reasonable amount to the overall amplitude of the perturbation. Thus, approximations of significant bandwidths must be made to improve the efficiency of calculations. Additionally as the amplitude method directly approximates the disturbance amplitudes themselves, experimental, theoretical, or computational receptivity coefficients along with disturbance field data is critical. As mentioned previously, many prior receptivity results are either based on highly empirical fits of experimental data or only have data for discrete frequencies at very specific configurations. Thus, more comprehensive receptivity correlations are critical to the further development of amplitude methods.

Several studies have presented attempts to simplify the amplitude method relation for modern application purposes. In a recent paper Fedorov and Tumin[92] suggest evaluating the integral using an asymptotic method approach in order to increase the computational efficiency of the method without relying on overly extreme simplifications. Marineau[6] instead uses an iterative scheme based on correlated experimental and computational data to approximate the amplitude method integral for a selection of sharp and blunt cone cases from the AEDC windtunnel 9. The iterative procedure developed by Marineau is presented in Fig. 1.7.

In this procedure, an initial guess is first made for the transition location. Based on this guess, the edge Mach number and the frequency of the strongest second mode disturbance are extracted from DNS and LST/PSE. These results are then fed into correlations to generate initial guesses for the maximum disturbance amplitude at transition and for experimental freestream noise. This noise amplitude is then used along with the most unstable second mode frequency to estimate the initial amplitude of the disturbance using an empirical receptivity correlation. Finally, the updated transition position estimate is made using a amplitude threshold based on maximum breakdown amplitudes. This procedure is repeated until satisfactory convergence [6]. Marineau showed that this method could predict transition for blunt cones and cones at angles of attack much more accurately than more traditional e^N methods, though issues were still observed for some cases. In particular, it was shown that the accuracy of the amplitude method-based prediction methodology became significantly worse for blunt cones, which indicate some inadequacies in his model. This may come from the receptivity correlations applied in Marineau's study which utilized highly empirical receptivity correlations derived from limited experimental data. Utilizing receptivity spectra derived from DNS simulations may provide improved precision to the initial ampitude calculations and potentially help to further improve the accuracy of these alternative transition estimation methods.

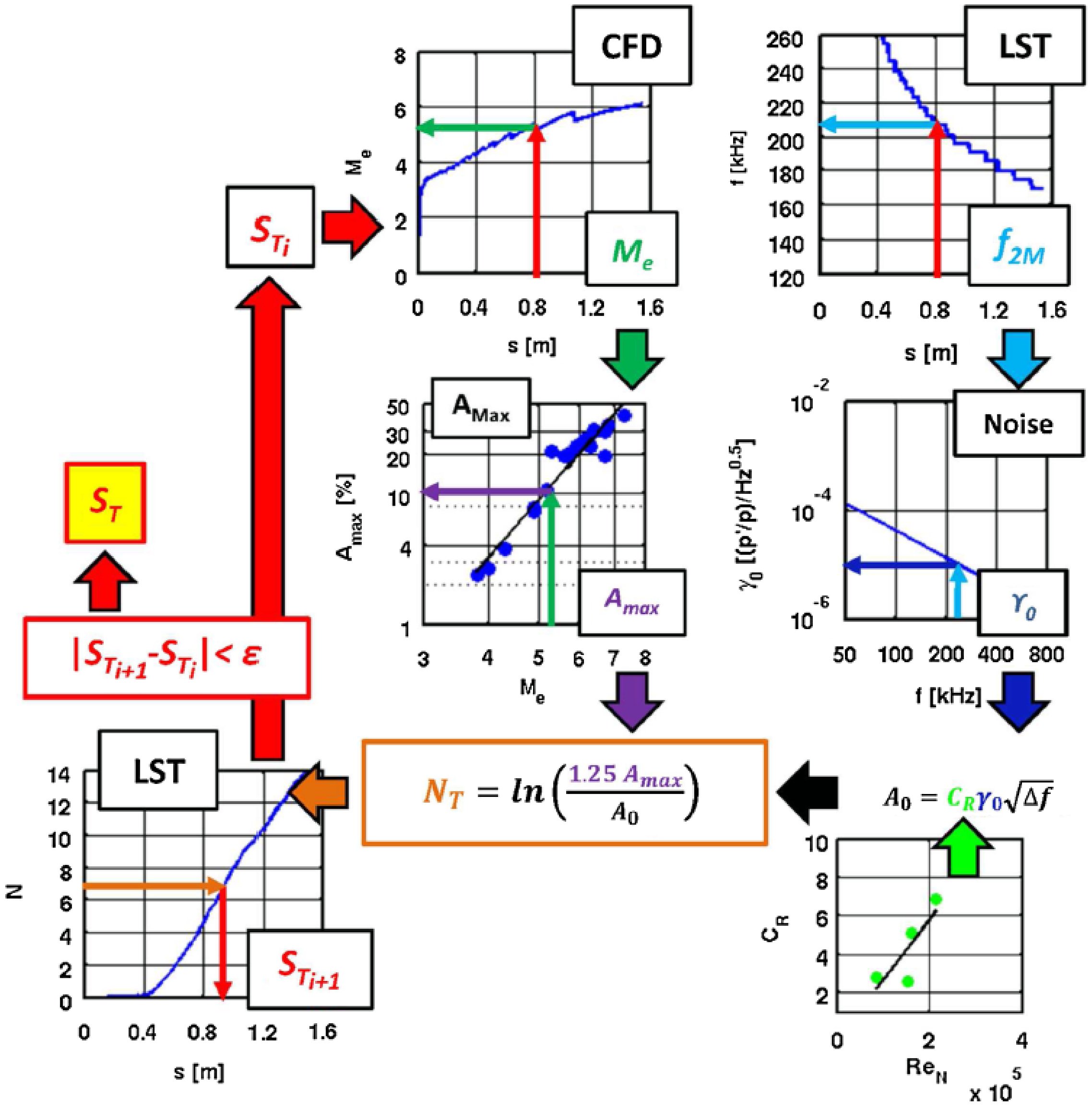

Figure 1.7: Iterative algorithm to estimate the start of transition, adapted from [6].

1.5 Motivation and Research Objectives

1.5.1 Objectives

While receptivity itself has been and continues to be an active area of study in the field of hypersonics, a large majority of past work has focused primarily on the response to discrete frequency disturbances [33, 62, 44, 2, 55, 12, 67]. In order to more accurately represent the noise environments present in flight and experiment receptivity studies must be expanded to consider broadband noise. While work by Goparaju, et al.[59], Chuvakhov, et al.[46], Huang and Zhong[4], and Balakumar and Chou[62] have investigated broadband disturbances, these individual studies have not attempted to characterize the general response to different freestream disturbance types as well as generate spectral receptivity coefficients for additional application. Additionally, while the effects of nose bluntness on the stability of hypersonic flows has been of great interest for many years there is relatively little work attempting to link the effects of nose bluntness on the receptivity to freestream disturbances. This is especially true for the case of broadband perturbations.

The current study presents a novel consideration of multiple disturbance types in order to generate a more complete view of the receptivity response of blunt cones to broadband frequency freestream pulse disturbances. Previous receptivity studies of similar geometries have focused primarily on less realistic discrete frequency disturbances, or very specifically on small selections of broadband acoustic or temperature disturbances. While these prior works provide valuable insight into the complex receptivity mechanisms present in hypersonic flow over blunt cones, a more complete overview of the disturbance responses is necessary to fully characterize receptivity. The receptivity mechanisms for both finite, spherical and planar geometry pulses are investigated. Fast acoustic, slow acoustic, temperature, and vorticity disturbances are modelled using both of the pulse geometries for a total of eight unsteady cases for each of two blunt cone meanflows. The baseflows are based on experiments by Marineau et al.[7] for Mach 10 flow over a selection of sharp and blunt cones from the AEDC windtunnel 9. Additionally, a meanflow for a sharper nose case also based on tunnel conditions from Marineau et al.'s work is also converged for a preliminary investigation of an azimuthally varying 3-D pulse.

The receptivity of these cones is investigated using both DNS and LST to track to the development of modal disturbances in the boundary layer. Based on these simulations, receptivity coefficients are generated for the dominant second mode instability for each of the meanflow geometries to the eight freestream pulse disturbances discussed previously. The resulting receptivity spectra are then applied to Marineau's[6] approximation of Mack's Amplitude method[93]. Additionally, the effects of nose bluntness on the receptivity response of the flow fields is investigated to further clarify the coupled effect of this design parameter on the stability of hypersonic flows. Finally, preliminary analysis of 3-D acoustic pulses over a small bluntness straight cone is performed to extend our analysis to more complex disturbances that may be present in general flight conditions. This work aims to further study the complex receptivity mechanisms associated with a wide range of different broadband disturbances and provide a basis for the further development of transition prediction methodologies.

1.5.2 Approach

For the axisymmetric pulse cases the numerical study in this paper consists of three primary components: (1) the steady base flow simulation and LST analysis, (2) the unsteady DNS simulation using the freestream pulse disturbances, and (3) the generation of the spectral receptivity coefficients by combining the LST and unsteady DNS results. First, steady meanflows are converged based on the geometry and freestream conditions presented by Marineau et al.[7] for their experiments in the AEDC windtunnel 9. The converged meanflows from these steady simulations are analyzed using LST to predict the unstable second mode frequencies and their relative amplifcation along the geometries. Unsteady DNS is also be used to perturb these meanflows with freestream acoustic, temperature, and vorticity pulse disturbances that are designed to encompass the range of unstable second mode frequencies. The peak freestream amplitudes of these disturbances are chosen from prior experience to ensure linear disturbance development throughout the pertinent flow domain. A Fourier spectral decomposition is then used to decompose the unsteady surface pressure perturbation data into it's discrete frequency components from which spectral surface pressure and disturbance phase angle can be extracted. The LST results will then be used to identify modal disturbances in the unsteady DNS results and validate the observed disturbance patterns in the boundary layer. Finally receptivity coefficients for the second mode, which are defined as the initial amplitudes of the second mode disturbance at the beginning of the unstable region, will be isolated from the unsteady DNS by normalizing the sampled spectral disturbance data with LST-derived amplification factors (N-factors).

Preliminary 3-D receptivity analysis is also performed on a sharper cone based on wind-tunnel conditions from Marineau, et al.[7]. The meanflow is converged to a length of 0.5 m to account for the more stringent comptutational requirements of the 3-D disturbance. The sharper nose of the case ensures that significant second mode amplificaiton should still occur, however. Axisymmetric LST is also performed to identify the primary band of unstable frequencies. 2-D planar acoustic pulses are advected through the domain and the results are compared with the blunter cone cases. 3-D pulses modelled with gaussian distributions along the axis of symmetry and the azimuthal direction are also advected, with the surface results being decomposed at various streamwise positions to track the development of disturbances in the boundary layer.

The axisymmetric pulse receptivity data is applied to the iterative amplitude method presented by Marineau[39] in an attempt to further refine his results. Freestream acoustic noise profiles are fit according to relations reported by Marineau[39] and Balakumar and Chou[62]. Additional necessary data such as edge mach number profiles, the most unstable LST frequencies, and the maximum N-factor profiles of the geometries are produced and applied to the iterative scheme. The results are then compared against Marineau's original experimental cases.

1.5.3 DNS Cases

Table 1.1: Freestream flow conditions for DNS simulations.

Case	R_n (mm)	M_∞	$h_{0,\infty}$ (MJ/kg)	ρ_∞ (kg/m^3)	p_∞ (kPa)	T_∞ (K)	U_∞ (m/s)	Re/m $(1E6/m)$
B	9.525	9.79	1.07	0.0427	0.65	51.0	1426	18.95
I	5.080	9.81	1.06	0.0422	0.64	50.8	1425	19.11
S	1.0	9.6	1.06	0.0168	0.27	54.6	1446	7.09

The first part of this investigation focuses on two primary cone geometries derived from Marineau et al.'s[7] experiments. These include Case B with a 9.525 mm nose radius based on run 3752 and Case I with a 5.080 mm nose radius based on run 3746. Both of these cases

Table 1.2: Freestream disturbance case labels for axisymmetric unsteady DNS.

Disturbance Type	Case B	Case I
Finite Spherical Fast Acoustic	B1	I1
Finite Spherical Slow Acoustic	B2	I2
Finite Spherical Temperature	B3	I3
Finite Spherical Vorticity	B4	I4
Planar Fast Acoustic	B5	I5
Planar Slow Acoustic	B6	I6
Planar Temperature	B7	I7
Planar Vorticity	B8	I8

were at 0° angle of attack. These cases otherwise share very similar freestream parameters. The cases were chosen due to the detailed transition data available for them and because they were seen to experience significant second mode disturbance growth. A third Case S with a 1.0 mm nose radius is also converged in order to perform 3-D receptivity analysis. This sharper nose case is based on another set of runs from Marineau, et al.'s experiments which represent higher atmospheric conditions. The smaller effective bluntness of this case also improves the numerical stability of the shock-fitting algorithm for 3-D simualtions, which otherwise has difficulties resolving 3-D geometries in the nose region for the blunter cases.

The cone geometry for Case B is 1.9 m in length, for Case I it is 1.5 m in length, and for Case S it is 0.5 m in length. The DNS simulations used 240 points in the wall-normal direction and roughly five points per millimeter on the surface of the cone in the streamwise direction. Four points are used in the periodic spanwise direction for the axisymmetric cases, though only one point is directly calculated at each timestep. The azimuthal grid density is expanded to 32 points that are all directly calculated for Case S. This density was chosen as the azimuthal pulse is constrained to excite only a small selection of lower wave number modes. The flow conditions for this study are summarized in Table 1.1. The wall temperature is fixed utilizing the ratio $T_w/T_{0,\infty} = 0.3$, which leads to relatively warm wall conditions. These are traditionally stabilizing to supersonic mode instabilities, especially in the low enthalpy flows considered in this study. However, it is shown later that unsteady broadband disturbances are also capable of inducing qualitatively observable supersonic modes. The Prandtl number is also fixed to a value of $Pr = 0.72$ in all cases.

The axisymmetric unsteady DNS cases are differentiated based on both the freestream disturbance type and the disturbance geometry. Two pulse geometries will be used for the axisymmetric receptivity and nose bluntness investigation: a finite, spherical geometry and a planar geometry that is finite in x but infinite in the y-z plane. These cases are listed and labelled in Table 1.2 below for Case B and Case I. The details of the pulse geometries and freestream disturbance formulations are given in section 3.3.

The DNS code used in this study utilizes a shock-fitting formulation with the parameters in Table 1.1 defining the freestream conditions upstream of the shock formed over the body. Marineau et al.[7] used curve fits of experimental data to generate the viscosity used for the Reynolds number calculations instead of Sutherland's Law. This lead to approximately a 15% increase in the calculated freestream unit Reynolds numbers between this work and Marineau's.

CHAPTER 2

Governing Equations

The solution methods for the DNS and LST codes were originally developed and implemented by Zhong and Ma citezhong1998,ma2005 and are formulated for a calorically perfect gas. This assumption was made based on the low freestream stagnation enthalpy reported in Table 1.1 for all of these test conditions, as determined by prior experience. While the extreme conditions that define hypersonic flow are highly conducive to thermal and chemical nonequilibrium as previously studied in works such as Mortensen and Zhong[48, 94], Knisely and Zhong[3, 24, 25], and by Prakash, et al.[95], at certain low enthalpy atmospheric conditions the calorically perfect gas assumption has been found to be sufficient.

The freestream parameters modelled in this study are more consistent with upper atmospheric conditions. Under these relatively low density, low pressure model conditions the flow is expected to experience minimal thermochemical effects. The formulation of the governing equations is highlighted here for clarity. The three-dimensional Navier-Stokes equations in conservative form consist of a single species mass conservation equation, three momentum conservation equations, and the energy equation. The governing equations in vector form are written as

$$\frac{\partial U}{\partial t} + \frac{\partial F_j}{\partial x_j} = \frac{\partial G_j}{\partial x_j}, \ \ (j = 1, 2, 3) \tag{2.1}$$

where U is the state vector of conserved quantities, F_j is the inviscid flux vector, and G_j is the viscous flux vector. Here, the j indices indicate cartesian coordinates with the x axis running parallel to the central axis of symmetry of the cone. The conservative vector U is comprised of five conservative flow variables for mass, momentum, and energy:

$$U = \begin{bmatrix} \rho & \rho u_1 & \rho u_2 & \rho u_3 & e \end{bmatrix}^T \tag{2.2}$$

Additionally, the inviscid F_j and viscous G_j flux vectors are written as:

$$F_j = \begin{bmatrix} \rho u_j \\ \rho u_1 u_j + p\delta_{1j} \\ \rho u_2 u_j + p\delta_{2j} \\ \rho u_3 u_j + p\delta_{3j} \\ (e+p)u_j \end{bmatrix} \tag{2.3}$$

$$G_j = \begin{bmatrix} 0 \\ \tau_{1j} \\ \tau_{2j} \\ \tau_{3j} \\ \tau_{jk}u_k - q_j \end{bmatrix} \tag{2.4}$$

Since this study assumes a calorically perfect gas, the system of equations is closed by the perfect gas equation of state:

$$p = \rho R T \tag{2.5}$$

along with additional transport equations:

$$e = \rho(C_v T + \frac{1}{2}u_k u_k) \tag{2.6}$$

$$\tau_{ij} = \mu(\frac{\partial u_i}{\partial x_j} + \frac{\partial u_j}{\partial x_i}) - \lambda\frac{\partial u_k}{\partial x_k}\delta_{ij} \tag{2.7}$$

$$q_j = -\kappa\frac{\partial T}{\partial x_j} \tag{2.8}$$

Furthermore, the viscosity coefficent μ is calculated through Sutherland's law for nitrogen gas

$$\mu = \mu_r \left(\frac{T}{T_0} \right)^{\frac{3}{2}} \frac{T_r + T_s}{T + T_s} \tag{2.9}$$

In these equations R is the gas constant while c_p and c_v are the constant pressure and constant volume specific heats respectively. These values are assumed to be constant for a given ratio of specific heats γ. Here, the environment is assumed to be composed entirely of diatomic nitrogen which results in $\gamma = 1.4$. The coefficient λ is assumed to be $-2\mu/3$ and the heat conductivity coefficient κ is computed through a fixed Prandtl number of 0.72 in all steady meanflow and unsteady DNS simulations.

CHAPTER 3

Numerical Methods and Disturbance Model

3.1 DNS

The DNS code utilizes a high-order shock-fitting method for a perfect gas flow that was developed to compute the flow field surrounding a blunt cone moving at hypersonic speeds. The numerical method is summarized here for clarity. First, the Navier-Stokes equations are transformed into computational space

$$\frac{1}{J}\frac{\partial U}{\partial \tau}+\frac{\partial E'}{\partial \xi}+\frac{\partial F'}{\partial \eta}+\frac{\partial G'}{\partial \zeta}+\frac{\partial E'_v}{\partial \xi}+\frac{\partial F'_v}{\partial \eta}+\frac{\partial G'_v}{\partial \zeta}+U\frac{\partial (1/J)}{\partial \tau}=0 \tag{3.1}$$

where J is the Jacobian of the coordinate transformation and (ξ, η, ζ) are the transformed computational coordinates in the streamwise, radial, and azimuthal directions of the cone. The original curvilinear coordinates of the grid are converted using a coordinate transformation in order to better facilitate the application of high-order finite difference stencils. This transformation is given in Eq. 3.2.

$$\begin{cases} \xi = \xi(x,y,z) \\ \eta = \eta(x,y,z,t) \\ \zeta = \zeta(x,y,z) \\ \tau = t \end{cases} \Longleftrightarrow \begin{cases} x = x(\xi,\eta,\zeta,\tau) \\ y = y(\xi,\eta,\zeta,\tau) \\ z = z(\xi,\eta,\zeta,\tau) \\ t = \tau \end{cases} \tag{3.2}$$

A schematic diagram showing the resulting curvilinear grids in physical coordinates is presented in Fig. 3.1. The grids are heavily coarsened in this schematic in comparison to the actual simulations in order to improve visual clarity. An exponential stretching function is used to concentrate wall-normal grid points near the surface of the cone in order to effectively resolve the sharp gradients present in the boundary layer.

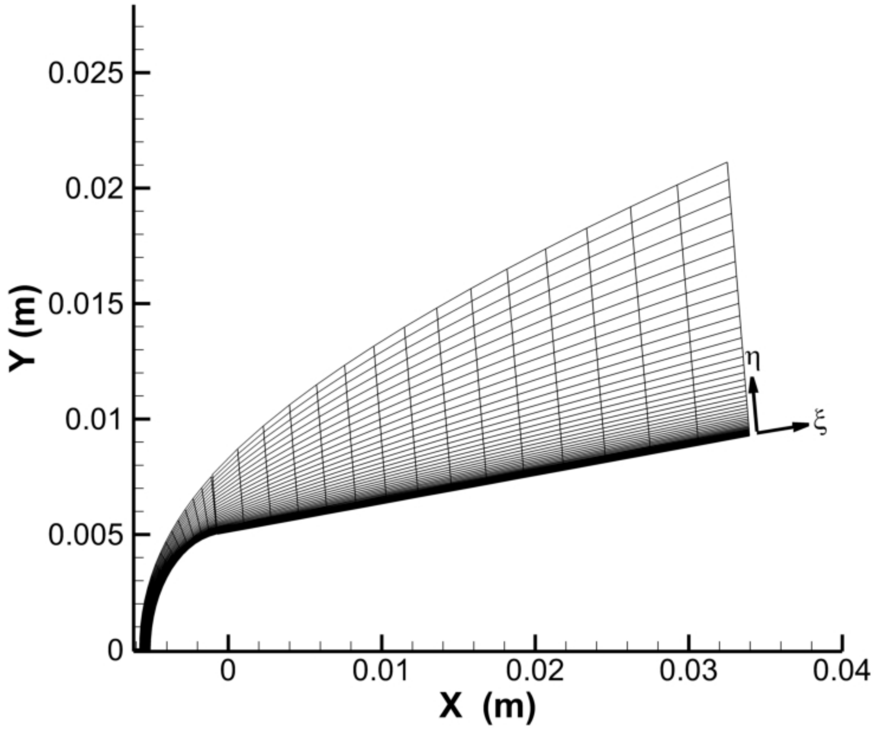

Figure 3.1: Schematic diagram of grids near the nose/frustum region of a cone. Grids are coarsened from an actual simulation to improve clarity.

The transformed fluxes in the computational coordinates are then given by

$$E' = \frac{F_1\xi_x + F_2\xi_y + F_3\xi_z}{J} \tag{3.3}$$

$$F' = \frac{F_1\eta_x + F_2\eta_y + F_3\eta_z}{J} \tag{3.4}$$

$$G' = \frac{F_1\zeta_x + F_2\zeta_y + F_3\zeta_z}{J} \tag{3.5}$$

$$E'_v = \frac{G_1\xi_x + G_2\xi_y + G_3\xi_z}{J} \tag{3.6}$$

$$F'_v = \frac{G_1\eta_x + G_2\eta_y + G_3\eta_z}{J} \tag{3.7}$$

$$G'_v = \frac{G_1\zeta_x + G_2\zeta_y + G_3\zeta_z}{J}. \tag{3.8}$$

A low-dissipation, fifth-order upwinded stencil is used for the inviscid fluxes while a sixth-order central stencil is used to discretize the viscous terms as shown in Eq. 3.9.

$$\frac{\partial f_i}{\partial x} = \frac{1}{hb_i}\sum_{k=-3}^{3} \alpha_{i+k} f_{i+k} - \frac{\alpha}{6!b_i}h^5\left(\frac{\partial f^6}{\partial^6 x}\right) \tag{3.9}$$

where the coefficients α and b are defined as

$$\begin{aligned}
\alpha_{i\pm3} &= \pm1 + \frac{1}{12}\alpha, & \alpha_{i\pm2} &= \mp9 - \frac{1}{2}\alpha \\
\alpha_{i\pm1} &= \pm45 + \frac{5}{4}\alpha, & \alpha_i &= -\frac{5}{3}\alpha \\
b_i &= 60
\end{aligned}$$

Here, h is the step size, $\alpha < 0$ generates an upwind explicit scheme, and $\alpha = 0$ leads to a central scheme. In this study the inviscid terms use $\alpha = -6$ for a low dissipation fifth order upwinded difference, and the viscous terms are again discretized with a sixth order central scheme using $\alpha = 0$. Flux derivatives in the azimuthal direction are calculated using a spectral Fourier collocation method due to the axisymmetry of the cone geometry. To compute second derivatives, the first order derivative operator is applied twice. Flux splitting is applied to the inviscid fluxes with a local Lax-Friedrichs formulation, resulting in

$$F = F^+ + F^- \tag{3.10}$$

where the matrices $F^\pm$ are defined as

$$F^\pm = \frac{1}{2}(F \pm \Lambda U) \tag{3.11}$$

and Λ is a diagonal matrix that ensures that F^+ contains only positive eigenvalues and F^- contains only negative eigenvalues.

In the shock-fitting formulation the shock itself is treated as a computational boundary at

$$\eta(x, y, z, t) = \eta_{max} = constant \tag{3.12}$$

Since the shock position isn't stationary, the grids are also a function of time. The shock position can then be solved for simultaneously as another independent variable at each timestep.

The flow variables after the shock are determined through a combination of the Rankine-Hugoniot relations across the shock and a characteristic compatibility relation behind the shock. Additionally, the position $H(\xi, \zeta, \tau)$ and velocity $H_\tau(\xi, \zeta, \tau)$ of the bow shock in computational coordinates are also concurrently solved at each timestep with the other flow variables. Isothermal and viscous boundary conditions are imposed at the cone surface where the wall temperature ratio is fixed as $\frac{Tw}{T_0} = 0.3$. High order extrapolation is utilized at the domain outlet. Finally, the solution is advanced in time using a selection of low-storage Runge-Kutta (RK) methods from Williamson[96]. Both 1st order and 3rd order explicit RK methods are utilized depending on the flow regions. Additional details of this shock-fitting formulation and the general numerical method can be found in Zhong[97].

3.2 LST

The linear stability analysis (LST) implementation used in this study was originally developed and verified by Ma and Zhong[12, 2, 55, 60] and then extended to study perfect gas flow over cone geometries by Lei and Zhong[34] and Huang and Zhong[4]. The LST relations are derived from the governing Navier-Stokes equations in Eq. 2.1 by substituting in the instantaneous flow, which can be decomposed into a mean and fluctuating component:

$$q(x, y, z, t) = \overline{q}(x, y, z) + q'(x, y, z, t) \tag{3.13}$$

Here $q(x, y, z, t)$ is the total instantaneous flow for a given dsturbance variable, $\overline{q}(x, y, z)$ is the mean component, and $q'(x, y, z, t)$ is the fluctuating component. This instantaneous flow is then reintroduced into the governing equations. Since the steady mean flow component is assumed to satisfy the governing equations, the meanflow contribution can be subtracted out of the total system. To further simplify the calculations the mean flow is then assumed to be both axisymmetric/2-D and quasi-parallel to reduce any remaining meanflow terms to functions of only y.

$$\overline{q}(x,y,z) = \overline{q}(y) \tag{3.14}$$

The disturbances are assumed to be small enough that they remain in the linear regime, thus quadratic and higher order perturbation terms (q') are cancelled out. The linearized governing equations can then be written in the form

$$\begin{multline}\tilde{\Gamma}\frac{\partial q'}{\partial t} + \tilde{A}\frac{\partial q'}{\partial x} + \tilde{B}\frac{\partial q'}{\partial y} + \tilde{C}\frac{\partial q'}{\partial z} + \tilde{D}q' + \tilde{V}_{xx}\frac{\partial^2 q'}{\partial x^2} + \tilde{V}_{yy}\frac{\partial^2 q'}{\partial y^2} \\ + \tilde{V}_{zz}\frac{\partial^2 q'}{\partial z^2} + \tilde{V}_{xy}\frac{\partial^2 q'}{\partial x \partial y} + \tilde{V}_{xz}\frac{\partial^2 q'}{\partial x \partial z} + \tilde{V}_{yz}\frac{\partial^2 q'}{\partial y \partial z} = 0 \end{multline} \tag{3.15}$$

The system is further simplified by the introduction of a normal mode wave solution in the form of $q' = \hat{q}(y)\exp\left[i\left(\alpha x + \beta z - \omega t\right)\right]$, where ω is the circular frequency of the disturbance and α and β are the spatial wavenumbers of the x streamwise and z spanwise coordinates respectively. In this study we primarily focus on a 2-D spatial stability approach. For this spatial stability approach the circular frequency of a disturbance mode, ω^* defined as $\omega = 2\pi f$, must be manually set at a real number while β is set to 0 for a two dimensional disturbance. This ω is chosen based on whatever particular disturbance frequency is of interest. Under this approach the wavenumber α is complex and results in the dispersion relation $\alpha = \Omega(\omega, \beta)$. The complex spatial wavenumber α can be written as $\alpha = \alpha_r + i\alpha_i$. Here, $-\alpha_i$ is defined as the growth rate of the disturbance. With these assumptions the problem can now be reduced to a coupled set of 5 ordinary differential equations defined in Eq. 3.16.

$$\left(\mathbf{A}\frac{d^2}{dy^2} + \mathbf{B}\frac{d}{dy} + \mathbf{C}\right)\vec{\phi} = \vec{0}. \tag{3.16}$$

where $\vec{\phi} = \left[\hat{u}, \hat{v}, \hat{P}, \hat{T}, \hat{w}\right]^T$ comprises the disturbance eigenfunctions of the system and $\mathbf{A}$, $\mathbf{B}$ and $\mathbf{C}$ are complex square matrices of size 5. This is now a boundary value problem where the derivative operators can be discretized and the equations solved numerically. The boundary conditions for Eq. 3.16 are defined as:

$$y = 0; \qquad \phi_1 = \phi_2 = \phi_3 = \phi_4 = \phi_5 = 0 \tag{3.17}$$

$$y \to \infty; \qquad \phi_1, \phi_2, \phi_3, \phi_4, \phi_5 \to 0 \tag{3.18}$$

These conditions ensure that the resulting disturbances remain bounded in the unbounded flow domain about a cone geometry. The final system of equations is solved using using a multi-domain spectral method based on Malik's[98] which allows for clustering of points near domains of interest.

The wavenumber results from spatial LST can also be used to derive the characteristic phase speed of a disturbance. The non-dimensional phase speed of a disturbance is defined from LST as

$$c_r = \frac{(\omega^*/U^*_\infty)}{\sqrt{\beta^2 + \alpha_r^2}} \tag{3.19}$$

which, for a two-dimensional disturbance, can be reduced to

$$c_r = \frac{(\omega^*/U^*_\infty)}{\alpha_r} \tag{3.20}$$

This phase speed is non-dimensionalized by the characteristic freestream velocity. The results of spatial LST can be further non-dimensionalized using the local Reynolds number R for streamwise position and a non-dimensional frequency F. These are quantities are defined as:

$$R = Re_x^{1/2} = \sqrt{\frac{\rho^*_\infty U^*_\infty s}{\mu^*_\infty}} = \frac{\rho^*_\infty U^*_\infty L^*}{\mu^*_\infty} \tag{3.21}$$

$$F = \frac{\omega^* \mu^*_\infty}{\rho^*_\infty U^{*2}_\infty} \tag{3.22}$$

where additional spatial non-dimensionalization is performed using a local boundary layer height parameter L^*, that is based on the local streamwise position and freestream parameters. L^* is defined in Eq. 3.23.

$$L^* = \sqrt{\frac{\mu^*_\infty s^*}{\rho^*_\infty U^*_\infty}} \tag{3.23}$$

While LST can be used to identify both the unstable disturbance frequencies and their growth rates, it does not directly specify the exact amplitude of the disturbance. As discussed in Chapter 1, boundary-layer transition is conventionally estimated using LST or PSE through an amplification criterion known as the e^N or the N-factor method. This N-factor is given in Eq 3.24:

$$e^{N(s,f)} = \frac{A(s,f)}{A_0(f)} = \exp\left[\int_{s_0}^{s} -\alpha_i(s,f)ds\right] \tag{3.24}$$

Here $A(s,f)$ is the local disturbance amplitude, $A_0(f)$ is the initial modal disturbance amplitude, s_0 is the location where the disturbance first becomes unstable at the branch I neutral point, and $-\alpha_i$ is the spatial amplificatifon rate obtained from LST. The integration is performed for a constant frequency f, and is done numerically using trapezoidal integration. Note that $-\alpha_i > 0$ results in disturbance growth while $-\alpha_i < 0$ results in disturbance decay. The N-factor is specifically the exponent of e^N. In-flight transition N-factors are commonly understood to be between 5 and 10. However, this transition N-factor seems to hold only for sharp cones. Lei and Zhong[34], Aleksandrova et al.[78], and Balakumar and Chou[62] found that N-factors decreased considerably at similar streamwise locations for blunter cones. Marineau et al. [7] also found that blunt nose N-factors calculated at the beginning of transition were significantly lower than those for sharp nose cases, reaching as low as 0.5. Pure considerations of the N-factor are observed to be insufficient to reliably determine transition throughout a wide variety of conditions.

3.3 Freestream Disturbance Model

3.3.1 Axisymmetric Pulses

The stability of the two cone geometries is also studied using unsteady DNS simulations. Freestream pulses composed of fast acoustic, slow acoustic, temperature, and vorticity disturbances with broadband frequency spectra are used to perturb the meanflow. These pulses are introduced upstream in the meanflow prior to the nose region of the given cone geometry, and are then advected in the streamwise direction along the axis of symmetry. Two pulse geometries are utilized: finite spherical pulses which isolate disturbances upstream on the cone and planar pulses which also force the flow downstream on the cone. Since the shock is treated as a computational boundary in the simulations, these pulses can be represented analytically in the freestream by Eq. 3.25, with the input parameters for the pulses listed in Table 3.1.

$$q(x,y,z,t) = |q'|_\infty exp\left(-\frac{(R_c)^2}{2\sigma^2}\right) + q_\infty \tag{3.25}$$

A schematic diagram is given in Fig. 3.2 for the finite pulse cases. The finite dimensions of this pulse geometry ensure that the pulse only interacts with the flow in the far upstream regions of the cone, and induce only leading edge disturbances at the nose and upstream frustum of the cone. These are expected to experience gradual decay as the primary modal instabilities have not yet been excited at these points on the cones.

A schematic diagram for the planar pulses is also given in Fig. 3.3. The modelled pulse is now essentially infinite in the y-z plane, which results in additional forcing constantly being introduced to the flow as the pulse is propagated downstream. This is more representative of the level of noise that may be expected from wall radiation in a tunnel environment.

The term q is a stand in for the perturbation variables for density, pressure, velocity, and entropy. Similarly, $|q'|_\infty$ is a stand in for the peak freestream perturbation amplitudes of these variables $|\rho'|_\infty$, $|P'|_\infty$, $|u'|_\infty$, $|v'|_\infty$, and $|s'|_\infty$ as defined by the dispersion relations in Eqns. 3.26-3.29. The brackets utilized here are not indicative of absolute values or norms of

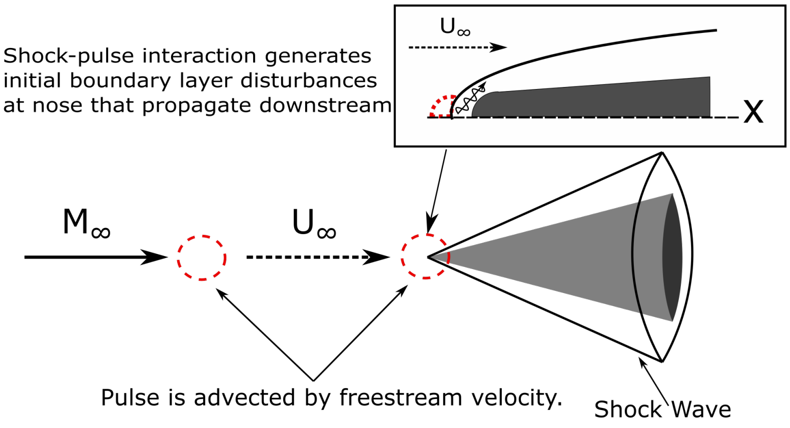

Figure 3.2: Schematic diagram of the unsteady simulation setup for a finite, spherical pulse disturbance in the freestream.

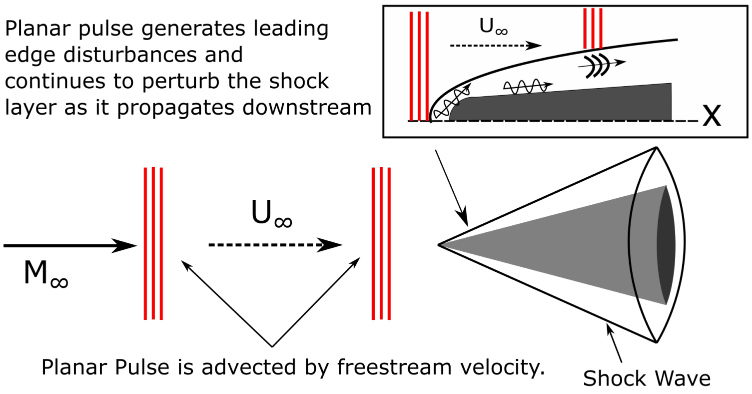

Figure 3.3: Schematic diagram of the unsteady simulation setup for a planar pulse disturbance in the freestream.

the particular perturbation variables, and the ∞ subscript denotes that the perturbations originate from the freestream.

A freestream fast acoustic disturbance is defined using the following relation:

$$|\rho'|_\infty = \frac{|P'|_\infty}{\gamma} = |u'|_\infty M_\infty = \epsilon M_\infty, \quad |s'|_\infty = |v'|_\infty = 0 \tag{3.26}$$

A slow acoustic disturbance in the freestream is governed by a very similar dispersion relation:

$$|\rho'|_\infty = \frac{|P'|_\infty}{\gamma} = -|u'|_\infty M_\infty = \epsilon M_\infty, \quad |s'|_\infty = |v'|_\infty = 0 \tag{3.27}$$

Table 3.1: Gaussian pulse parameters for unsteady axisymmetric DNS cases.

Case	Pulse Geometry	ϵM_∞	σ	x_0, m
B (3752)	Finite Spherical	5E-4	1E-3	-0.02
B (3752)	Planar	1E-6	1E-3	-0.02
I (3746)	Finite Spherical	1E-6	1E-3	-0.02
I (3746)	Planar	1E-8	1E-3	-0.02

A freestream entropy disturbance is described by:

$$|\rho'|_\infty = -|s'|_\infty = \epsilon M_\infty, \quad |u'|_\infty = |v'|_\infty = |p'|_\infty = 0 \tag{3.28}$$

And a freestream vorticity disturbance is described by:

$$|v'|_\infty M_\infty = \epsilon M_\infty, \quad |u'|_\infty = |p'|_\infty = |s'|_\infty = 0 \tag{3.29}$$

The ϵM_∞ variable prescribed in Table 3.1 governs the relative peak disturbance amplitude of the freestream pulse and is chosen to ensure that boundary layer disturbances remain linear. Since the receptivity response to the planar pulses is expected to be much stronger than that for the finite spherical pulses due to the additional forcing induced by the planar pulse front, the amplitude parameter ϵM_∞ was reduced for these cases. These peak amplitudes were further reduced for Case I due to the stronger expected second mode response. The variable σ controls both the spatial width of the pulse as well as the frequency bandwidth of the disturbance. This parameter was chosen to encompass significant freestream disturbances at frequencies of up to 600 kHz in order to ensure the excitation of the primary modal instabilities predicted by LST, and resulted in a pulse radius of approximately 3 mm.

This gaussian pulse model allows for an analytically continuous representation of a broadband disturbance in the freestream. As such, the incident pulse is expected to excite significant broadband modal disturbances in the boundary layer of the cones. A sample of the freestream pressure time history and spectral profile of a sample pulse is given in Fig. 3.4.

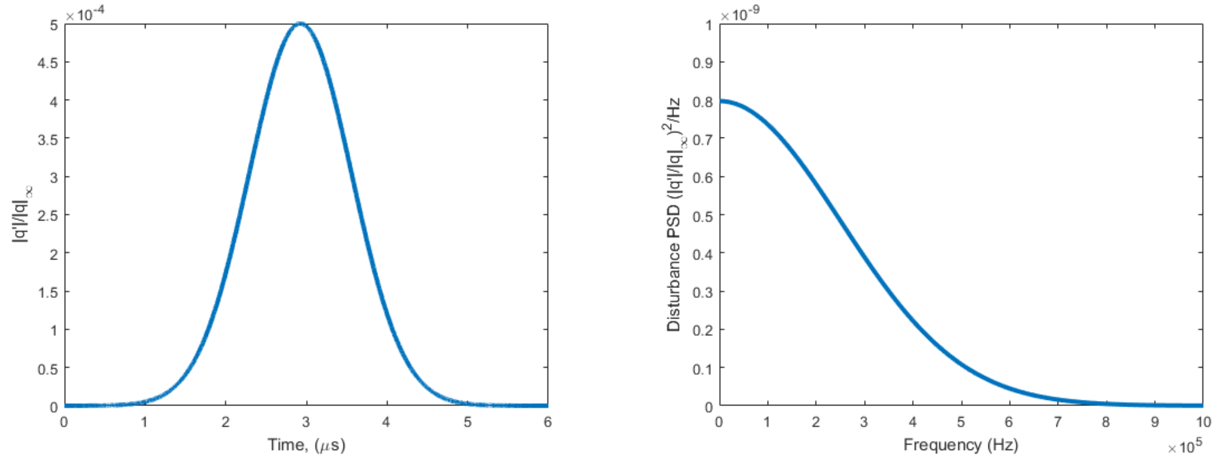

(a) (b)

Figure 3.4: Sample freestream disturbance distribution over (a) time and (b) frequency for an axisymmetric pulse with the given bandwidth parameters.

The term R_c refers to the radial distance from the center of the pulse to a point (x, y, z) in the flow field. For the finite, spherical pulses this distance R_c is measured in all three spatial dimensions as shown below in Eq. 3.30.

$$R_c = \sqrt{(x - x_{pulse})^2 + (y - y_{pulse})^2 + (z - z_{pulse})^2} \tag{3.30}$$

For planar pulses only the streamwise x-distance from the pulse center is taken into account, as seen in Eq. 3.31.

$$R_c = \sqrt{(x - x_{pulse})^2} \tag{3.31}$$

For both Case B and Case I the pulse is advected in the streamwise direction by $x_{pulse} = x_0 + C_\infty t$ where C_∞ is the disturbance speed in the freestream. These speeds are defined as $C_\infty = U_\infty + a_\infty$ for fast acoustic disturbances, $C_\infty = U_\infty - a_\infty$ for slow acoustic disturbances, and $C_\infty = U_\infty$ for entropy/vorticity disturbances. The pulse width term σ is scaled by $1 + 1/M_\infty$ for a fast acoustic disturbance and by $1 - 1/M_\infty$ for a slow acoustic disturbance to ensure uniform frequency spectra in all of the freestream pulses.

3.3.2 3-D Pulses with Azimuthal Variation

The 3-D pulse receptivity analysis utilizes a very similar freestream pulse model as the axisymmetric cases. Specifically, the freestream representation of the planar acoustic pulses is repurposed here, where an additional azimuthal gaussian distribution is applied. This gaussian azimuthal variation allows the pulse excitation to be limited to only a few azimuthal positions, and also constrains the excited wavenumbers to a select band. This includes significant excitation for the zero wavenumber disturbance, which corresponds to the primary second mode instability that is the primary mode of interest in our previous analysis. The model equation for the freestream pulse is given in Eq. 3.32, with the input parameters for the pulses listed in Table 3.2.

$$q(x,y,z,t) = |q'|_\infty exp\left(- \frac{(R_c)^2}{2\sigma^2} \right) exp\left(- \frac{(R_k)^2}{2\pi^2\sigma_k^2} \right) + q_\infty \tag{3.32}$$

The input parameters are largely the same, with the freestream pulse width parameter R_c being defined using the planar pulse distribution in Eq. 3.31. The major difference lies in the second pulse distribution which accounts for the azimuthal variation. The σ_k term is the azimuthal pulse width term which again governs both the dimensional width of the pulse in the azimuthal direction, as well as the bandwidth of excited azimuthal wavenumbers in the freestream pulse. This was selected to induce disturbances in a range of wavenumbers without causing issues with the axisymmetric boundary conditions of our numerical method. The R_k term defines the spectral radius centered about a given central position along the azimuth of the cone, as defined in Eq. 3.33.

$$R_c = \sqrt{(\psi - \psi_0)^2} \tag{3.33}$$

Here ψ is the azimuthal position in radians, while ψ_0 is the defined center of the pulse along the azimuth. These factors are also given in Table 3.2.

The 3-D pulses are advected in a similar manner in the streamwise direction parallel to the axis of symmetry of the cone in Case S. The analysis here focuses on the fast and slow

Table 3.2: Gaussian pulse parameters for unsteady 3-D DNS cases.

Case	Pulse Geometry	ϵM_∞	σ	σ_k	x_0, m	ψ_0
S (3752)	3-D	1E-7	1E-3	0.1	-0.02	$3\pi/2$

acoustic instabilities, which were found to induce the most dominant modal instabilities as well as excite the most significant extramodal responses in the boundary layer from the Case B and Case I axisymmetric pulse results.

3.4 Boundary Layer Receptivity

3.4.1 Axisymmetric Pulse Receptivity

The pulse disturbances imposed onto the cone in the unsteady simulations were chosen to induce broadband frequency perturbations in the boundary layer of the cone. In order to study the evolution of discrete frequency disturbances and correlate the unsteady DNS results with LST, the unsteady DNS is decomposed into its constituent frequency components. This was done using Fourier spectral analysis.

The time-dependent perturbation variables can be expressed in terms of their Fourier spectral components, obtained through a Fast Fourier Transform (FFT):

$$h(t_k) \equiv h_k \approx \sum_{n=0}^{N-1} H(f_n) e^{-2\pi i f_n t_k} \tag{3.34}$$

where $H(f_n)$ is the frequency space Fourier coefficient corresponding to the nth discretized frequency f_n . Additionally, N corresponds to the total number of Fourier collocation points used to discretize the time-dependent function $h(t)$. The discretized time function h_k is defined as being the value of the time dependent function $h(t)$ at a given time $t = t_k$.

In this study, the variable $h(t)$ corresponds to local boundary-layer perturbations in the surface pressure, though other flow variables such as temperature and density may also be considered. Surface pressure was chosen since the primary instability modes in the boundary layer are expected to be acoustic in nature. The complex Fourier coefficients $H(f_n)$ represents the spectral value of the boundary layer perturbations in the frequency domain. The complex component of $H(f_n)$ corresponds to the phase angle of the surface pressure perturbation through the relation:

$$\phi_n = tan^{-1}\left(\frac{Im(H(f_n))}{Re(H(f_n))}\right) \tag{3.35}$$

and $|H(f_n)|$ defines the amplitude of the surface pressure perturbation at the frequency f_n.

Since LST was used to validate the results of the unsteady DNS analysis, local growth rates and wavenumbers need to be calculated from the Fourier decomposed perturbation data. Following a similar procedure to Ma and Zhong[12] and Huang and Zhong[4], the local growth rates for each frequency are determined by

$$-\alpha_i = \frac{1}{|H(f_n)|}\frac{d|H(f_n)|}{ds} \tag{3.36}$$

and the local wave numbers are determined by

$$\alpha_r = \frac{d\phi_n}{ds} \tag{3.37}$$

where s corresponds to the local streamwise coordinates, f_n is the nth disturbance frequency of interest, and ϕ_n is the disturbance phase angle of the nth frequency. The non-dimensional phase speed of a disturbance at a given frequency is defined as

$$c_r = \frac{2\pi f_n}{U_\infty \alpha_r} \tag{3.38}$$

The response of the system to each freestream disturbance environment can be represented through a receptivity coefficient. The receptivity coefficient in this study $C_{rec}(f)$ is defined as the ratio of the initial amplitude of the second mode disturbance at the branch I neutral point for a given discrete frequency f to freestream forcing of the same frequency. This coefficient is determined using a combination of LST and unsteady DNS through the same process as recommended by Huang[72] and Schneider[73]. This additional decomposition aims to isolate the second mode amplitudes from the complex multimodal disturbance environment induced by the transient pulse disturbance. Assuming significant second mode amplification, the receptivity coefficient can be calculated through Eq. 3.39.

$$C_{rec}(f_n) = A_0(f_n) = \frac{A(s^*, f_n)}{e^{N(s^*, f_n)}} \tag{3.39}$$

Here $A(s^*, f_n)$ is the Fourier decomposed surface pressure amplitude and $e^{N(s^*, f_n)}$ is the exponentiated N-factor determined through LST for a given frequency f_n and a streamwise location s^*. The non-dimensional amplitude spectral density $A(s^*, f_n)$ for the acoustic and entropy disturbances is derived by normalizing the local surface pressure perturbation of a given frequency by the freestream pulse density perturbation of the same frequency $\rho'_\infty = |\rho'|_\infty G(f_n)$. $|\rho'|_\infty$ is the peak density perturbation amplitude defined in the previous dispersion relations. $G(f_n)$ is the analytical frequency domain representation of the incident pulse at the frequency f_n. This is given as:

$$G(f_n) = \frac{\sigma\sqrt{(2\pi)}}{C_\infty} exp\Big(\frac{-2\pi^2\sigma^2 f_n^2}{C_\infty^2}\Big) \tag{3.40}$$

The vorticity pulses are similarly normalized using the freestream velocity disturbance $v'_\infty = |v'|_\infty M_\infty G(f_n)$, since density disturbances aren't imposed in the freestream. The normalizations are based on the the relative peak amplitude ϵM_∞ from the dispersion relations given in Section 3.3, and account for the non-uniform frequency distribution of disturbance amplitudes in the freestream pulses.

The phase angle coefficients can also be extracted using a similar decomposition method. The corresponding phase angle coefficients at the branch I neutral point can be calculated using Eqn. 3.41.

$$\phi_{n,0}(f_n) = \phi_n(s^*, f_n) - \int_{s_0^*}^{s^*} \alpha_r(s, f_n) ds \tag{3.41}$$

Here, ϕ_n represents the FFT phase angle from Eqn. 3.35 at a given frequency f_n and sampling location s^* and α_r is the LST derived real component of the spatial wavenumber at the same frequency and spatial position. This is taken from the fact that the streamwise wavenumber is defined as the streamwise gradient of the local disturbance phase angle.

3.4.2 3-D Pulse Receptivity

The receptivity of the 3-D acoustic pulse disturbances is investigated in a similar manner as well. Due to the introduction of spanwise variation in the incident pulse disturbance, a distinct band of azimuthal wavenumbers is now also excited outside of the zero wavenumber second mode. Due to the linear nature of the Fourier transform, however, this additional dimensionality is easily treatible. The time dependent flow variables can be expressed as the components of a 2-D discrete Fourier Transform in the form of Eq. 3.42.

$$h(t_k, z_k) \equiv h_k \approx \sum_{s=0}^{S-1} \sum_{n=0}^{N-1} H(f_n, \beta_s) e^{-2\pi i f_n t_k} e^{-2\pi i \beta_s z_k} \tag{3.42}$$

Again, $H(f_n, \beta_s)$ is the frequency space Fourier coefficient corresponding to the nth discretized frequency f_n and the sth discretized spanwise wavenumber β_s . Additionally, N corresponds to the total number of Fourier collocation points used to discretize the time-dependent function $h(t, z)$ in Fourier space while S represents the number of sampling points in the azimuthal direction of the cone. The discretized time function h_k is defined as being the value of the time dependent function $h(t, z)$ at a given time $t = t_k$ and azimuthal position $z = z_k$.

Using this discrete Fourier representation, the surface pressure disturbance at different streamwise positions can be decomposed into its distinct azimuthal wavenumber and frequency spectra. These are used to track the development of modal instabilities in the flow field. The Fourier transforms are computed using FFT algorithms based on those in Ref. [99] for both the 1-D FFT utilized for the axisymmetric receptivity study and the 2-D FFT utilized for the azimuthally varying 3-D pulse.

$$G(f_n) = \frac{2\sigma\sigma_k\pi^2}{C_\infty} exp\Big(\frac{-2\pi^2\sigma^2 f_n^2}{C_\infty^2}\Big) exp\Big(-2\pi^4\sigma_k^2\beta_s^2\Big) \tag{3.43}$$

The FFT decomposed surface pressure disturbances for the 3-D acoustic pulses are further normalized by the freestream pulse density perturbation, in a very similar way to the axisymmetric pulse cases. The normalization parameter is again expressed as $\rho'_\infty = |\rho'|_\infty G(f_n)$.

$|\rho'|_\infty$. However, the pulse parameter $G(f_n)$ is corrected to account for the pulses' azimuthal component. This is shown in Eqn. 3.43. In this relation, the σ_k term accounts for the azimuthal bandwidth parameter and β_s is the non-dimensional azimuthal wavenumber term.

CHAPTER 4

Axisymmetric Pulse Receptivity and the Effects of Nose Bluntness

4.1 Steady Flow Field Results

The steady meanflows are converged using the high-order shock-fitting code, and are used as direct inputs to both the unsteady DNS simulations and the LST stability calculations. Due to the large grid resolutions the simulations of the cone must be split into a selection of successive smaller downstream subdomains that are converged separately. The results of the outlet at the previous subdomain are used as inlet conditions of the next downstream subdomain. This structure is retained in the unsteady DNS simulations as well.

4.1.1 Case B Steady Flow Field Solution

The steady DNS pressure and temperature meanflow contours for the cone in Case B are shown in Fig. 4.1a for the first and second computational zones near the nose and the beginning of the cone frustum. For this simulation a total of 240 points were used in the η direction, while the distribution in the ξ ranged from 30 points per mm at the nose to 5 points per mm at the end of the geometry. These distributions were chosen based on prior experience with flows at similar conditions, and ensure sufficient resolution to capture the disturbance modes of interest. A total of 10,080 points were used in the ξ direction to resolve the cone to 1.9 m. Marineau[7] studied cones up to lengths of 1.5m. The domain here was lengthened to allow for the development of a more amplified second mode which would be use to generate spectral receptivity data for the studied pulse disturbances.

The temperature contours in Fig. 4.1a depict a broad temperature gradient in the frustum region immediately after the nose. This is indicative of a similarly extensive entropy gradient, and is representative of the generation of a significant entropy layer as expected for this relatively blunt nose. Fig. 4.1b similarly show a significant surface normal temperature gradient extending far downstream from the nose and indicates that the entropy layer is not swallowed for a large portion of the computational domain. These entropy layers reduce local flow velocities and density, and in turn reduce local Reynolds numbers. Since transition locations have been correlated with larger local Reynolds numbers, this process has been used to explain the transition delaying mechanism for intermediate nose bluntness[100]. However, this fails to explain transition reversal effects observed in large bluntness flows[34]. Zhong and Ma[60] observed the emergence of an additional generalized inflection point in the entropy layer of their blunt cone which may be indicative of inviscid instability. These entropy layer instabilities can be absorbed by the boundary layers in blunt cones and potentially lead to early transition, though they have been observed to be relatively weak in perfect gas flows. They also pointed out that non-modal instabilities may have stronger influence in blunt cones, and cause this reversal. Balakumar and Chou [62] also observed large oscillations in the entropy layer before second mode disturbances eventually began to dominate further downstream on their straight blunt cone cases. Wan, Su, and Chen[64] also show that discrete frequency freestream acoustic modes can induce instabilities in the entropy layer that go on to force the downstream second mode, further emphasizing the importance of the entropy layer in transition. Further investigation of the effects of freestream receptivity in the entropy layer may be of interest in resolving this problem.

The wall-normal profiles of both velocity and entropy are presented in Fig. 4.2. The velocity profiles in Fig. 4.2a demonstrate weak variation in boundary layer height after approximately $s^* = 0.7405$ m. The extent of the entropy layer is defined in Fig. 4.2b in which it is shown to extend above the boundary layer across much of the cone. The entropy layer and boundary layer are observed to merge near approximately $s^* = 0.9881$ m, after which both the velocity and entropy profiles experience relatively minor variation in the streamwise direction. While the more extensive entropy profile variation prior to $s^* = 1$

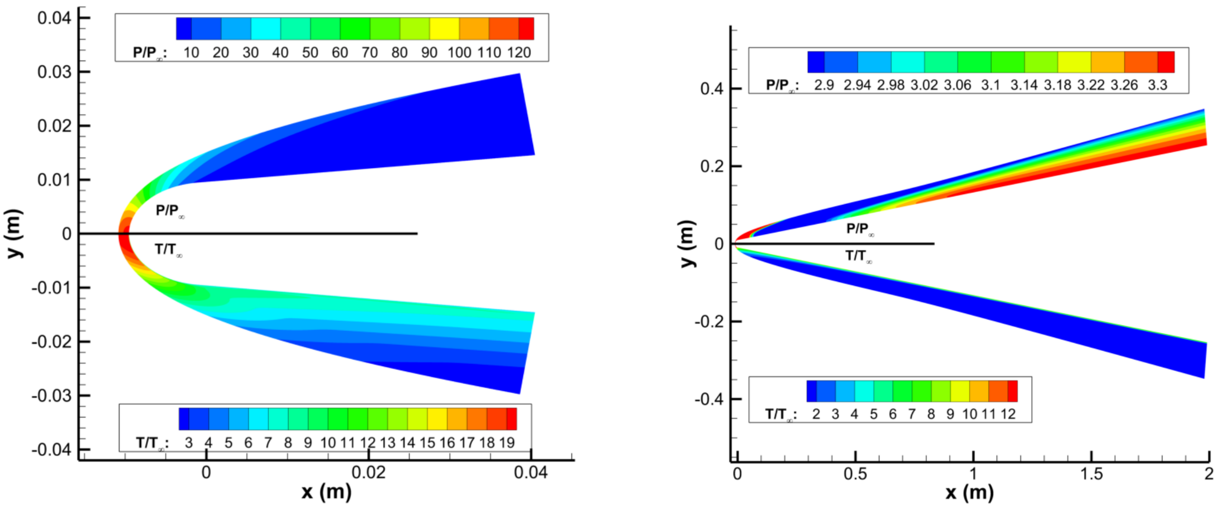

(a) (b)

Figure 4.1: Partial view of pressure (top) and temperature (bot) contours for (a) zones 1 and 2 near the nose region and (b) the total cone length for Case B.

m indicates potential non-parallel effects in the thermal boundary layer up to this point, it was found that the modal disturbance amplification profile does not vary much when taking non-parallelism into account for this case. Thus, a locally parallel assumption was utilized in the linear stability analysis for this study.

The convergence of the meanflow simulation is validated by comparing the current 240 point grid in the wall normal direction with a further refined 480 point result. This refinement is only done in the wall normal direction because flow variable gradients in this direction are particularly extreme for high-speed wall-bounded shear flows. In particular, the boundary layer must be sufficiently well resolved in order to ensure accurate analysis of disturbances. The results of this convergence study are shown in Fig. 4.3 for wall normal velocity and temperature profiles at a streamwise location of $s^* = 0.705$ m.

The profiles of the current 240 point grid and the refined 480 point grid qualitatively look nearly identical, implying convergence. The difference between the two grids can be further quantified by the infinity norm of the relative error, which is defined as the maximum error in the temperature or velocity profile. The infinity norm based on the velocity is 1.65×10^{-6}.

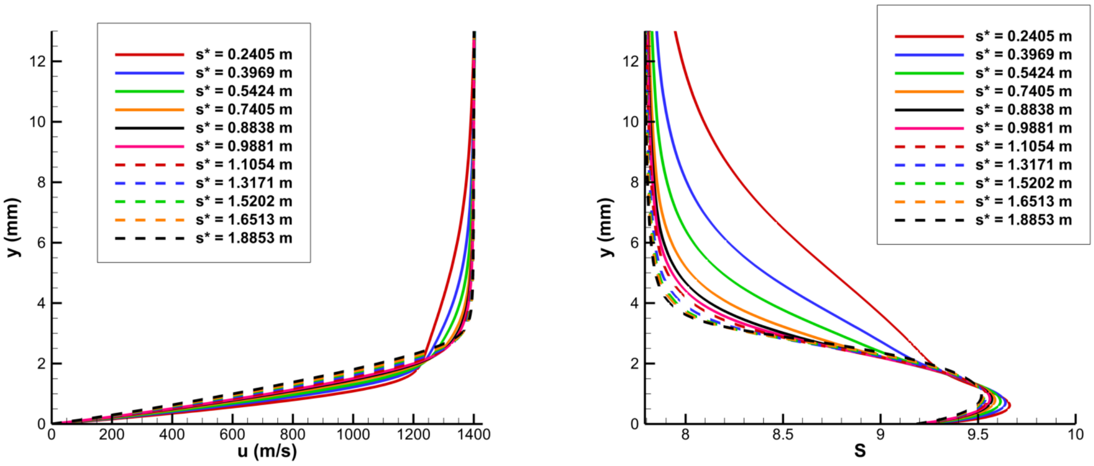

(a) (b)

Figure 4.2: Wall normal (a) U velocity and (b) S entropy profiles at different positions along the cone.

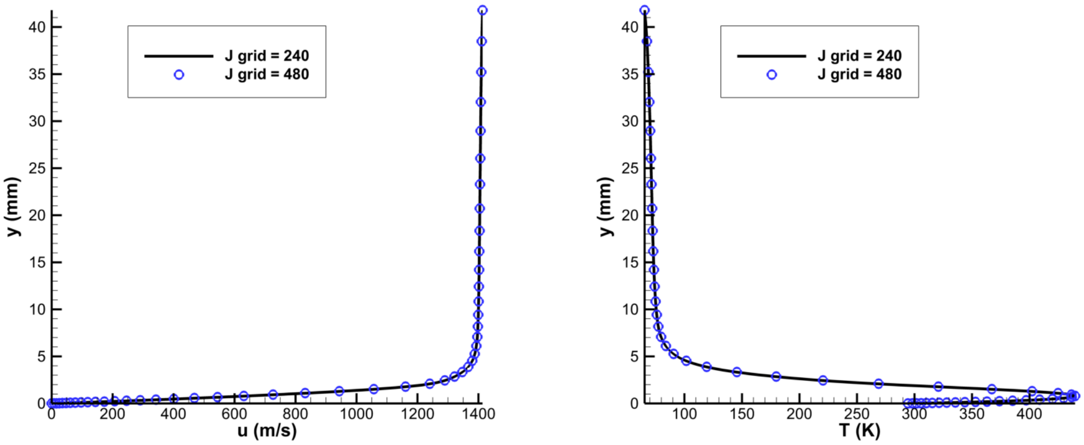

(a) (b)

Figure 4.3: Grid convergence comparison of wall normal (a) U velocity and (b) T temperature profiles at $\mathbf{s}^* = \mathbf{0.705}$ m.

4.1.2 Case I Steady Flow Field Solution

The steady DNS pressure and temperature meanflow contours for Case I are shown in Fig. 4.4a at the nose and near the beginning of the cone frustum. Similarly to the 9.525 mm nose radius cone in Case B, a total of 240 points were used in the η direction and approximately 5 points per mm were used in the ξ direction to resolve high frequency and low wavenumber disturbances. These distributions were chosen to provide sufficient resolution in the meanflow data so as to reduce numerical inconsistencies in the LST analysis. A total of 7,290 points were used in the ξ direction to resolve the cone to 1.5 m.

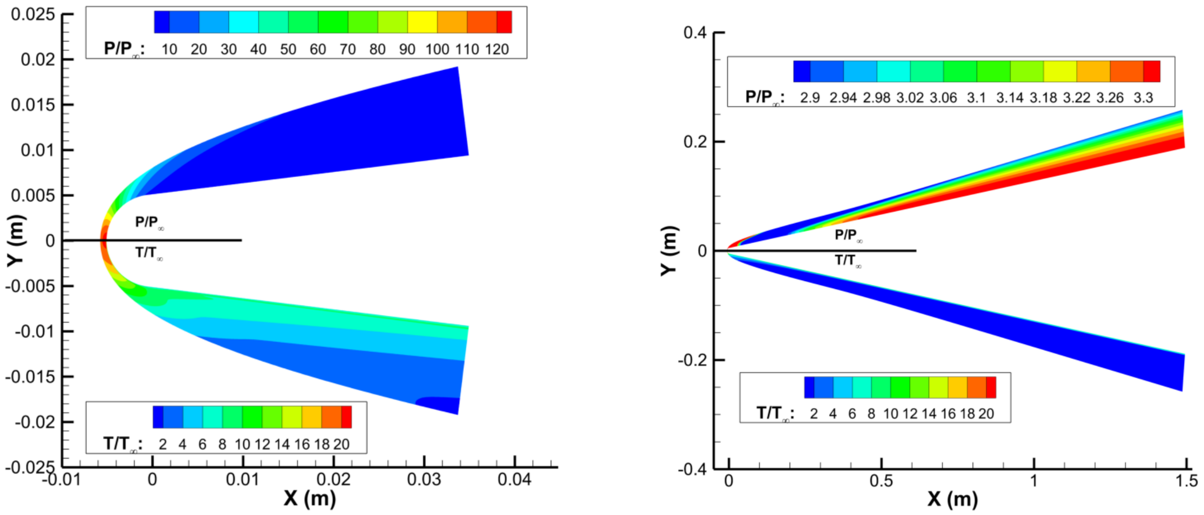

(a)

(b)

Figure 4.4: Partial view of pressure (top) and temperature (bot) contours for (a) zones 1 and 2 near the nose region and (b) the total cone length for Case I.

The meanflow pressure and temperature contours for the full cone are shown in Fig. 4.4b. Similar to Case B, an entropy layer is seen to emerge in the nose region in Fig. 4.4a. However, this entropy layer merges with the boundary layer significantly farther upstream on the cone than in Case B. This less pronounced entropy layer is not as effective in reducing local Reynolds numbers, resulting in the more upstream transition location for the equivalent case (run 3746) in Marineau et al.'s[7] study vs the blunter nose in Case B (run 3752).

The boundary and entropy layers can be visualized more clearly using wall-normal profiles of velocity and entropy. These are presented Fig. 4.5 at a selection of different streamwise positions. The boundary layer velocity profile in Fig. 4.5a demonstrates very little change in general shape or thickness throughout the downstream regions of the cone and shows that the locally parallel assumption holds for the purposes of LST. The entropy profiles in Fig. 4.5b show a significant entropy layer that does not merge with the boundary layer until approximately $s^* = 0.5$ m, and matches the results for a similar case from Balakumar and Chou[62]. In both the Case B and Case I geometries the entropy layers were observed to be swallowed approximately 100 nose radii downstream on the geometries. Additionally, the increased nose bluntness for Case B is shown to greatly extend the non-parallel development of both the boundary layer and entropy layer in Fig. 4.2. Though again, prior findings have shown that the boundary layer variation observed here has little effect on the total second mode stability profile of the meanflows in this study[65, 101].

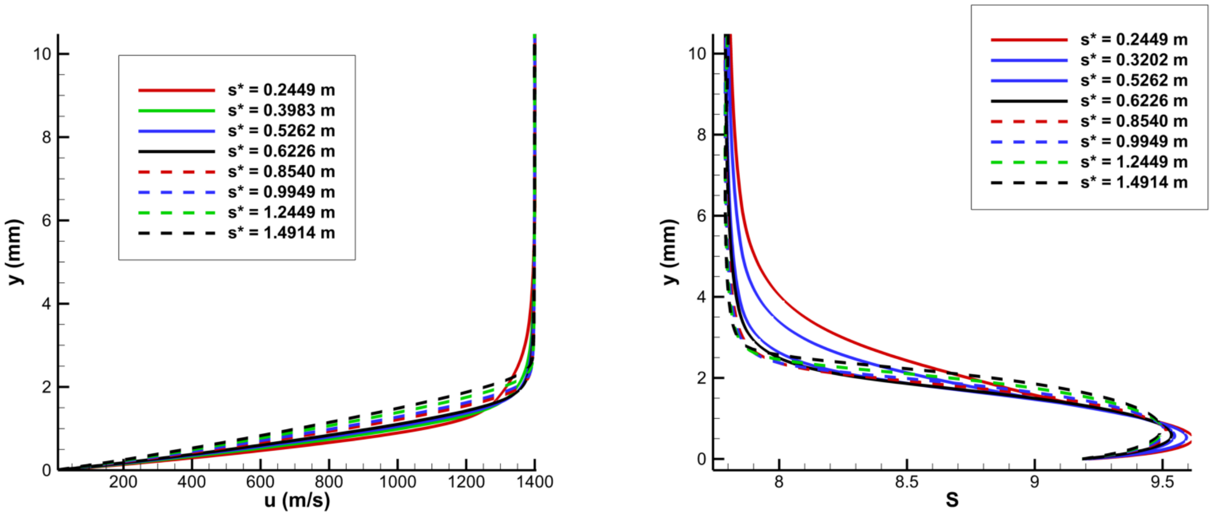

(a)

(b)

Figure 4.5: Wall normal (a) U velocity and (b) S entropy profiles at a selection of streamwise positions for Case I.

The convergence of the meanflow simulation for Case I is also validated by comparing the current 240 point grid in the wall normal direction with a further refined 480 point result. The results of this convergence study are shown in Fig. 4.6 for wall normal velocity and temperature profiles at a streamwise location of $s^* = 1.25$ m.

The nearly identical profiles in both the velocity and the temperature qualitatively indicate grid convergence. The infinity norm of the relative error was again used to quantify

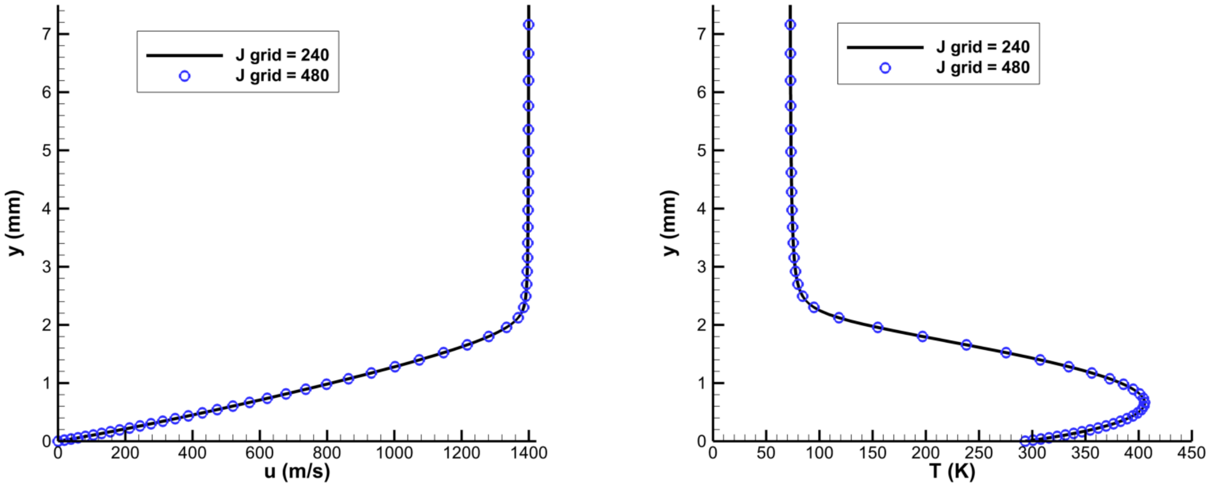

(a) (b)

Figure 4.6: Grid convergence comparison of wall normal (a) U velocity and (b) T temperature profiles at $\mathbf{s}^* = \mathbf{1.25}$ m for Case I.

the difference between the original and the refined result. The infinity norm based on the velocity for this case is 2.61×10^{-6}.

4.2 LST Results

4.2.1 Case B LST Results

The growthrate contours and the neutral stability curve is shown in Fig. 4.7. The neutral stability curve was generated by fitting the branch I and branch II neutral stability points and is highlighted in black. In this figure positive $-\alpha_i$ growthrates inside the curve correspond to the unstable second mode region. LST results indicate a strong amplified second mode band between frequencies of 118 kHz and 238 kHz. At the reported experimental transition location of $s^* = 1.037$ m for this case[7], the unstable second mode is found between frequencies of 150 and 185 kHz and compares well to Marineau's results.

The phase speed and growthrate of the 150 kHz disturbance are presented in Fig. 4.8 and are used later to validate the unsteady DNS results. This disturbance frequency was

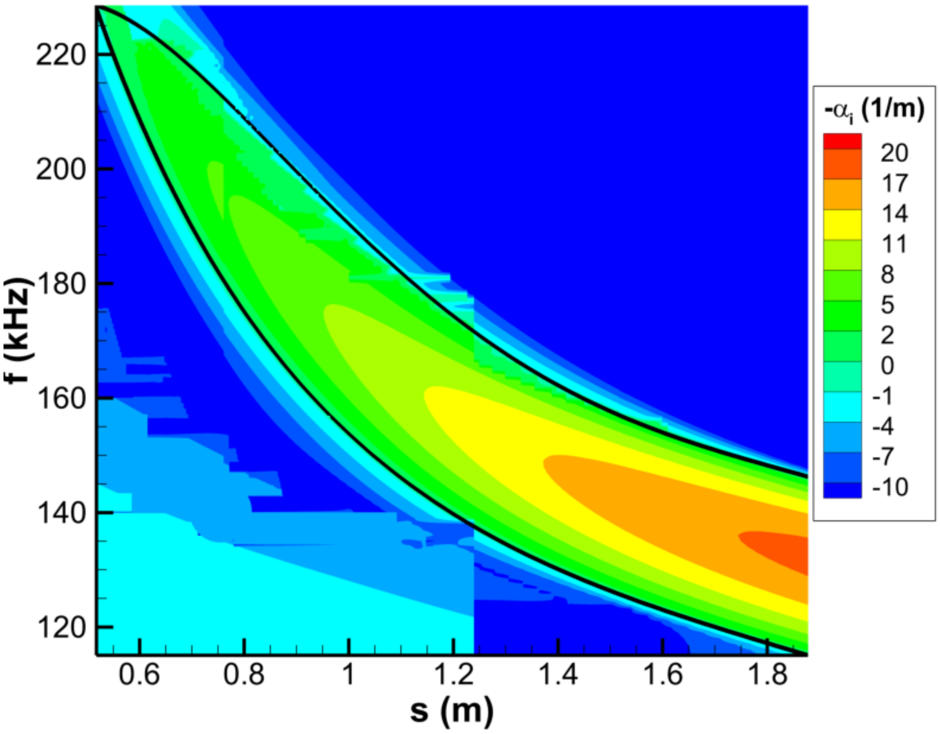

Figure 4.7: LST growthrate contour and neutral stability curve for Case B.

chosen because it was observed to contain a highly amplified second mode. It is shown that the primary second mode disturbance corresponds to the discrete mode F emerging from the continuous fast acoustic spectrum. The continuous spectra are indicated in the phase speed plot by the dashed lines at $1 + 1/M_\infty$ for the fast acoustic, 1 for the entropy/vorticity, and $1 - 1/M_\infty$ for the slow acoustic modes. Additionally, Fig. 4.8 shows that this particular frequency demonstrates an extensive synchronization region between mode F and mode S, lying between 1.1 and 1.7 m along the cone.

The N-factor of the discrete frequency disturbances can be calculated using Eq. 3.24 to integrate the growthrates in the streamwise direction. The results of this analysis are depicted in Fig. 4.9. For this case (which corresponds to Run 3752), Marineau et al[7] reported an experimentally determined transition location of $s^* = 1.037m$, along with a corresponding N factor of 1.6 at a peak disturbance frequency of approximately 176 kHz. A direct comparison between the LST N-factors in Fig. 4.9a and Marineau's PSE derived

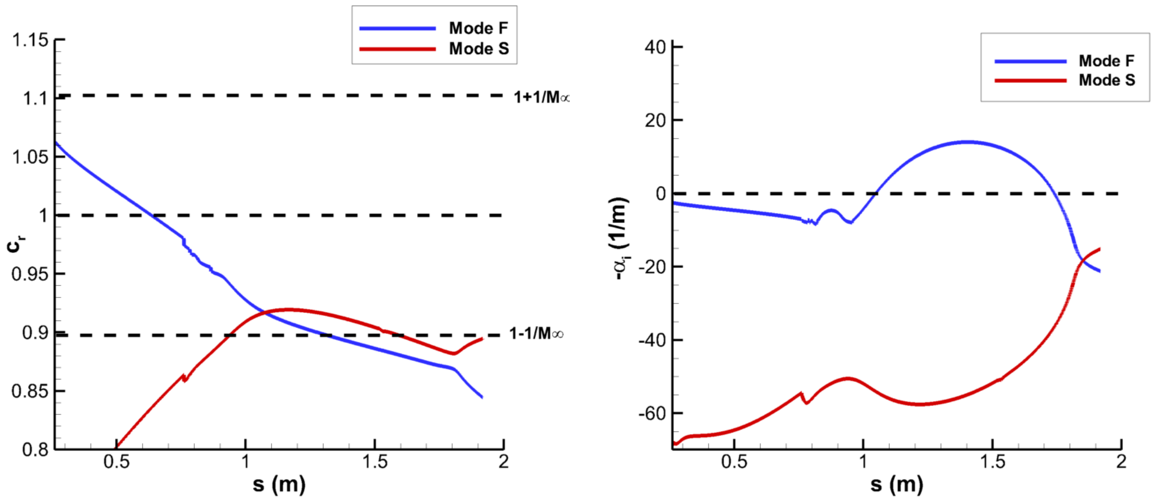

(a) (b)

Figure 4.8: Streamwise LST results at f = 150 kHz for (a) Phase Speed (b) growthrate.

N-factors are shown in Fig. 4.9b, which was made by fitting the curve profiles for each of the sampled LST frequencies. The LST results of this study report an N-factor of approximately 1.7 at the experimental transition location and are consistent with Marineau's results for this case. In general, the LST results correlate reasonably well with the PSE data reported by Marineau, with our LST overpredicting the N-factors slightly throughout the downstream sections of the domain. This difference can be attributed to the increased unit Reynolds number of our meanflow, which is caused by differences in our freestream viscosity models.

Several of the higher frequency N-factor curves in Fig. 4.9a show some deviation from the expected smooth curve shape. This is indicative of discontinuities in the growthrate, and may be caused by either numerical resolution issues in the LST solution algorithm or more complex multi-modal disturbance interactions that were not captured in the current analysis. Examples of this include the interaction of additional higher discrete modes that emerge from the fast acoustic spectrum or from an amplified supersonic mode instability. This particular point is discussed further in the analysis of the unsteady DNS cases.

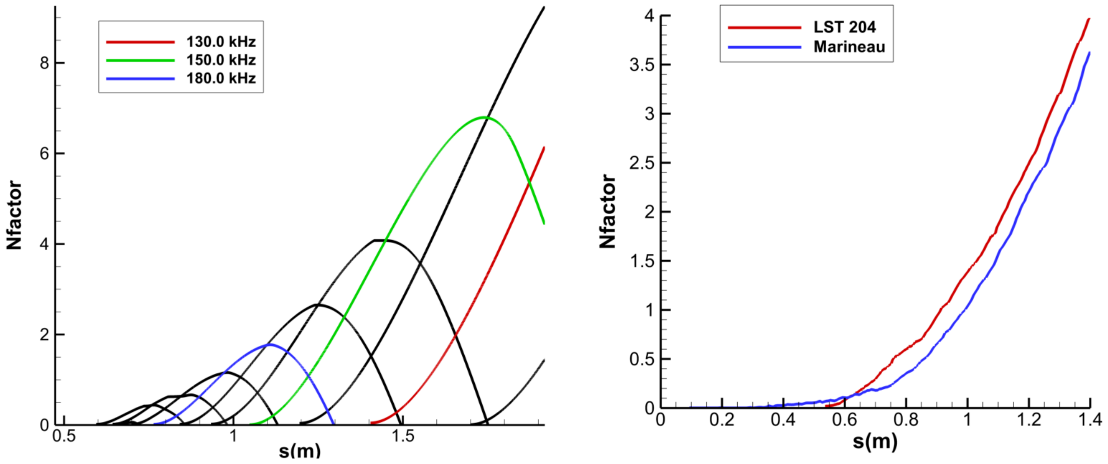

(a) (b)

Figure 4.9: Case B LST Results: (a) N-factor data ranging between 120 kHz to 220 kHz with $\Delta f = 10$ kHz. (b) LST N-factors vs. Marineau's[7] reported PSE N-factors.

4.2.2 Case I LST Results

The growthrate contours and neutral stability curves are shown in Fig. 4.10 for Case I. The contour shows that for Case I the second mode band is observed to lie between frequencies of approximately 135 and 300 kHz. The disturbances in Case I are higher frequency than those of Case B, which is expected as the blunter geometry in Case B results in a larger boundary layer thickness. This leads to larger amplified wavelengths and lower amplified frequencies in Case B when compared to Case I[7, 34]. The dimensional growthrates for Case I in Fig. 4.10 are significantly higher than those of Case B in Fig. 4.7, and reflect the stabilizing nature of nose bluntness on second mode disturbances as seen in prior computational studies [33, 34]. This has also been directly predicted in prior experimental work as well [31, 32, 7].

In a similar manner to Case B, phase speed and growthrate curves for a 200 kHz disturbance are plotted for Case I in Fig. 4.11. This frequency was again chosen due to its significant modal amplification, and is higher in frequency than the chosen Case B result due to the meanflow effects discussed previously. One primary difference between the two cases lies in the destabilized discrete mode. In general, second mode amplification begins after

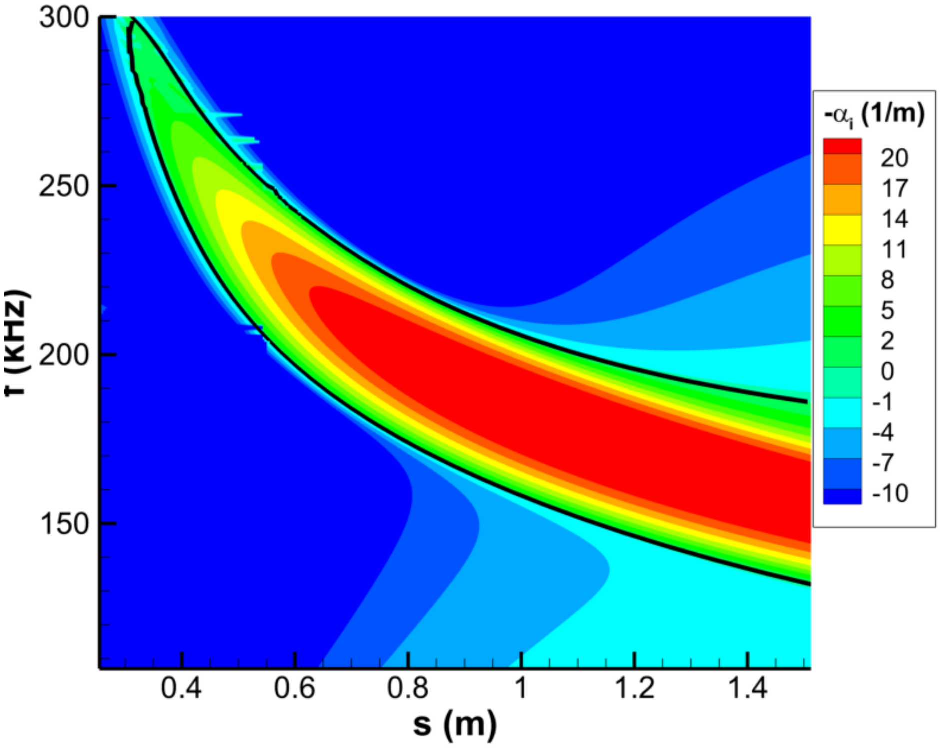

Figure 4.10: LST growthrate contour and neutral stability curve for Case I.

synchronization between the discrete mode F and mode S disturbances destabilizes one of the modes. In a large portion of stability studies over blunt cones and flat plates, the discrete mode S has generally been the destabilized mode [4, 2, 60], as it is here for Case I. However, it is also possible for the discrete mode F to become unstable instead [24]. The results here indicate that for the sharper Case I the discrete mode S becomes the unstable second mode after synchronization, while the discrete mode F becomes unstable for the blunter Case B. A prominent discontinuity is seen for the discrete mode F for Case I in both the phase speed plot in Fig. 4.11a and the growthrate plot in Fig. 4.11b between $s^* = 0.5$m and $s^* = 1$m. The solution method of the LST code oftentimes has issues resolving the weaker discrete mode as the synchronization phenomenon creates a singularity that may be difficult to resolve numerically [81, 24]. Additionally, the wave numbers of the discrete modes in this synchronization region may be sufficiently similar that conventional LST and PSE numerical tools can have difficulty differentiating them[79, 82].

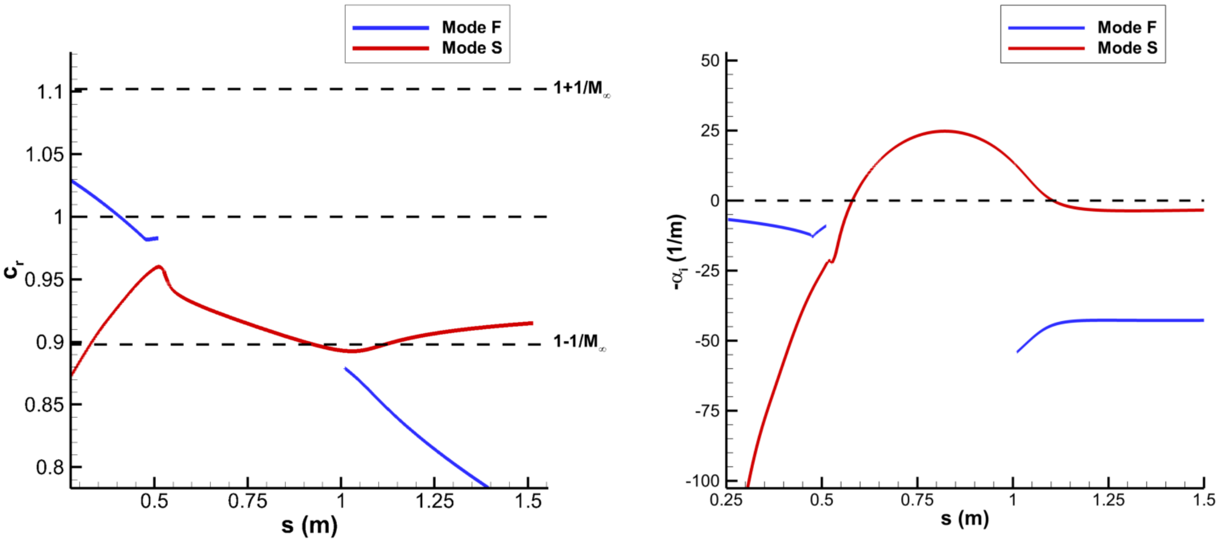

(a) (b)

Figure 4.11: Streamwise LST results at f = 200 kHz for (a) Phase Speed (b) growthrate for Case I.

The growthrate data for a discrete frequency disturbance can be integrated in the streamwise direction using Eqn. 3.24 to produce the individual N-factors for Case I, which when combined together can be used to create the total N-factor envelope of the 2nd mode disturbance for the flow. The resulting maximum N-factor envelope for both cases is compared against Marineau et al.'s PSE derived N-factors in Fig. 4.12. While the disturbances in Case B only reach second mode N-factors of approximately 9 by the end of the cone, Case I sees the lowest frequency disturbances reach values of approximately 14. This indicates that second mode disturbances are expected to experience several orders of magnitude more amplification in this sharper nose case and further denotes the strong stabilization effect that nose bluntness has traditionally been found to have on second mode instabilities.

For Case I, which corresponds to Marineau, et al.'s[7] Case 3746, the experimental transition location was reported at $s^* = 0.683$ m along with a transition N-factor of 2.7. The LST analysis for this meanflow demonstrates a transition N-factor of approximately 2.9 at a maximum disturbance frequency of 224 kHz. This peak frequency is slightly higher than Balakumar and Chou's[62] predicted 210 kHz for a similar case, though this is likely due to the higher unit Reynolds number for our simulation which stems from slightly different freestream viscosity models. In both cases the LST algorithm utilized in this study seems to slightly overpredict Marineau's PSE N-factor throughout the downstream regions of the cones where the second mode is most dominant. However, this overprediction is small, and is also significantly reduced in the sharper Case I. This can be attributed to the weaker non-parallel effects found in sharper cone geometries.

The boundary layer profiles discussed previously in Fig. 4.2 for Case B and Fig. 4.5 for Case I also reflect this. The boundary layer for Case I is not only observed to become essentially parallel much further upstream in the domain, the variation between the boundary layer profiles is also seen to be much weaker than in Case B. When comparing the total N-factor profiles for Case I in Fig. 4.12a with those of Case B in Fig. 4.9a we further see a dramatic upstream shifting of initial second mode destabilization for Case I. The larger bluntness in Case B is shown to delay the onset of instabilities as well as the total amplification rate of second mode disturbances. In general, the stability analysis utilized in this study show excellent agreement with Marineau's calculated amplifcation factors for the tested cases as well as expected trends from prior work in the field.

In general, the effects of nose bluntness on the stability of the flows as measured through LST is consistent with prior findings by Lei and Zhong[63], Kara, et al.[33], and Aleksandrova, et al.[78]. Namely, the increased nose bluntness in Case B is shown to directly lead to decreased second mode amplification. Spatial growthrates are shown to be significantly lower for Case B, and the total N-factor envelopes show the expected amplification is orders of magnitude weaker. Similarly, second mode amplification is also observed to be pushed downstream in Case B. The meanflow variations caused by the larger bluntness also result in a thicker boundary layer, which in turn amplify lower frequency disturbances and shift the second mode band to lower frequencies.

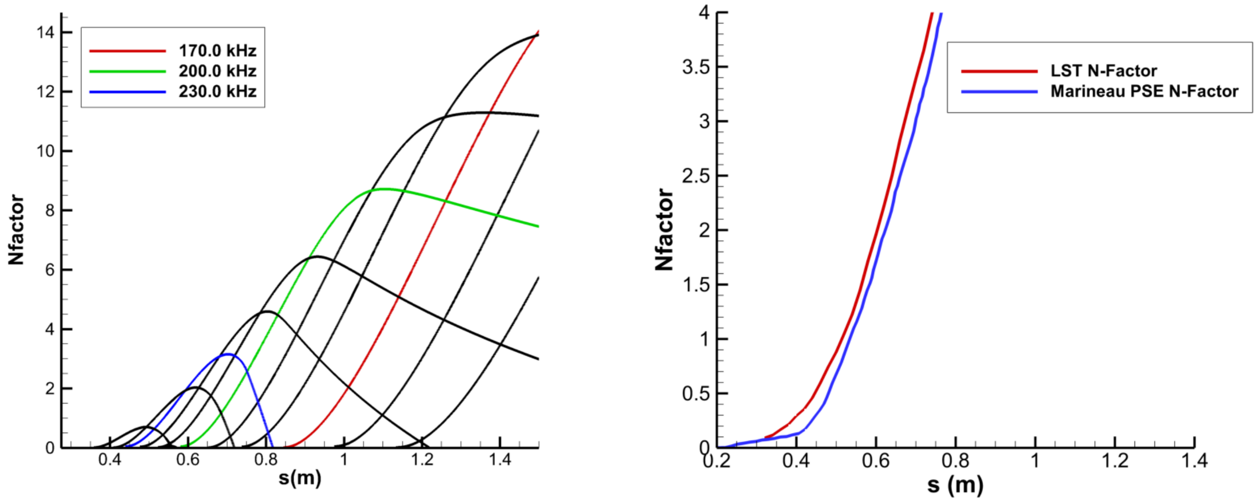

(a)

(b)

Figure 4.12: Case I LST Results: (a) N-factor data ranging between 120 kHz to 220 kHz with $\Delta f = 10$ kHz. (b) LST N-factors vs. Marineau's[7] reported PSE N-factors.

4.3 Unsteady DNS Results

The receptivity behaviors of the two cones were studied in response to a variety of axisymmetric, broadband frequency freestream disturbances. To do this, the pulse disturbances described in section 3.3 were introduced in the freestream. These pulses were then allowed to advect along the central axis of symmetry in the streamwise direction over the meanflows. The resulting boundary layer disturbances on the cone surfaces were studied using FFT to decompose the surface pressure perturbations into their spectral frequency components. The specific disturbance cases and their respective labels are given in Table 1.2. The disturbances are differentiated by both their freestream perturbation type and their geometry. The fast acoustic, slow acoustic, temperature, and vorticity disturbances are defined by the freestream dispersion relations in Eq. 3.26, 3.27, 3.28 and 3.29 respectively. While the peak amplitudes of the planar pulses were reduced to accomodate the expected increased receptivity response to those pulses and ensure linear boundary layer disturbances, the excited frequency bandwidths were fixed to be the same between the two geometries.

4.3.1 Finite Pulse Unsteady DNS Results

Fig. 4.13 depicts the instantaneous pressure and temperature disturbances immediately after the finite pulse interaction at the nose for Cases B1. The pressure disturbance contours in Fig. 4.13a depict acoustic waves propagating toward the cone surface and being reflected back towards the bow shock in the manner expected of acoustic disturbances. Similarly, the temperature disturbance profiles at the nose are plotted for Case B1 in Fig. 4.13b. Instead of the acoustic reflection seen for the pressure disturbances, the temperature perturbations are seen piling up near the surface of the cone as they propagate to the end of the computational zone. This behavior reflects the emergence of excited entropy modes immediately after the bow shock[4]. The observed differences in these perturbation variables denote the wide range of perturbed disturbance modes present in the initial shock-pulse interaction at the nose.

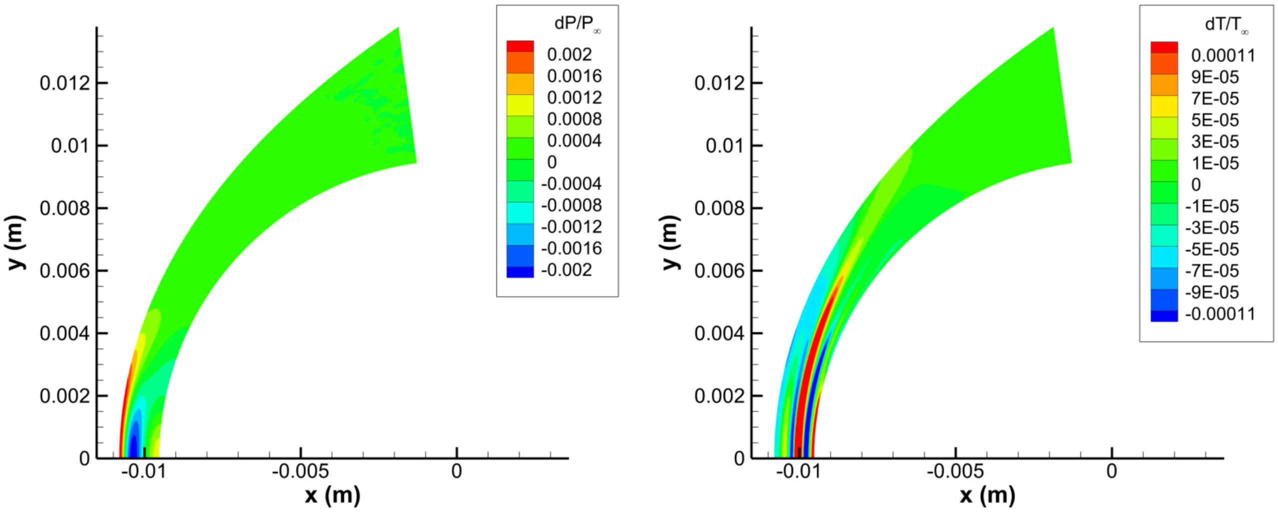

(a) (b)

Figure 4.13: Normalized (a) pressure perturbations and (b) temperature perturbations at the nose region for Case B1.

Fig. 4.14 depicts shock-layer disturbances at a downstream location for Case B1. The other finite pulse cases were observed to demonstrate very similar behaviors[101, 65] and as such are omitted. The pressure perturbations in Fig. 4.13a indicate the development of strongly amplified acoustic modes in the boundary layer which are characteristic of the second mode. The temperature disturbance profile in Fig. 4.13b also demonstrates a disturbance that is primarily isolated to the boundary layer. This disturbance contains the conventional banded rope-like structures commonly identified with second mode amplification, and further corroborates that the second mode is significantly amplified at this downstream position on the cone.

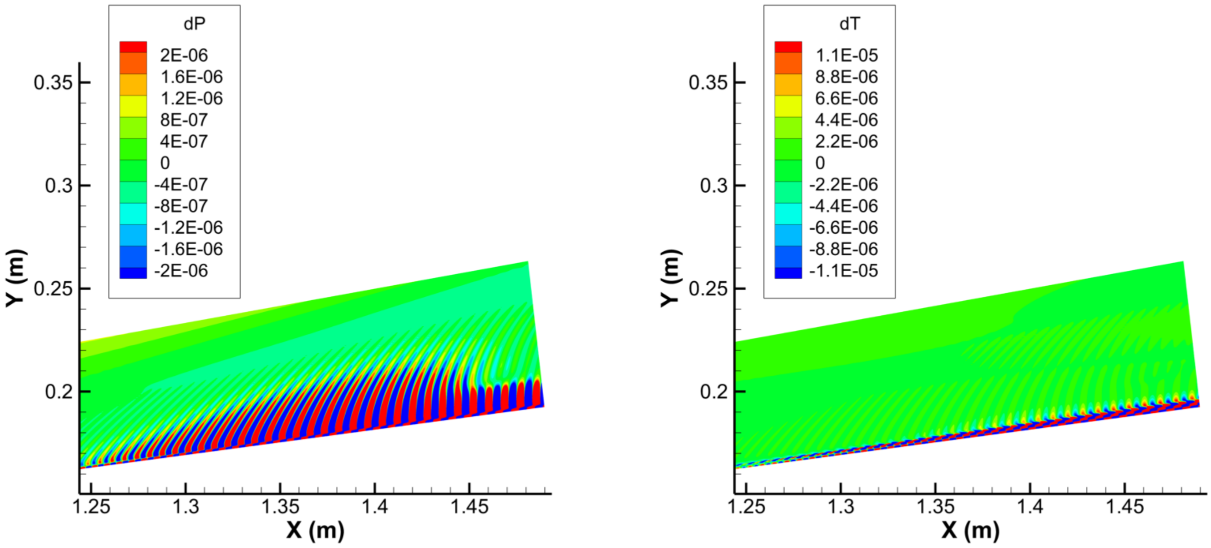

(a) (b)

Figure 4.14: (a) Pressure and (b) temperature perturbations near $x = 1.5$ m after the finite spherical fast acoustic perturbation (Case B1).

In addition to the conventional second mode, mach wave-like radiating structures can be observed near the tail end of the disturbance wavepacket between $x = 1.25$ m and $x = 1.45$ m. This behavior is characteristic of a supersonic mode, which is a discrete mode instability which propagates supersonically relative to the local meanflow[3]. Recent studies have shown that these supersonic modes may have disturbance amplitudes which are similar to or even greater in strength when compared to the primary second mode instability, and as a result may be of significant importance in the process of transition [3, 24, 25, 94]. Of particular note is that the extensive supersonic mode observed here occurs in a low enthalpy perfect gas case whereas Knisely[3, 24, 25] and Mortensen[94] primarily observed strong supersonic modes in high-enthalpy flows with strong thermochemical nonequilibrium effects. This indicates that significant supersonic modes may be present in a wider range of conditions than previously believed. While the supersonic mode seen here is relatively weak compared to the primary second mode disturbance and emerges far enough downstream on the cone that it isn't likely to effect transition, it may play a role in downstream phenomena such as nonlinear breakdown.

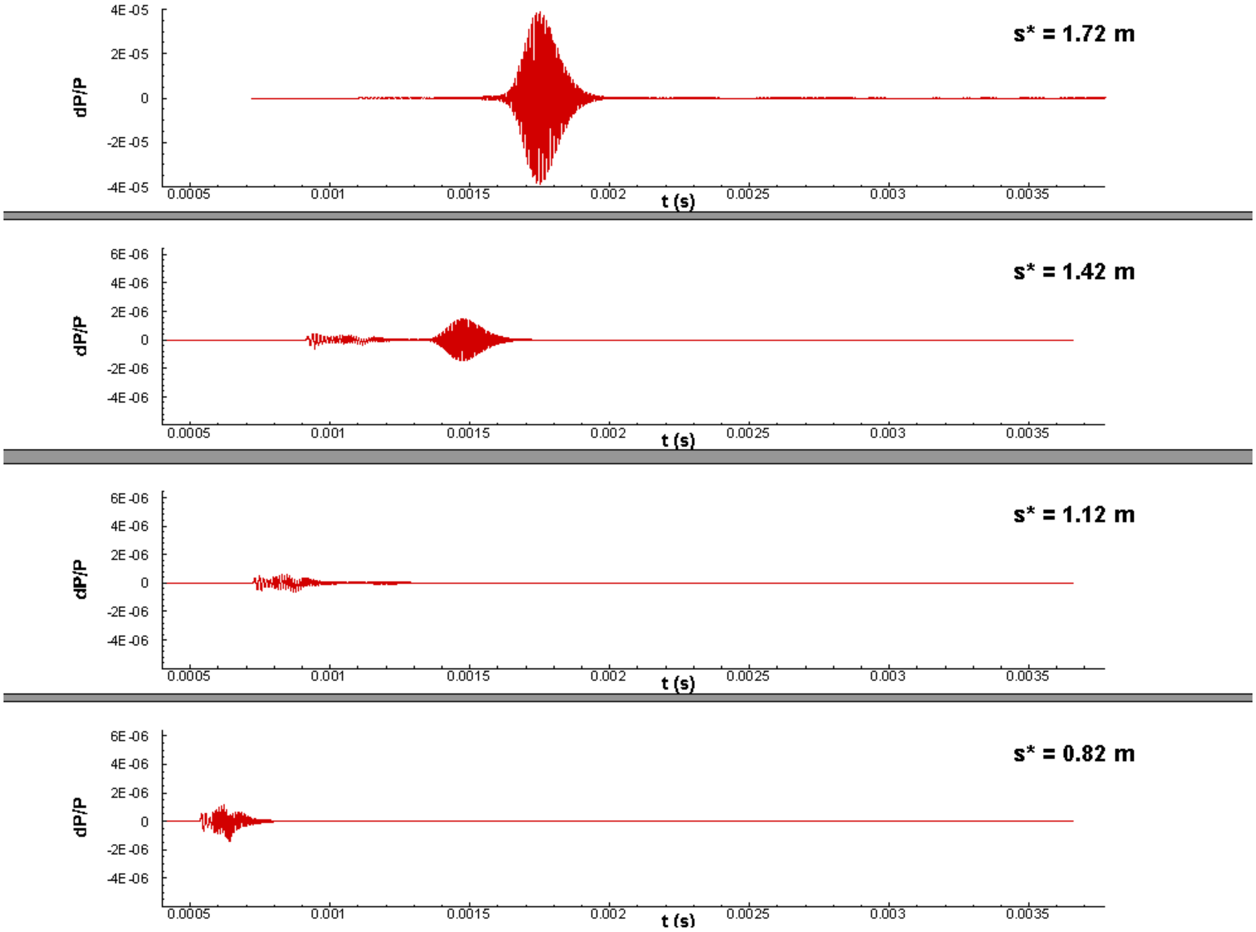

Figure 4.15: Time history of normalized surface pressure perturbations resulting from finite spherical fast acoustic pulse disturbance (Case B1).

The normalized surface pressure perturbations along the cone after excitation by a finite spherical fast acoustic pulse (Case B1) are presented in Fig. 4.15 for a selection of streamwise positions. Before the second mode region, the wavepacket is highly irregular and is dominated by oscillations associated with non-modal forcing. This disturbance packet consists of the primary discrete acoustic and entropy modes introduced upstream in the initial shock-disturbance interaction, as well as any continuous mode instabilities introduced as well during this interaction. The previous LST shows that at the initial sampling position at $s^* = 0.82$ m minimal modal amplification has occurred for only a select number of frequencies. As such, no particular instability mode dominates. These forcing waves are shown to decay upstream of the second mode region for the most unstable frequencies, between the shown positions of $s^* = 0.8$ m and $s^* = 1.27$ m before experiencing significant amplification further downstream. The increasingly regular wavepackets seen at $s^* = 1.42$ m and $s^* = 1.72$ m are indicative of the presence of a dominant second mode instability, and the rapid increase in the amplitude of the wavepacket denotes the strong destabilizing effect of the second mode.

The total surface disturbances depicted in Fig. 4.14 and Fig. 4.15 may be studied more quantitatively through the use of Fourier decomposition. The surface pressure perturbation signal is decomposed into its spectra of discrete frequency disturbances using a Fast Fourier Transform (FFT) algorithm taken from Ref. [99]. The resulting normalized surface pressure spectral contours for the finite spherical fast acoustic (Case B1), slow acoustic (Case B2), temperature (Case B3), and vorticity (Case B4) disturbances are shown in Fig. 4.16 for the blunt Case B geometry. These Fourier decomposed pressure disturbances are normalized by the spectral content of the initial freestream disturbance shown in Fig. 3.4b to account for the non-uniform amplitude spectra of the initial pulse[72]. Additionally, the LST neutral curve is also plotted in solid black lines in these figures in order to help validate the unsteady results. The most amplified frequency for the studied domain was observed to be approximately 155 kHz and agrees well with the LST N-factors results presented previously. The neutral curves align as expected with the band, since peak unsteady amplification for the second mode disturbance should be centered about the branch II neutral line[3]. While there is a slight offset between the maximum amplitude of the second mode amplification lobe and the branch II curve, this is attributed to the nonparallel effects disregarded by the LST calculations. However, it is observed later in Fig. 4.20 for the 150 kHz disturbance that these nonparallel effects are very miniscule, and our DNS and LST demonstrate close agreement at the peak disturbance frequencies.Thus, while the LST results do not account for freestream forcing waves, the resultant downstream perturbation spectra are shown to be dominated by the modal instability predicted by LST and the neutral curve is still relevant to the amplification behavior of the primary second mode.

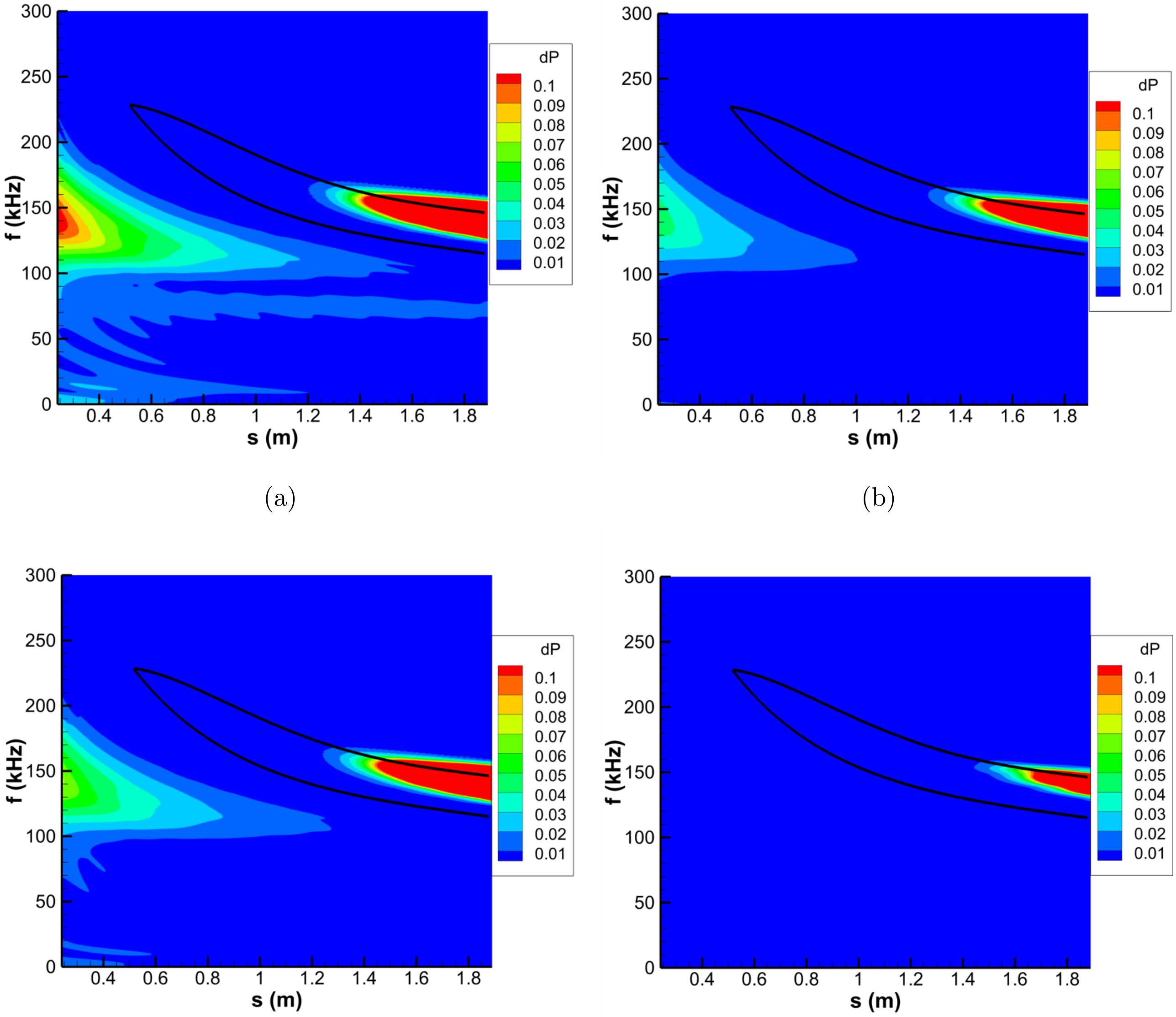

(a)

(b)

(c)

(d)

Figure 4.16: Surface FFT pressure distribution for the finite pulse disturbances in (a) Case B1, (b) Case B2, (c) Case B3 and (d) Case B4.

Fig. 4.16 shows that the four finite spherical pulses similarly excite the second mode in the downstream portions of the cone. The primary band of instabilities observed in all four cases is centered between approximately 140 and 170 kHz, depending on streamwise position. An additional disturbance band between 100 kHz and 200 kHz is observed at the beginning of the domain in cases B1 through B3 and corresponds to the forcing waves generated by the shock-disturbance interaction upstream. A similar phenomenon is observed in Case B4 as well, though the general receptivity of the meanflow to freestream vorticity disturbances is weak enough that this forcing cannot be seen in the uniform contour levels in Fig. 4.16d. Similarly to Fig. 4.15 these initial lower frequency perturbations are attenuated until the second mode region, where modal amplification begins. Both the initial forcing and the second mode disturbance amplitudes were strongest for the finite spherical fast acoustic disturbance (Case B1), followed by the temperature (Case B3), the slow acoustic (Case B2), and finally the vorticity (Case B4) disturbances respectively. The finite vorticity pulse in particular is observed to have an extremely weak receptivity response relative to the other finite pulse cases, though it does induce the same second mode growth as the other pulses.

The FFT decomposed surface pressure perturbations at different streamwise locations both upstream and downstream of the second mode amplification region are also presented in Fig. 4.17 for Cases B1 through B4. As expected, the spectral surface pressure distributions for the finite spherical cases are very similar to each other. Again, we see that Case B1 excites the strongest overall pressure perturbations downstream in the second mode region. Case B1 also generates stronger initial disturbance waves upstream of the second mode amplification region, as observed in the normalized surface pressure contours. Distinctive peaks in the disturbance amplitude can also be seen here, initially centered around frequencies of approximately 170-180 kHz. As the sampling point moves further downstream this peak disturbance band shifts to center around lower frequencies while also growing in overall amplitude, eventually centering around 145-155 kHz near the end of the computational domain. The high amplitude peaks observed here correspond to the primary second mode instability for this flow. This shift to lower frequencies in the downstream regions can also be seen in the LST results in Fig. 4.7, as optimal disturbances are expected to follow with the branch II neutral point, and is due to the gradual thickening of the boundary layer downstream along the cone. The broadband disturbance dampening and amplification pattern is clearly

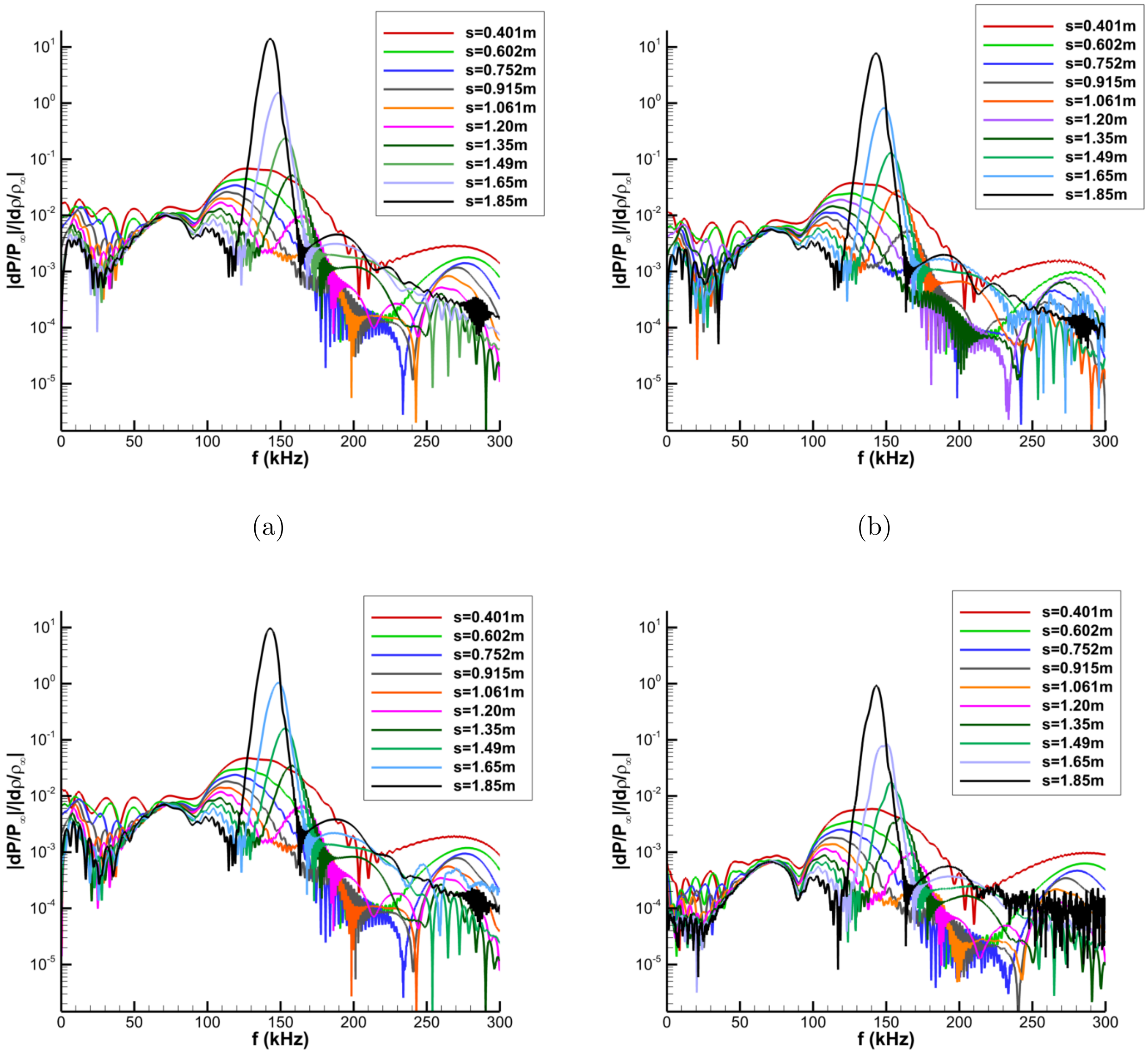

(a) (b)

(c) (d)

Figure 4.17: FFT decomposed surface pressure spectra at various streamwise locations for (a) Case B1, (b) Case B2, (c) Case B3, and (d) Case B4.

seen again here. While the spectral amplitudes for Cases B2, B3, and B4 are smaller, the same general trends are observed.

The spatial development of surface pressure perturbation amplitudes for a selection of highly amplified second mode frequencies is given for Cases B1 through B4 in Fig. 4.18. In the plot, each of the sampled frequencies initially start with significant amplitudes associated

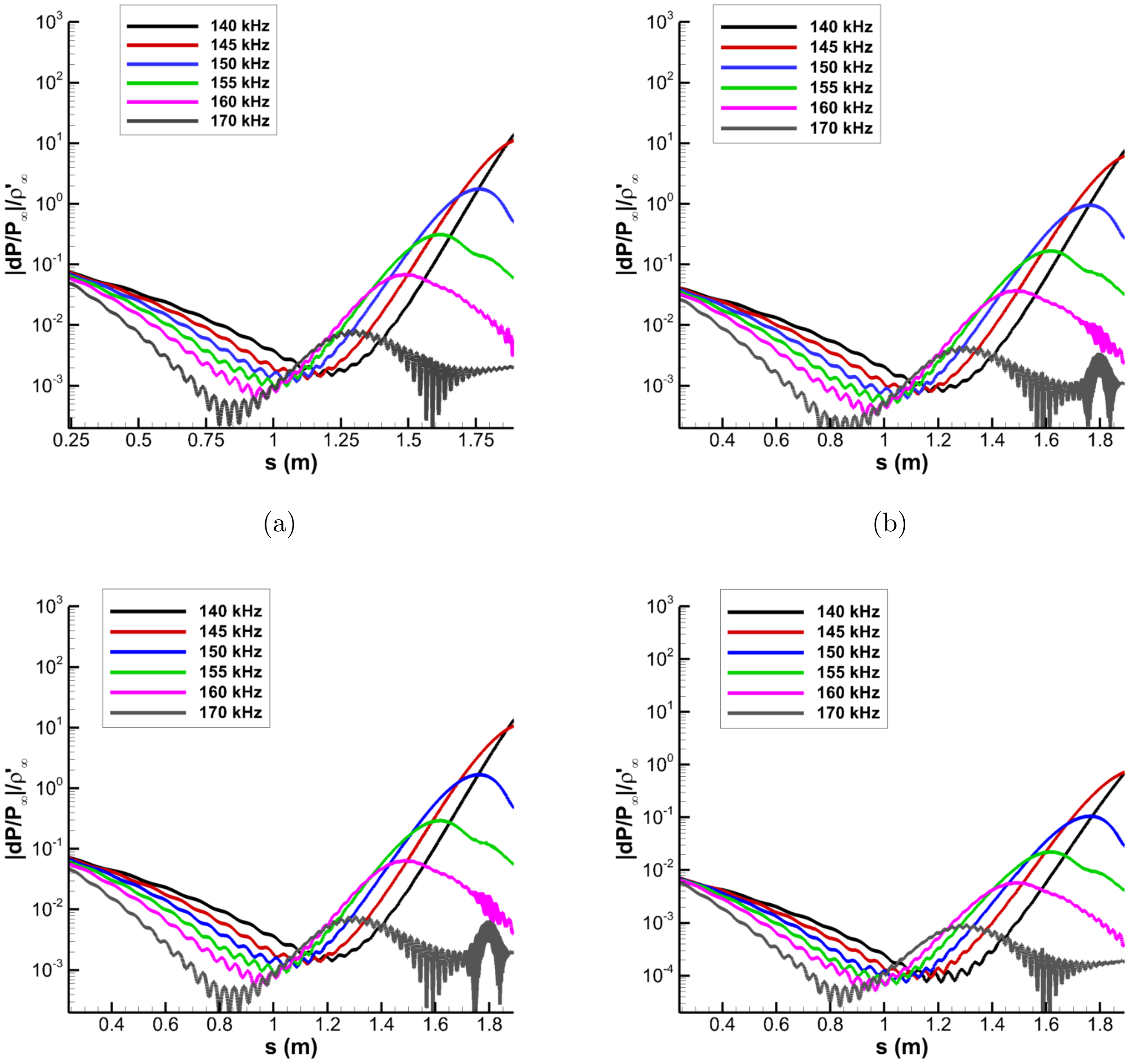

(a)

(b)

(c)

(d)

Figure 4.18: Surface pressure disturbance amplitudes at selected second mode frequencies for (a) Case B1, (b) Case B2, (c) Case B3, and (d) Case B4.

with the forcing excited upstream at the leading edge of the cone by the initial shock-disturbance interaction. Similar to what was observed in Fig. 4.15 and Fig. 4.16 these disturbances are attenuated until second mode amplification takes hold downstream. The oscillations in these signals are indicative of modal interference effects which can be observed near the local minima of each frequency, which correspond to the branch I neutral point of the disturbance of the frequency. The 160 kHz and 170 kHz sampled frequencies also exhibit the modal oscillation behavior near the end of the domain which is indicative of interactions with additional disturbance modes. This is particularly apparent in the slow acoustic (Case B2) and temperature pulse (Case B3) cases which see the development of an additional amplification peak. This localized amplification may be due to a number of reasons including both the development of supersonic mode instabilities or from the development of higher Mack mode disturbances. These higher Mack modes occur when additional discrete fast acoustic modes emerge downstream on the cone. These can also synchronize with the discrete slow acoustic mode, which may result in additional destablization. This is can be seen in Fig.1.2 in the introduction.

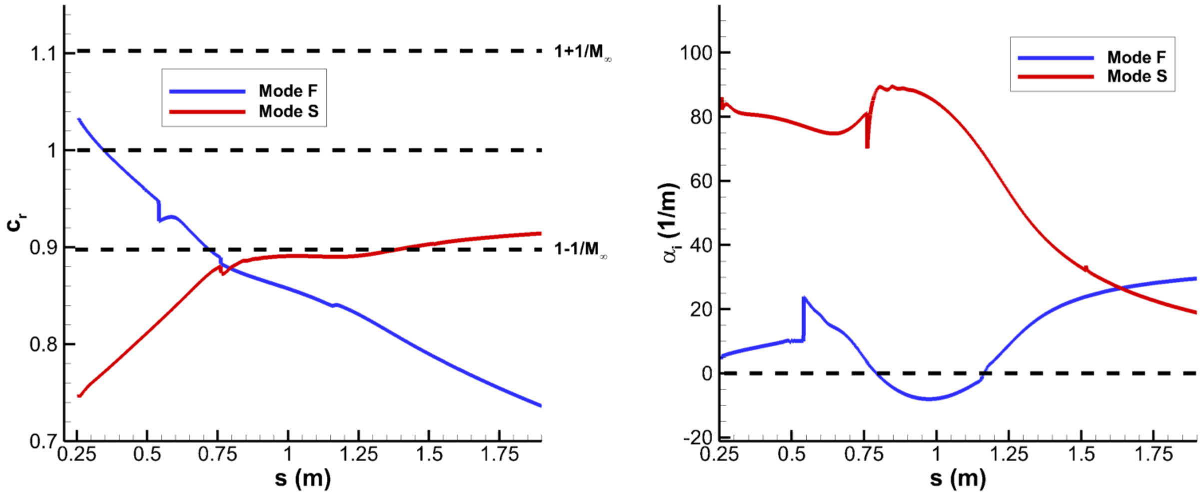

(a)

(b)

Figure 4.19: Case B LST (a) Phase Speed and (b) growthrate for a 170 kHz disturbance.

The LST analysis was unable to detect a destabilized higher mode. Additionally, this localized disturbance amplitude peak is not universal in all of the unsteady finite pulse cases. As such, it is unlikely for this localized instability to be just from an unstable higher mack mode. An excited supersonic mode may instead be responsible for this local destabilization. The 155 kHz disturbance also demonstrates a distinct kink near $s^* = 1.7$ m that shows some minor localized amplification not observed for the other disturbance frequencies. Unstable supersonic modes have previously been shown to increase growthrates and distort and the resulting N-factor curves[24]. Such behavior seems to be isolated to a very small range of frequencies for Case B1, and is not observed in our LST analysis. This is likely due to the relatively warm walls of the meanflows in this study ($T_w/T_\infty = 1.01$), which have been shown to make supersonic modes difficult to detect with LST[3]. Looking at the phase speed and growthrate LST results for a 170 kHz disturbance in Fig. 4.19 it is seen that the discrete mode F passes the slow acoustic spectrum and becomes supersonic relative to the meanflow for a significant portion of the flow. Subsequent mode F instabilities can emerge downstream along the cone from the continuous fast acoustic spectrum (which are named successively as mode F2, F3, etc...). Conventionally, these are also expected to synchronize with the continuous spectra as well as the discrete mode S to possibly generate additional Mack mode instabilities. They may also become supersonic as well. This can result in a weak, localized supersonic mode instability for a small band of frequencies and generate the anomalies in some of the amplification curves shown in Fig. 4.18. Variations in these secondary peaks indicate differences in the receptivity responses of these additional instabilities. However their downstream location, narrow frequency ranges of significance, and relatively low amplitudes indicate that they should have a minimal effect on the total stability behavior of Case B.

Through Eq. 3.36, 3.37, and 3.38 the Fourier decomposed unsteady DNS can be used to calculate the growthrates and phase speeds of different discrete frequency surface perturbations. The 150 kHz frequency disturbance in particular was used in order to validate the results of the unsteady DNS. The results for the 150 kHz frequency disturbance for the finite spherical fast acoustic (Case B1), slow acoustic (Case B2), temperature (Case B3), and vorticity (Case B4) pulses are presented in Fig. 4.20, 4.21, 4.22, and 4.23 respectively.

The pulse disturbance is observed to primarily excite the discrete mode F upstream on the cone. Furthermore, the unsteady DNS results for case B1 show good general agreement with LST, demonstrating that the discrete mode F is unstable for this case. The LST predicts an extensive synchronization range for this frequency between streamwise locations of 1.1 m and 1.8 m. Near the beginning of the synchronization region, significant oscillations in both

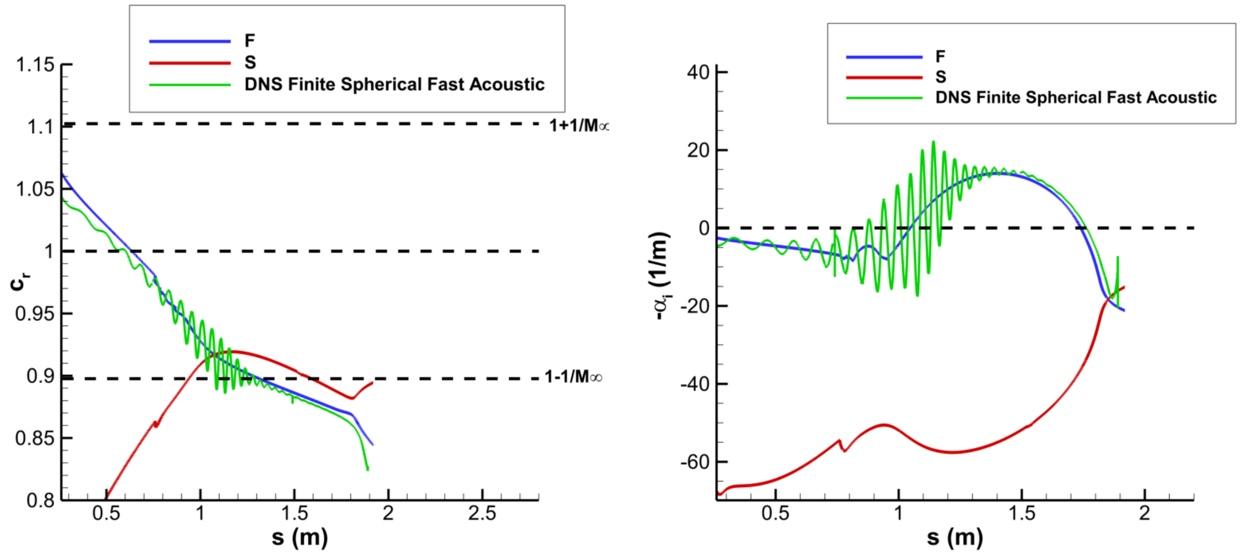

(a) (b)

Figure 4.20: Case B1 unsteady DNS vs. LST predicted results for 150 kHz disturbances (a) Phase Speed (b) growthrate.

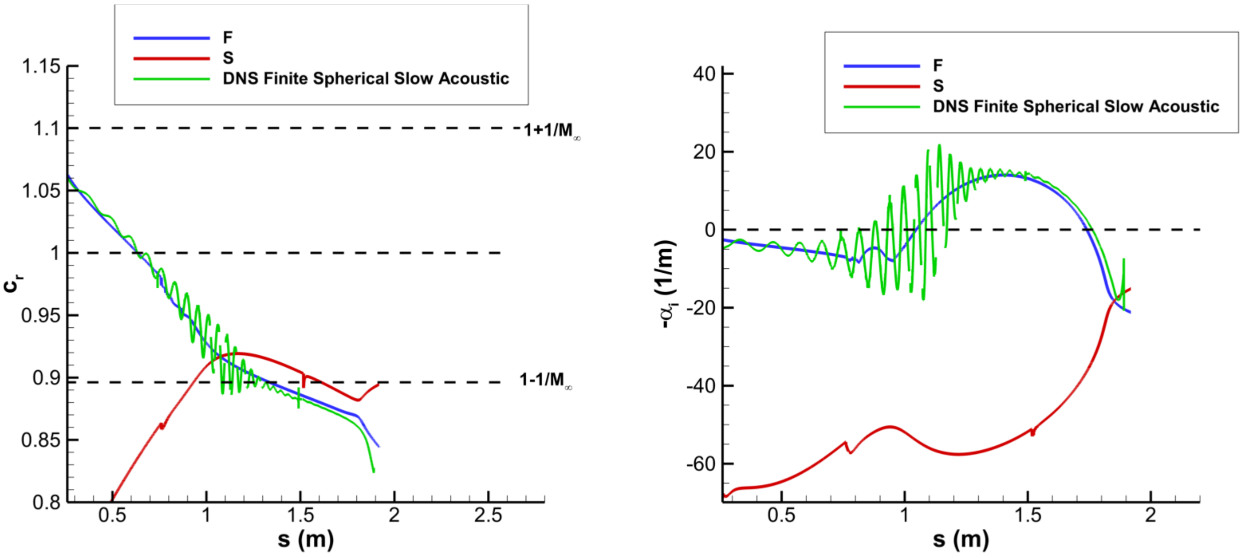

(a) (b)

Figure 4.21: Case B2 unsteady DNS vs. LST predicted results for 150 kHz disturbances (a) Phase Speed (b) growthrate.

the phase speed and growthrates can be observed in the DNS results. This oscillation is indicative of modal interactions associated with the synchronization of the discrete modes, though it is still apparent that the unstable mode F dominates the flow. These oscillations dampen out significantly as the disturbance propagates through the end of the domain for Case B1 in Fig. 4.20.

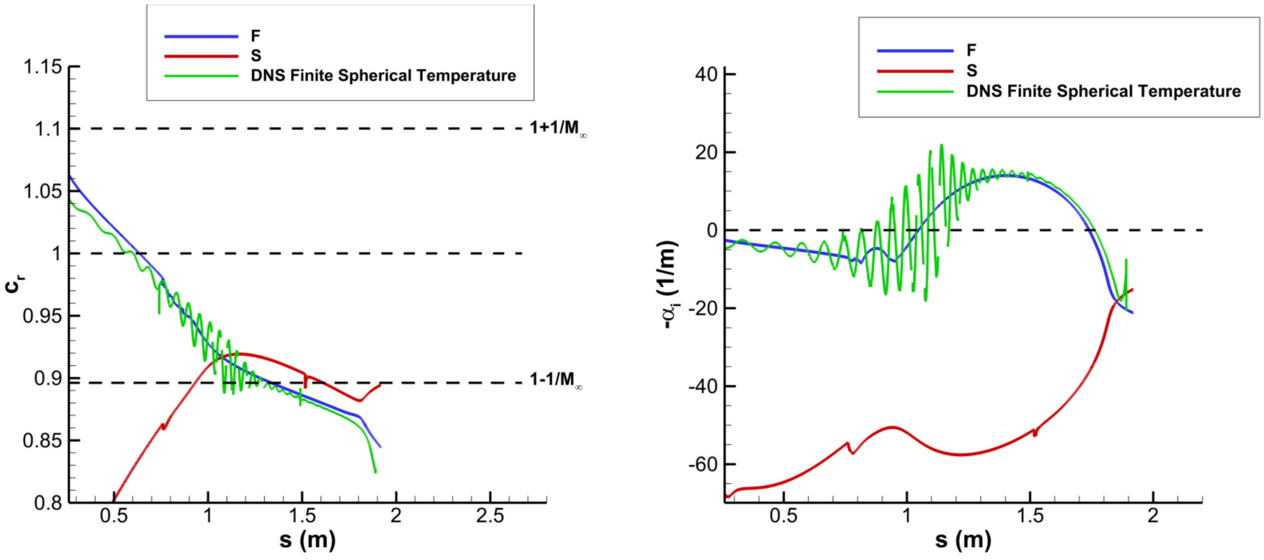

(a)

(b)

Figure 4.22: Case B3 DNS vs. LST predicted results for 150 kHz disturbances (a) Phase Speed (b) growthrate.

The results for Case B2 in Fig. 4.21, Case B3 in Fig. 4.22, and Case B4 in Fig. 4.23 similarly follow the unstable mode F disturbance, with the pulses uniformly exciting strong discrete mode F disturbances in the boundary layer for all four unsteady cases. Similar signal modulations are observed near synchronization in all four cases as well, though these are more significant for the finite vorticity pulse in Case B4. This may be due to the fact that the general receptivity response for Case B4 was significantly weaker than the other cases, which allowed for nonmodal noise to become more prevalent in the unsteady signal.

The unsteady DNS results for the 150 kHz for the finite pulses in Cases B1 through B4 share many similarities. However, significant differences in the upstream receptivity response are observed in the total FFT decomposed surface amplitude spectra. It can be concluded that while all of the finite pulse cases were able to significantly excite the second mode, they do not share the same general receptivity response. This necessitates the further study

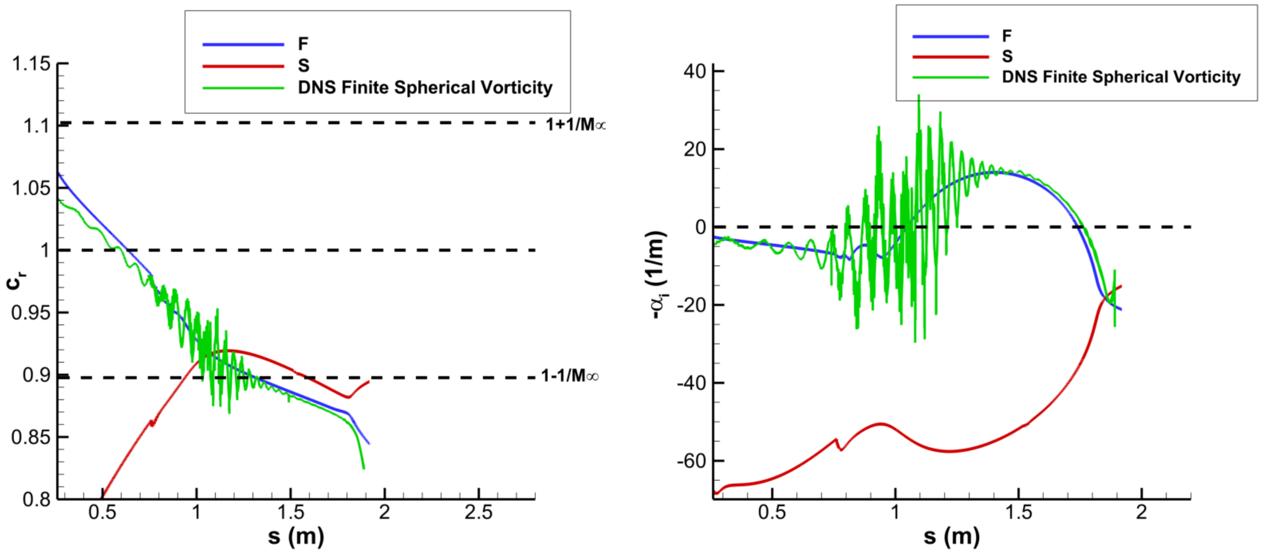

(a) (b)

Figure 4.23: Case B4 DNS vs. LST predicted results for 150 kHz disturbances (a) Phase Speed (b) growthrate.

of these disparate freestream disturbance types in order to fully characterize the possible responses the meanflow can have to different sources of environmental perturbation.

Fig. 4.24 depicts the instantaneous pressure and temperature disturbances immediately after the finite pulse interaction at the nose for Case I1. Similar to the previous results for Case B in Fig. 4.13a, the pressure disturbance contours depict acoustic waves propagating toward the cone surface and being reflected back towards the bow shock in the manner expected of acoustic disturbances. The temperature perturbations are again seen to pile up near the surface of the cone as they propagate to the end of the computational zone in a manner expected from excited entropy modes. However, distinct differences in the spatial extent of the shock layer perturbations are observed in both the temperature and pressure disturbance contours between Case B and Case I. This is a direct result of the pulse model used, as the σ term which governs the disturbance bandwidth of the pulse also determines its spatial extent. Since this parameter was fixed between both Case B and Case I, the pulses remain the same size. As Case I has a smaller nose radius, the resulting disturbance field is much more extensive relative to the flowfield at the nose.

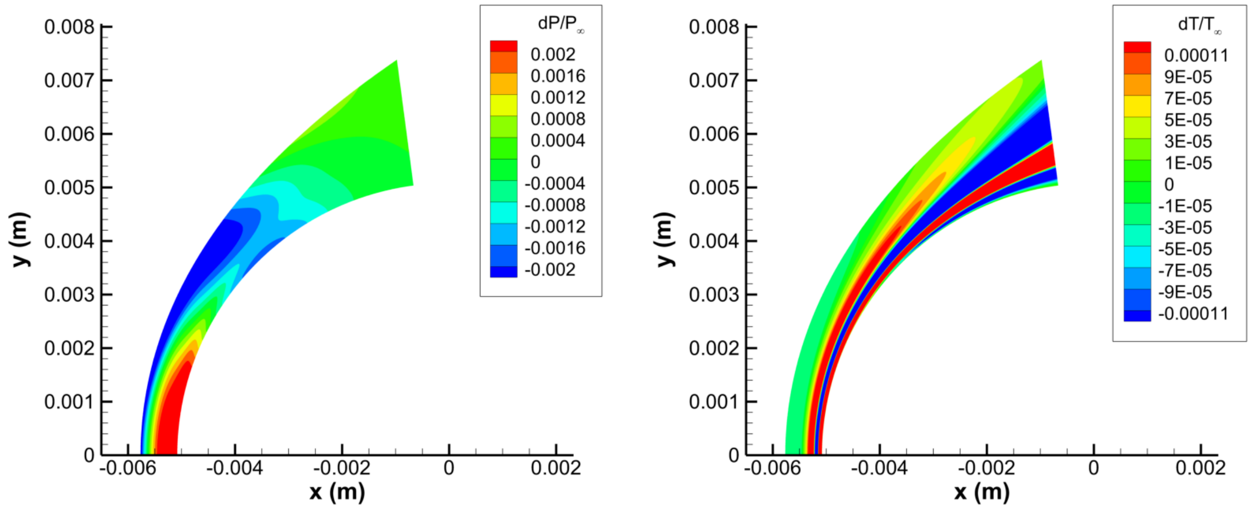

(a)

(b)

Figure 4.24: Normalized (a) pressure perturbations and (b) temperature perturbations at the nose region for Case I1.

Fig. 4.25 depicts shock-layer pressure disturbances downstream on the cone for Case I1. The leading front of the wavepacket is captured in Fig. 4.26a and Fig. 4.26b, which contains excited boundary layer modes as well as continuous mode disturbances that are distributed throughout the entire shock layer. This is similar to what was observed previously for Case B, as well as for Huang's entropy spot cases from Ref. [4]. A more significantly amplified second mode is contained in the tail of the wavepacket in Fig. 4.26c. Weak acoustic radiation is also qualitatively observed here, between $x = 1.25$ m and $x = 1.38$ m, indicating the presence of supersonic modes in this case as well. However, this radiation is noticeably weaker than in Case B1. As such, it is unlikely to be significant in these unsteady cases.

The other three finite pulse cases (Cases I2, I3, and I4) show very similar general second mode structures in Fig. 4.26, and also demonstrate acoustic the radiation characteristic of a supersonic mode. Similar to the results for Case I1 shown earlier, however, this acoustic radiation is extremely weak in the rest of these cases as well. Furthermore, Cases I1 through I4 are shown to experience a sudden decrease in perturbation amplitude between 1.35 m and 1.40 m near the boundary layer edge. This is attributed to interference between the

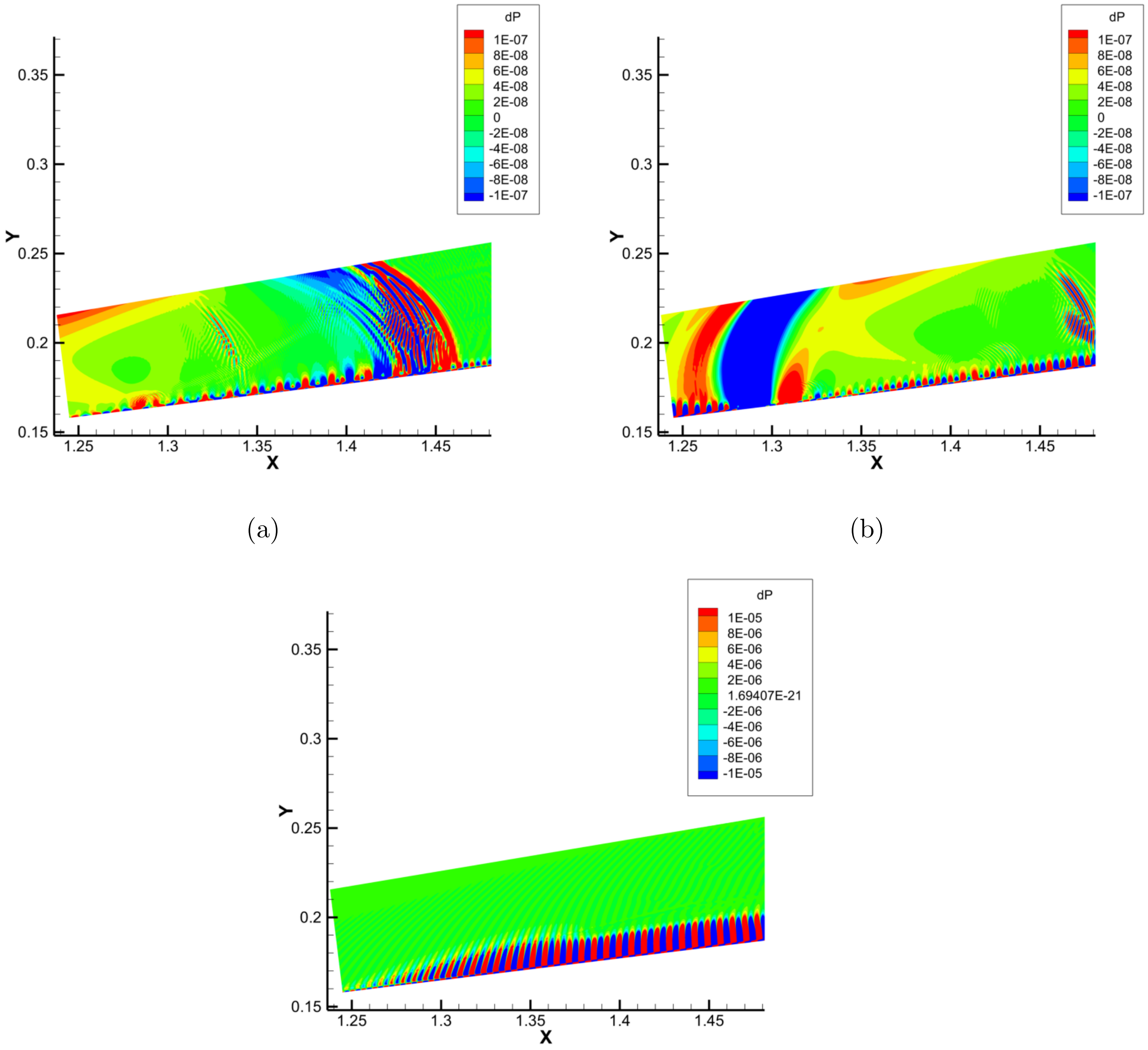

(a)

(b)

(c)

Figure 4.25: Pressure snapshots in the shocklayer downstream on the cone for Case I1 for (a) Forward disturbance front, (b) Rear disturbance front, and (c) second mode disturbance.

primary unstable mode S and the satellite waves of a stable supersonic mode F. This is highly similar to a result observed by Haley and Zhong[102] for low enthalpy hypersonic flow over a slender cone. The extent of this effect is unknown in terms of its impact on boundary layer transition, but it is indicative of a much more complex set of interactions in the unsteady boundary layer than initially expected.

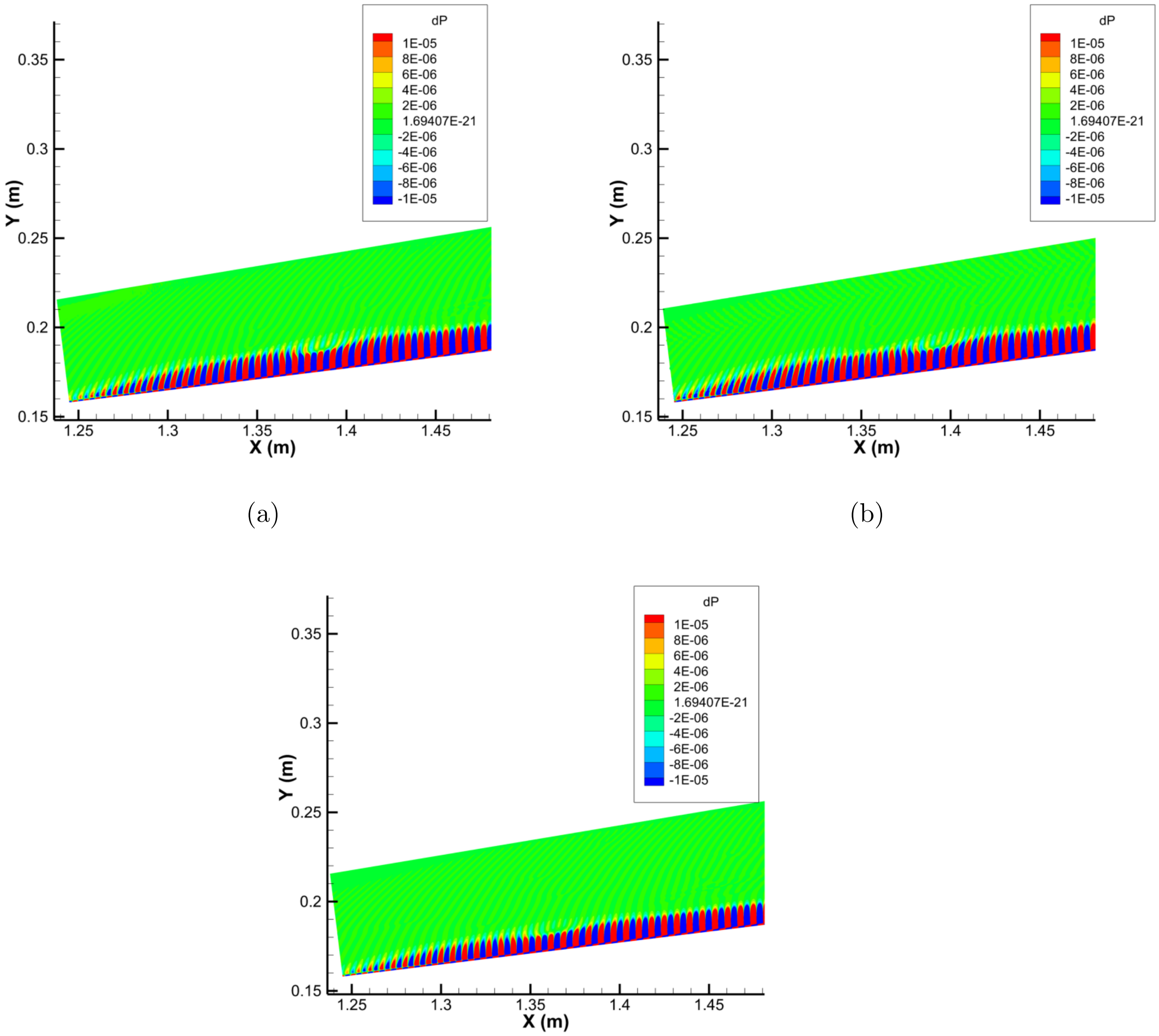

(a)

(b)

(c)

Figure 4.26: Second mode pressure disturbance snapshots downstream for (a)Case I2, (b) Case I3, and (c) Case I4.

A time history of the total surface pressure perturbations at different streamwise positions along the cone is also presented in Fig. 4.27 up to 0.7 m for Case I1. Similar to the Case B1 results in Fig. 4.15 the most upstream sampled wavepacket at $s^* = 0.3$ m is highly irregular and contains a multitude of disparate forcing modes excited by the shock-disturbance interaction at the nose. This forcing follows the standard behavior observed previously, and decays initially as the packet propagates downstream until the unstable second mode region, where significant amplification causes a more defined modal wavepacket shape to take form. This modal wavepacket begins forming near $s^* = 0.599$ m until modal amplification causes it to dominate the acoustic disturbance profile at $s^* = 0.700$ m.

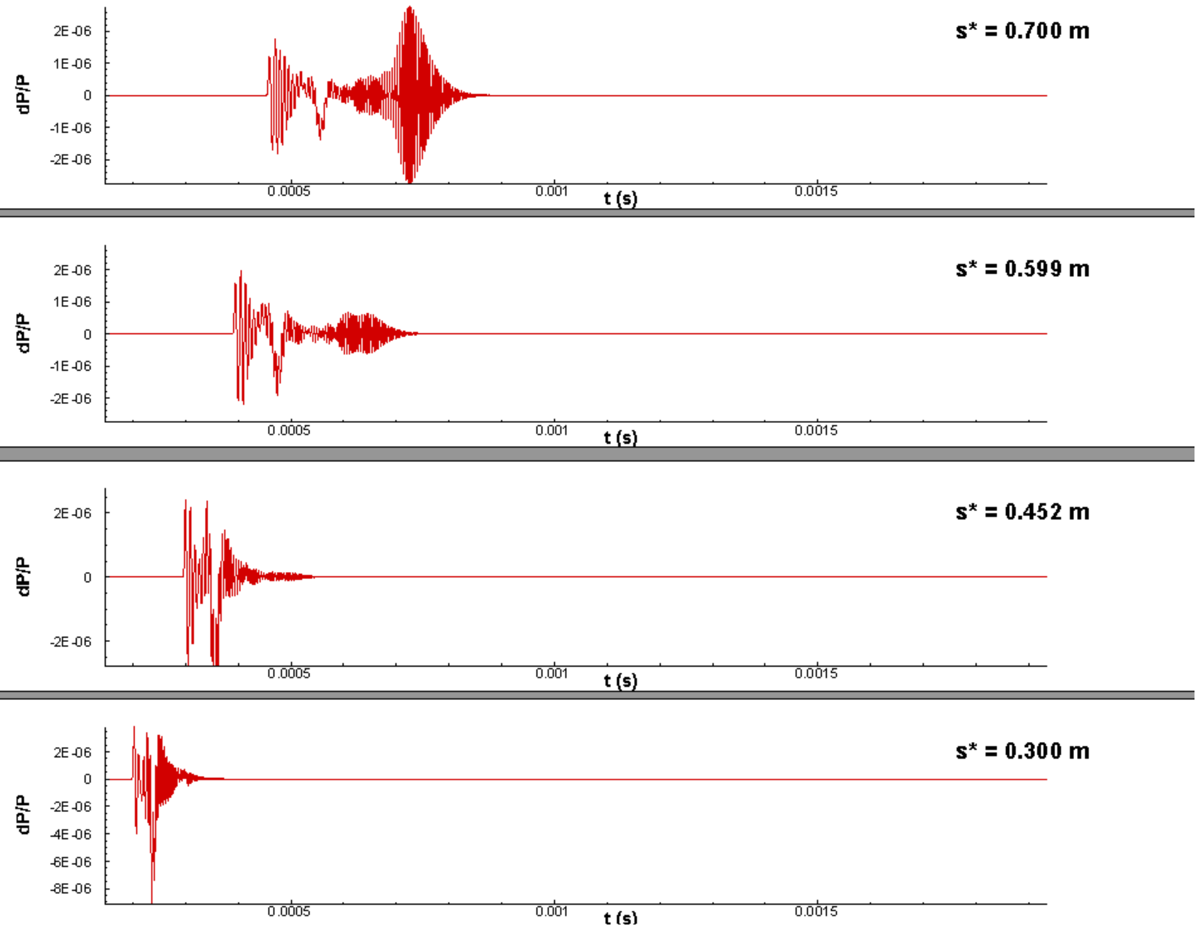

Figure 4.27: Time history of normalized surface pressure perturbations resulting from Case I1 up to 0.7 m.

Fig. 4.28 presents the same surface perturbation time history at additional downstream locations. The y-axis for the figure at $s^* = 1.103$ m and at $s^* = 1.495$ m are not uniform with the upstream regions due to the much higher disturbance amplitudes at the downstream positions. It can be seen from these results that the second mode induces extreme amplification in the wavepacket downstream of $s^* = 0.7$ m. An additional secondary node in the wavepacket is observed at the final two sampling locations that also experiences significant amplification and is likely a higher order Mack mode.

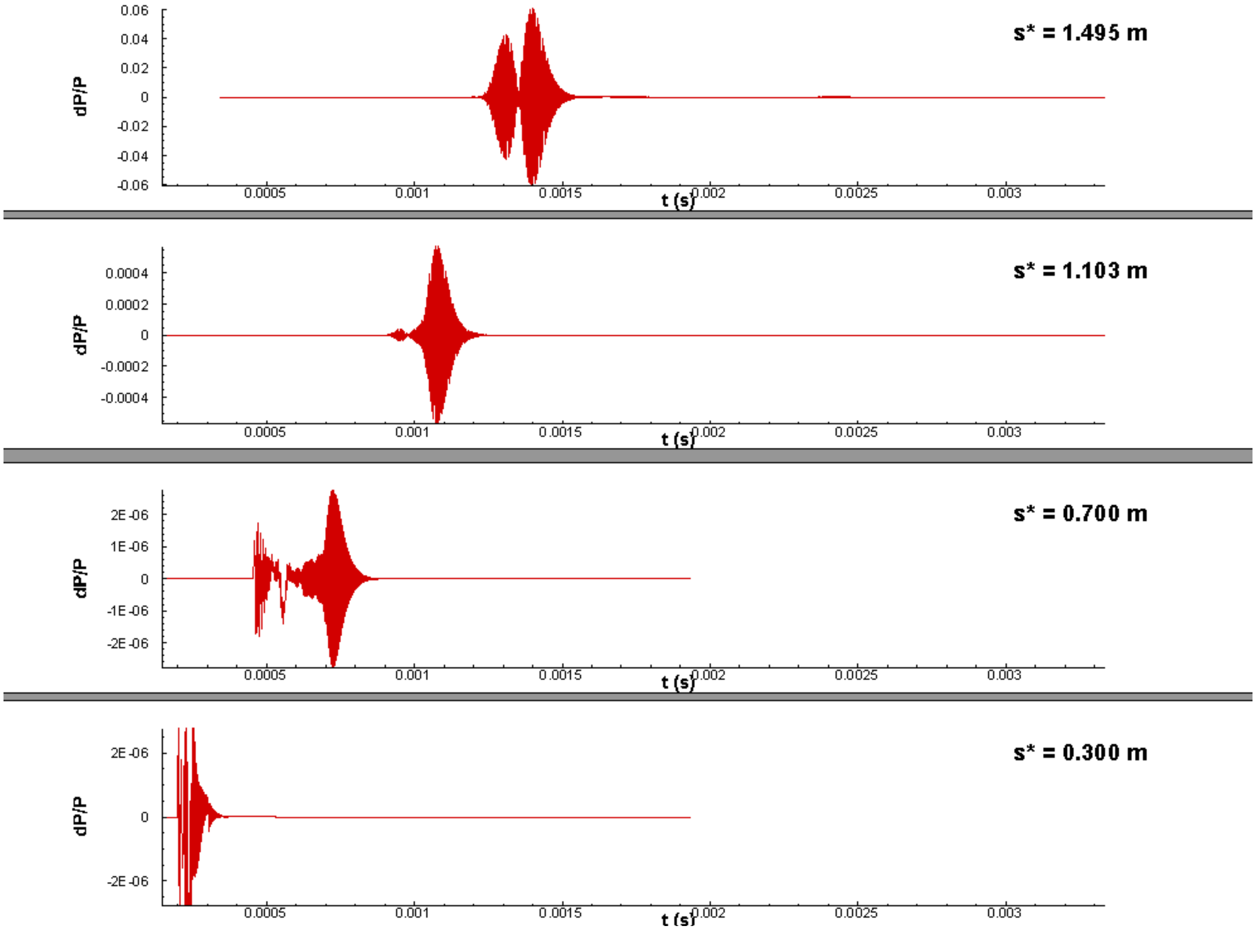

Figure 4.28: Time history of normalized surface pressure perturbations resulting from Case I1 up to 1.5 m.

The unsteady surface pressure data for Cases I1 through I4 are again decomposed using FFT, and the resulting surface pressure amplitude spectra is depicted in Fig. 4.29. The LST neutral curve is also plotted in these figures as a solid black line to corroborate our LST and unsteady DNS results. Again the finite pulse cases for all four disturbance types exhibit very similar normalized surface pressure spectra with each other, and also follow the general pattern observed for the finite pulses in Case B. In particular, each of the pulses demonstrates upstream excitation of lower frequency forcing which experience gradual attenuation. Second mode amplification then occurs and generates a dominant disturbance band centered about the branch II neutral curve.

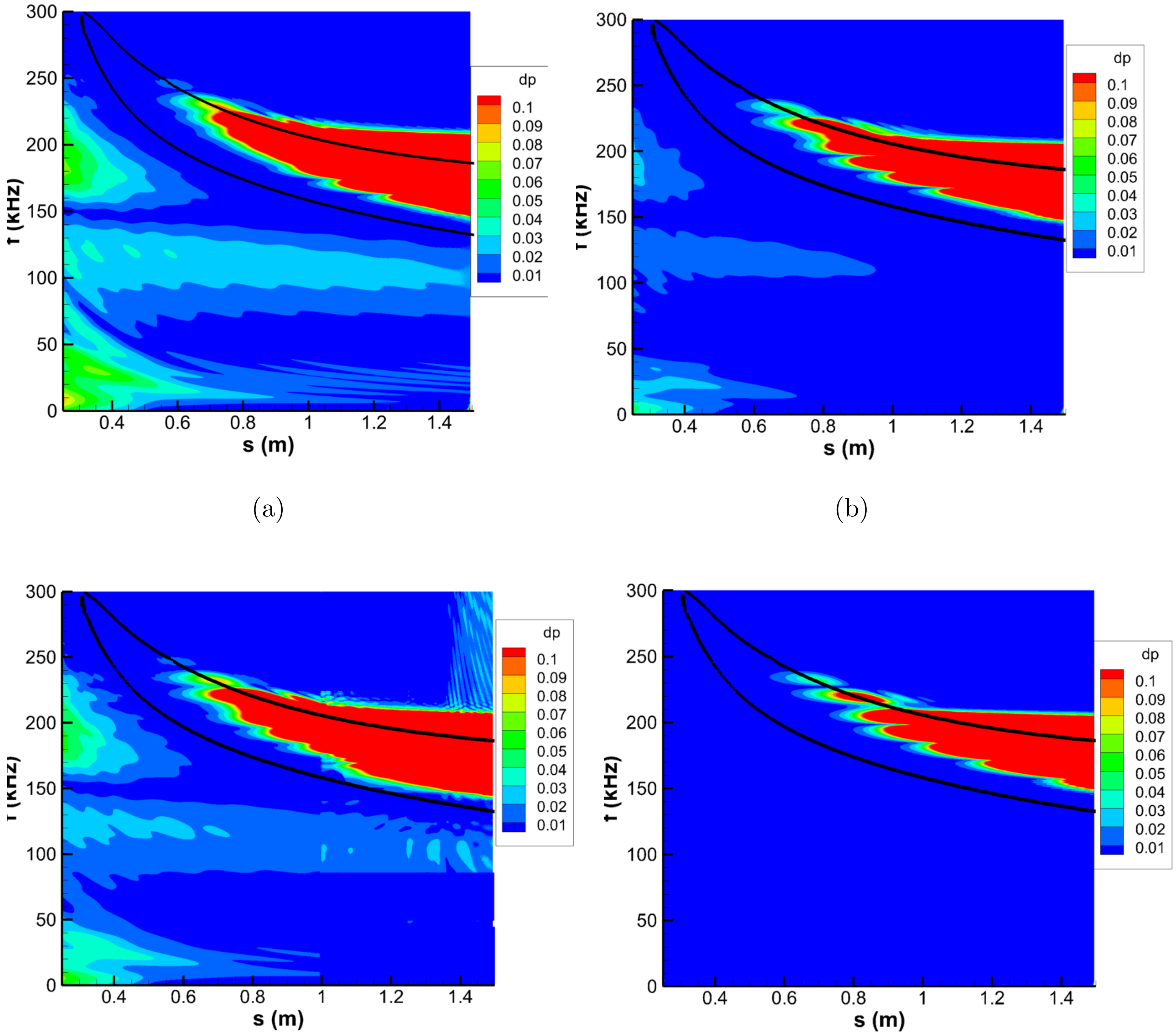

(a) (b)

(c) (d)

Figure 4.29: Normalized FFT surface pressure contour for (a) Case I1, (b) Case I2, (c) Case I3 and (d) Case I4.

While the general spectral behaviors of the flows are the same, some key differences are observed between the surface pressure spectra for Cases B1 through B4 and Cases I1 through I4. For one, the unstable second mode region is observed to occur at both a higher frequency and earlier along the cone geometry for Case I. In particular, the LST predicts second mode destabilization at $s^* = 0.305$ m for Case I and at $s^* = 0.517$ m for Case B.

In non-dimensional coordinates, this is approximately 55 to 60 nose radii downstream on both cones. While the second mode region begins at approximately the same downstream location in non-dimensional coordinates, the disturbance growthrates are directly observed to be higher by both LST and unsteady DNS analysis for the sharper Case I. This is directly related to the sharper nose geometry, which causes the boundary layer to be thinner for Case S. This in turn leads to smaller amplified wavelengths and higher amplified frequencies for sharper noses[7, 34]. The reduced nose radius also results in a thinner entropy layer that is swallowed earlier along the cone. The entropy layer acts as a buffer that locally reduces the Reynolds number, which in turn weakens second mode development. The less pronounced entropy layer thus allows earlier second mode amplification. As such, the growthrates were observed to be larger on average throughout the unstable second mode region in the LST results, resulting in the much more extensive band of excited frequencies observed in Fig. 4.29.

Additionally, while the general amplification patterns are the same between the two cases are the same, the nature of the upstream forcing varies significantly between the finite pulse results in Case B and Case I. In both the finite pulse Case B and Case I results, lower frequency disturbance bands are observed originating from the upstream regions. These may be attributed to other forced disturbance modes, such as continuous modes. Case B1 in Fig.4.16a demonstrates weak upstream excitation of a band of disturbances between 50 kHz and 100 kHz that experiences attenuation as it is propagated downstream. Similar results are observed for Cases B2, B3, and B4 in Fig. 4.16, though the upstream forcing is much weaker there. This is particularly true for Case B4, in which the upstream forcing cannot be observed without further reducing the minimum contour level. The upstream forcing is strongest for Case B1, which also most strongly demonstrates additional lower frequency forcing bands at approximately 80 kHz and near 0 kHz. The disturbances near 80 kHz are extremely weak, but propagate throughout the entire downstream domain without experiencing significant amplification or attenuation. These may be neutrally stable continuous modes that are excited upstream and continue to propagate throughout the flow field. The disturbances near 0 kHz are often associated with excited modes originating from the entropy layer that have been shown recently to also be involved in the destabilization of the second mode[64]. As such, the increased receptivity of these forcing frequencies for Case B1 may explain the stronger receptivity response observed in that case.

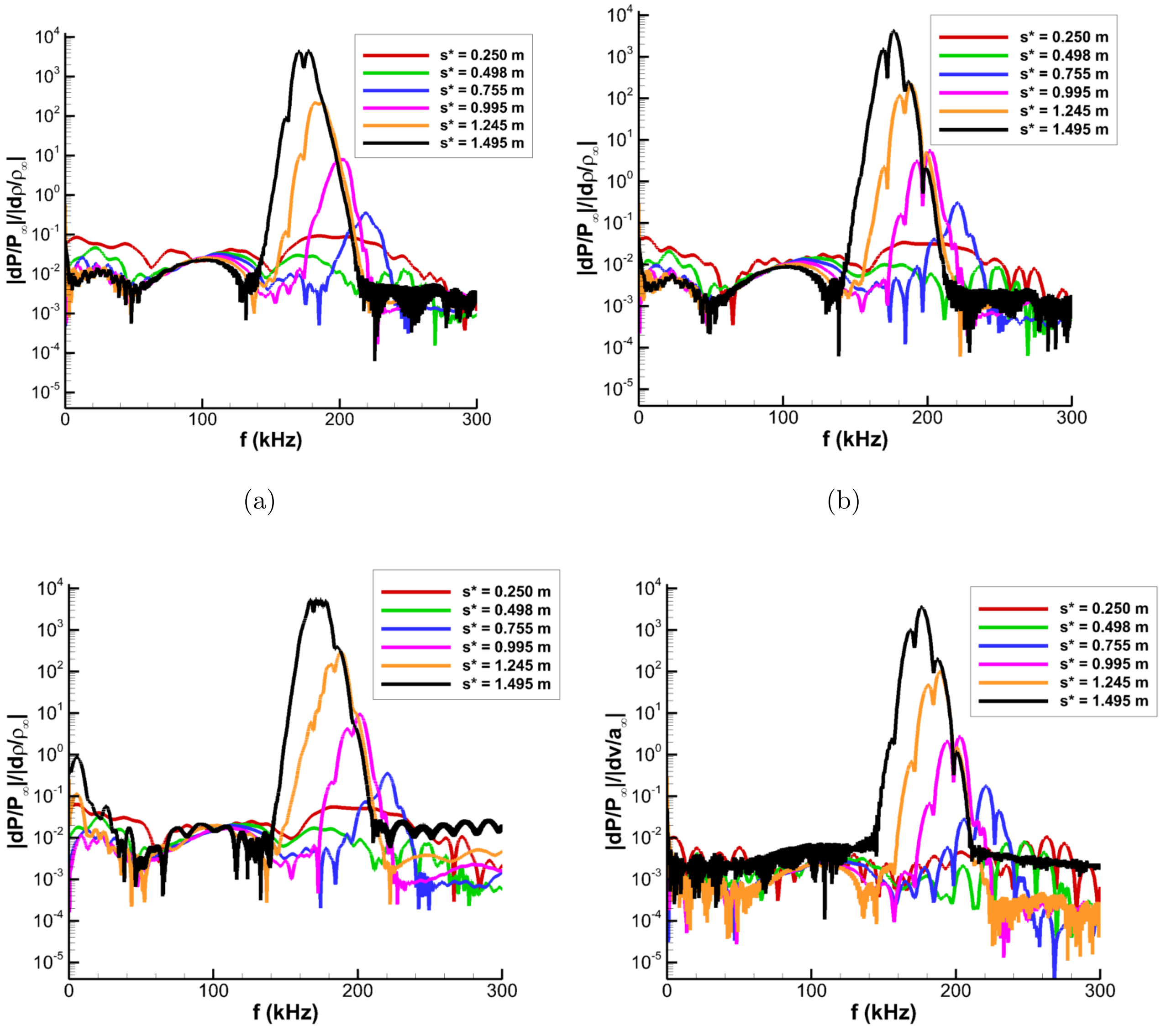

(a)

(b)

(c)

(d)

Figure 4.30: FFT decomposed surface pressure spectra at various streamwise locations for (a) Case I1, (b) Case I2, (c) Case I3, and (d) Case I4.

Similar, upstream forcing disturbances are also observed for Case I1 in Fig. 4.31a in the frequency range between 150 kHz and 250 kHz that is dampened immediately before the primary second mode region. Previous results from Balakumar and Kegerise[103] and Kara, Balakumar, and Kandil[33] have shown that first mode instabilities can also exist in blunt cones, though they are significantly weaker than the second mode. As such, these small disturbance bands may be remnants of stable first mode disturbances that were initially excited in the non-parallel regions near the leading edges. These are present in Cases I2, I3, and I4 as well though they are also weaker in these other cases. The finite vorticity pulse in Case I4 similarly demonstrates weak upstream forcing that cannot be observed without reducing the contour level. An additional intermediate band of disturbances between 100 and 150 kHz is also observed in these cases. For Case I1 and Case I3 this band demonstrates minor attenuation, but continue to the end of the domain. This band is significantly weaker in Case I2 and seems to dampen below observability by $s^* = 1.0$ m. This is similar to the intermediate forcing band observed in Case B1, and is attributed to neutrally stable/very weakly attenuated continuous modes. The extremely low frequency disturbances likely corresponding to swallowed entropy layer instabilities are significantly stronger for the finite pulses in Case I, particularly in Case I1 and Case I3. This indicates a stronger receptivity response for these modes for the intermediate bluntness case. In general we see that the high frequency forcing upstream on the cone is significantly stronger in the blunter Case B, while the low frequency perturbations associated with entropy layer instabilities are much higher for Case I.

The FFT decomposed surface pressure perturbations at different streamwise locations are also presented in Fig. 4.30 for Cases I1 through I4 for a selection of different streamwise positions. Again, the familiar trends are seen with an initial decay in boundary layer forcing followed by exponential modal amplification. The second mode disturbance is clearly identifiable between the frequencies of approximately 150 and 200 kHz. Very similar disturbance spectra are observed across all of the finite pulse cases. Contrary to the Case B results, the primary second mode peaks seem to experience some minor modulations. In particular, the strange multi-peak behavior is most obvious in the Case I2 and Case I4 results. These reflect the bulges found in the primary second mode bands in Fig. 4.29 for these cases. The origin of this multi-peak behavior has not been concretely identified, but recent experimental re-

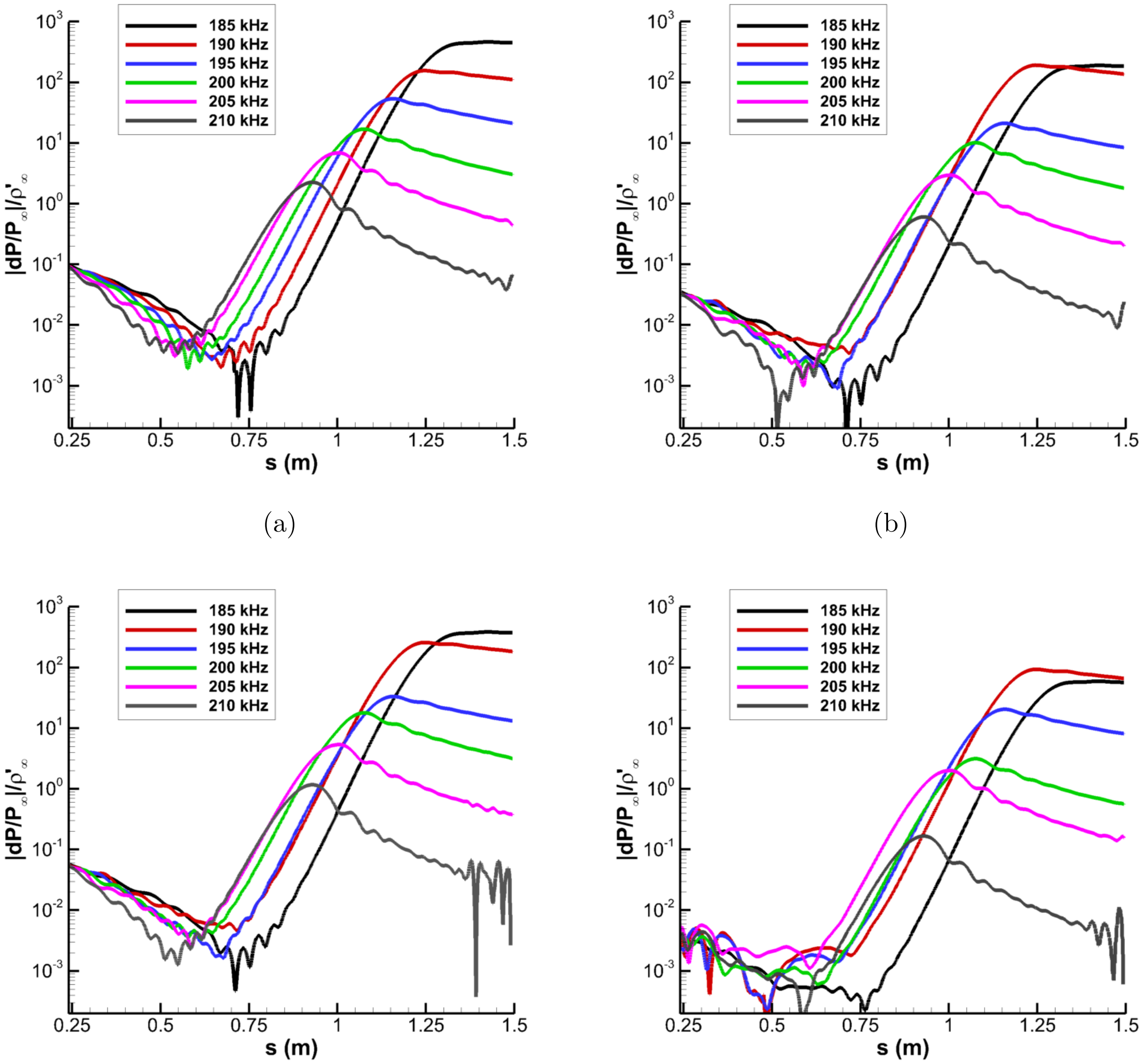

(a)

(b)

(c)

(d)

Figure 4.31: Surface pressure disturbance amplitudes at selected second mode frequencies for (a) Case I1, (b) Case I2, (c) Case I3, and (d) Case I4.

sults presented at the AIAA Scitech 2020 open forum by Professor Schneider of Purdue have shown that similar behaviors have been in experiment. One possible source of this behavior is the localized constructive and destructive interference of disturbances in the boundary layer due to wave dispersion[102]. This can occur due to the broadband nature of disturbances in boundary layer, as perturbations of different frequencies travel at different phase speeds. This can lead to localized constructive or destructive interference. However, the exact nature of this behavior and why this phenomenon is so much more prevalent in Case I remains unknown. The general receptivity response of the flow to the different disturbance types can be directly observed in these surface pressure spectra. The finite fast acoustic pulse (Case I1) was found to generate the strongest second mode and higher mode disturbances, followed by the finite temperature pulse (Case I3), the finite slow acoustic pulse (Case I2), and finally the finite vorticity pulse (Case I4).

The spatial development of surface pressure perturbation amplitudes for a selection of highly amplified second mode frequencies are given for Cases I1, I2, I3, and I4 in Fig. 4.31. Once again, similar general behaviors are observed with upstream forcing experiencing gradual attenuation before the unstable second mode region causes exponential growth in the disturbance amplitudes. The higher second mode growthrates for Case I cause the normalized disturbance amplitudes to be significantly higher for Case I in general, with peak values at the selected frequencies being approximately one to two orders of magnitude higher. The distinctive change in slope or the secondary maxima near the end of the domain is not observed for any second mode frequencies in Case I. This may be due to the weaker supersonic mode response observed in general for Case I, which is in part due to the fact that the destabilized discrete mode for Case I is mode S. Conventionally, the discrete mode S disturbance is understood to emerge from the continuous slow acoustic spectrum in the nondimensional phase speed diagram. While mode S can potentially synchronize with the continuous entropy/vorticity spectrum which propagates at the speed of the meanflow, it does not continue to increase in speed and pass the continuous fast acoustic spectrum. As such, it is unlikely for a discrete mode S to become supersonic in this way. The discrete mode S is also unlikely to slow significantly enough to synchronize again with the continuous slow acoustic spectrum. Therefore it is highly unlikely for the discrete mode S to induce an unstable supersonic mode, though external forcing may cause it to emerge in unsteady DNS[102]. The supersonic mode observed here is likely due to the forced mode F disturbances that are not fully attenuated at the observed locations in the unsteady contours.

The LST phase speed and growthrate results for the 200 kHz disturbance discussed

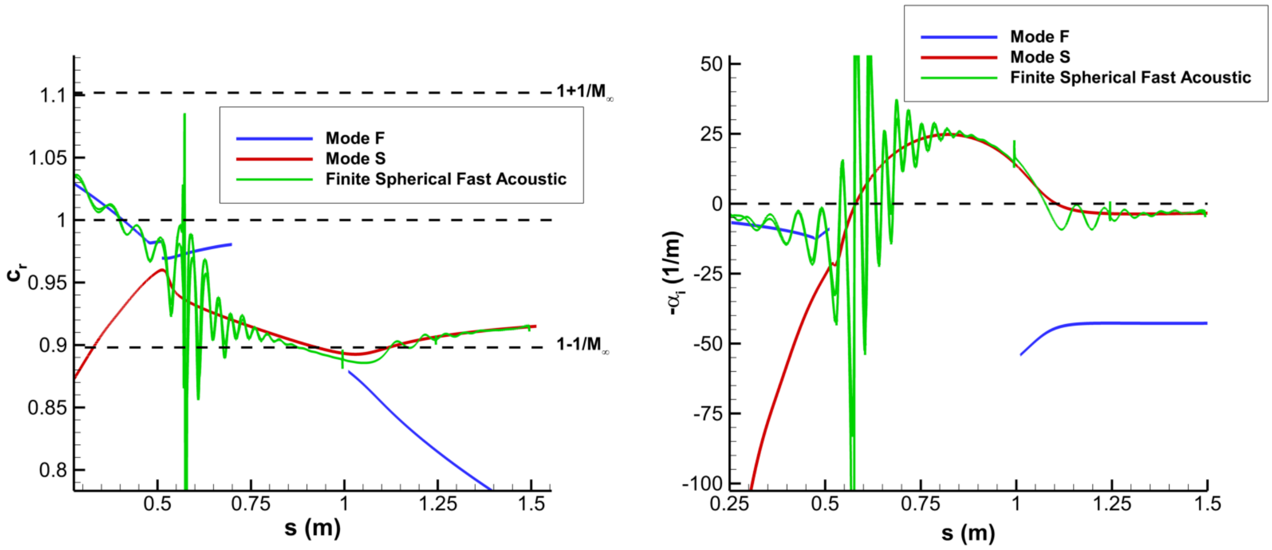

(a) (b)

Figure 4.32: Case I1 unsteady DNS vs. LST predicted results for 200 kHz disturbances (a) Phase Speed (b) growthrate.

previously are used here to further verify the results of the unsteady simulations. The comparisons for Case I1, Case I2, Case I3, and Case I4 are presented in Fig. 4.32, 4.33, 4.34, and 4.35 respectively.

The unsteady DNS results for Case I1 demonstrate good agreement with LST, and show that the finite pulses here also primarily generate mode F disturbances upstream on the cone in the initial shock-disturbance interaction. Furthermore, the results confirm that mode S becomes unstable after synchronization. This agrees with the general upstream receptivity mechanism observed previously for Cases B1 through B4 and other receptivity simulations for blunt cones[4, 60] in which fast acoustic disturbances are introduced by freestream forcing. The unsteady signal immediately jumps to mode S after synchronization near $s^* = 0.5$ m in Fig 4.32, with additional modulations in the unsteady signal occurring at synchronization. While the unsteady discrete mode S destabilizes and dominates the flow beginning at this initial synchronization point, the process involves strong multimodal interactions that muddle the unsteady signal. This results in the modulated signal seen both here and in the unsteady Case B results.

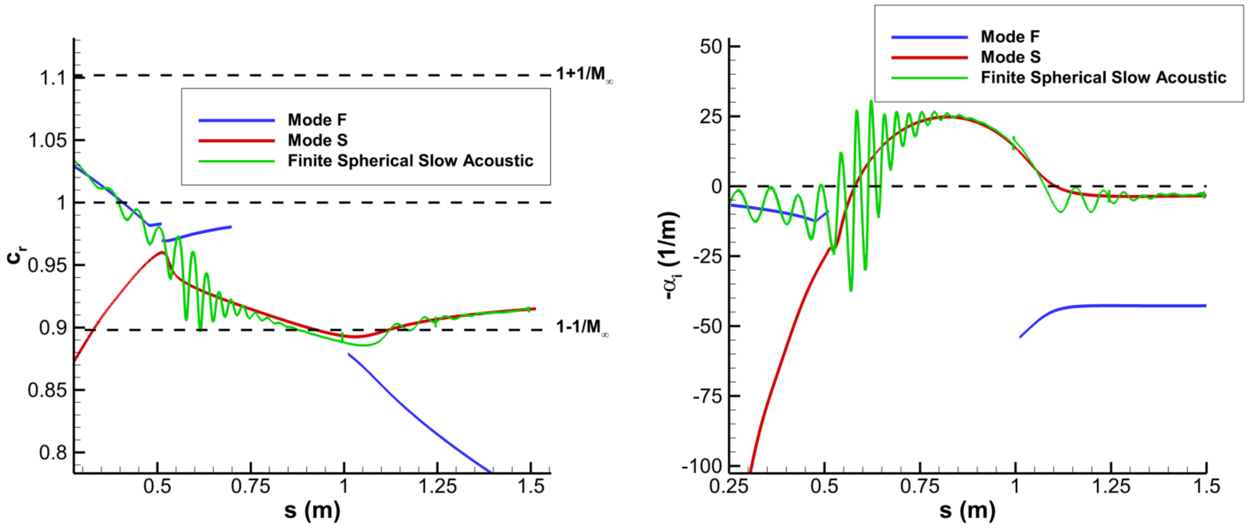

(a) (b)

Figure 4.33: Case I2 unsteady DNS vs. LST predicted results for 200 kHz disturbances (a) Phase Speed (b) growthrate.

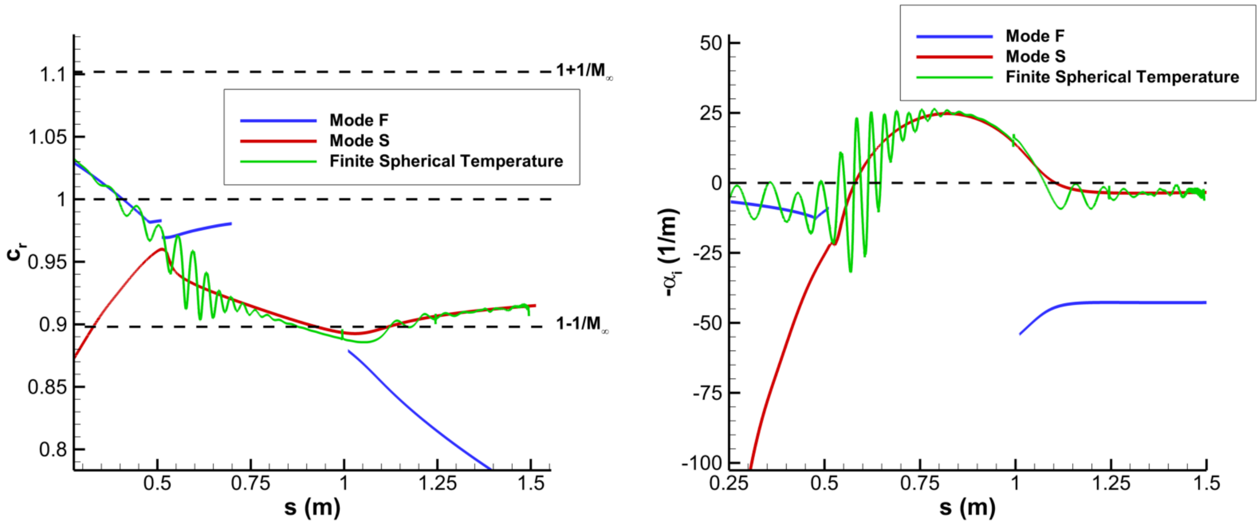

(a) (b)

Figure 4.34: Case I3 DNS vs. LST predicted results for 200 kHz disturbances (a) Phase Speed (b) growthrate.

While the primary dominant disturbances of the flow are the same for each of the unsteady pulse cases, the modal interactions resulting from different forcing can also vary somewhat.

This can be directly observed in the synchronization oscillations between the cases. Case I1 demonstrates significantly stronger modulations than the other Case I pulses at the initial synchronization location, indicating stronger intermodal exchanges at this point as a result of fast acoustic forcing. This is also reflected in the growthrate in Fig. 4.32b. Case I2 in Fig. 4.33 and Case I3 in Fig. 4.34 have nearly identical disturbance profiles with low modulations at synchronization when compared with Case I1, reflecting strong commonalities between the receptivity response of the temperature and slow acoustic pulses. However, the total disturbance response at this frequency for the acoustic and temperature pulses was observed to be very similar downstream in the domain. Case I4 in Fig. 4.35 also demonstrates a different modal oscillation structure upstream of and near synchronization. The modulations for this case are much less regular and may be indicative of stronger noise components in the signal due to the relative weakness of the second mode response for freestream vorticity disturbances. This can be seen in the growthrate for Case I4 in Fig. 4.35b in which the signal is seen to oscillate roughly about a neutrally disturbance signal instead of solely on the mode F disturbance.

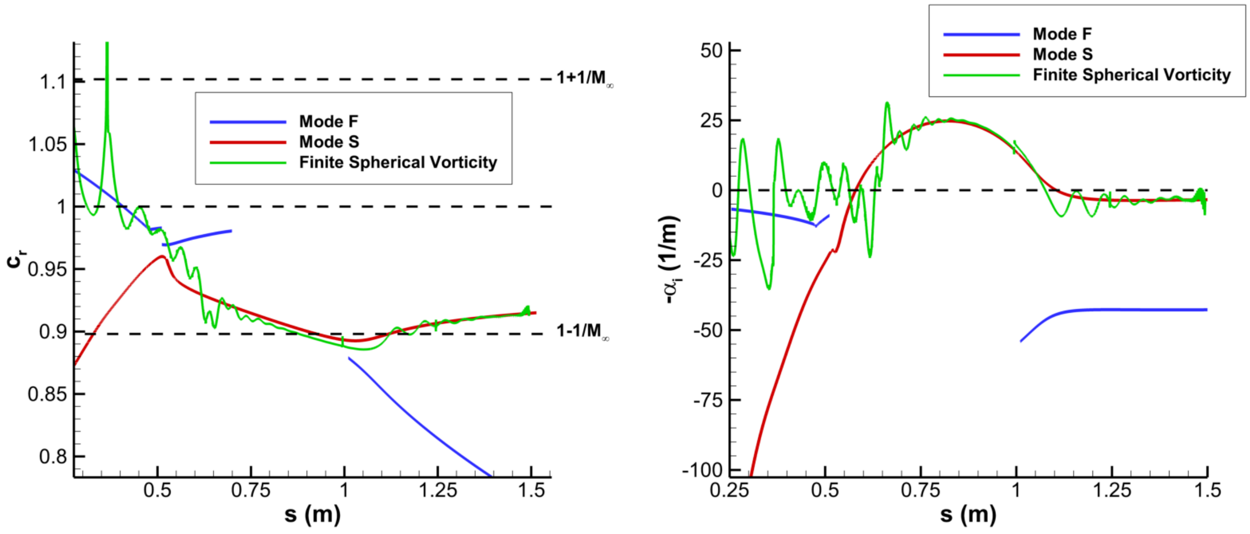

(a) (b)

Figure 4.35: Case I4 DNS vs. LST predicted results for 200 kHz disturbances (a) Phase Speed (b) growthrate.

4.3.2 Planar Pulse Unsteady DNS Results

While the finite pulses can only interact with the nose regions of the cones, the planar pulses are able to induce significantly more complex disturbance environments. Fig. 4.36 presents snapshots of the disturbance pressure contours resulting from the planar fast acoustic pulse in Case B (Case B5) over a downstream region of the cone at two different instances. Since the planar pulses are infinite in the y-z plane, they continue interact with and introduce forcing to the shock layer as they propagate in the streamwise direction. In particular, Fig. 4.36a depicts the front of the downstream shock-disturbance interaction and the wake of disturbances it excites while Fig. 4.36b shows the slower band of amplifying second mode disturbances behind the pulse front. In Fig. 4.36a a sharp interface can be seen at the leading edge of the disturbance front at $x = 1.46$ m and is attributed to continuous fast acoustic disturbances as well as other sources of non-modal noise that are generated in the shock layer by the local shock-disturbance interactions. This distinctive edge propagates with the speed of the acoustic pulse and shows significant forcing being generated by the disturbance which directly interacts with the boundary layer.

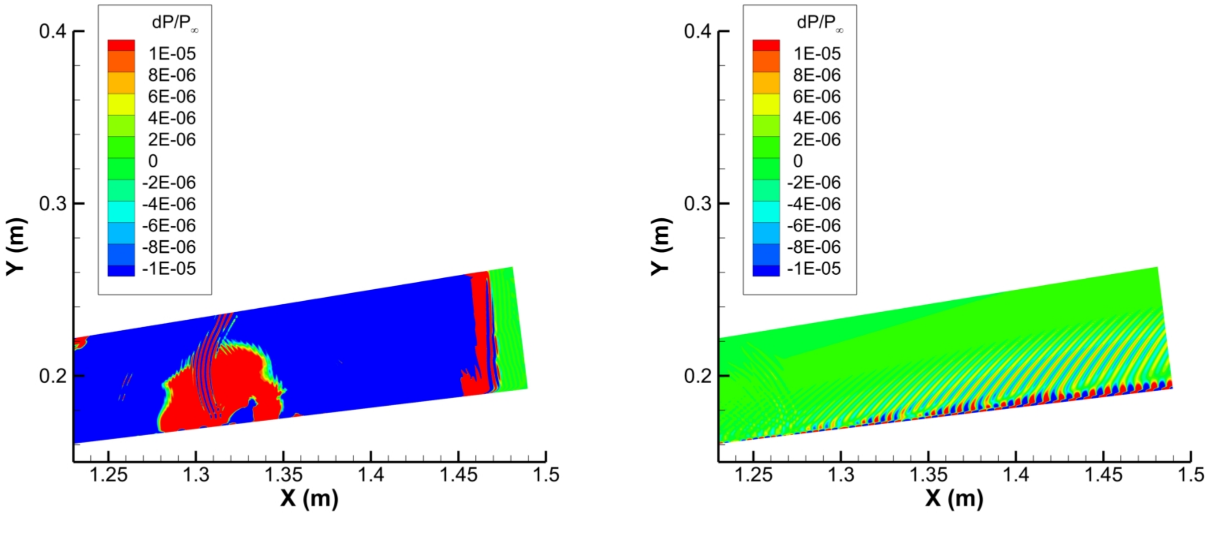

(a)

(b)

Figure 4.36: Pressure perturbations near $s^* = 1.5$ m after the planar fast acoustic perturbation (Case B5) for (a) the pulse front and (b) the primary second mode.

A secondary band of disturbances distributed throughout the shock layer is also seen to be centered about approximately $x = 1.32$ m, which contains the excited continuous slow acoustic disturbances. Similar to the finite pulse cases, the primary second mode wavepacket lags behind this initial disturbance front and is depicted in Fig. 4.36b. The second mode wavepacket somewhat follows the trends observed in the finite spherical disturbance cases. A clear band of isolated, growing boundary layer disturbances is shown isolated near the wall which are associated with the amplified second mode. Additionally, hallmark acoustic-like waves are observed radiating from these wall-bound perturbations deep into the shock layer, once again indicating the presence of a substantial supersonic mode. The deeper penetration of these acoustic waves indicate a strongly excited supersonic mode in this case. The second mode wavepacket shows many localized reductions in amplitude that are attributed to strong wavepacket interference effects. This may have been caused by the strong shock-disturbance front induced by the planar pulse.

The result of the strong additional forcing for the planar fast acoustic pulse in Case B5 can be observed in the normalized surface pressure time history plots in Fig. 4.37 which depicts a strong secondary disturbance spike caused by the planar forcing that propagates throughout computational domain. This spike is observed to experience relatively weak amplification as the sampling point moves further downstream, which is likely due to a combination of the excited modes being neutrally stable and the planar pulse continuing to force the flow as it propagates downstream. The primary second mode band does not become apparent until very far downstream on the cone at approximately $s^* = 1.42$ m where the magnitude of the forcing disturbance overshadows that of the amplifying second mode disturbance wavepacket. It is only near the end of the cone where the primary second mode disturbance begins to dominate.

Similar pressure snapshots and time history results are presented for Case B6 in Fig. 4.38 and Fig. 4.39, which also closely reflect the characteristics of Cases B7 and B8. The surface pressure disturbance contours in Fig.4.38 demonstrate significant differences between Cases B5 and B6. The local disturbance front in Fig. 4.38a has a much smaller magnitude than Case B5. Furthermore, the sharp pulse front propagating at the speed of the continuous

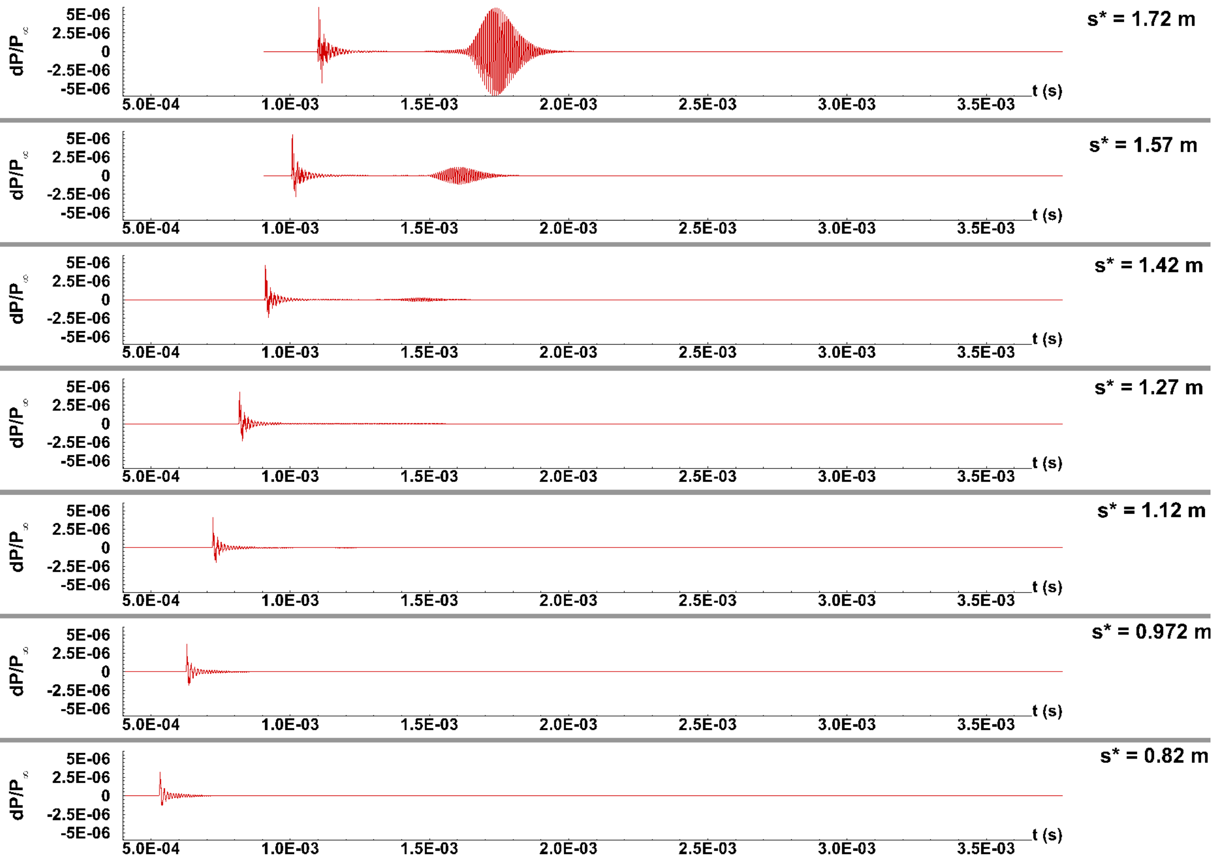

Figure 4.37: Time history of normalized surface pressure perturbations resulting from planar fast acoustic pulse disturbance (Case B5).

fast acoustic modes is not directly observed for the Case B6. Insteady additional oscillatory structures are observed in the shock layer near the excited slow acoustic wavepacket which do not seem to propagate to and force the wall disturbances. This is also reflected in the surface pressure disturbance time history in Figure 4.39 where the secondary spike like that of Case B5 is not found. The surface disturbance profile follows a very similar pattern to what was observed in the finite pulse simulations for both Case B and Case I. The pressure disturbance structures in Fig. 4.38b also reflect a strong second mode disturbance. However, the acoustic radiation characteristic of a supersonic mode is exceptionally weak in comparison to Case B5. While the second mode instability is observed to be universally excited for all of the disturbance cases, the general receptivity of both the second mode and supersonic mode are observed to vary significantly between both the freestream disturbance type and

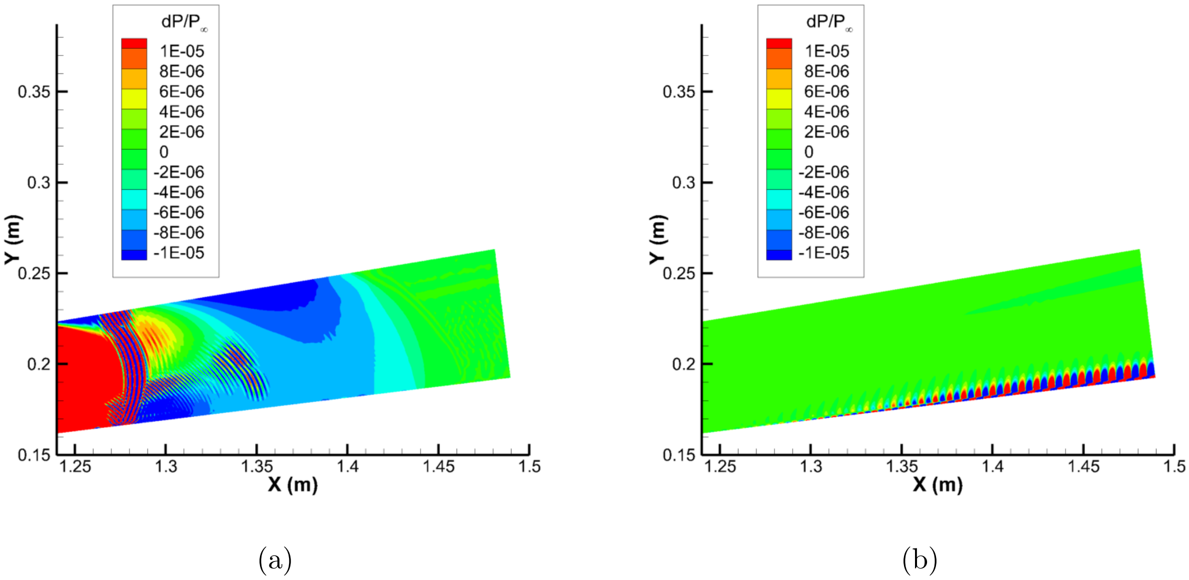

(a) (b)

Figure 4.38: Pressure perturbations near $s^* = 1.5$ m after the planar slow acoustic perturbation (Case B6) for (a) the pulse front and (b) the primary second mode.

the pulse geometry. Further studying the receptivity of the both the conventional discrete mode instabilities as well as the supersonic mode will be necessary to further characterize the stability behavior of a flow.

The FFT decomposed surface pressure contour maps for the planar fast acoustic (Case B5), slow acoustic (Case B6), temperature (Case B7) and vorticity (case B8) disturbances are presented in Fig. 4.40. The total surface disturbance spectra share many similarities to the finite spherical pulse cases. In particular, Fig. 4.40b for Case B6 and Fig. 4.40c for Case B7 depict strong initial forcing near the beginning of the domain that experiences limited attenuation compared to their finite pulse counterparts before second mode amplification. These lower frequency forcing waves remain much more significant in the downstream regions of the cone due to the additional introduction of forcing from the planar pulses. While a similar range of peak disturbance frequencies is excited in each of these cases, the total profile of these different unsteady cases vary significantly. The contours for Case B6 in Fig.4.40b demonstrate a unique feathering pattern and low amplitude perturbation band directly upstream of the second mode region. Case B7 in Fig. 4.40c, however, seems to have

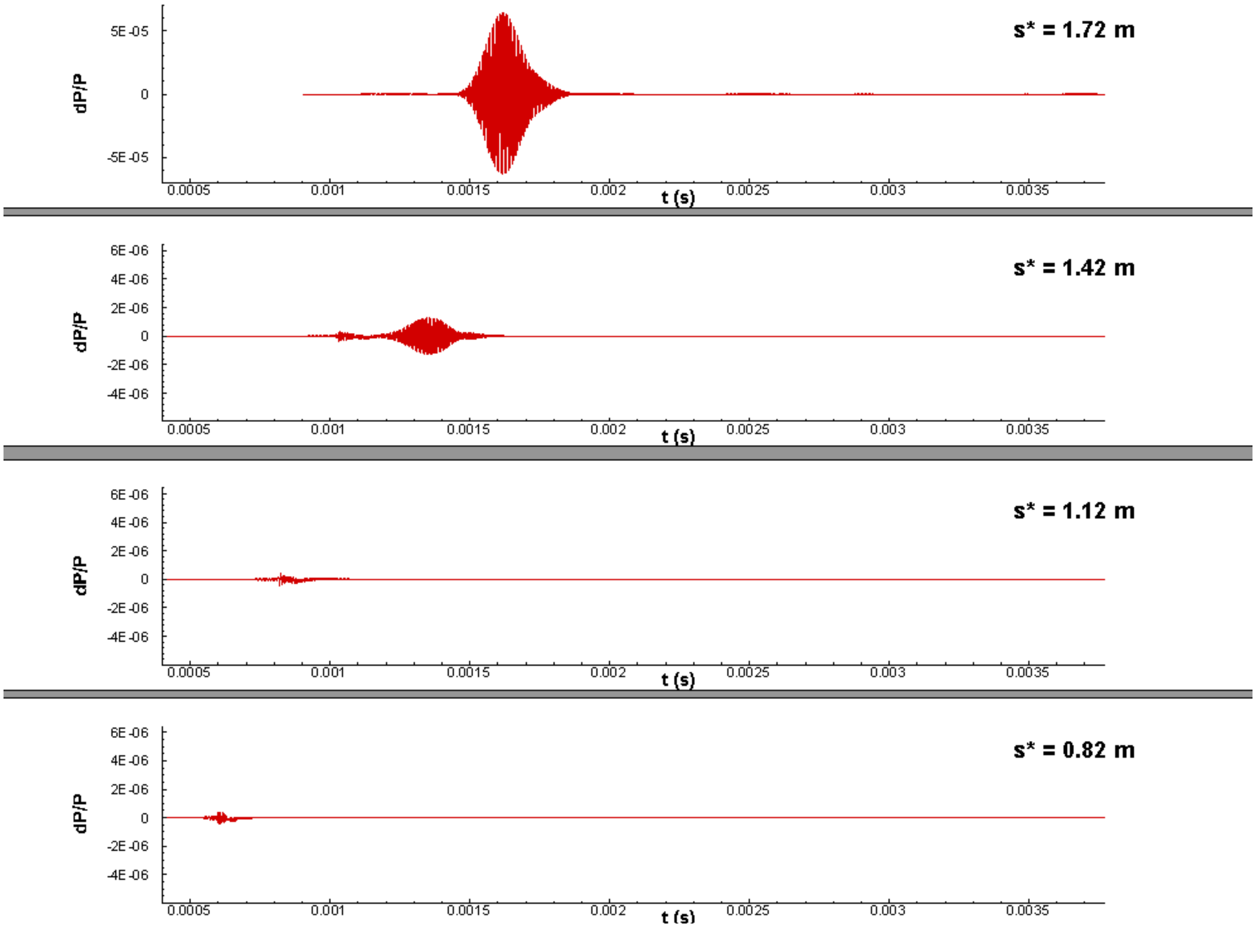

Figure 4.39: Time history of normalized surface pressure perturbations resulting from planar slow acoustic pulse disturbance (Case B6).

significant multi-peak behaviors in the spectra that were also previously observed in the Case I finite pulse results. These indicate significant variation in the upstream forcing content introduced by these different disturbance types. While noise effects are noticeably stronger for the planar cases, they are still observed to strongly excite primary second mode disturbances downstream on the cone and agree well with LST predictions. Minor perturbations near 0 kHz are also observed in both the Case B6 and Case B7 results, which may be indicative of continuously excited entropy modes in the boundary layer that again arise from local shock interactions. These, however, are noticeably weaker than other disturbances in the spectra and may also be due to non-modal noise excited by the local disturbance interactions as well.

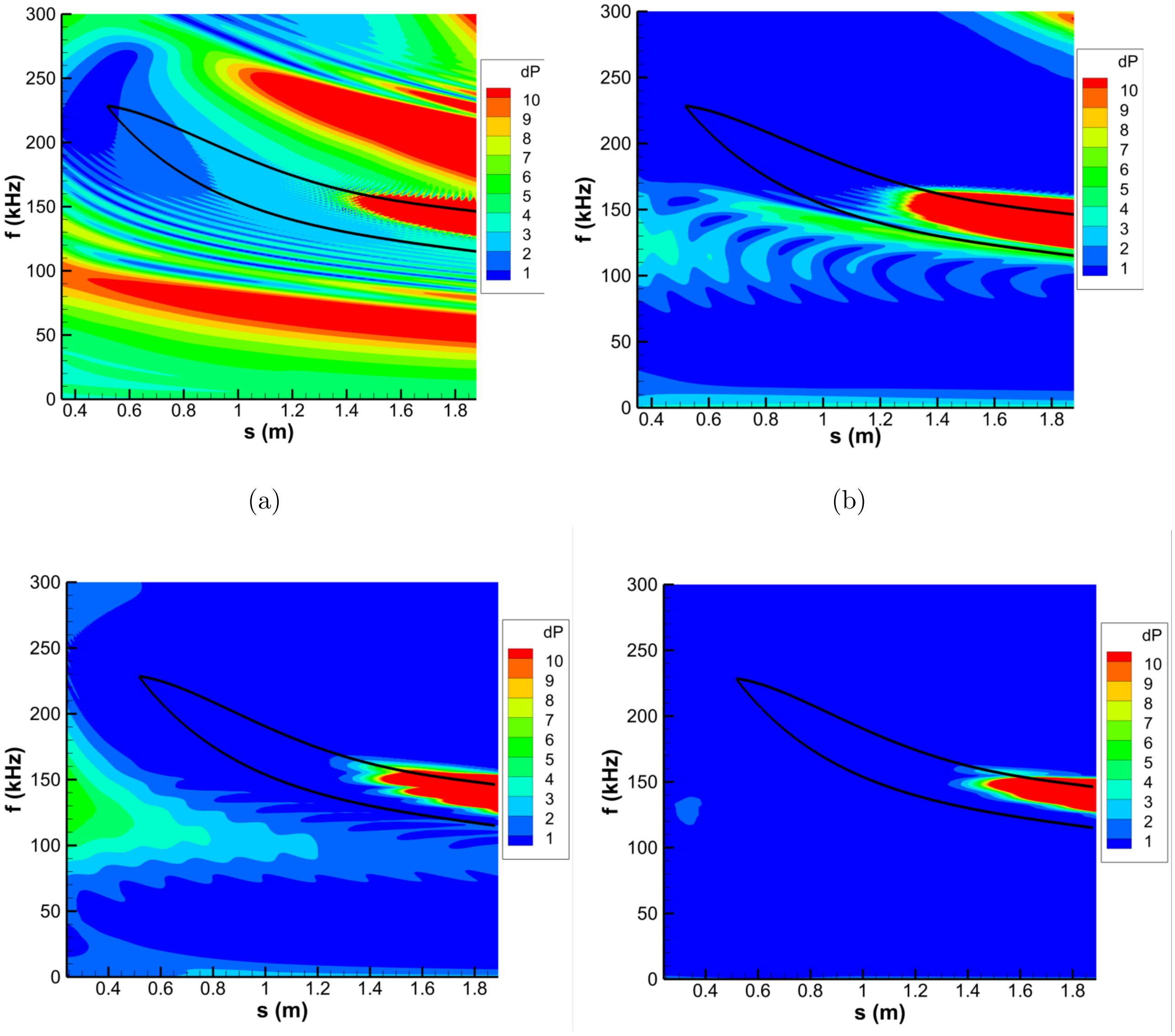

(a) (b) (c) (d)

Figure 4.40: Surface FFT pressure distribution for (a) Case B5, (b) Case B6, (c) Case B7, and (d) Case B8.

The disturbance spectrum for Case B5 in Fig. 4.40a is significantly more complex. A strong low frequency disturbance band is observed near 100 kHz while another additional band of unstable frequencies between 180-260 kHz is also apparent. Contrary to the other cases, these additional disturbance bands seem to experience amplification as they propagate downstream through the domain; though the second mode is observed to have the highest amplitudes throughout. The amplitudes of the primary second mode band centered near approximately 140 kHz at the end of the cone is two to three orders of magnitude larger than those of the external bands. These additional disturbance bands may be continuous modes and other discrete modes which may be more consistently receptive to external fast acoustic forcing, and can be observed in the secondary spike wavepacket in Fig. 4.37. While these other instabilities are generally much weaker than the second mode for hypersonic flows[23, 104] at the end of the cone, they may still have considerable impact on the flow. The presence of strong forcing and multimodal disturbances in the planar pulse cases necessitates the use of modal decomposition techniques in order to extract useful receptivity data for instabilities of particular interest, especially in noisy enivronments such as those considered in this study.

The normalized surface pressure spectra at different streamwise locations for Cases B5-B8 are shown in Fig. 4.41. Case B5 in Fig. 4.41a follows closely with the behavior observed in the finite spherical cases.However, the second mode amplitudes for Case B5 are an order of magnitude smaller than those for Case B6 in Fig. 4.41b and 30% to 50% smaller than those observed for Case B7 in Fig. 4.41c and for Case B8 in Fig. 4.41d. Cases B6-B8 share very similar low frequency forcing structures outside of the second mode frequency band, between 0 and 50 kHz and in general demonstrate very similar spectra throughout. However, Case B7 also demonstrates the distinctive multi-peak behavior previously observed in the finite pulse results. This is attributed to interference between different disturbance frequencies in the wavepacket. Case B5 is also observed to have significantly higher disturbance amplitudes outside of the second mode frequency range. In particular, the low frequency forcing near 50 kHz is between two to three orders of magnitude higher for Case B5 than the other cases. Furthermore, the higher frequency disturbances observed at 200-250 kHz are also shown to experience amplification as they propagate downstream for Case B5 and are up to three orders of magnitude stronger than similar frequencies in the other cases. This indicates that the receptivity response for Case B5 seems to distribute the forcing in a broadband manner rather than directly excite the second mode in particular. Cases B6, B7, and B8 on the other hand seem to much more readily excite the second mode discrete instability in the boundary

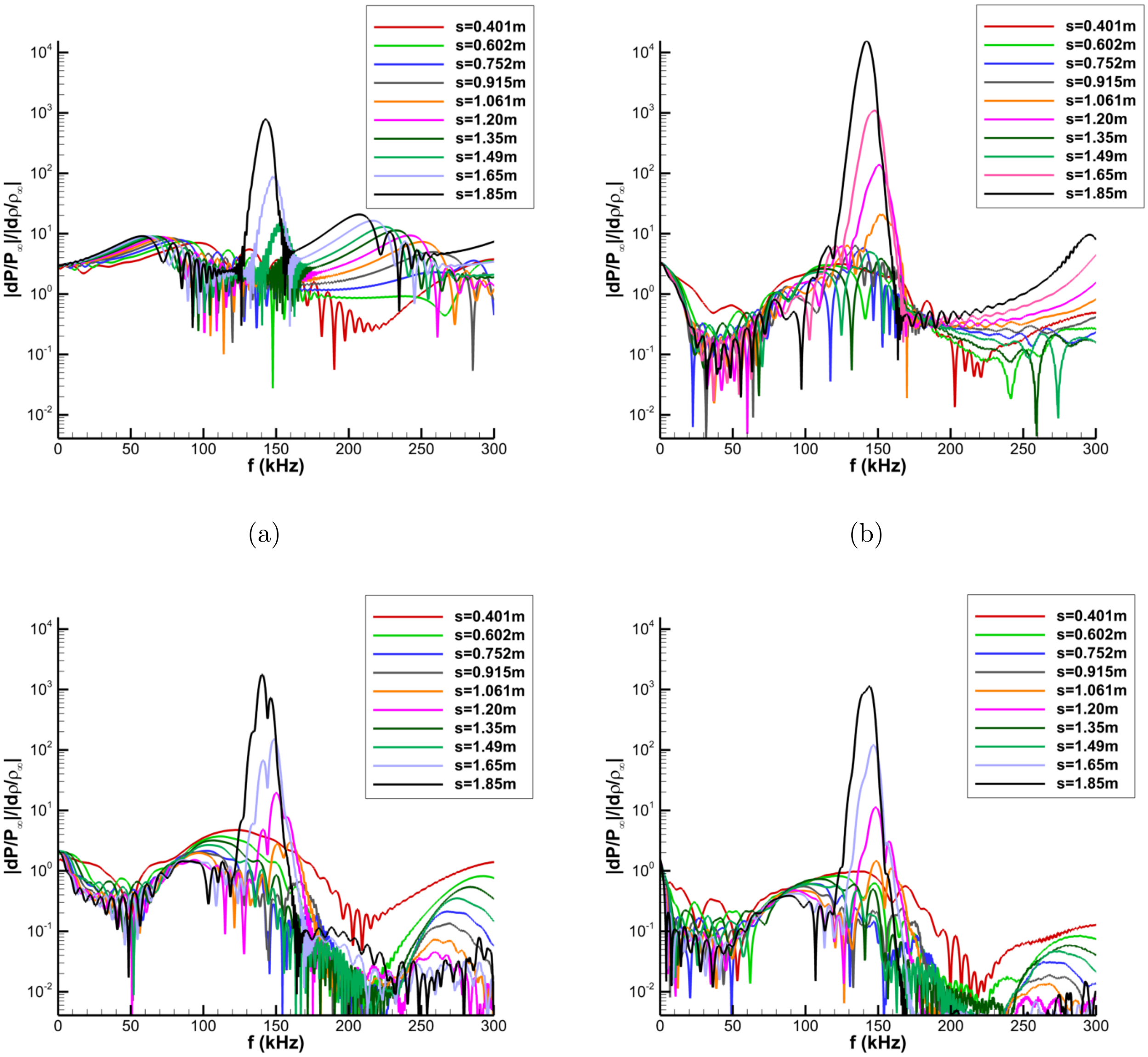

(a) (b)

(c) (d)

Figure 4.41: FFT decomposed surface pressure spectra at various streamwise locations for (a) Case B5, (b) Case B6, (c) Case B7, and (d) Case B8.

layer.

The spatial development of surface pressure perturbation amplitudes is plotted again in Fig. 4.42 for Cases B5 through B8. The general amplification profiles are very similar to what was observed for the finite pulses in Cases B1-B4, though the lowest and most amplified frequencies for the planar disturbances seem to experience minimal attenuation of

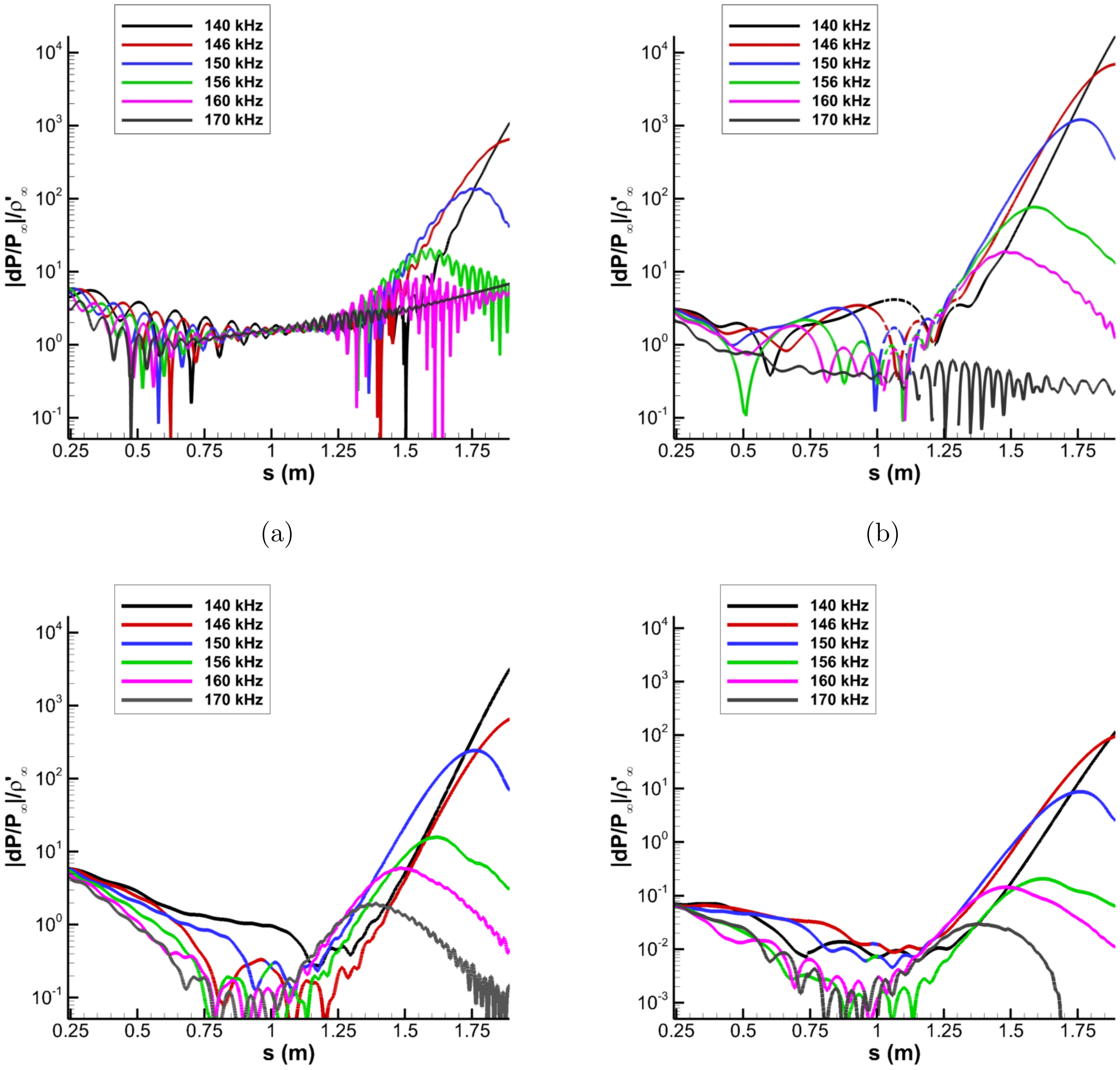

(a) (b) (c) (d)

Figure 4.42: Surface pressure disturbance amplitudes at selected second mode frequencies for (a) Case B5, (b) Case B6, (c) Case B7, and (d) Case B8.

the disturbances introduced upstream on the cone. Again, this is likely due to the additional perturbations introduced as the planar pulse propagates through the entire domain. Similar modal interference patterns and the distinct kink in the 156 kHz disturbance shown here are also observed in each case, which further indicate that higher disturbance modes and the supersonic mode may also play a further role in the downstream development of these disturbances.

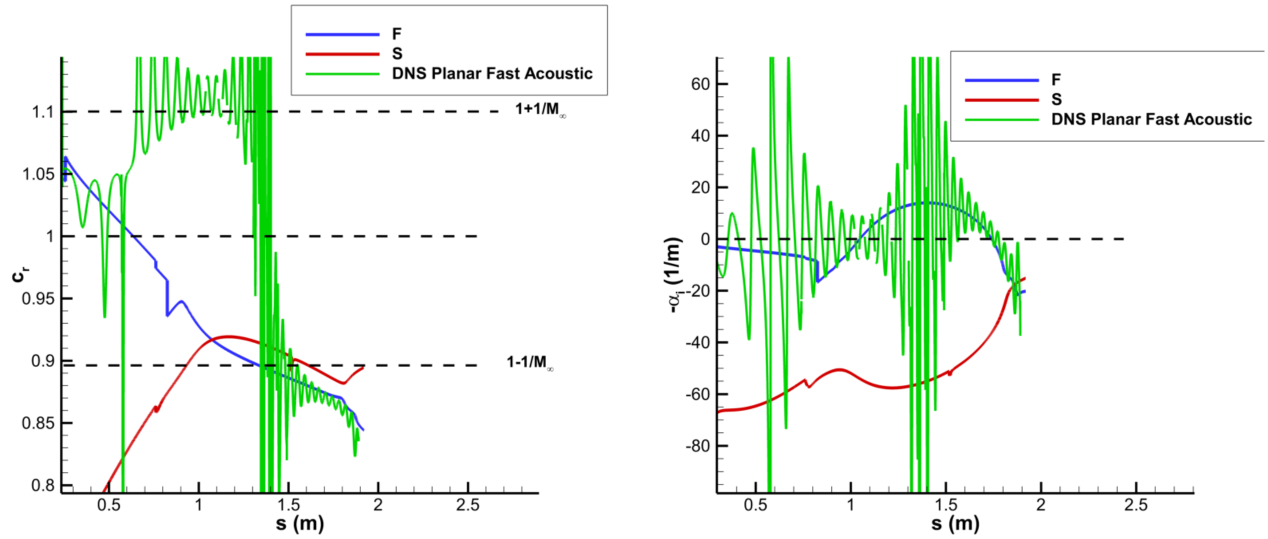

(a)

(b)

Figure 4.43: Case B5 unsteady DNS results vs. LST predicted results for 150 kHz disturbances (a) Phase Speed (b) growthrate.

The results for Case B5 show significantly weaker second mode amplification, though the upstream forcing levels are much higher than they are for Cases B6 through B8. Furthermore, these upstream disturbances experience little to no damping prior to second mode amplification, which indicates that the meanflow in this case is much more receptive to the forcing modes introduced by the planar fast acoustic pulse than the other unsteady pulse configurations. The disturbance signal for the higher frequency curves (at 150 kHz and higher) in Case B5 are observed to be much more noisy and oscillatory than each of the other planar cases. Additionally, the modal amplification pattern essentially disappears for the 170 kHz disturbance in total. This is due to the strong nonmodal response of the flow field to the planar fast acoustic pulse in general, and these oscillations are likely due to the strong prevalence of continuous modes and other sources of noise in the boundary layer. While each of the planar pulse cases demonstrates oscillatory structures at the highest sampled frequencies, none of them demonstrate it to the same degree as Case B5.

The DNS and LST phase speed and growthrate comparisons for the 150 kHz disturbance

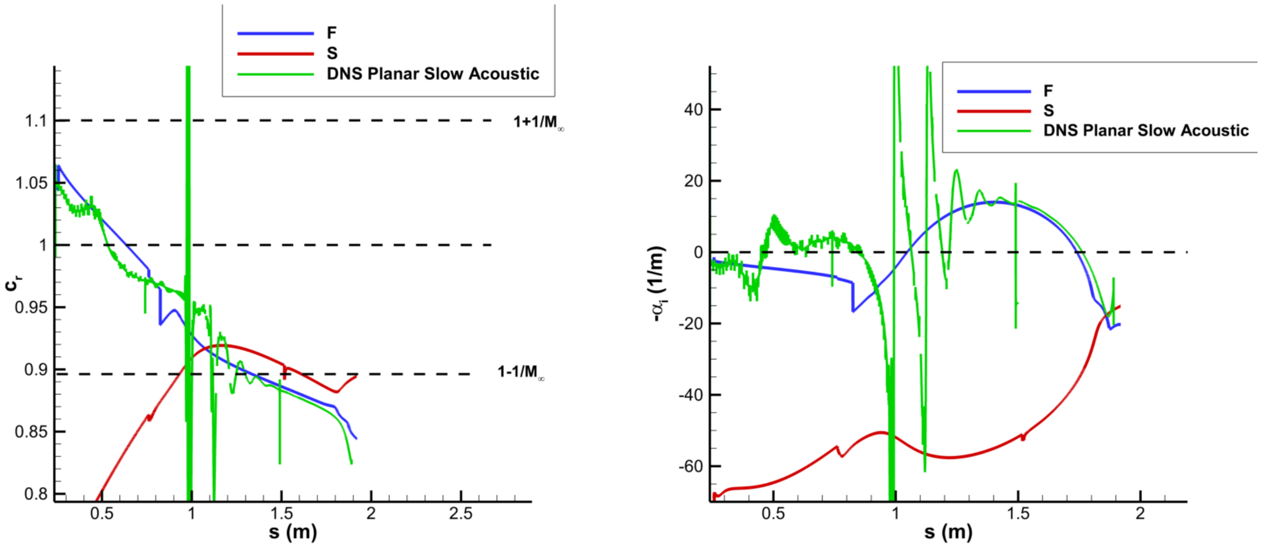

(a)

(b)

Figure 4.44: Case B6 unsteady DNS results vs. LST predicted results for 150 kHz disturbances: (a) Phase Speed (b) growthrate.

are also given in Fig. 4.43 for Case B5, Fig. 4.44 for Case B6, Fig. 4.45 for Case B7, and Fig. 4.46 for Case B8. The boundary layer disturbances resulting from Case B5 do not seem to become dominated by second mode instabilities until the far downstream regions of the cone. The growthrate shown in Fig. 4.43b is highly oscillatory and centered around a neutrally stable disturbance until approximately $s^* = 1.6m$.While the phase speed results in Fig. 4.43a show discrete mode F disturbances propagating from upstream, near the synchronization point the unsteady signal becomes dominated by the continuous fast acoustic mode. This further reflects the strong influence of continuous modes in the flow field before the onset of the primary second mode instability.

Case B6 is shown to correlate much better with the 150 kHz LST results with Fig. 4.44a demonstrating strong agreement with the LST phase speed. The growthrate shown in 4.44b further corroborates this, though the results prior to 1.4 m still show signifcant oscillations. These oscillations are primarily centered about the synchronization point again, and are generated from the multimodal energy exchange that initially causes the second mode to become unstable. From this it can be seen that Case B6 behaves similarly to the finite

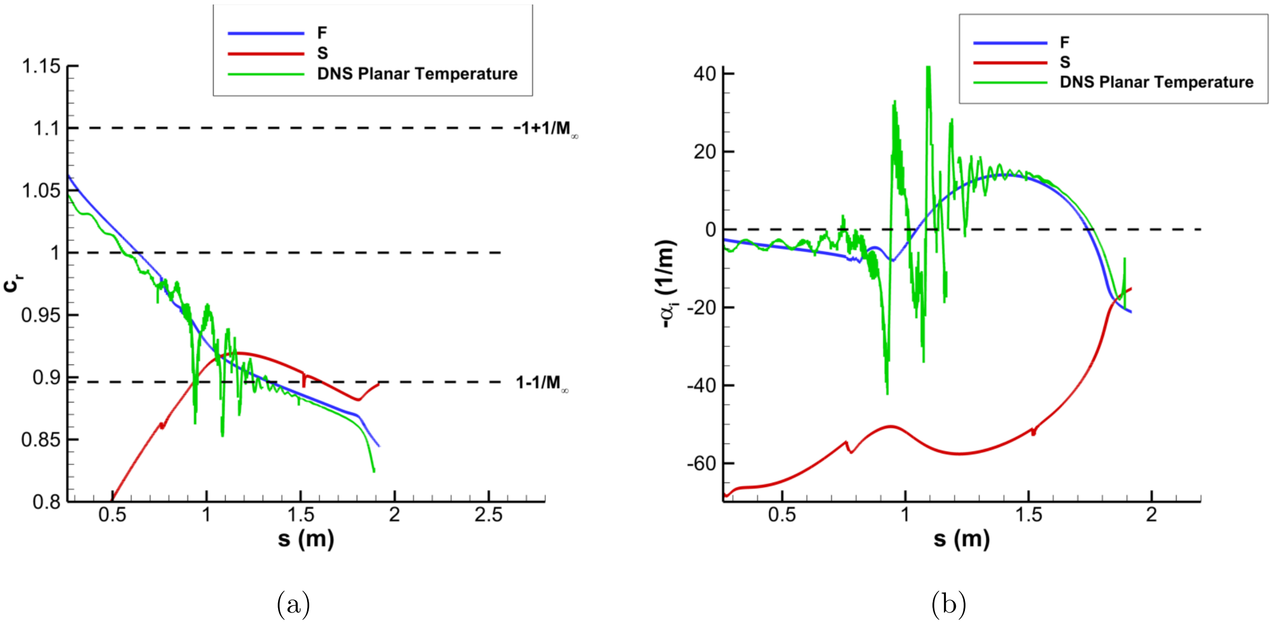

(a) (b)

Figure 4.45: Case B7 unsteady DNS results vs. LST predicted results for 150 kHz disturbances: (a) Phase Speed (b) growthrate.

spherical disturbances and primarily excites the second mode instability at this frequency, though multimodal effects are much stronger due to the more extensive noise environment.

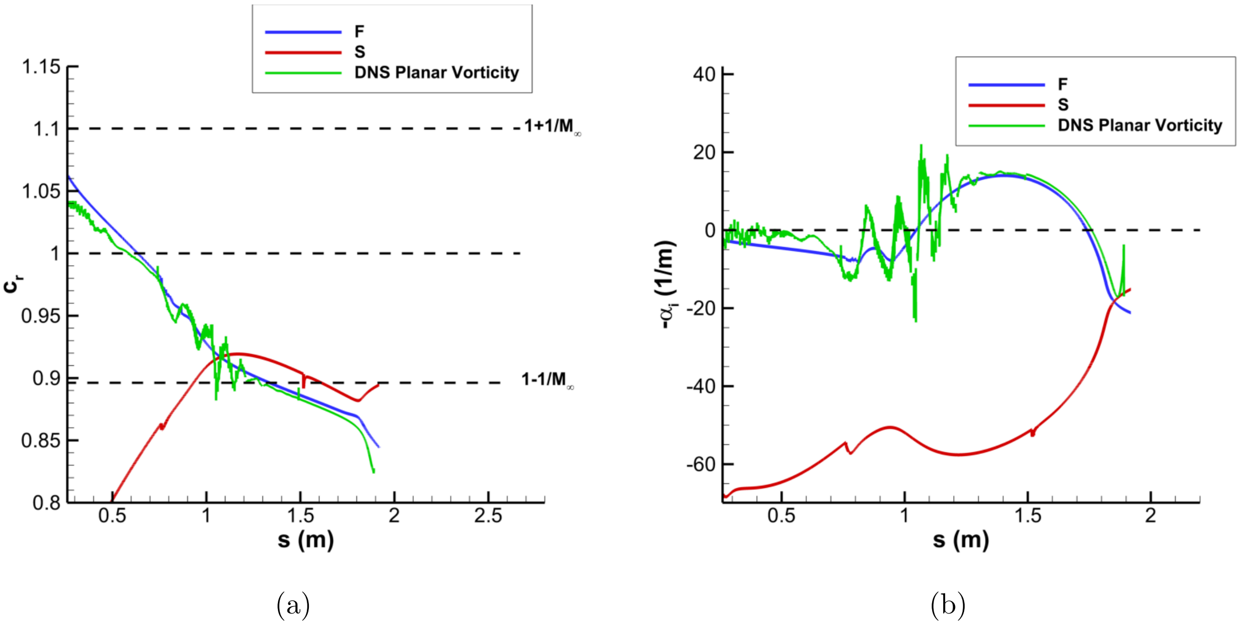

(a) (b)

Figure 4.46: Case B8 unsteady DNS results vs. LST predicted results for 150 kHz disturbances: (a) Phase Speed (b) growthrate.

Case B7 in Fig. 4.45 and Case B8 in Fig. 4.46 responded similarly for the 150 kHz disturbance. In fact, the modulation was significantly weaker in amplitude for these cases, indicating weaker multimodal receptivity responses. In all, it is shown that for this blunt cone case each of the planar pulse disturbances also effectively excited the primary second mode through a similar pathway. Namely, the pulse disturbances induce a variety of disturbances in the shock layer upstream on the cone through complex shock-disturbance interactions at the nose and further downstream along the frustum of the cone. Further downstream, the boundary layer modes become dominated by the discrete mode F, which becomes unstable after synchronization with the discrete mode S. Though, the disturbance content outside of the second mode is observed to be very different between each of these pulse cases.

The results of the planar pulse perturbations for Cases I5-I8 are presented here. Fig. 4.47 shows pressure perturbation snapshots near the end of the cone for Case I5 while similar results for Case I6 are found in Fig. 4.49. The pressure perturbation contours for Case I7 and Case I8 were observed to be very similar to Case I6, and as such are omitted.

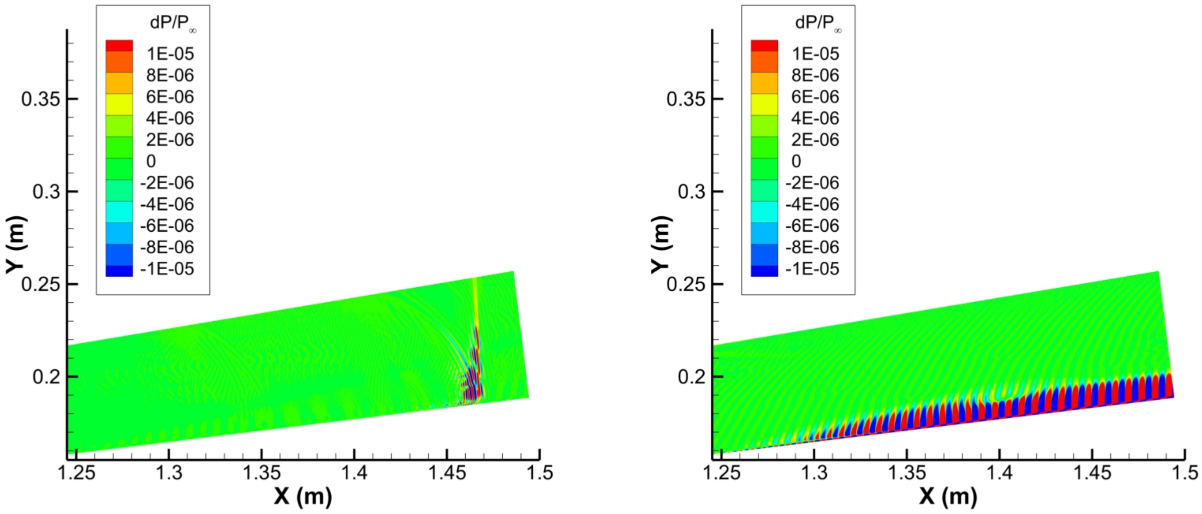

(a)

(b)

Figure 4.47: Pressure perturbations near $s^* = 1.5$ m after the planar fast acoustic perturbation (Case I5) for (a) the pulse front and (b) the primary second mode.

A strong pulse front is observed in Fig. 4.47a for the planar fast acoustic pulse in

Case I5 which is induced by local shock-pulse interactions. This is similar to what was observed in Case B5 in Fig. 4.36a, and is indicative of a common mechanism associated with broadband freestream fast acoustic forcing. However, the relative magnitude of this disturbance compared to the second mode is much smaller in comparison to our previous findings for the blunter cone in Case B. Similarly, the general shock layer disturbance profiles immediately behind the shock front are significantly weaker both for Case I5 and for Case I6 as well in Fig. 4.49a. Compared to the planar Case B results, Cases I5 through I8 demonstrate much weaker perturbations in the leading wavepacket. This is likely due to the stronger second mode instability due to Case I's sharper nose.

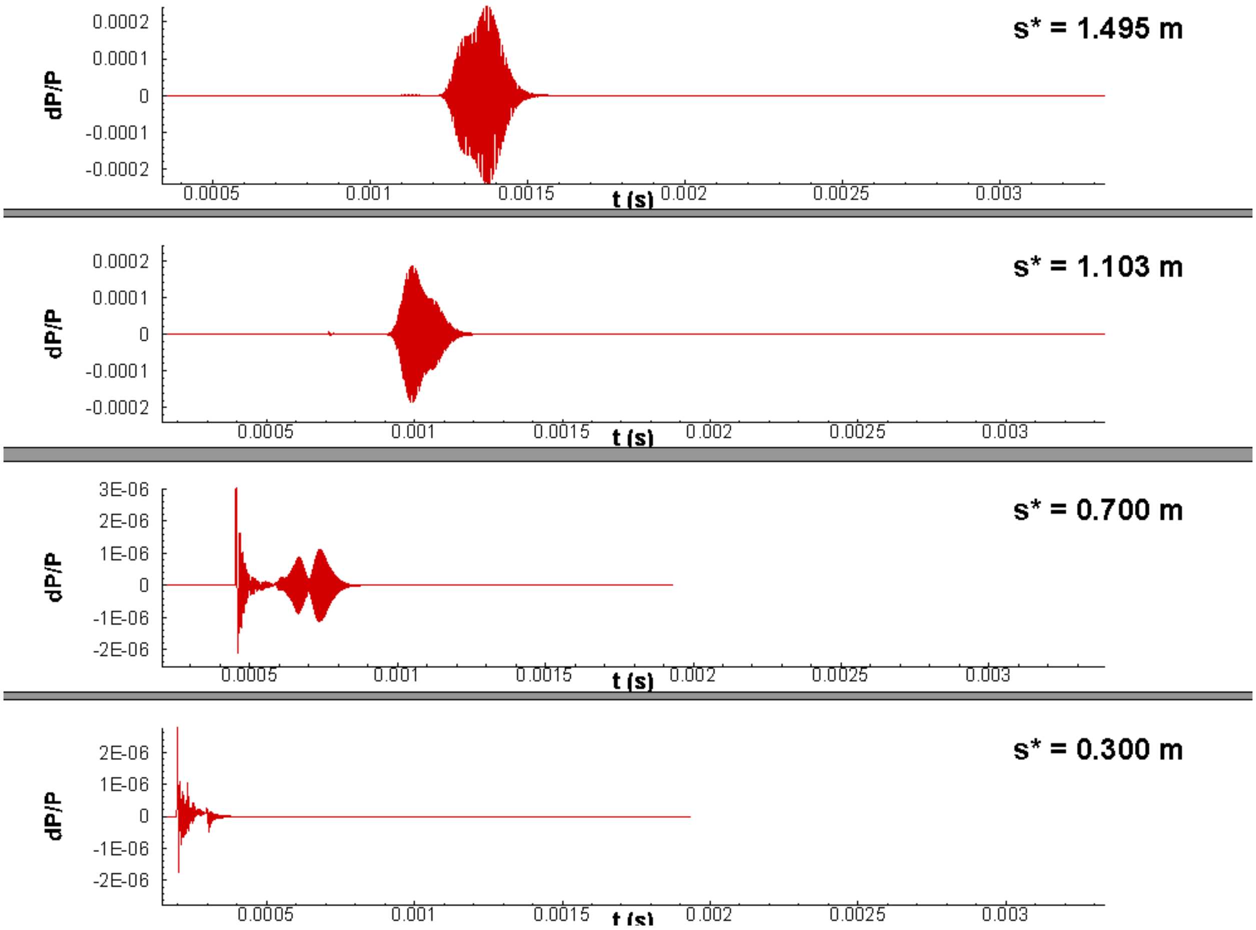

Figure 4.48: Time history of normalized surface pressure perturbations resulting from Case I5.

We also see evidence of strong second mode amplification as well in Fig. 4.47b for Case

I5 and Fig. 4.49b for Case I6 from the highly amplified wall bound perturbations. Moderate levels of acoustic radiation can also be observed near $x = 1.35$ m in both Fig. 4.47b and Fig. 4.49b, again indicating the presence of excited supersonic modes. However, this acoustic radiation is markedly weaker than what was observed for corresponding planar acoustic pulses in Case B. This further indicates the reduced receptivity of this meanflow to the supersonic mode. Additionally, in Fig. 4.47b for Case I5 a small localized reduction acoustic radiation is observed near $x = 1.4$ m. Similar phenomena is also observed in Fig. 4.26 for Cases I2 through I4 and in Fig. 4.36b for Case B5. This is attributed to constructive/destructive interference patterns in the local wavepacket causing localized weaking of the supersonic mode and its characteristic acoustic radiation[102].

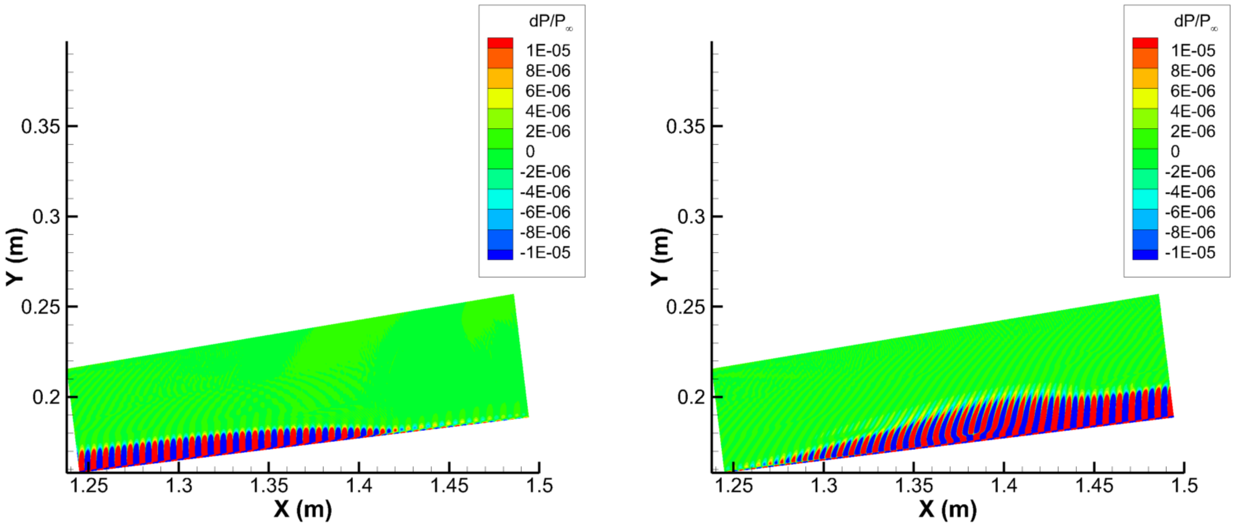

(a) (b)

Figure 4.49: Pressure perturbations near $s^* = 1.5$ m after the planar slow acoustic perturbation (Case I6) for (a) the pulse front and (b) the primary second mode.

A time history of the total surface pressure perturbations at different streamwise positions along the cone is presented in Fig. 4.48 for the planar fast acoustic pulse in Case I5. Similar to previous results, the initial sampling point at $s^* = 0.300$ m is highly irregular and contains a multitude of forcing modes. A portion of this forcing gradually decays while a coherent pulse containing the amplifying second mode emerges by the second sampled point at $s^* = 0.700$

m. We also see the influence of the secondary disturbance front for the planar fast acoustic pulse in this case. Again, similar to Case B5, the pressure disturbance spike associated with the strong secondary forcing is observed to be highly dominant for a significant portion of the cone. At the upstream sampling position $s^* = 0.300$ m the magnitude of the disturbance spike is seen to vastly outstrip the other disturbance content in the boundary layer. Further downstream on the cone at $s^* = 0.700$ m, approximately halfway along the geometry, the perturbation spike associated with the pulse front remains significantly stronger than the amplifying second mode wavepacket. We again do not see significant second mode dominance in this case until further downstream on the cone, though the second mode in Case I5 does become dominant significantly earlier than in Case B5. In particular, the amplitude of the modal wavepacket at $s^* = 1.103$ m is shown to vastly outstrip the local forcing front disturbances. The earlier occurrence of second mode dominance in Case I5 compared to Case B5 is due to the much stronger second mode amplification caused by the lower nose radius.

Fig. 4.50 presents the same surface perturbation time history for the planar slow acoustic pulse in Case I6. Similar to the finite pulse cases, we do not observe a disturbance spike like the one found in Case B5 or I5 previously. The pulse here is observed to follow standard second mode amplification behavior, and results in notably higher disturbance amplitudes than Case I5. In particular, the amplitude of the primary second mode wavepacket in Case I6 is approximately one order of magnitude higher when compared to Case I5 at the $s^* = 1.495$ m sampling position.

The FFT-decomposed surface pressure spectra along with the LST neutral curves are shown in Fig. 4.51 for the unsteady planar pulses in Cases I5 through I8. Again, the planar pulse cases for all four disturbance types exhibit strongly amplified second mode bands. This second mode is seen in a primary band of instabilities is observed between approximately 150-220 kHz in the results for all four planar pulses, in a manner similar to the finite pulse cases. The LST results agree roughly with the FFT decomposed spectra, though the LST seems to predict a higher peak disturbance frequency than the DNS. This may be attributed to nonparallel effects associated with the relatively blunt nose. The planar slow acoustic

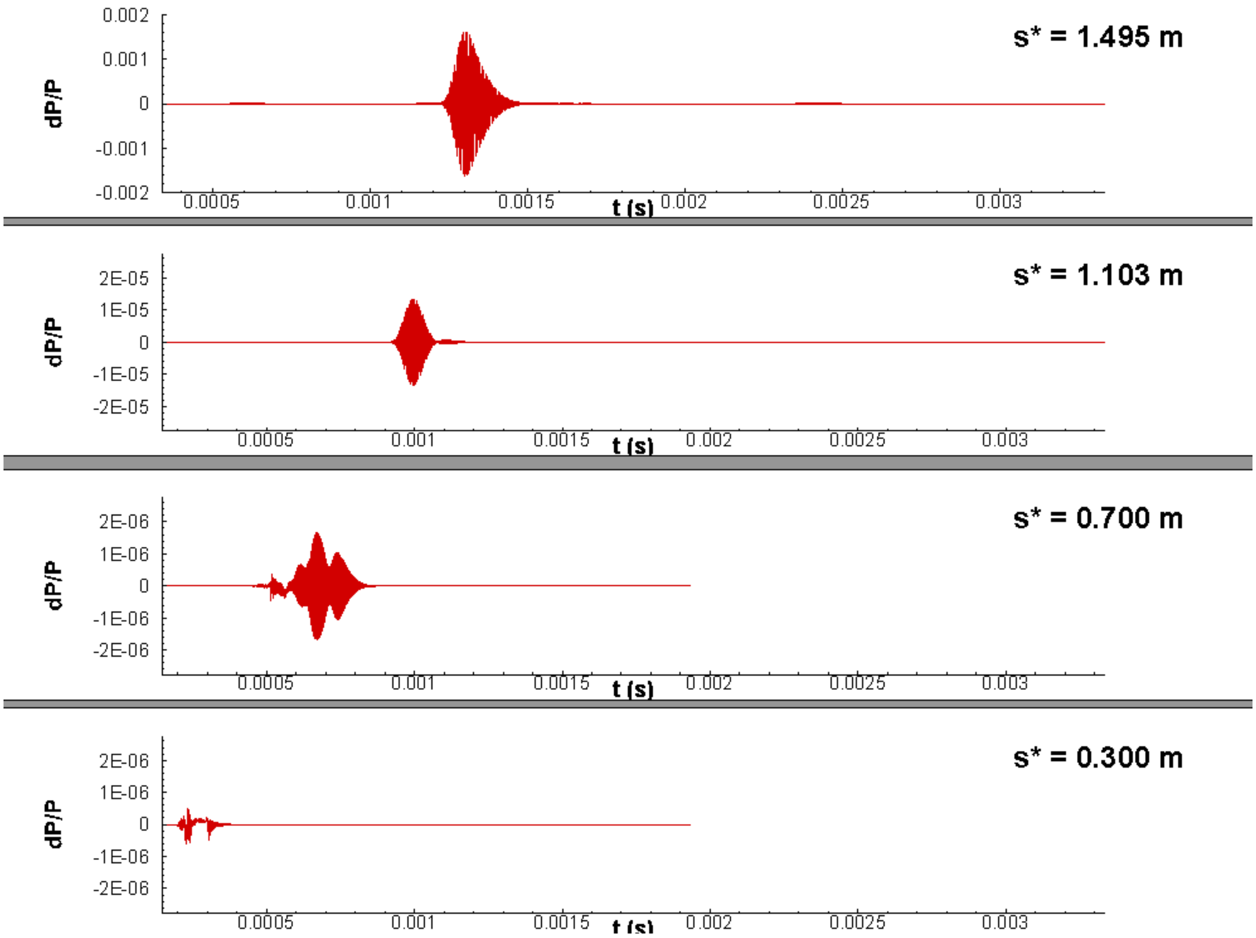

Figure 4.50: Time history of normalized surface pressure perturbations resulting from Case I6.

pulse (Case I6) and the planar voriticty pulse (Case I8) demonstrate similar disturbance profiles when compared to their counterparts in Cases B6 and B8. However, the upstream forcing is observed to be much weaker relative to the primary second mode in these two cases. This is due to the much stronger second mode amplification expected by the end of the Case I meanflow as well as the reduced freestream pulse strength in Case I.

Additional structures in the surface pressure spectra are observed in both the planar fast acoustic pulse (Case I5) and the planar temperature pulse (Case I7). The spectra for Case I5 in Fig. 4.53a is highly reminiscient of that for Case B5 in Fig. 4.40a. Namely, while the primary second mode is still strongly excited, additional secondary bands of frequencies are observed as well. These are also primarily isolated in a lower frequency band between

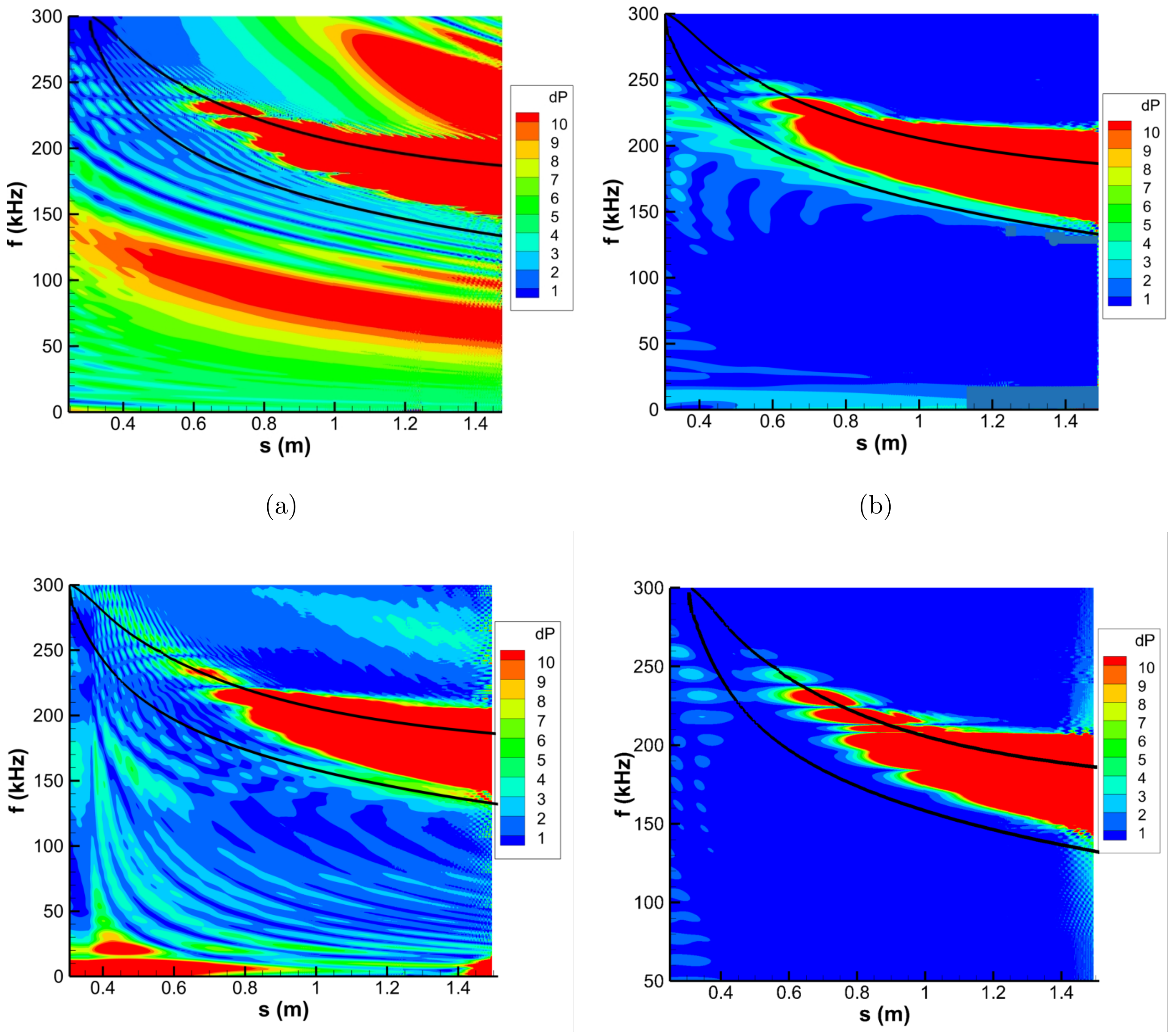

(a)

(b)

(c)

(d)

Figure 4.51: Surface FFT pressure distribution for (a) Case I5, (b) Case I6, (c) Case I7, and (d) Case I8.

100 and 150 kHz and a higher frequency band between 200 and 300 kHz. These secondary bands are slightly higher in frequency than their counterparts in Case B5, likely due to the same boundary layer effects the sharper nose in Case I has on the second mode instability. Otherwise, the general trends are the same between Case B5 and Case I5. Of additional note is that the normalized pressure amplitude densities in these secondary instability bands

remains on the same order of magnitude between Case B5 and Case I5, with dP peaking at approximately 12 for the lower frequency band and 23 for the higher frequency band in both cases. The second mode amplitude remains several orders of magnitude larger than these secondary bands in both planar fast acoustic cases. The similar values of these secondary bands indicates minimal variance in the receptivity of these secondary disturbances in response to the differing nose bluntnesses.

Dissimilarities were also observed for the planar temperature pulses in Case B7 from Fig. 4.40c and Case I7 in Fig. 4.52c. Though Case B7 demonstrates a more concentrated band of amplified lower frequency disturbances between 100 kHz and 200 kHz, Case I7 shows a much noisier forcing environment in a manner reminiscient to the planar fast acoustic results in Cases B5 and I5. In particular, a similar high frequency disturbance band is seen to be amplified between 250 kHz and 300 kHz, though it is much weaker when compared to the secondary band in Cases B5 and I5. The lower frequency band between 100 kHz and 150 kHz is also observed to not be excited. Instead, weak broadband perturbations are observed throughout most of the spectrum. Additional very low frequency disturbances between 0 kHz and 30 kHz experience signficant upstream excitation before they show gradual attenuation and re-amplification at the end of the cone. These likely consist of excited entropy layer modes similar to what was observed by Wan, Su, and Chen[64] for a different cone case. These low frequency entropy layer modes were shown to be only very weakly excited by the finite pulses in both Case B and Case I, and were demonstrated to experience only moderate excitation as a result of planar pulse disturbances in cases other than Case I7. Entropy modes and entropy layer perturbations have been shown to play significant roles in the excitation of the second mode disturbance[64, 67] and may be responsible for the differences observed in peak receptivity magnitudes observed for the temperature pulse cases in Section 5.2. These results indicate stronger entropy layer receptivity for Case I, particularly in the case of freestream temperature disturbances. Similar low frequency waves appear for the planar slow acoustic pulse in Case I6, and are comparable to similar structures observed for Case B6 previously. While these may also arise from local continuous entropy mode excitation it may also be due to the influence of local low frequency noise induced by the

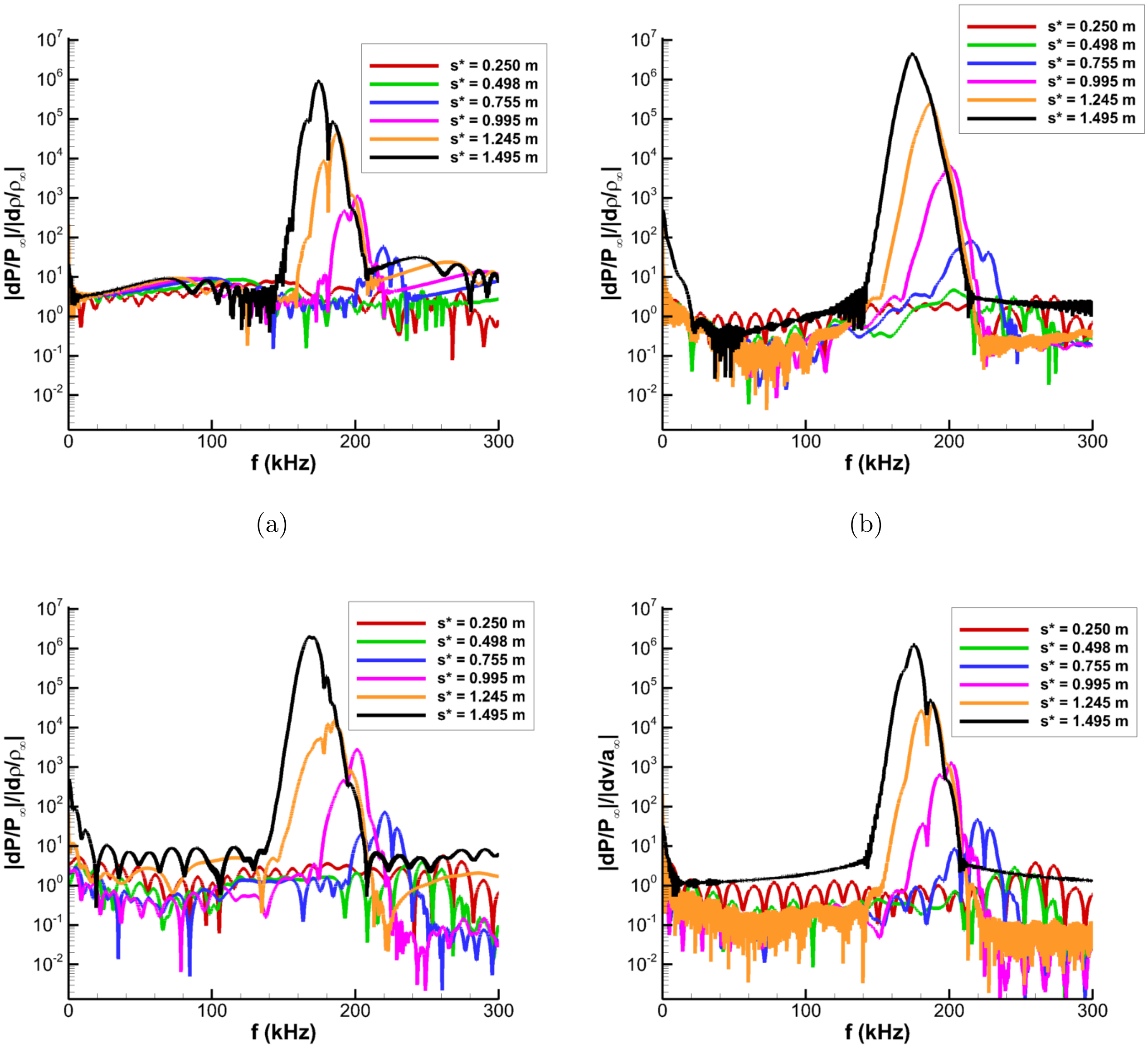

(a) (b)

(c) (d)

Figure 4.52: FFT decomposed surface pressure spectra at various streamwise locations for (a) Case I5, (b) Case I6, (c) Case I7, and (d) Case I8.

shock-disturbance interactions. However, the exact source of these distributed low frequency and low amplitude disturbances remains unknown.

The FFT decomposed surface pressure perturbations at different streamwise locations are also presented in Fig. 4.52 for Cases I5 through I8 for a selection of different streamwise positions. Again, the familiar trends are seen with an initial decay in boundary layer forcing followed by exponential modal amplification. The second mode disturbance is clearly identifiable between the frequencies of approximately 150 and 200 kHz at the final sampling location. Broadband forcing is stronger in Case I5, though the primary second mode is response is significantly weaker than the other cases. Another factor of note is the increased prevalence of the multipeak behavior associated with wavepacket interference. The Case I planar results here seem to indicate stronger general multi-peak behaviors. This is especially of note for the Case I5 results which is different from Case B in which only the planar temperature pulse in Case B7 demonstrated significant interference in the second mode peak. This denotes significant variation in the wavepacket interference behaviors, though the exact source of this has not been pinpointed.

The normalized surface pressure amplitude curves at a selection of second mode frequencies for Case I5 through Case I8 are presented in Fig. 4.53. Case B5 in Fig. 4.42a and Case I5 in Fig. 4.53a follow similar observed trends in the finite spherical cases, with distinctive second mode amplification occurring in the expected frequency range predicted by LST. However, the second mode amplitudes for the planar fast acoustic pulses are an order of magnitude smaller than those for planar slow acoustic pulses in Fig. 4.42b for Case B6 and Fig. 4.53b for Case I6. This indicates a similar weakness of the planar fast acoustic pulse in exciting the primary second mode in both cones. Additionally, modulations in the high frequency curves are found to be much stronger in the planar fast acoustic pulse results for both cases as well. While the general profile of these disturbance amplitude curves matches the behavior expected of a second mode dominated disturbance, the higher frequency perturbations in particular demonstrate significant levels of oscillation that are not observed for most of the planar slow acoustic, temperature, or vorticity pulse results. In the 156 kHz curve in particular for Case B5 the degree of these multimodal oscillations mask the region in which the localized increase in growthrate was observed for Cases B1-B4, and Cases B6-B8. While these other disturbances do not directly dominate the surface perturbation profiles, their modulation is much more significant in the higher second mode frequencies for the planar fast acoustic pulses and further indicate a strong tendency of the fast acoustic disturbance in exciting a broad range of disturbances in the flow.

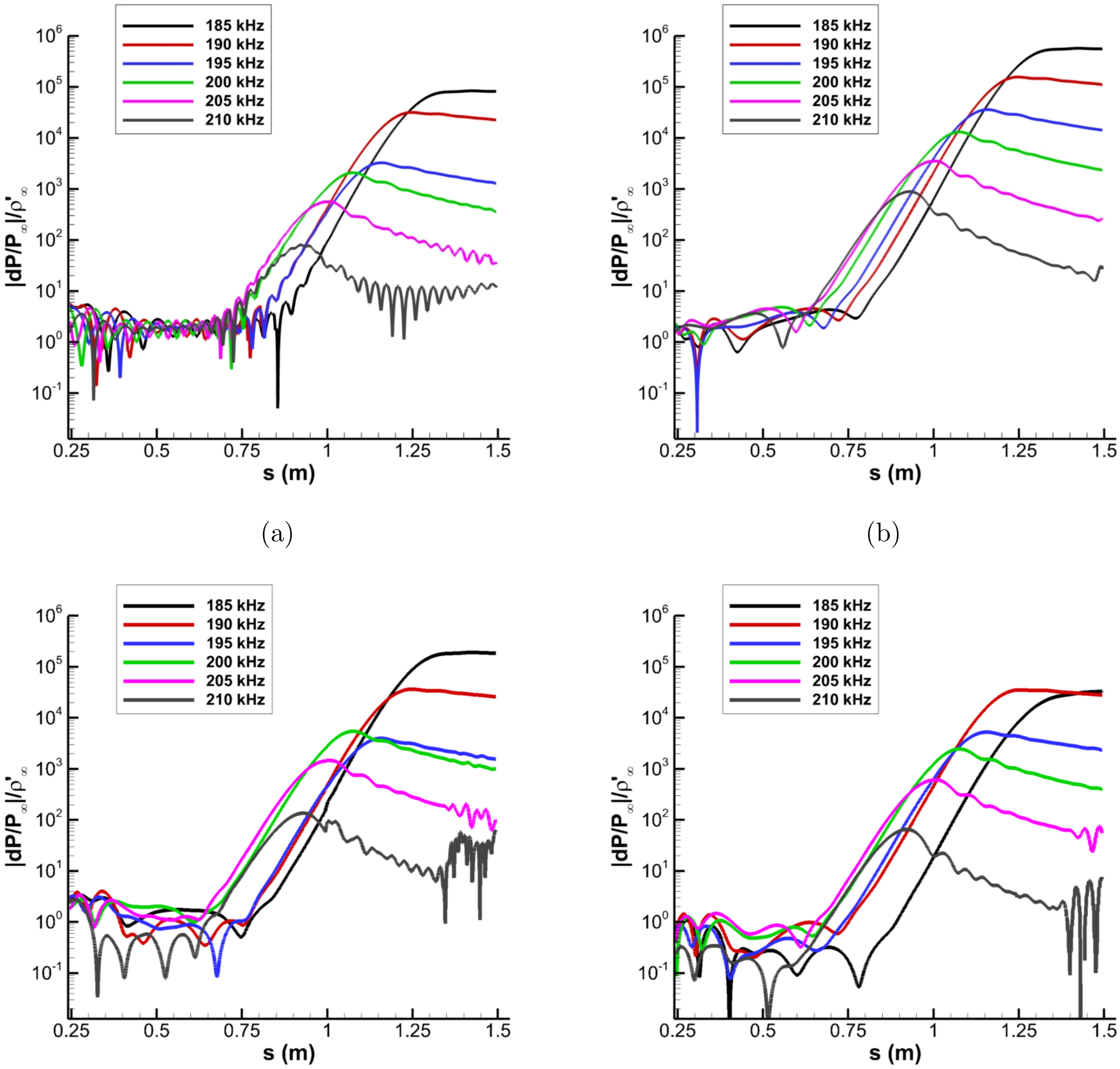

(a) (b)

(c) (d)

Figure 4.53: Surface pressure disturbance amplitudes at selected second mode frequencies for (a) Case I5, (b) Case I6, (c) Case I7, and (d) Case I8.

The streamwise amplitude curves for Cases I7 and I8 follow standard amplification trends. Of note is that while they do not experience significant oscillations attributed to multimodal interactions when compared to Case B5, distinctive structures are apparent for the highest sampled 210 kHz frequencies. In particular, both Case I7 and Case I8 demonstrate small localized disturbance amplifications at this frequency that are not clearly identifiable in the planar acoustic pulses. This is similar to the localized destabilization seen in Case B2 and Case B3 in Fig. 4.18. The supersonic mode in this case is not expected to be unstable as the destabilized discrete mode S remains subsonic throughout the domain. As such, it is likely that this local amplification comes from other sources, such as higher Mack mode instabilities. Similar to the second mode, these other modes can also have highly variable receptivity responses to different disturbance types in the freestream.

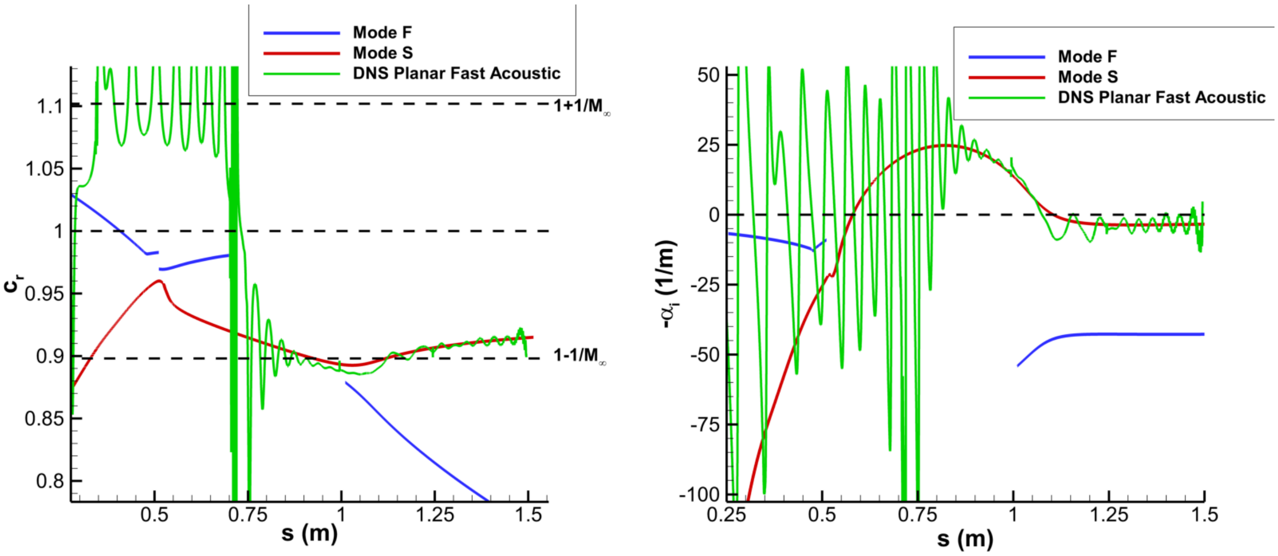

(a) (b)

Figure 4.54: Case I5 unsteady DNS results vs. LST predicted results for 200 kHz disturbances (a) Phase Speed (b) growthrate..

The LST phase speed and growthrate results for the 200 kHz disturbance discussed previously are used here to further verify the results of the unsteady simulations. The comparisons for Case I5, Case I6, Case I7, and Case I8 are presented in Fig. 4.54, 4.55, 4.56, and 4.57 respectively.

The unsteady DNS results for Cases I6 through I8 demonstrate good agreement with LST, and show that these planar pulses also primarily generate mode F disturbances upstream on the cone in the initial shock-disturbance interaction. However, prior to the synchronization location the signal is much more oscillatory than for the finite pulse cases in Fig. 4.32 through Fig. 4.35. This indicates a more complex disturbance environment prior to the

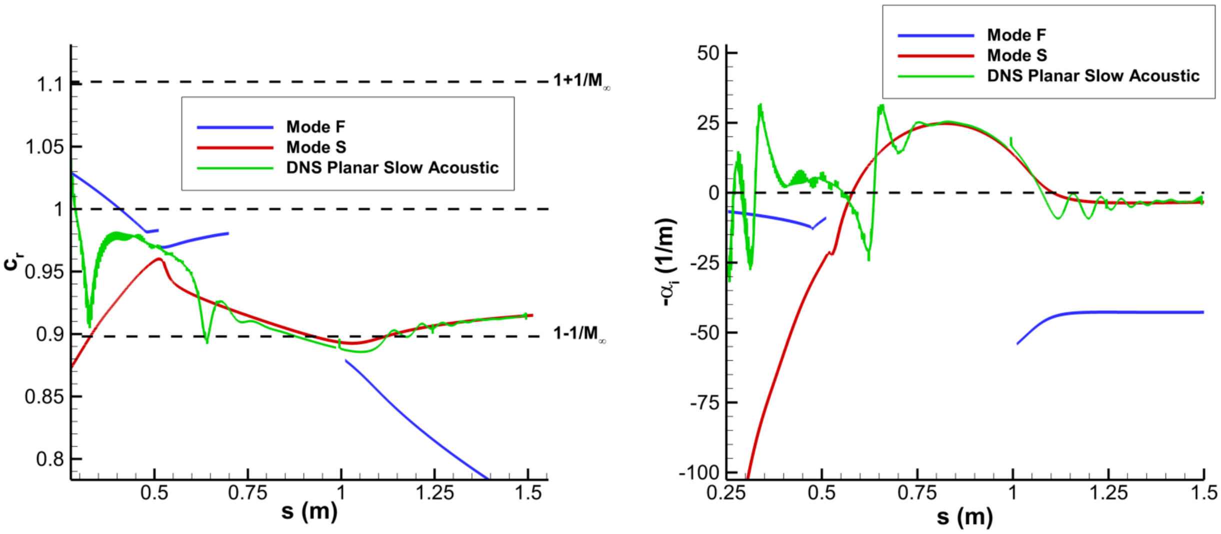

(a) (b)

Figure 4.55: Case I6 unsteady DNS results vs. LST predicted results for 200 kHz disturbances (a) Phase Speed (b) growthrate.

development of the second mode, which is expected from the more complex disturbance interactions generated by the planar pulse. Furthermore, similar to Case B5, the unsteady signal for Case I5 in Fig. 4.54 is dominated by neutrally stable continuous fast acoustic disturbances immediately prior to and during synchronization. While the disturbance signal eventually gravitates towards the second mode disturbance, the impact of forcing outside of the second mode instability is again observed to be highly significant in the case of the planar fast acoustic pulse.

The unsteady DNS results show good agreement with the LST data, showing that in the majority of the tested unsteady cases the second mode dominates significantly over other disturbance modes. This indicates that modal decomposition using the N-factor method is feasible to generate spectral receptivity coefficients for this cone case.

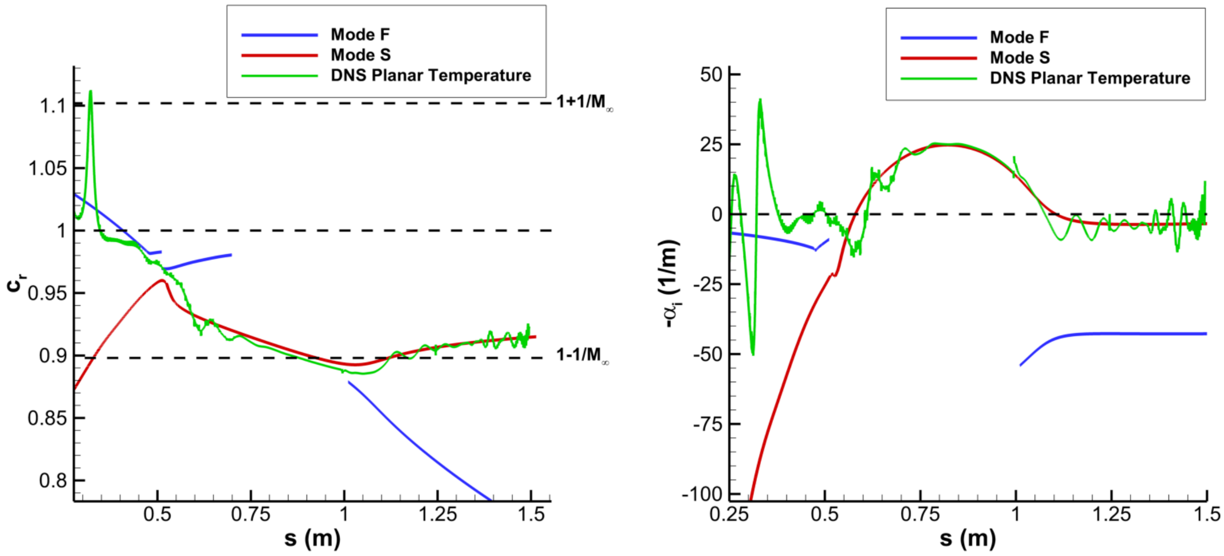

(a) (b)

Figure 4.56: Case I7 unsteady DNS results vs. LST predicted results for 200 kHz disturbances (a) Phase Speed (b) growthrate.

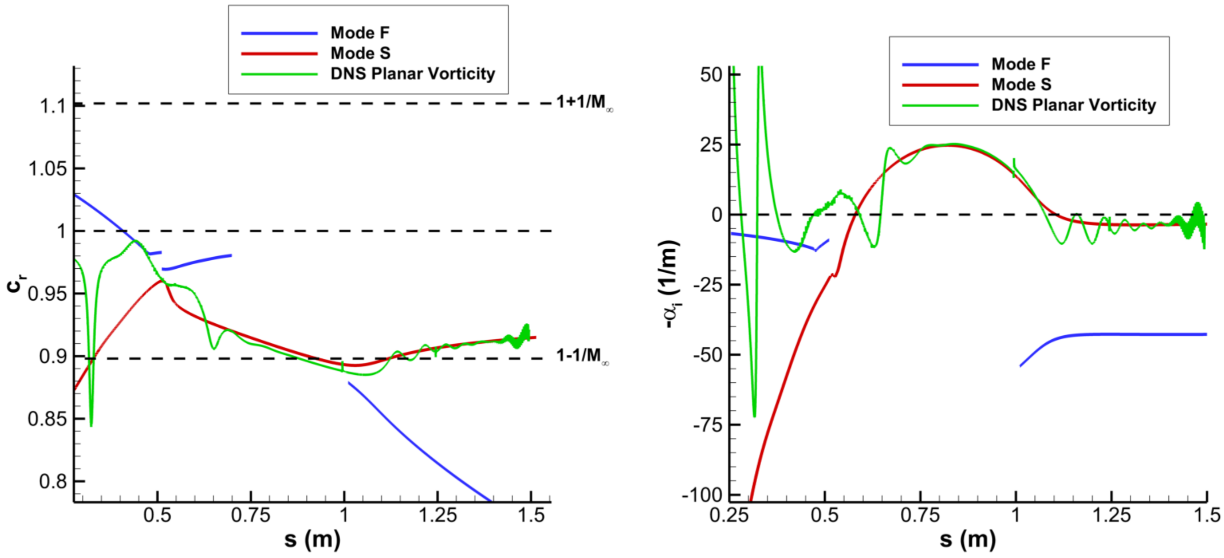

(a) (b)

Figure 4.57: Case I8 unsteady DNS results vs. LST predicted results for 200 kHz disturbances (a) Phase Speed (b) growthrate.

4.4 Secondary Disturbance Bands in the Planar Fast Acoustic Spectra (Case B5 and Case I5)

The planar fast acoustic pulses in Case B5 in Fig. 4.40a and Case I5 in Fig. 4.51a denote significant amplified instability bands outside of the second mode. In order to help identify these instabilities, the pressure eigenfunction profiles for the planar fast and slow acoustic cases at a selection of frequencies are plotted for both cones. The eigenfunctions for Cases B5 and B6 at the dominant second mode frequency of 153 kHz at $s^* = 1.5$ m are shown in Fig.4.58. In each of the figures in this section, the LST eigenfunctions and wall normal distance are normalized by the peak wall pressure and local shock height respectively. The LST mode F and mode S eigenfunctions demonstrate very similar profiles, though the secondary peak of mode F is lower in amplitude. These discrete modes are clearly identifiable as their oscillations are isolated to the boundary layer[24]. The planar slow acoustic (Case B6) results demonstrate close adherence to the LST mode F results, which is the destabilized second mode in this case. The planar fast acoustic pulse (Case B5), however, demonstrates significant deviation near the edge of and outside of the boundary layer. While the signal for Case B5 initially follows closely with mode F, it eventually diverges to mode S before transitioning to become highly oscillatory outside of the boundary layer. Additionally, the eigenfunction does not decrease in amplitude, demonstrating strong excitation throughout the shock layer. These oscillations and the unbounded nature of the eigenfunction are indicative of continuous mode excitation at this frequency[24]. This corroborates prior phase velocity results in Fig. 4.43 at a similar frequency for Case B5 which indicate significant excitation of continuous fast acoustic modes.

Similar eigenfunction plots are shown for the 55 kHz and 225 kHz disturbance frequencies for Case B5 and Case B6 in Fig. 4.59. Throughout these frequencies Case B5 demonstrates relatively similar behavior, with decent wall-bounded agreement inside the boundary layer followed by significant non-decaying oscillations outside of it. These behaviors again denote significant continuous mode excitation at these outer frequencies. From prior phase speed data in He and Zhong[105], the planar fast acoustic pulse tended to more readily excite

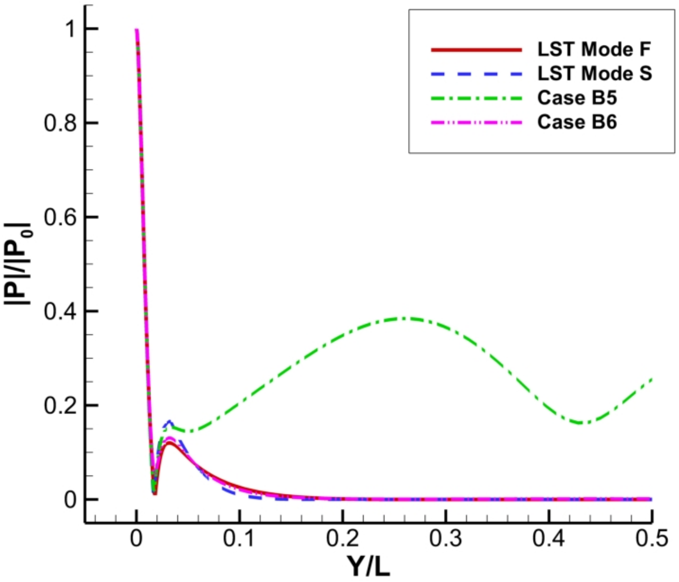

[h!]

Figure 4.58: Case B5 and Case B6 pressure eigenfunctions at $s^* = 1.5$ m for 153 kHz disturbance.

continuous fast acoustic modes at the suboptimal second mode frequencies. The Case B6 results are much more variable. At 55 kHz the boundary layer portion of the eigenfunction is similar in profile to mode S, but falls between mode F and mode S. This indicates potential contributions of both of these discrete modes to the DNS signal. Oscillations are also observed outside of the boundary layer for Case B6, though they are more irregular throughout the shear layer. The modal content of this is hard to identify without more complex analysis tools such as mulitmode decomposition. Similar irregular oscillations are observed outside of the boundary layer for Case B6 in the 225 kHz eigenfunctions as well. However, it should be noted that the absolute magnitude of the pressure disturbances is not equivalent between Case B5 and Case B6 at the three sampled frequencies. At 153 kHz the peak pressure amplitude for Case B6 is approximately an order of magnitude larger than that for Case B5, while the reverse is true for the other two sampled frequencies. Additionally, the peak magnitudes for the 55 kHz and 225 kHz pressure eigenfunctions are approximately 50% smaller than the primary second mode value at 153 kHz for Case B5. The peak eigenfunction values at these secondary frequencies are almost two orders of magnitude weaker than the 153 kHz value for Case B6. As such, the results for Case B6 at these secondary frequencies may be more sensitive to non-modal noise due to the extremely small disturbance amplitudes.

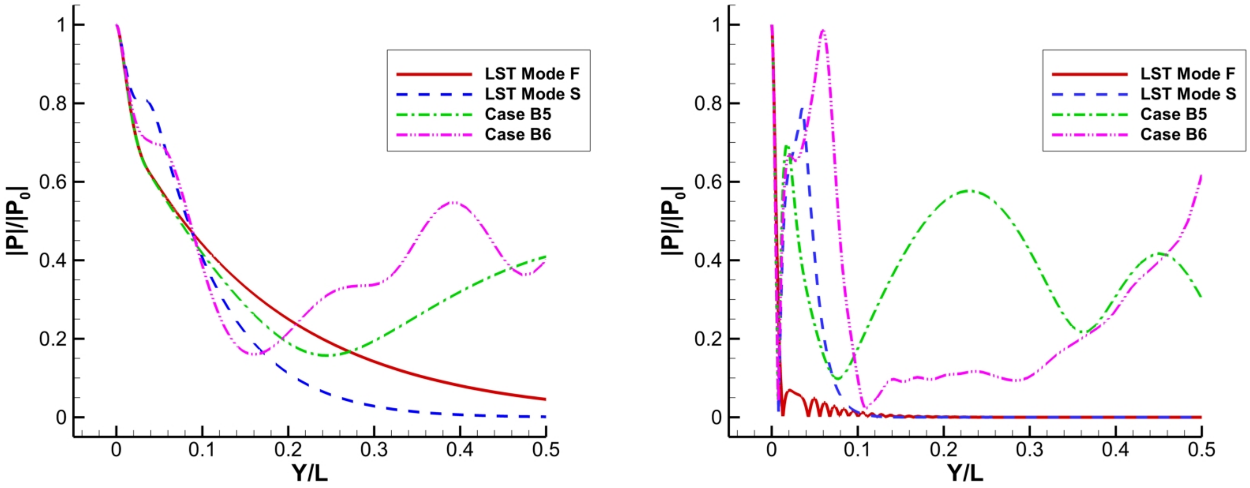

(a)

(b)

Figure 4.59: Case B5 and Case B6 pressure eigenfunctions at $s^* = 1.5$ m for (a) 55 kHz and (b) 225 kHz disturbance.

Similar eigenfunctions are plotted for Case I5 and Case I6 below. Fig. 4.60 demonstrates the pressure eigenfunctions at the primary second mode frequency of 180 kHz, while Fig. 4.61 presents eigenfunctions at 70 kHz and 260 kHz, which correspond to the secondary bands at a streamwise position of $s^* = 1.25$ m. The primary second mode frequency results in Fig. 4.60 are very similar to what was observed previously for Case B at 153 kHz. Namely, excellent agreement is seen between the unsteady DNS eigenfunctions and the destabilized second mode. In this case, this corresponds to the discrete mode S. However, the planar fast acoustic pulse in Case I5 is not shown to induce a significant oscillatory signal outside of the boundary layer, and instead decays to 0 as expected of a dominant discrete mode disturbance. This is likely due to the stronger second mode amplification present in Case I causing the destabilized discrete mode to dominate strongly over any potential continuous mode excitation. Additionally, at the 180 kHz frequency the peak Case I6 amplitude is an order of magnitude higher than that for Case I5, similar to what was observed previously.

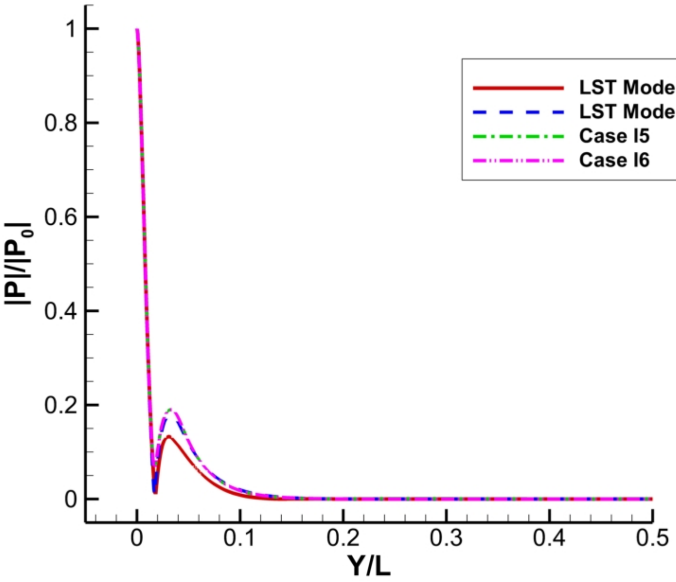

Figure 4.60: Case I5 and Case I6 pressure eigenfunctions at $s^* = 1.25$ m for 180 kHz disturbance.

The Case I5 results in Fig. 4.61 demonstrate very similar profiles to the eigenfunctions for Case B5 in Fig. 4.59 at the secondary frequency lobes. When considering phase speed data from Fig. 4.54 which also showed strong excitation of the continuous fast acoustic modes for Case I5, it is likely that similar excitation patterns are present here. Namely, the planar fast acoustic pulse is introducing continuous fast acoustic modes throughout the flow as it propagates through the domain. Since these secondary bands are outside of any regions of modal instability, they are not overshadowed like they are in the 180 kHz results. Furthermore, if the peak non-normalized pressure eigenfunction values are compared between Case I5 and Case B5 at the most amplified frequencies of the secondary bands, we see very similar values with dP ranging between 12 through 15.

The Case I6 results demonstrate some significant differences compared to the Case B6 results. Namely, the agreements with the LST discrete modes is much weaker and the general oscillations are much stronger. This is particularly true for the 260 kHz results in which the Case I6 eigenfunction essentially devolves into highly oscillatory noise. The secondary frequencies at this streamwise position are well outside of the unstable second mode region, and are predicted by LST to be highly attenuated. Since the planar slow acoustic pulses are not expected to induce significant continuous mode excitation, there seems to be minimal excitation at the secondary frequencies for cases other than B5 and I5. This weak excitation may result in the increased sensitivity to non-modal noise observed in the eigenfunctions here.

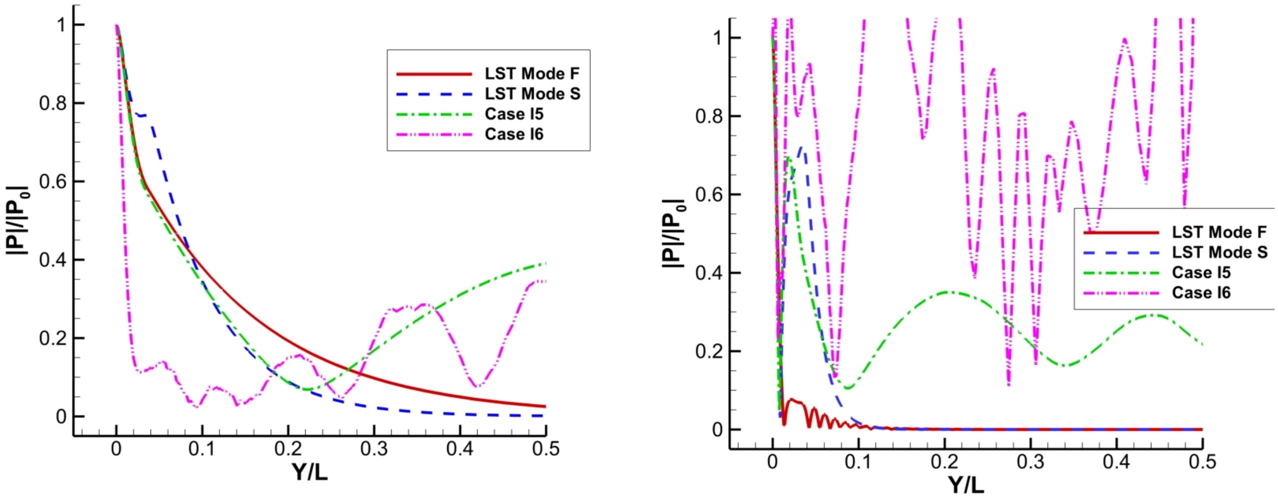

(a)

(b)

Figure 4.61: Case B5 and Case B6 pressure eigenfunctions at $s^* = 1.25$ m for (a) 70 kHz and (b) 260 kHz disturbance.

The similar oscillatory structures in the shear layer for the planar fast acoustic pulses indicate similar modal excitation mechanisms downstream in both Case B5 and Case I5. Since continuous mode instabilities are characterized by shear layer oscillations that aren't isolated to the boundary layer, it is likely that the secondary lobes found in Fig. 4.40a and Fig. 4.51a originate from excited continuous mode perturbations that are introduced throughout the flow field by the planar pulse as it propagates through the domain. Additionally, from prior phase speed analyses for Case B and for Case I, it is likely that these lobes are comprised of the continuous fast acoustic mode in particular. While the supersonic mode also induces oscillatory eigenfunctions outside of the boundary layer[25], their effects are observed much further downstream in a very small selection of frequencies in the second mode band. As such, they are unlikely to be responsible for the secondary bands.

4.5 Shock Layer Spectra

While the drag and heating loads experienced by a hypersonic vehicle are wholly dependent on the conditions in the boundary layer of the flow, an extended view of the excited disturbances throughout the entire shock layer also has a distinct application in the study of hypersonic transition. Computational studies of the nonlinear breakdown phenomena, such as in works by Lei and Zhong[63, 86] and Hader and Fasel[77, 5], require the simulation of finite amplitude disturbances which cause strong nonlinear interactions in the boundary layer. Contemporary studies are often interested in simulating the ”natural transition” pathway which contains both the linear receptivity response to weak freestream noise as well as the nonlinear breakdown at finite disturbance amplitudes. However, this requires significant computational time to both resolve the computational domain at the downstream locations at which the breakdown phenomena are expected to occur and to propagate unsteady disturbances to that point. Spectral data throughout the shock layer at downstream positions can be used to reconstruct unsteady inlet profiles for these simulations and reduce the computational resources necessary to simulate upstream portions of the flow, given that the data itself remains in the linear regime. This section presents such data that may be useful in this application.

As the acoustic pulses are observed to excite the strongest receptivity responses and the planar disturbances induce the most significant receptivity coefficients, the discussion here will focus on those results in particular. Fig. 4.62 depicts the FFT decomposed surface pressure spectra at $s^* = 1.25$ m for both Case B5 and Case B6, sampled throughout the entire shock layer. The differences in the excitation mechanisms between the planar fast acoustic and planar slow acoustic pulses is even more evident here. The planar slow acoustic pulse in Fig. 4.62b depicts the second mode disturbance band near a frequency of 140 kHz

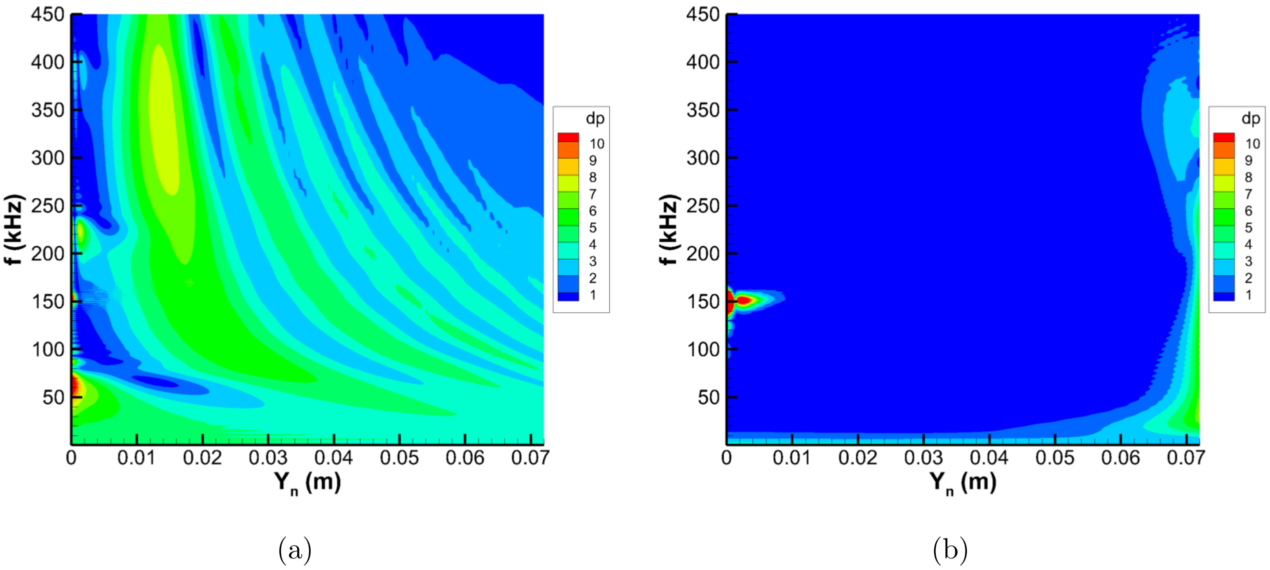

(a)

(b)

Figure 4.62: Pressure disturbance spectra throughout the shock layer at $s^* = 1.25$ m for (a) Case B5 and (b) Case B6.

that is isolated underneath $Y_n = 0.01$ m. Near the top of the domain, weak broadband frequency oscillations are observed which are caused by the reintroduction of forcing by the local slow acoustic pulse front. The forcing in this case is highly irregular and does not depict the introduction of strong modal perturbations into the shock layer.

Fig. 4.62a, for the planar fast acoustic pulse in Case B5, shows a vastly different excitation pattern in both the shock layer and the boundary layer. While the primary second mode band is also present, it is significantly weaker due to the reduced second mode receptivity to the fast acoustic pulse. The previously observed secondary boundary layer disturbance bands centered near 60 kHz and 230 kHz are also present and similarly remain isolated near the surface of the geometry. What is more of note, however, are the very distinct broadband disturbance patterns located outside of the local boundary layer. The regularity of these broadband perturbations reflects the presence of modal disturbances rather than random noise, and their unbounded nature from the boundary layer indicates that these are likely a mixture of continuous modes excited by the planar fast acoustic shock-disturbance front. These continuous modes are observed to interact strongly with the secondary disturbance bands, effectively forcing them in the boundary layer.

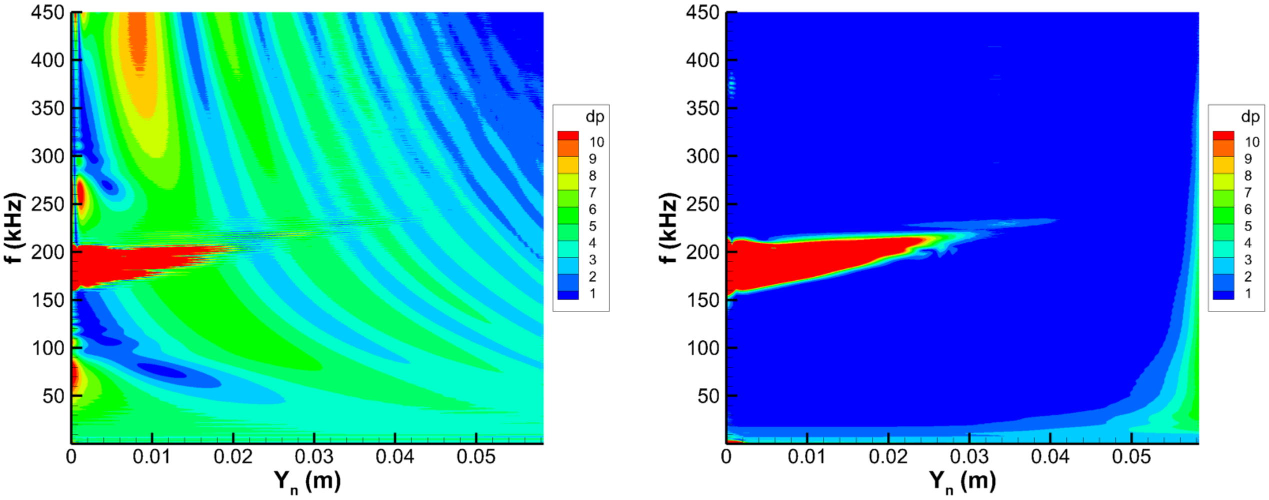

(a) (b)

Figure 4.63: Pressure disturbance spectra throughout the shock layer at $s^* = 1.25$ m for (a) Case I5 and (b) Case I6.

Similar shock layer distributions are plotted for the planar acoustic pulse results for Case I5 and Case I6 in Fig. 4.63. In these cases, much of the same general phenomena are observed. The planar slow acoustic pulse in Case I6 excites little to no continuous mode forcing and also primarily introduces additional noise that is isolated near the shock. In this case, only the primary second mode experiences significant growth. The planar fast acoustic case in Case I5 also shows the same general disturbance profile as Case B5, with an excited primary second mode band along with a selection of secondary disturbances at higher and lower frequencies that are forced by the heavily excited continuous modes in the shock layer. The primary difference here lies in the extent of the disturbances, as the Case I results demonstrate both much higher disturbance amplitudes and much higher prevalence of the second mode band in the boundary layer spectral profile. Disturbances in the second mode band also penetrate much deeper into the shock layer, though they are found to degrade exponentially outside of the boundary layer as expected. This is due to the sharper nose geometry, which results in a much stronger local amplification of the second mode disturbance. The temperature and vorticity pulses were generally observed in both cases to follow very similar patterns as well. Using these FFT-decomposed shock layer pressure spectra, arbitrary disturbance flow fields further downstream on the cone can be reconstructed for breakdown simulations or further receptivity analyses.

4.6 Receptivity Results

The spectral receptivity coefficient for each of the disturbances is calculated from Eq. 3.39 using FFT decomposed surface pressure perturbation data. This spectral disturbance data is then normalized by the amplitude spectra of the incident pulse to account for the variable frequency distribution of the incoming disturbance. Using a method originally applied by Huang and Zhong[4, 72] and proposed by Schneider[73], the second mode receptivity coefficient is extracted using LST-derived N-factors to backtrace the initial second mode amplitudes from the unsteady DNS data. Isolating the contributions of different modal disturbances to the total initial disturbance amplitudes allows for greater specificity when tracking the development of instabilities across a flow domain, especially in cases with significant multimodal content. More rigorous methods for decoupling the modal boundary layer disturbances exist, like the bi-orthogonal decomposition method developed by Tumin[83] and utilized by Miselis et al.[84]. They showed that this bi-orthogonal decomposition could be used to isolate receptivity coefficients for each of the different discrete and continuous instability modes in a flow, rather than just the second mode like the method utilized in this work. However, this more rigorous decomposition model requires additional development before it can be applied to the results here and in general for other computational receptivity studies.

4.6.1 Receptivity Coefficient Spectra

Using the methodology described in Section 3.4, the receptivity coefficients are calculated for each of the disturbance cases. Since these receptivity calculations may be sensitive to sampling location[72], a comparison of the receptivity spectra for different sampling locations was made for the finite spherical and planar disturbances respectively in Case I and Case

B. The receptivity spectra for Case B1, Case B2, Case B3, and Case B4 at several sampling locations are presented in Fig. 4.64. The sampling locations were chosen to be the branch I neutral stability point x_{brI}, the branch II neutral stability point x_{brII}, and an intermediate location defined at $x_{sample} = 1.3 * x_{brI}$ for each discrete frequency. These points were chosen to ensure the sampling location remained within the unstable second mode region. The branch I sampling point compares directly to conventional receptivity results reported by Balakumar and Chou[62], Kara et al.[33], Zhong and Ma[60], and Huang[72] as the normalization factor in this case is simply 1. In other words, the unsteady signal is dreictly sampled without any additional alterations. Huang stated that the total acoustic response at the branch I neutral point is likely to be contaminated by the multimodal content of the disturbance. This may make it difficult to apply the receptivity results for transition studies in which only particular instability modes are of interest. However,for Cases B1 through B4, Fig. 4.64 shows that second mode disturbances dominate for the finite spherical pulse cases. While the branch I sampling case does show significantly more oscillations indicative of multimodal disturbances[72] and/or interference in the wavepacket[102], the general shape and magnitude of the receptivity coefficients is in line with the other sampling locations.

This good agreement in the finite pulse cases is likely due to the fact that the geometry of the pulse limits shock-disturbance interactions to a small location far upstream on the cone at the nose. This limited interaction induces relatively weak initial forcing waves in the flow, which after the initial attenuation results in extremely weak downstream noise content outside of the second mode. Additionally, this weak initial forcing means the initial amplitudes before second mode amplification are also very low, which explains the extremely low receptivity coefficients that are observed for the finite pulse cases.

Fig. 4.65 presents the same data for the planar freestream pulses in Case B5, Case B6, Case B7, and Case B8. The receptivity coefficient spectra for Case B5 in Fig. 4.65a differ significantly from the finite spherical pulse cases, while the results in Fig. 4.65b, Fig. 4.65c, and Fig. 4.65d for Cases B6, B7, and B8 respectively are similar to those in Fig. 4.64 in that they peak near the maximum downstream second mode frequencies. The magnitudes of the receptivity coefficients for the planar cases are also much higher. This is because

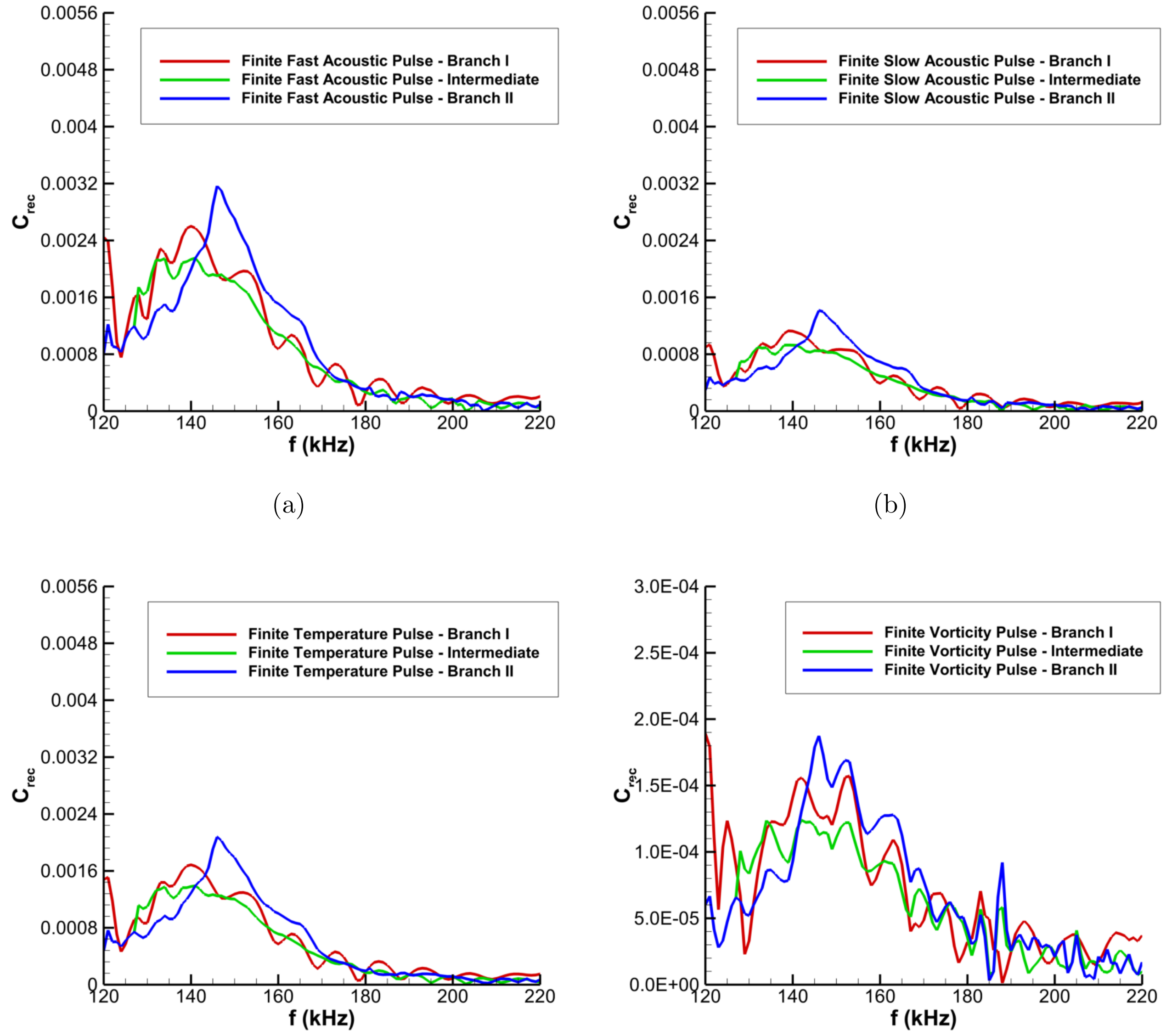

(a) (b)

(c) (d)

Figure 4.64: Receptivity coefficients at different sampling locations for (a) Case B1, (b) Case B2, (c) Case B3, and (d) Case B4. The y-axis in Case B4 is of a different scale to better visualize the curve shape.

planar disturbances generate significantly stronger boundary layer perturbations relative to the initial freestream disturbance amplitudes, as a result of the additional forcing they introduce downstream on the cone.

Case B6 and Case B7 seem to very readily excite both second mode and additional low frequency disturbances attributed to noise. The low frequency disturbances in particular are observed to be excited much more readily than in the finite pulse cases. This can also be seen in the FFT contours shown in Fig. 4.40 where again the low frequency forcing generated by the planar pulse is observably much more present throughout the domain. The branch I sampling location demonstrates the influence of this much more significantly in both Cases B6 and B7, indicating that modal decomposition is necessary to capture the behaviors of specifc disturbance modes like the second mode. On the other hand, the intermediate and branch II sampling locations show very similar results, peaking at frequencies between 125 and 145 kHz. The temperature pulse results for Case B7 and the vorticity pulse results in Case B8 are also noticeably more oscillatory than the acoustic pulses, though they still follow the general trends and peak near the most amplified downstream second mode frequencies. This likely reflects the multi-peak oscillatory structures observed in the previous amplitude spectra that have been attributed to localized wavepacket interference. It remains unclear what mechanism causes these modes to be more sensitive to this interference pattern, though it does not seem to affect the overall trend of the receptivity spectrum.

The results for Case B5 in Fig. 4.65a differ significantly from the finite pulses in Cases B1 through B4 as well as the other planar pulses in Cases B6 through B8. The branch I sampling location produces a continuous broadband receptivity coefficient distribution, similar in nature to the spectra of the incident freestream pulse. This indicates that the broadband forcing excited by the planar fast acoustic pulse is strong enough to mask the initial second mode instability at the branch I neutral point, and that the planar fast acoustic pulse excites a very broad range of frequencies in comparison to all the other cases. The resulting combined disturbances at this location result in perturbation amplitudes far larger than those expected of the pure second mode. The other sampling locations also show that the receptivity coefficients are highest near 200 kHz, contrary to the finite spherical cases. Looking again at Fig. 4.40a it can be seen that an additional band of amplified disturbances can be found at these frequencies. This secondary unstable frequency band is attributed to the strong surface forcing generated by the shock-disturbance interaction seen in Fig. 4.37. While significant second mode amplification is observed in all of the cases, Case B5

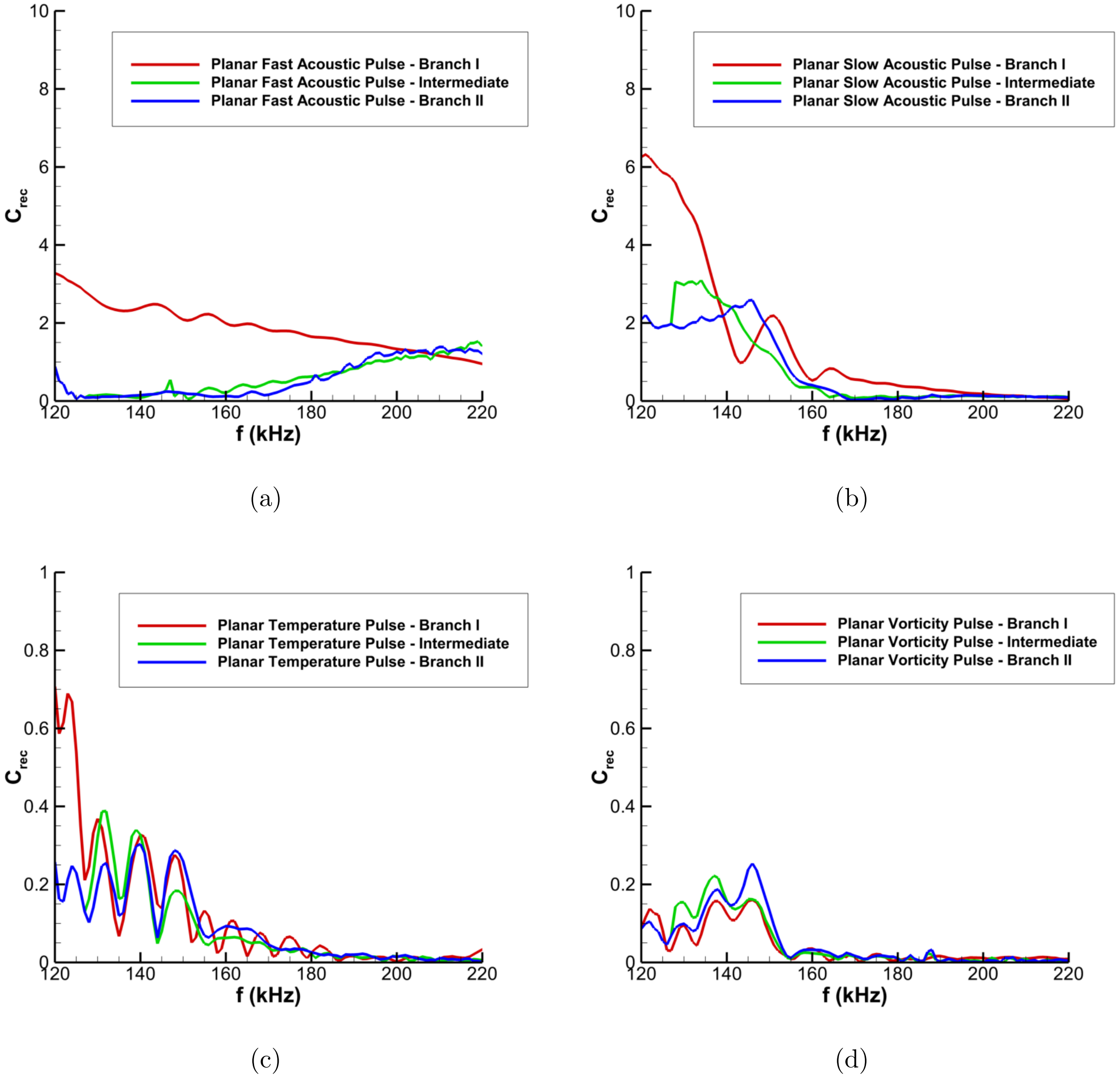

Figure 4.65: Receptivity coefficients at different sampling locations for (a) Case B5, (b) Case B6, (c) Case B7, and (d) Case B8.

demonstrates that sufficiently noisy environments of fast acoustic disturbances in particular can excite significant boundary layer disturbances not associated with the second mode. This can potentially account for the somewhat weak association between transition and the second mode for Case B that Marineau et al. observed [7].

Similar receptivity results are plotted below for Case I. A comparison of different sampling locations is again made for the finite pulse receptivity coefficients for Cases I1 through I4 in Fig. 4.66. The sampling locations are the same as those in Case B. Relatively good agreement is seen between the branch II and the intermediate sampling points for all of the finite pulse cases,though the branch I results predict slightly highly receptivity coefficients. This may be due to the larger spatial extent of the initial upstream disturbances on the nose for Case I, since the pulse geometry was fixed between the two meanflows. The sharper nose in Case I was previously observed to have a much more widely distributed response to the incident pulses, which may have induced noisier upstream boundary layer disturbances. This may also potentially account for the more oscillatory spectra observed here.

A similar comparison for the different sampling positions is presented in Fig. 4.67 for the planar pulses in Cases I5 through I8. The sampling positions used here are the same as those for the finite pulse cases. It is observed that the branch I sampling position significantly overpredicts the receptivity coefficients before the suboptimal second mode frequencies under 250 kHz when compared to the intermediate and the branch II sampling points. Furthermore, the intermediate and branch II sampling points are found to generally have good agreement. This disagreement between the branch I sampling point and the other sampling points follows our expectations. Namely, more complex noise environments arise from the additional forcing introduced by the planar disturbance pulses which in turn introduce much more multimodal content into the boundary layer. Additionally, similar to Case B5 we observe in Fig. 4.67a for Case I5 that the branch I sampling position here is not dominated by a particular mode. Instead, the receptivity spectra demonstrates a relatively smooth broadband profile. This shows that planar fast acoustic disturbances can excite significant disturbances outside of the second mode in different blunt nose configurations, inducing highly complex and broadband boundary layer disturbances. Additionally, it is seen in Fig. 4.67c for Case I7 (the planar temperature pulse) that a particularly strong band of oscillations is observed at frequencies higher than 250 kHz. We can see in Fig. 4.51c that the planar temperature pulse in Case I7 seems to also induce a significantly broadened disturbance band compared to the other cases, with a smaller secondary lobe structure between 250 and 300 kHz. Additionally, further upstream within the second mode region itself highly oscillatory disturbance structures are

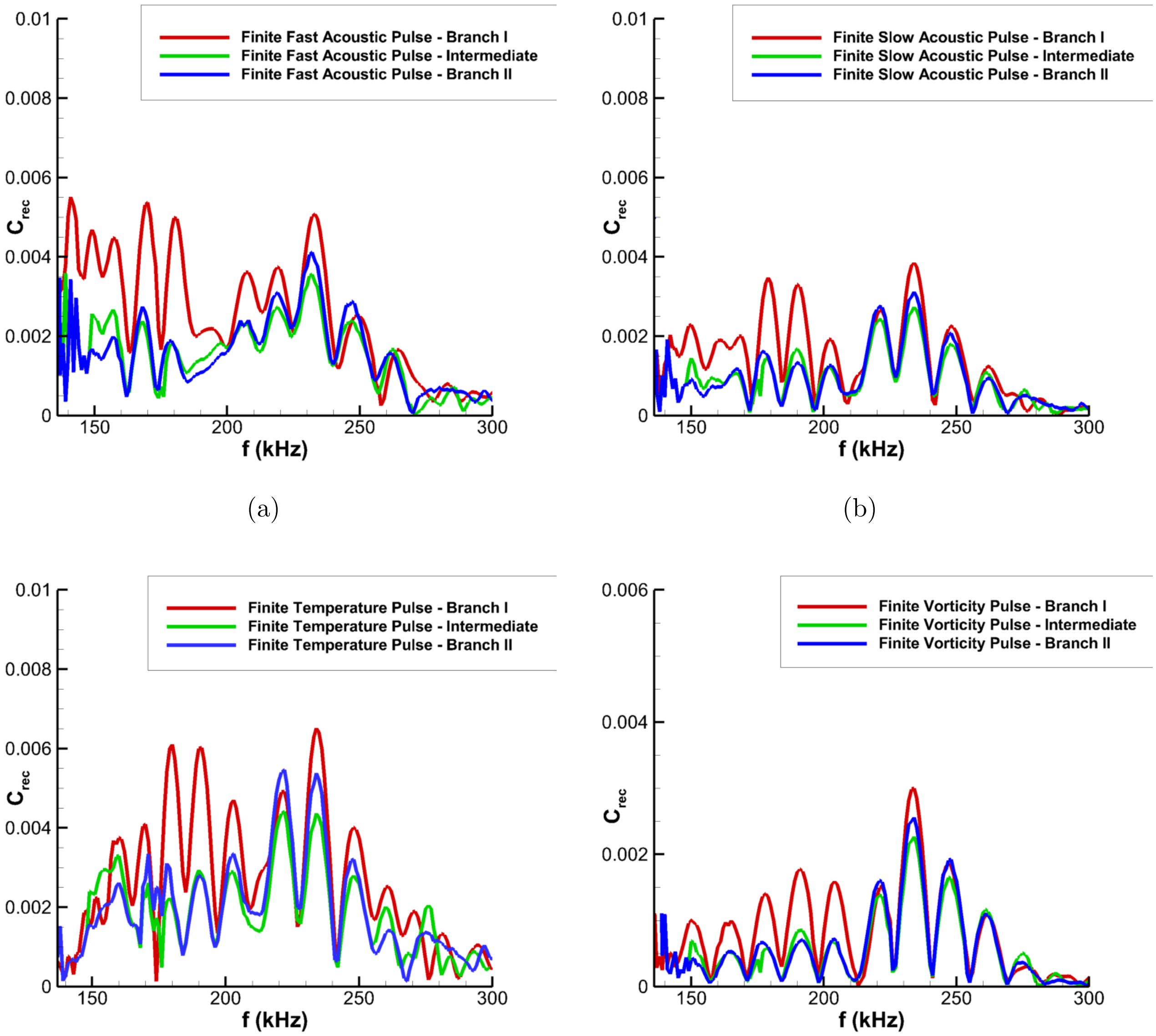

(a)

(b)

(c)

(d)

Figure 4.66: Preliminary receptivity coefficients at different sampling locations for (a) Case I1, (b) Case I2, (c) Case I3, and (d) Case I4. The y-axis for Case I4 are altered to better showcase profiles.

observed to extend to these higher frequencies. These frequencies are not as excited in the other planar pulses. These oscillatory disturbances seem to generally be centered about the branch II neutral point as a second mode disturbance should. The greater receptivity of these high frequency disturbances for the planar temperature pulse is reflected in the receptivity coefficient spectra, which is noticeably higher in amplitude than the other planar pulses for frequencies above 250 kHz. The high degree of oscillation found in the branch II sampling results for Case I7 is due to the oscillatory spectra observed at these higher frequencies, which themselves may be influenced by interference with the secondary 250 to 300 kHz disturbance band observed previously.

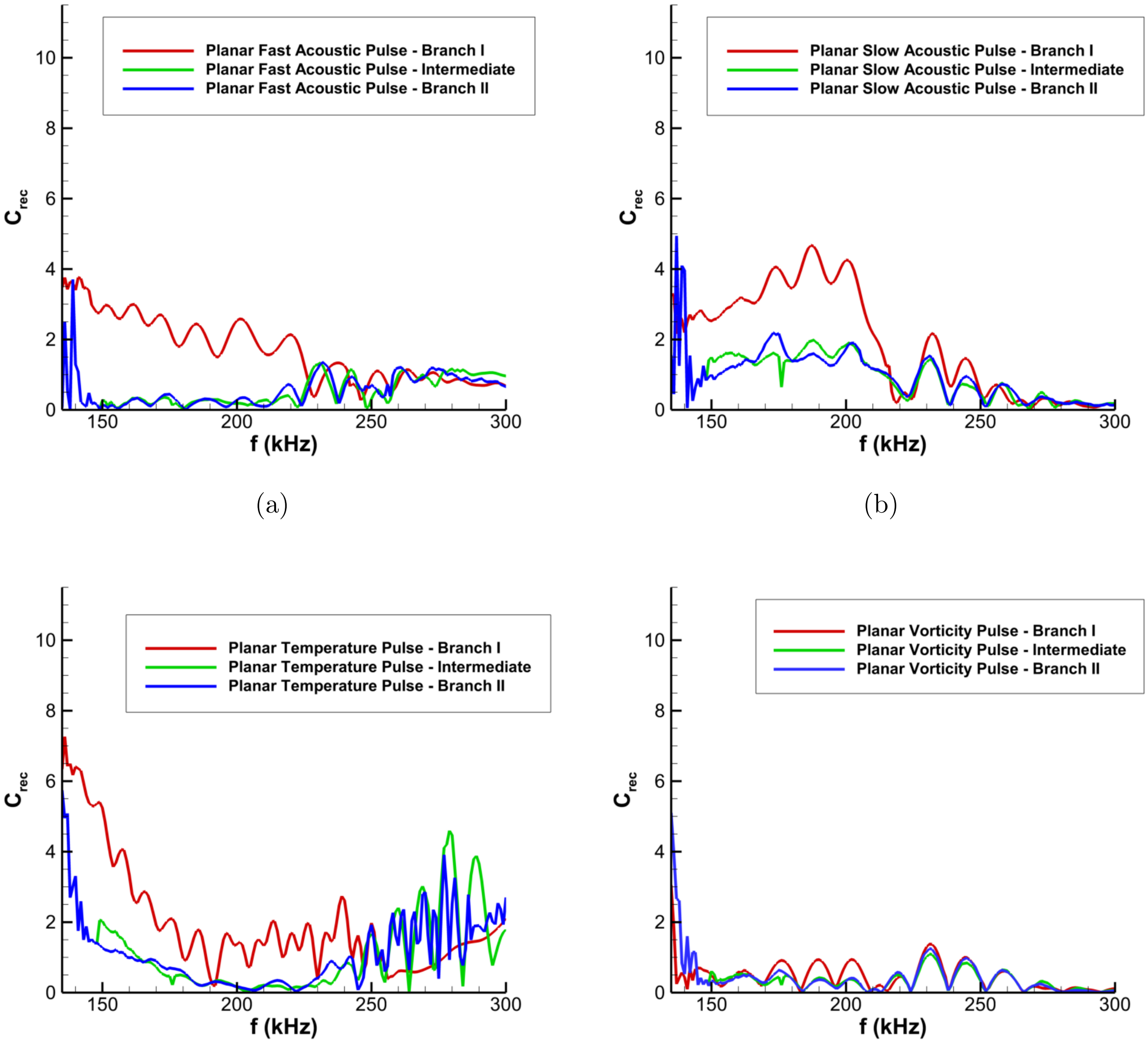

(a)

(b)

(c)

(d)

Figure 4.67: Preliminary receptivity coefficients at different sampling locations for (a) Case I5, (b) Case I6, (c) Case I7, and (d) Case I8.

4.6.2 Comparison of Case B and Case I Spectral Receptivity Coefficients

Fig. 4.68 presents the total spectral receptivity coefficient results for the finite pulse cases. For Case B, the finite fast acoustic pulse is observed to induce the strongest second mode response, followed by the finite temperature, slow acoustic, and vorticity pulses. The finite pulse results for Case I indicate stronger receptivity responses for the temperature pulse, followed by the fast acoustic, slow acoustic, and vorticity pulses again in that order. While the general order of magnitude for most of the finite pulse cases is consistent between the meanflows for Case B and Case I, some distinct discrepancies in the receptivity spectra are also observed. For one, variations in the peak frequencies and amplified disturbance bands can be attributed to meanflow variations caused by the different nose bluntness configurations, which is also reflected in the LST results. Another primary disparity is in the overall oscillatory behavior of the spectra. As a whole, the results for Cases I1-I4 demonstrate much more strongly modulated signals than for Cases B1-B4, indicating stronger modal interactions within the boundary layer for Cases I1-I4. This may be due to increased multimodal excitation upstream on the cone from the larger spatial extent of the pulse in Case I. While the pulses themselves are the same bandwidth and diameter between the two cones, the sharper nose in Case I causes shock-pulse interactions to occur through a larger extent of the flow field near the nose. Due to the curvature of the shock near this region, this introduces significantly more multimodal content in Case I. In general, the receptivity coefficient spectra for Cases I1-I4 follow the same general pattern as the Case B finite pulse results, with a peak centered around the most amplified second mode frequency.

In terms of the receptivity coefficient magnitudes, we see that the finite fast acoustic pulses in Case B1 and Case I1 have near equal peak amplitudes. Case B1, with a maximum disturbance near 140 kHz, has a peak receptivity coefficient of approximately 0.0031 while Case I1 has a maximum receptivity coefficient of approximately 0.0034 near 225 kHz. The finite slow acoustic as well as the entropy and vorticity cases are shown to have much more variable receptivity responses. For the finite slow acoustic pulses, case B2 is shown to have a peak receptivity coefficient of approximately 0.0015 while the peak receptivity coefficient of Case I2 is approximately 60% larger at 0.0025. This indicates a much stronger second mode response for slow acoustic disturbances in the sharper nose case, and reflects the strong receptivity response to slow acoustic disturbances observed in prior studies of cone geometries[62].

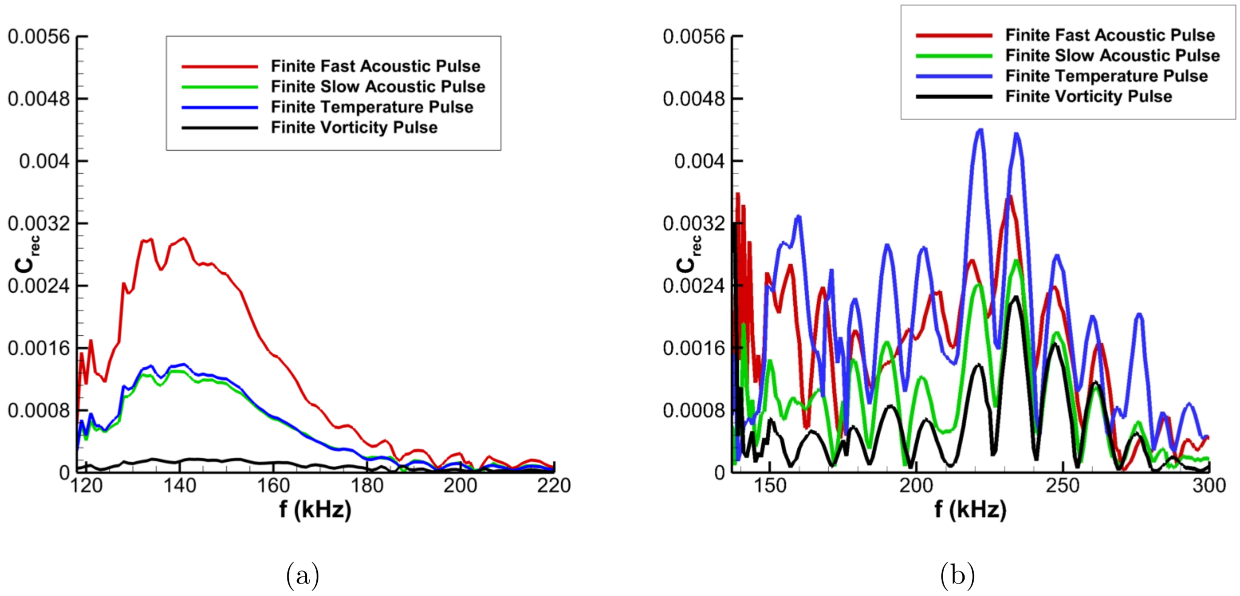

(a)

(b)

Figure 4.68: Receptivity coefficient spectra for the finite pulse cases: (a) Cases B1 through B4 and (b) Cases I1 through I4.

The greatest differences in receptivity response between Case B and Case I for the finite pulses are observed in the vorticity and temperature disturbances. In Case B the finite temperature pulse (Case B3) was observed to be of a very similar value to the slow acoustic pulse. The finite vorticity pulse (Case B4) resulted in a peak receptivity coefficient of approximately $1.6E-4$, which is an order of magnitude smaller than the other pulses for Case B. While the finite vorticity disturbance (Case I4) also results in the weakest receptivity coefficient for Case I, its amplitude is much more on par with the other cases. With a peak value of 0.0023 it is over an order of magnitude larger than its counterpart in Case B. The finite temperature pulse (Case I3) is also much stronger relative to the other disturbances, with it inducing the strongest second mode receptivity coefficient in the finite pulses for Case I. In particular the peak second mode receptivity coefficient of approximately 0.047

is approximately 300% larger than its counterpart in Case B3, which has a peak value of approximately 0.015. These results denote a wide variance in the in the receptivity response between the disturbance types with regards to the nose bluntness.

The receptivity spectra for the planar pulses are plotted in a similar manner for Cases B5 through B8 in Fig. 4.69a and for Cases I5 through I8 in Fig. 4.69b. The receptivity coefficients for the planar pulses in Fig. 4.69 are several orders of magnitude larger than those for the finite pulses in Fig. 4.68 due to the different spatial extents of the incoming freestream disturbances. The finite pulses only interact with the cone geometries near the nosetip, while the planar pulses are infinite in the y-z plane and continue to interact with the bow shock as they are advected downstream along the cone. This additional forcing results in much higher amplitude disturbances within the shock layer relative to the strength of the freestream pulse.

The planar slow acoustic pulse dominates at lower second mode frequencies in both Case B and Case I. Additionally, the peak receptivity coefficient of the slow acoustic pulse in Case B6 is approximately 100% larger than that for Case I6, even though LST predicts stronger second mode amplification in Case I. This counterintuitive behavior may be attributed to the increased receptivity of Case B to instabilities outside of the standard second mode. The planar fast acoustic pulse was shown for both Case B5 and Case I5 in Fig. 4.40a and Fig. 4.51a respectively to excite bands of unstable frequencies outside of the second mode, though these were orders of magnitude weaker than the primary second mode instability. The planar slow acoustic cases were similarly shown to induce significant upstream fluctuations at frequencies slightly below the second mode in Fig.4.51b and Fig. 4.40b that are attributed to local excitation in the flow by the planar pulse front. While Case I6 had a much more highly amplified second mode, the lower frequency forcing upstream of the second mode region was up to 60% stronger for Case B6. It is likely that significant extramodal excitation in the planar acoustic cases can cause issues with the decomposition method used here. This can be partially credited to weaker second mode amplification in Case B, as the decomposition method utilized in this work requires sampling at locations of significant second mode instability to effectively exctract second mode coefficients. This indicates that although the second mode in Case I is more amplified, Case B is more receptive to other disturbances excited by extensive broadband forcing from the freestream. This, when combined with the relatively weak second mode amplification in Case B may have caused issues with extracting the primary second mode receptivity coefficient using the methodology of this work.

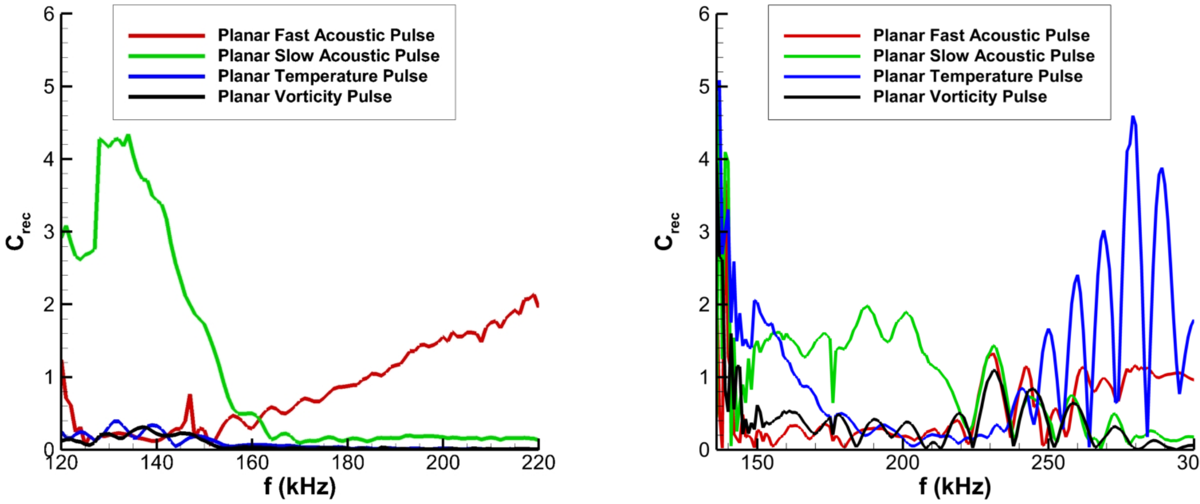

(a)

(b)

Figure 4.69: Receptivity coefficient spectra for the planar pulse cases: (a) Cases B5 through B8 and (b) Cases I5 through I8.

While the planar slow acoustic pulse in both cases is most dominant at the lower second mode frequencies, they are not necessarily the highest for the peak frequencies at the experimental transition locations from Marineau, et al.[7]. For Case B the peak frequency at transition is predicted to be 176 kHz while for Case I it is 224 kHz. For Case B the planar fast acoustic pulse produces the highest receptivity coefficient at this frequency with a value of 0.78. The planar slow acoustic pulse for the same cone results in a much smaller receptivity coefficient of 0.18 at the same frequency. In Case I the planar slow acoustic pulse is strongest at the peak transition frequency, and results in a peak receptivity coefficent of 1.35. This compares well to Balakumar and Chou's[62] reported case 4 receptivity coefficient of 1.2 for a discrete frequency slow acoustic wave. The increased peak frequency and receptivity coefficient of our case is likely due to differences in our freestream gas model, resulting in a higher unit Reynolds number for Case I here. While the forcing regimes of these two configurations are very different, these findings reinforce that similar generalized results can be expected between continuous, discrete wave forcing and the pulses used in this study in the linear receptivity regime.

The planar fast acoustic cases demonstrate similar receptivity magnitudes, and have very similar structures. Case B5 and Case I5 both demonstrate small receptivity coefficients in the lower second mode frequencies, while they gradually increase over higher frequencies instead of reaching maximums near the most amplified frequency. This behavior reflects the complex, broadband response of both flows to the planar fast acoustic pulse[65]. The peak receptivity coefficient for Case B5, at a value of approximately 1.9, is 50% larger than the peak coefficient for Case I5 at the higher second mode frequencies. This can again be attributed to the weaker second mode in Case B. Since the secondary instabilities for the planar fast acoustic pulses were previously shown to be relatively invariant with nose bluntness, the weaker second mode in Case B results in the decomposition method being less capable of removing the influence of the higher frequency noise. This is compounded by the fact that the second mode growthrates were weakest at the higher frequencies for both Case I and Case B.

The planar vorticity and temperature pulses are seen to have peak receptivity coefficients that are an order of magnitude larger in Cases I7 and I8 when compared to Cases B7 and B8, similar to what was observed in the finite pulse results previously. The stronger receptivity response for Case I7 in particular is most apparent at the extremes of the second mode frequency band. In Case I the planar temperature pulse in Case I7 results in low receptivity coefficients at the peak disturbance frequency, but the highest peak coefficients near 150 kHz and beyond 250 kHz. This is likely due to the excitation of nonmodal high and low frequency perturbations in a similar manner to the planar fast acoustic pulses. The stronger oscillations at these frequencies can also be traced to the noisier response seen in the disturbance spectra for Case I7 in Fig. 4.51c. The spectral fluctuations for this case appear to cause issues with the receptivity decomposition at the highest and lowest frequencies of the second mode band in Case I7 in particular, in a manner similar to what was observed for the planar fast acoustic pulses.

4.6.3 Disturbance Phase Angle Spectra

The phase angles of the disturbances can also be extracted from the FFT decomposition. Using a combination of the receptivity coefficient spectra and the phase angle spectra, the initial receptivity response of the flows to an arbitrary axisymmetric freestream disturbance can be reconstructed[4, 63, 65]. These initial disturbances can then be used to define initial perturbation conditions for more advanced transition predicted methods like Mack's amplitude method[93], which most recently have seen development by Marineau[6] and Fedorov and Tumin[92]. Another application for this data is in the construction of arbitrary unsteady inlets for simulations studying phenomena such as nonlinear breakdown [63, 85]. The receptivity phase angle spectra for the unsteady simulations is given in Fig. 4.70 for the finite spherical pulses in Cases B1-B4 and I1-I4 while Fig. 4.71 presents the results for the planar disturbances in Cases B5-B8 and I5-I8.

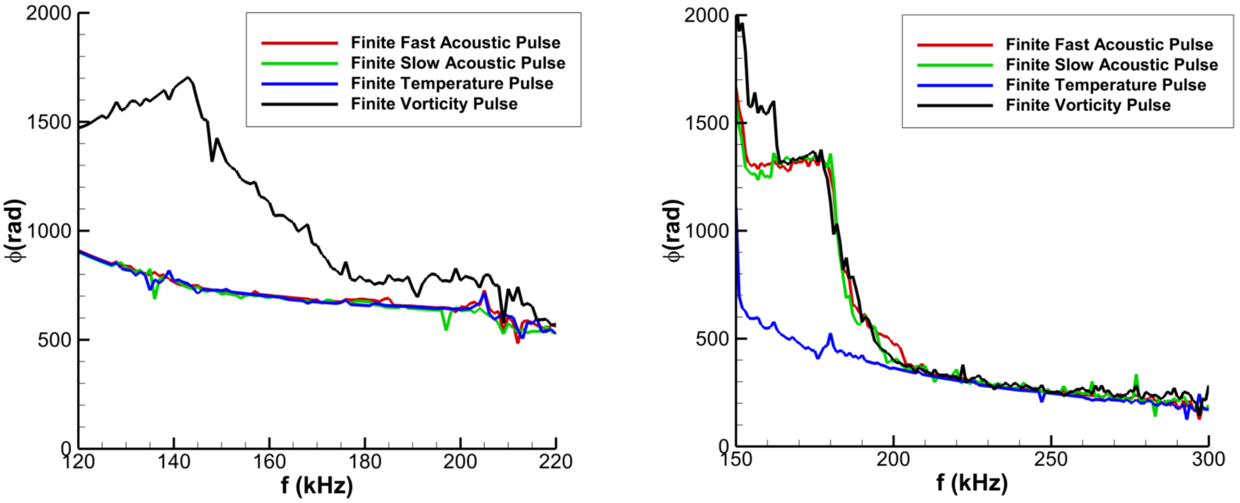

(a) (b)

Figure 4.70: Receptivity phase angle spectra after finite pulse disturbances for (a) Cases B1-B4 and (b) Cases I1-I4. Frequency axes not to scale between (a) and (b).

In terms of the finite pulses, strong agreement is observed between the acoustic and temperature pulses for Case B. The finite vorticity pulse, however, shows substantial divergence from the other spectra at the lower second mode frequencies before converging to the other pulses at higher frequencies. Similar behavior is observed for the finite pulses in Case I, though the agreement is strongest between the acoustic and voriticity pulses instead here. These three disturbances induce similar low frequency spikes in the phase spectra as observed for the finite vorticity pulse in Case B, while the finite temperature pulse retains the same continuous spectra as its counterpart in Case B. These large low frequency gradients in the spectra are attributed to the influence of excited extramodal disturbances in the boundary layer, and roughly coincide in frequency to the upstream disturbance bands in Fig. 4.16. These upstream modes contain a combination of continuous mode instabilities, as well as potentially nonmodal instabilities that greatly complicate the disturbance profile in the flow, reflecting in the sharp variations in the spectral phase profile. This forcing was previously found to be absent at the higher second mode frequencies, allowing for the convergent agreement observed here. The rapid amplification of the second mode at these higher frequencies also likely results in these tertiary disturbances being drowned out in the unsteady signal.

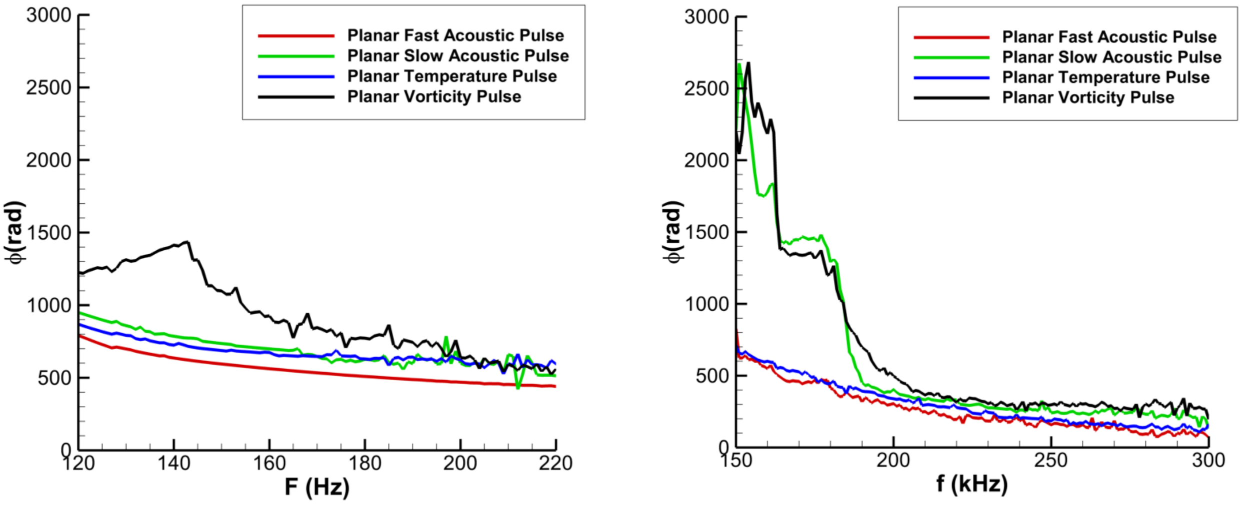

(a) (b)

Figure 4.71: Receptivity phase angle spectra after planar pulse disturbances for (a) Cases B5-B8 and (b) Cases I5-I8. Frequency axes not to scale between (a) and (b).

For the planar pulses, Cases B5-B8 in Fig. 4.71a demonstrate very similar general profiles to their finite pulse counterparts. The primary difference now lies in additional offsets between the spectral phase coefficient lines that were not present for the finite pulse cases. This is due to intrinsic phase differences caused by the different freestream advection speeds of the incident disturbances[65]. This is similarly true for the planar pulse results for Case I in Fig. 4.71b, which sees another difference arising in the behavior of the planar fast acoustic pulse's phase spectra. The planar fast acoustic pulse is now seen to share much better agreement at the lower frequencies with the planar temperature pulse, contrary to large low frequency gradients observed in the corresponding finite pulse case. This is due to the different excitation mechanism observed for the planar fast acoustic pulses in general. In Fig. 4.51a for Case I5 and Fig. 4.40a for Case B5, it was shown that the planar fast acoustic pulse induces a much more broadband spectral disturbance profile in the boundary layer. This includes much more distinct high and low frequency disturbance bands that are not consistent with the upstream forcing observed in the other cases for the same cones. As these excited disturbances lie outside of the range of the standard second mode, either because they are too low frequency or occur downstream of the second mode region, they do not affect the spectral phase profile. In general the differences in the extramodal excitation between the two cones causes substantial differences in the overall low frequency distribution of the phase spectra, though the higher frequency behavior is very similar due to the onset of a dominant second mode at these frequencies.

4.7 Summary of Axisymmetric Pulse Receptivity and the Bluntness Effect

Case B was found to have an amplified second mode instability corresponding to the discrete mode F. Supersonic modes were qualitatively observed in many of the unsteady pulses in Case B, though the impact of these supersonic modes was deemed to be relatively weak. Case I, on the other hand, was shown to have the discrete mode S destabilize into the second mode after synchronization instead. While a supersonic mode was also qualitatively observed for several unsteady configurations in Case S, they were much less prominent than they were for the blunter cone in Case B. This is attributed to the destabilized discrete mode itself, as the mode F instability is much more likely to become supersonic relative to the local meanflow as it propagates through the domain.

FFT of the surface pressure data shows generally good agreement between the unsteady DNS results and the LST in terms of phase speed, growthrate, and amplification patterns. Some small variations are attributed to non-parallel boundary layer effects that the core LST algorithm ignores, but have been shown to have minimal effects on the overall stability profile of the flows. The finite pulses are shown to induce very similar disturbance profiles in both cases, with small bands of upstream forcing modes experiencing attenuation before second mode growth induces rapid development of the dominant boundary layer instability. Case I and Case B both demonstrated significant variability in their receptivity responses to different freestream pulses. Contrary to conventional discrete frequency forcing wave studies, the finite pulse results show that the fast acoustic pulses are highly capable of exciting both upstream forcing and downstream second modes in both cones. In particular, the finite fast acoustic pulse induced the strongest receptivity response in Case B and the second strongest receptivity response for Case I. The planar pulses, on the other hand, show that broadband fast acoustic disturbances can induce peak second mode amplitudes that can be orders of magnitude lower than those resulting from other disturbance types. This indicates dramatic differences in leading edge and downstream receptivity mechanisms. Numerous factors can explain this stark difference including: the local surface curvature, boundary layer development, and the development of the entropy layer and whether or not it has been swallowed before perturbation is introduced into the system. The complex structure of a hypersonic flow requires additional consideration of each of these flow features as they have been shown to be sources of important instability mechanisms. While the planar pulse results show generally good agreement with regards to primary second mode amplification, the more complex noise profile demonstrates strong broadband receptivity for the planar fast acoustic cases, which induce secondary bands of instability outside of the second mode. These are associated with strong continuous mode forcing that is introduced throughout the domain as the pulse is propagated through it.

Receptivity coefficients are calculated using a combination of LST amplification factors and the unsteady surface pressure which has been decomposed using FFT into its spectral frequency components. The unsteady data are sampled at points at which the second mode is predicted by LST to be dominant, and then re-normalized using the LST derived N-factors. These spectral receptivity coefficients, as well as the corresponding phase data, may be applied towards amplitude method-based transition prediction. A preliminary application of these results is performed in a subsequent section of this work. The receptivity amplitude coefficients, particularly for the finite pulses, peak at the most amplified second mode frequencies in the calculated domain. The broadband forcing structure induced by planar fast acoustic pulses also induces highly broadband receptivity coefficient spectra that do not follow expected trends. This marks that more complex modal decomposition techniques might be necessary to successfully isolate the second mode contribution in particular for especially noisy spectra.

Significantly more oscillatory receptivity coefficient spectra are observed for the sharper cone in Case I. This is likely due to localized interference in the boundary layer disturbance wavepackets due to wave dispersion effects. Notable saddles in the spectral contours, and multi-peak patterns in the spectral lines of Case I results indicate that these interference effects are more prominent in the sharper cone, though the exact reason for this is not known. Acoustic pulse receptivity coefficients see minimal changes between Case B and Case I. Temperature and vorticity disturbances, however, cause much stronger receptivity responses in Case I which sees coefficients that are up to an order of magnitude higher than their counterparts in Case B in both the finite and planar pulse configurations. In general, broadband pulse disturbances have been found to excite significant modal responses in both blunt cone cases. Additionally, nose bluntness is observed to have highly variable effects on the general receptivity response depending on the disturbance type of the incident pulse.

CHAPTER 5

Application of 2-D Receptivity Spectra to Amplitude Method Transition Prediction

The primary objective of contemporary hypersonic stability analysis is the development of more efficient and more accurate models for transition prediction. This is due to the extreme increases in conditions such as surface drag and heating associated with turbulent boundary layers in hypersonic flow. This is reflected in results from Knisely, Haley, and Zhong[106] which show that further downstream along the cone, a fully turbulent boundary layer is expected to dramatically increase both drag and heat loading on the expected vehicle. In particular, the skin drag is over 2.8 times higher for the turbulent case while the turbulent heating rate is over 3.4 times higher. Successfully delaying the onset of transition can thus massively reduce both drag and heating loads, which in turn necessitate less extreme thermal protection systems. Thus, correctly predicting the onset of turbulent transition will provide significant gains in the design optimization process of hypersonic vehicles.

As discussed previously in Section 1.4.2 transition predictions have conventionally been done using the e^N method in which disturbance amplification factors taken from LST or PSE calculations are compared to experimentally correlated threshold values. This process focuses solely on the relative amplification of disturbance waves, and ignores the absolute amplitudes of disturbances in a hypersonic boundary layer as well as their highly broadband nature. Due to the varying freestream noise environments and receptivity mechanisms in different flows, this can lead to significant difficulties in relating results between different experiments or flight measurements with the same nominal meanflow conditions[41]. These stability theory based mechanisms have also seen significant difficulty in addressing the blunt body paradox[34]. The amplitude method, as proposed by Mack[90], arose in order to provide a transition prediction methodology that better took into account the effects of receptivity and the multi-frequency dependency of instability in a hypersonic flow. The basic amplitude method relation used to calculate the local amplitude of an arbitrary disturbance mode is given by Mack[90] as Eqn. 5.1.

$$A_d^2(R) = \int_0^\infty d\left(\frac{\omega\Lambda}{U_1}\right) \int_{-\infty}^\infty A_0^2\left(\frac{\omega\Lambda}{U_1}, \beta\Lambda\right) \frac{A}{A_0} \left[\frac{\omega\nu}{U_1^2}, \beta\left(\frac{\nu x}{U_1}\right)^{1/2}; R\right]^2 d(\beta\Lambda) \tag{5.1}$$

The relation in Eq. 5.1 is a generalized expression used to estimate the square of the local disturbance amplitude A_d^2 at a given streamwise position. This streamwise position is denoted in the relation by the local unit Reynolds numbe $R = (\frac{U_1 x}{\nu})^{1/2}$. Additionally, Λ represents an external disturbance lengthscale, ω is the circular frequency of the disturbance, U_1 refers to the freestream velocity, and β is the spanwise wavenumber of the disturbance of interest. As the amplitude ratio $\frac{A}{A_0}$ is representative of the relative amplification, or the N-factor of a given disturbance mode this relation can be further recasted in dimensionless form as Eqn. 5.2.

$$A_d^2(R) = \int_0^\infty d\omega \int_{-\infty}^\infty A_0^2(\omega, \beta) e^{2N[\omega,\beta;R]} d\beta \tag{5.2}$$

In essence the relations here estimate the local amplitude of a local boundary layer disturbance mode by integrating both its total frequency spectra and spanwise wavenumber spectra. While current applications of the amplitude method have focused on estimating the local amplitudes of the second mode in particular, this general representation may be applied to a wide variety of disturbance modes as long as the necessary receptivity and amplification data can be acquired. This can include more three-dimensional disturbances like crossflow modes, or even other discrete mack mode instabilities in the flow. This work will continue to primarily focus on the second mode disturbance.

Though the generalized amplitude method relation in Eqn. 5.1 and in Eqn. 5.2 is not particularly complex, some difficulties remain which prevent easy widespread application. Among these is a difficulty in identifying frequency and wavenumber bands of actual interest to the development of boundary layer instabilities. For instance, looking at the FFT decomposed surface pressure spectra for the finite pulses in Cases B1 through B4 in Fig. 4.16 only a very narrow band of disturbance frequencies in the two-dimensional spectrum see significant amplification downstream along the cone. Careful selection of pertinent disturbance bandwidths is critical to the amplitude method, but these bandwidths can vary significantly between different flows. The direct integration of these relations can also be somewhat inefficient, and so current works regarding the amplitude method have presented approximations for these generalized relations to make them more affordable for engineering application. Fedorov and Tumin[92], for instance, suggest an approximation based on an asymptotic approach. This method utilizes the maximum N-factor at a given sampling position, as well as its 2nd order derivatives in both frequency and spanwise wavenumber space based on the most optimally amplified frequency and wavenumber. However, this method has not been directly applied to experimental cases as of the time of this study.

Marineau[6] developed an interative method based on suggested simplifications of the governing relation in Eqn. 5.2 by Mack[90]. The following analysis will be based on this iterative method as it presents the clearest avenue to directly applying the previously derived receptivity coefficients for Case B and Case I. The governing relation can be approximated in a form such as Eqn. 5.3.

$$A_d^2(R) \approx A_0^2(\omega_{max}, \beta_{max}) e^{2N_{max}} \Delta\omega \Delta\beta \tag{5.3}$$

This approximation is also centered about the most unstable frequency and spanwise wavenumber of the disturbance, and the broadband scaling is approximated by variable spectral bandwidths of the disturbance in the $\Delta\omega$ and $\Delta\beta$ terms. For the analysis in this study the primary second mode disturbance is assumed to be purely two-dimensional in nature. As such, the disturbance amplitude relation can be further simplified by removing the spanwise wavenumber terms. The resulting 2-D amplitude method integral as utilized by Marineau[6] is found in Eqn. 5.4. In this formulation, the integral limits are reduced to a user defined envelope of frequencies encompassing the most unstable disturbance at a given streamwise position.

$$A^2(s) = \int_{f_1}^{f_2} A_0^2(f)e^{2N(s,f)}df \tag{5.4}$$

Following the simplification by suggested by Mack in Eqn. 5.3, the two-dimensional amplitude method relation can be approximated as Eqn. 5.5. Here, C_1 is assumed to be a constant of value 0.48, as Ref. [38] fits this parameter and demonstrates minimal variance among the meanflow cases. These include the cases corresponding to Case B and Case I in this study.

$$A^2(s) = C_1^2 A_0^2(f)e^{2N(s,f)}\Delta f \tag{5.5}$$

Following experimental findings which show that the amplitude at transition is approximately 60% of the maximum breakdown amplitude, the final threshold relation is expressed as a transition N-factor in Eqn. 5.6. Utilizing this threshold N-factor calculation, the transition location can be estimated using a combination of results from LST, DNS, and experimental correlations. The schematic of this process is presented in Fig. 1.7.

$$N_T = ln\left(\frac{1.25A_{max}}{A_0(f_T)}\right) \tag{5.6}$$

Beginning with an initial estimate of the expected transition location, correlations are used to predict both the maximum disturbance amplitude near breakdown as well as the initial amplitude of second mode disturbances in the boundary layer. These values are applied to the final transition N-factor relation in Eqn. 5.6, which when combined with the LST-derived maximum N-factor envelope can be used to iteratively determine the transition location of the flow. The necessary correlations and results of this implementation are discussed and compared with Marineau's results in the following sections.

5.1 Correlations for Marineau's Iterative Amplitude Method

Marineau's[6] iterative process requires the use of several correlations to approximate the freestream noise profile present in the flowfield, the initial amplitude of the second mode disturbance in the boundary layer, the maximum boundary layer disturbance amplitudes near breakdown, and the resulting N-factors near breakdown. These correlations are derived from a combination of LST data, DNS data, and experimental measurements. Following the procedure shown in Fig. 1.7, an initial estimate of the transition location is made from which estimates for the most unstable disturbance frequency, the freestream noise amplitude at the most unstable frequency, as well as the breakdown amplitude are made. Citing prior work by Fedorov and Kozlov[107] and Casper, Beresh, and Schneider[108] it is shown that the maximum breakdown amplitudes of the second mode disturbances can be fitted with the edge mach number of the flow. As this profile changes throughout the flow field, correctly identifying the local edge mach number is critical to applying the breakdown amplitude correlations utilized in the iterative method.

The boundary layer thickness δ_e has traditionally been described using a velocity criterion which stipulates that the boundary layer edge is located where the local velocity reaches 99% that of the freestream. While this is applicable in general to low speed flows, it is not necessarily valid for hypersonic conditions. Instead, a stagnation enthalpy criterion is utilized due to the fact that the stagnation enthalpy is expected to remain constant in the inviscid flow outside of the boundary layer[109]. The boundary layer edge is assumed to be the point at which the stagnation enthalpy of flow reaches 99.5% of the freestream value. The resulting profiles for Case B and Case I are compared against calculated results for corresponding cases from Paredes, et al.[8] and Marineau[6] in Fig. 5.1.

The resulting edge mach number profiles are observed to demonstrate excellent agreement with both Paredes' and Marineau's presented profiles, and as such will be applied to the generalized second mode breakdown amplitude correlation. The final correlation used to calculate the breakdown amplitudes is shown in Fig. 5.2, and relates the maximum second mode amplitudes at breakdown to the local edge mach number of the flow. This breakdown correlation was made using a collection of experimental data, including the original AEDC windtunnel 9 cases from Marineau, et al.[7] that Case B and Case I were originally based on.

Now, a method to approximate the initial amplitudes of the second mode disturbances

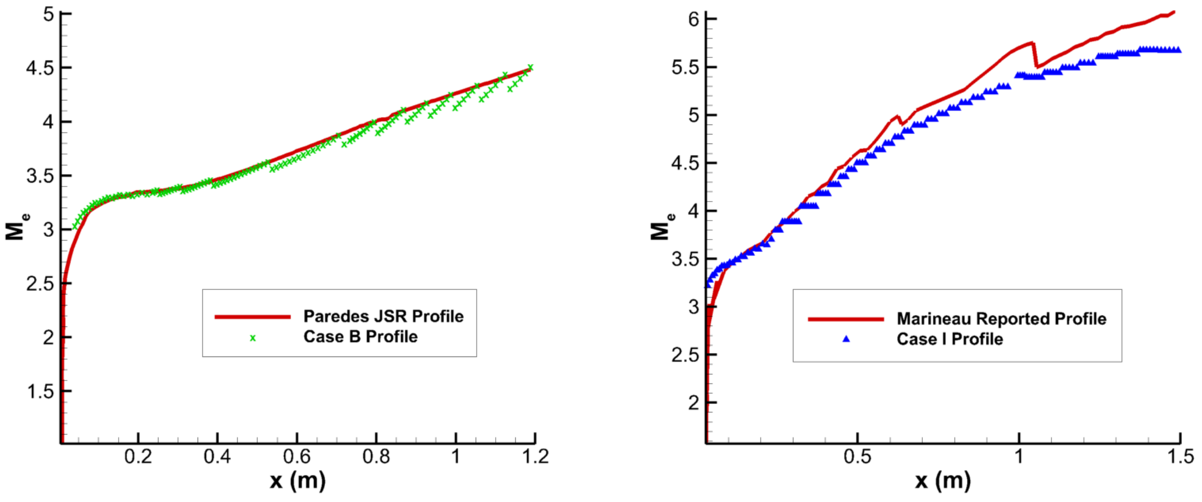

(a) (b)

Figure 5.1: Edge mach number profile using 99% total enthalpy criterion for (a) Case B compared to Paredes, et al.[8] and (b) Case I compared to Marineau[6].

is required. This is done by applying receptivity correlations to estimates or measurements of the freestream noise spectrum present in the flow field. Following the simplifications suggested by Mack[90], the reduced amplitude method integral in Eqn. 5.3 is seen to be centered about the most amplified frequency, followed by a bandwidth parameter assumed to be $\Delta f = f_{max}/4$. Additionally, as these cases are primarily concerned with two-dimensional disturbances, the contribution of the spanwise wavenumber β is disregarded. This maximum second mode frequency can be determined using either an LST or PSE derived stability profile for the given meanflow, along with initial guess of the transition location. The resulting maximum disturbance frequency profiles derived from LST results for both Case B and Case I are depicted in Fig. 5.3.

After this maximum LST frequency is taken from the LST data, it is used to find the amplitude of the incident freestream disturbance at the same frequency. Marineau, et al.[38] provides the approximate freestream noise profile as a corrected fit of pitot pressure measurements from other AEDC windtunnel 9 experiments under similar conditions. This is given in Fig. 5.4.

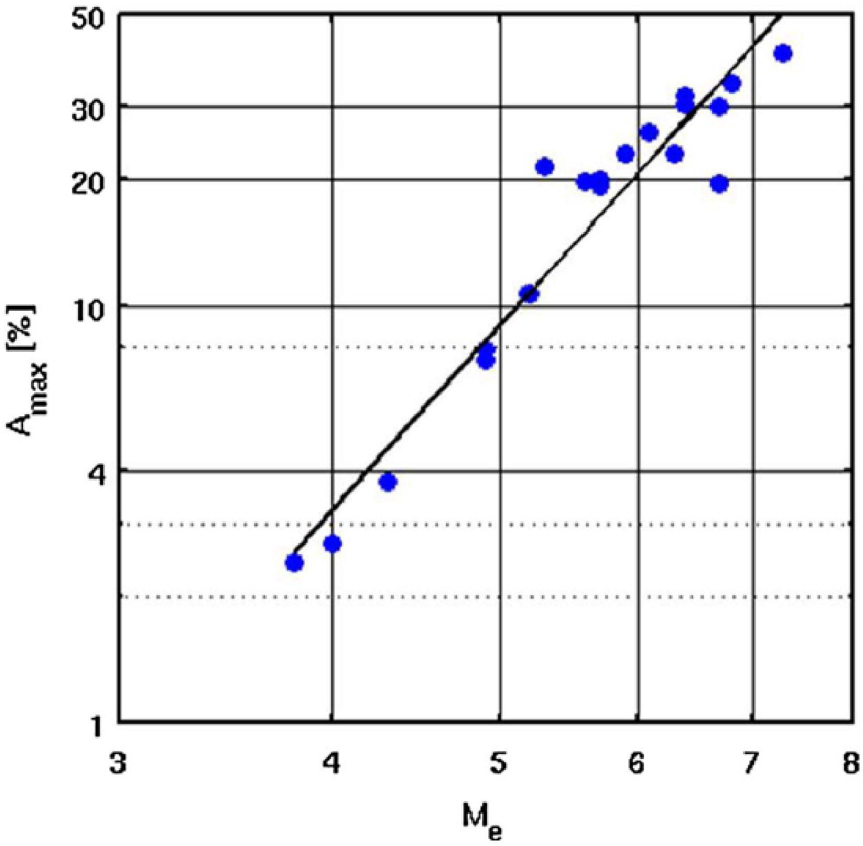

Figure 5.2: Edge mach number vs. maximum breakdown amplitude correlation based on experimentanl data by Marineau[6].

The low frequency disturbances for each case demonstrate excellent agreement with a f^{-1} frequency fit, followed by a $f^{-3.5}$ fit at frequencies higher than approximately 40 kHz. The higher Reynolds number cases demonstrate distortions in this slope, as well as strong noise at higher frequencies. Marineau[38] attributes these to increased noise sensitivity due to higher mach number, as well as acoustic wave reflection between the probe and the local shock. As such, following procedures made by Marineau[6] and Balakumar and Chou[62] the freestream noise is approximated using a linear fit. The freestream noise amplitude, referred to as γ_0, at the maximum disturbance frequency is given in Eqn. 5.7.

$$\gamma_0 = 2\sqrt{C\Delta f(f_{max})^{-3.5}} \tag{5.7}$$

The γ_0 term is the incident amplitude of the freestream disturbance, $C = 126.5E6$

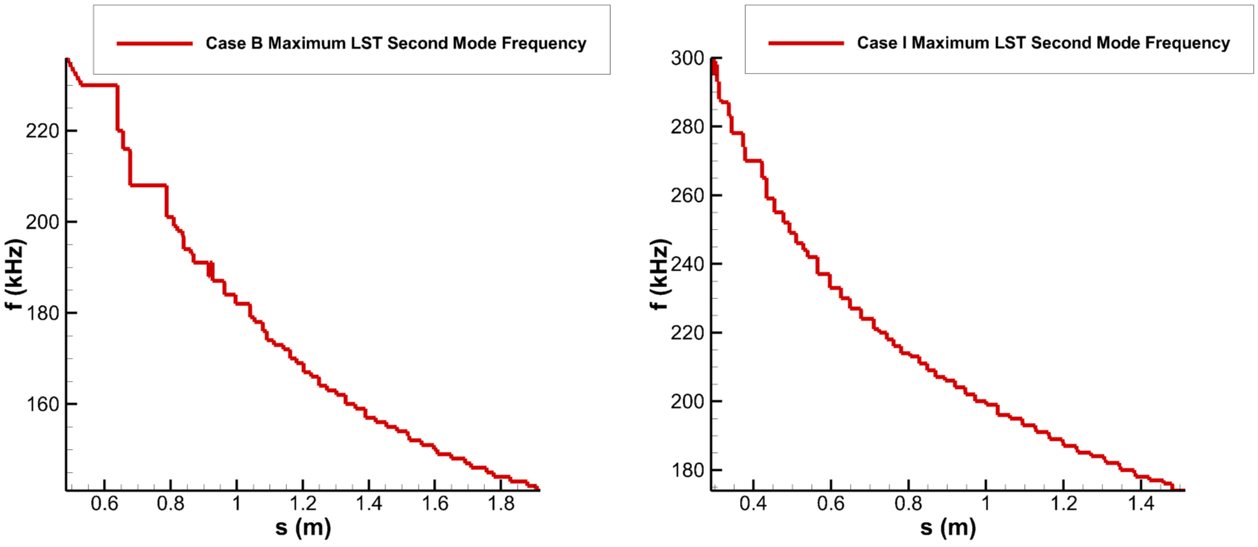

(a)

(b)

Figure 5.3: Maximum LST second mode frequency vs. streamwise location for (a) Case B and (b) Case I.

is a linear fit parameter, Δf is the second mode frequency bandwidth parameter that is fixed at $f_{max}/4$, and f_{max} is the maximum second mode frequency at the given streamwise location taken from the LST profile. The receptivity magnitude coefficients are simply defined as the disturbance amplitude response at a given frequency normalized by the freestream disturbance level. Therefore, following the same procedures as Marineau[6] the total initial amplitude at the local maximum disturbance frequency is simply defined as $A_0(fmax) = C_{rec}(f_{max})\gamma_0$.

Finally, the total maximum N-factor envelope is necessary in order to iterate on and refine the initial estimate of the transition location. The resulting LST derived N-factor envelopes are shown in Fig. 5.5 for both the Case B and Case I meanflows. As discussed previously, the N-factor for Case I is shown to be significantly larger than that of Case B throughout the cone domains. At the end of the cones Case I has a peak N-factor of approximately 14.6 while Case B peaks at an N-factor of 9.3. This is in spite of the reduced streamwise length of the domain for Case I, further emphasizing the increased dominance of the second mode instability in Case I. Both of these profiles were shown previously in Fig. 4.9b for Case B

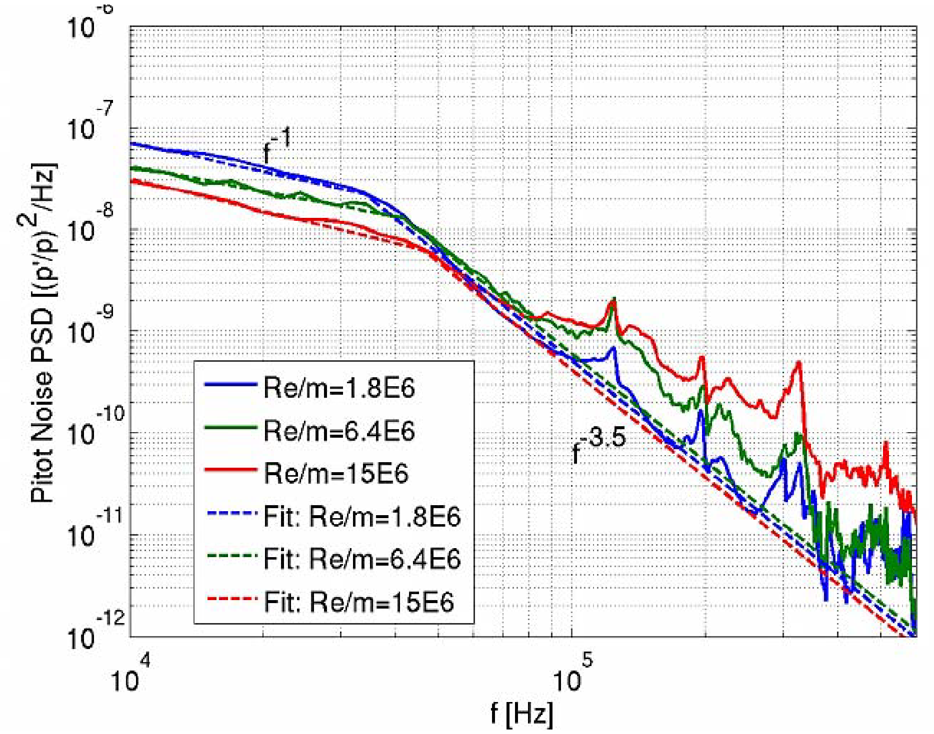

Figure 5.4: Normalized pitot pressure noise measurements for freestream disturbances as reported by Marineau, et al.[6].

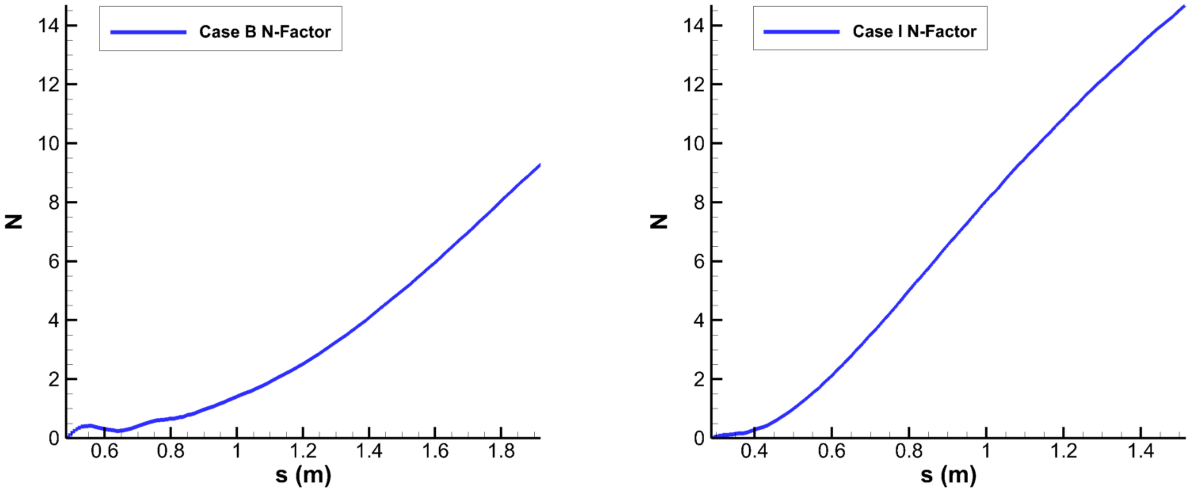

(a)

(b)

Figure 5.5: Maximum LST N-factor vs. streamwise location for (a) Case B and (b) Case I.

and Fig. 4.12b for Case I to agree well with Marineau's results.

5.2 Iterative Amplitude Method Results

Following the methodology and correlations discussed previously, the transition location of Case I and Case B can be estimated using receptivity field data for each of the canonical disturbance types in the freestream. The finite pulse results are not utilized as the isolated nose forcing is not expected to as accurately replicate the extensive noise profile present in a windtunnel test environment. First an initial estimate is made of the transition location. Using this initial guess the local maximum second mode frequency as well as edge mach number are calculated from LST and DNS data. From these values the local second mode breakdown amplitude as well as freestream noise amplitude are estimated using correlations. Receptivity coefficient data is combined with the freestream noise correlations to generate initial second mode amplitudes, which are used in concert with the breakdown amplitude estimates to calculate the local transition N-factor. Using the N-factor envelope taken from LST, this value is used to identify an updated guess for the transition location which is iterated upon in the same manner until convergence.

The predicted transition locations using the iterative method described previously are plotted for Cases B5 through Case B8 in Fig. 5.6. As the receptivity coefficients were observed to have significantly variable results between the sampling points for the planar pulses, the receptivity spectra between the branch I and branch II sampling points were utilized here. The branch II sampling point receptivity data is also fairly representative of the intermediate sampling point, as shown previously. An error bar for the uncertainty in the experimentally measured transition location is centered on Marineau's results in the figure. This error is derived from the limited distribution of pressure transducers in the original experiment[7]. The Case B results demonstrate significant divergence from Marineau's reported experimental and numerical transition result, and for the most part lie outside of the reported uncertainty region. On average this ranges for 60% to 30% error for the branch I results, while the branch II results range from approximately 60% to 40% error. In both

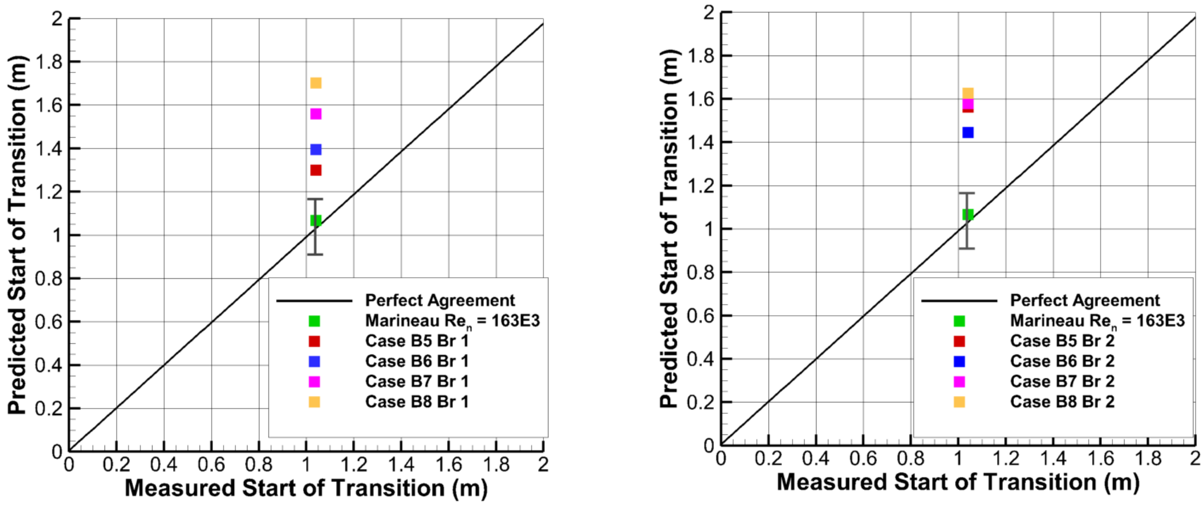

(a) (b)

Figure 5.6: Predicted transition locations vs. measured results for Cases B5 through B8: (a) branch I sampled receptivity data and (b) branch II sampled receptivity data.

cases the acoustic pulse data converges most readily towards the experimental result, with the fast acoustic pulse complying the best in the branch I results and the slow acoustic results complying the best for the branch II data.

Similar transition location results are plotted for Case I5 through I8 in Fig. 5.7. Marineau's results are again plotted with an error bar in gray, with the same error range. This is again due to the limited pressure transducer distribution, which was kept equal between the different test cones. It can be observed that the agreement for the Case I transition location is significantly better than it was in Case B. Looking at the branch I results in Fig. 5.7a each of the data points lies in the uncertainty range. The errors here range from approximately 21% for the vorticity pulse to 12% for the fast acoustic pulse. The branch II results in Fig. 5.7b diverge more from the measured transition position, with only the slow acoustic pulse result falling within the uncertainty range. Here, the error ranges from approximately 39% for the temperature pulse to 17% for the planar slow acoustic pulse. Similar to Case B, the acoustic pulses see the best agreement. This is likely attributed to the greater second mode receptivity response observed for the acoustic pulses in both Case B and Case I, as the higher

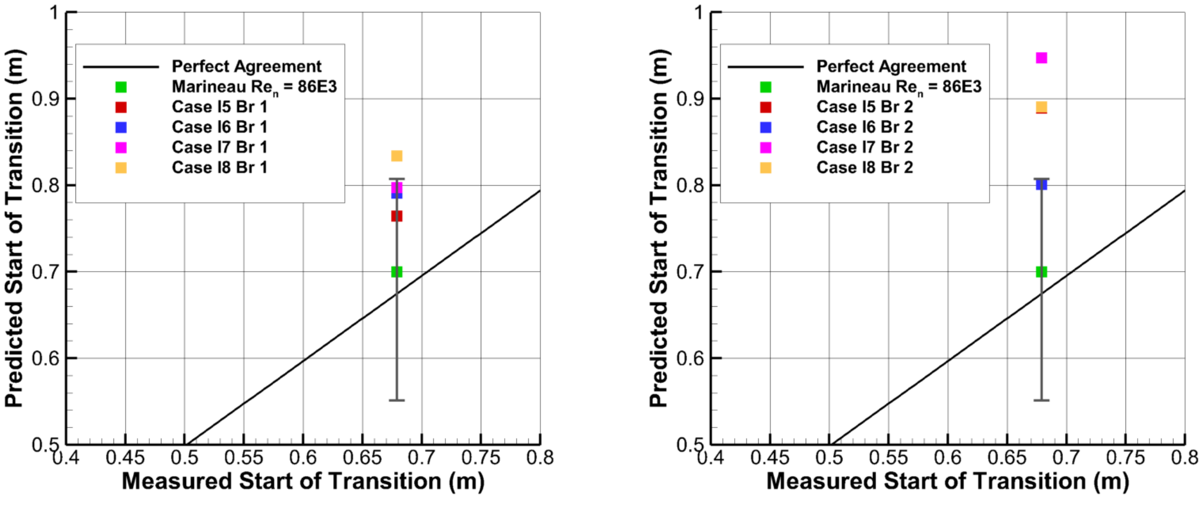

(a) (b)

Figure 5.7: Predicted transition locations vs. measured results for Cases I5 through I8: (a) branch I sampled receptivity data and (b) branch II sampled receptivity data.

receptivity coefficients result in larger initial amplitudes at a given streamwise position. The worst of the results here for the Case I results are comparable in error to the conventional constant N-factor criterion used for the e^N method, which Marineau found to have errors of approximately 40% for his test cases. Additionally, the most accurate results demonstrate similar levels of error to the average amplitude method error Marineau himself found, which was reported as approximately 14%. This indicates that the amplitude method, even in this highly simplified form based on empirical approximations, is capable of improving on currently established practices.

Figure 5.8 similarly shows the transition point N-factor predicted by the iterative method vs. the calculated N-factor at the measured transition location for Case B using both branch I and branch II receptivity data. The predicted N-factor is taken from the N-factor envelopes in Fig. 5.5 at the converged transition location guess. The uncertainty here is taken from Marineau, et al's[7] result and is also based on the uncertainty in the measured transition location due to pressure sensor placement. Again, significant disagreement is observed for every disturbance type, though the acoustic disturbances are closest to the measured re-

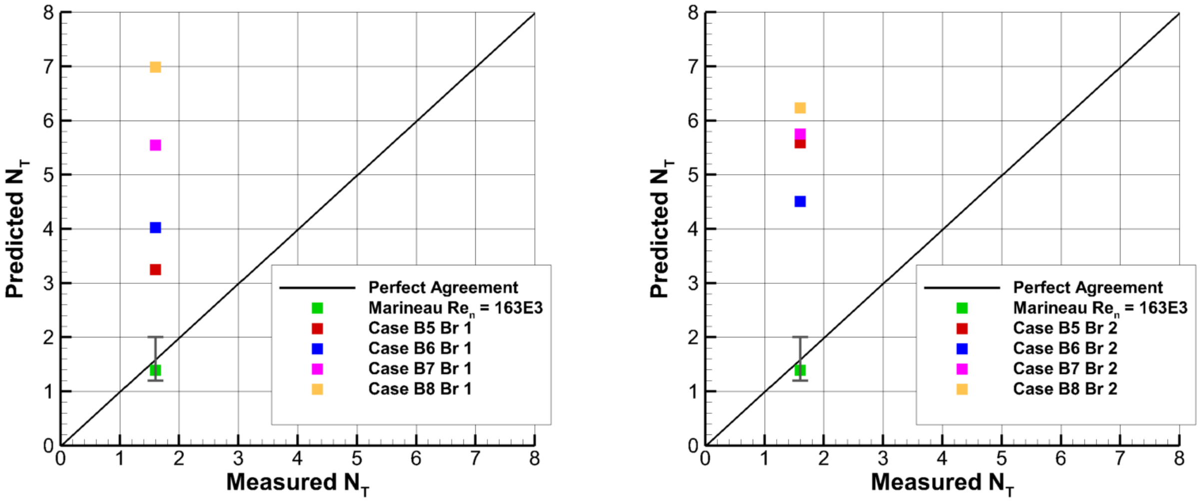

(a) (b)

Figure 5.8: Predicted transition N-factors vs. measured results for Cases B5 through B8: (a) branch I sampled receptivity data and (b) branch II sampled receptivity data.

sults for both the branch I and branch II data. Qualitatively, the accuracy of the transition N-factor is much worse than the transition location results. This is directly related to the disagreement in the prior transition location results, as the overprediction of transition location directly causes overprediction in the transition N-factor due to the monotonicity of the N-factor profile for Case B in Fig. 5.5a. This may be partially explained by the relatively weak second mode amplification observed in Case B, and it's respective experimental counterpart in Marineau, et al.'s[7] work.

The transition N-factors for Case I are presented in Fig. 5.9. Again, Case I adheres more closely to the experimental result due to the stronger second mode response. The overprediction of transition location for Case I also uniformly results in overprediction for the transition N-factor as well since the N-factor curves in Fig. 5.5 increase monotonically for both meanflows. The branch I results in particular are closest to both the experimental transition location and transition N-factor in both Case B and Case I. This is due to the overall larger receptivity coefficient from the branch I sampling spectra. While the transition N-factor results here massively overpredict the experimental N-factors reported by Marineau, they remain within the expected range of transition N-factors for the AEDC windtunnel which have generally ranged between 4 to 7 according to prior data[6].

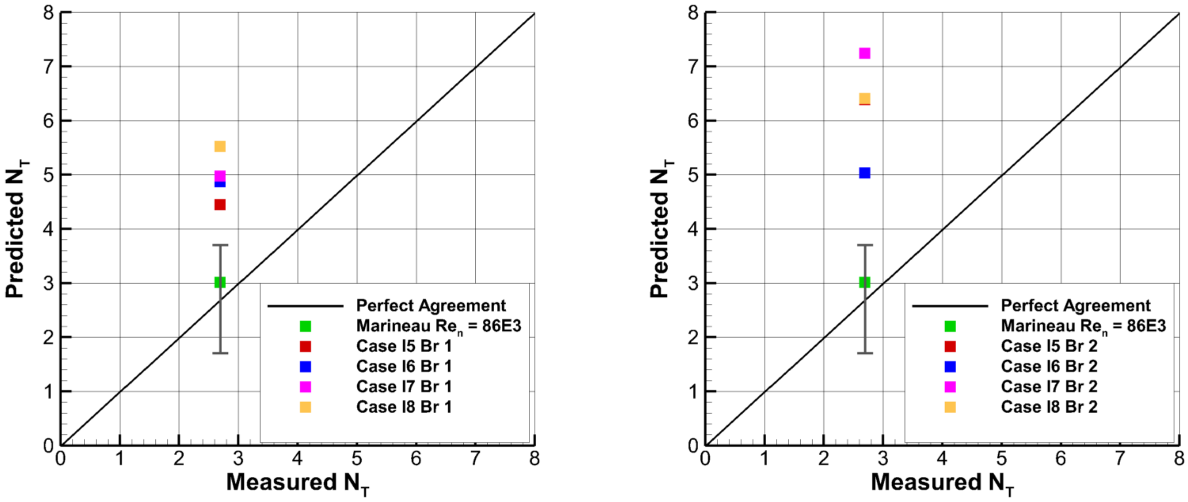

(a) (b)

Figure 5.9: Predicted transition N-factors vs. measured results for Cases I5 through I8: (a) branch I sampled receptivity data and (b) branch II sampled receptivity data.

The general disparity between the computed results here and Marineau's measured result can be attributed directly to the disparity in the initial input receptivity coefficients. In particular, the receptivity coefficients calculated in Section seem to underpredict the receptivity coefficients of the optimal disturbance Marineau[6] utilized. For Marineau's Run 3752, which corresponds to Case B, Marineau reported a peak receptivity coefficient of approximately 3.7. For Run 3746, which corresponds to Case I, he saw a slightly lower peak receptivity coefficient of 2.85. These were calculated by solving Eqn. 5.6 for $A_0(f_T)$. At the experimental transition location, experimental correlations were used to determine the maximum breakdown amplitude A_{max} while the N-factor at this location was calculated through stability theory. The results from Section show the peak Case B planar pulse receptivity coefficients were found to be approximately 1.2 for the most amplified frequency at the branch I sampling point. At the same conditions for Case I the peak coefficient was found to be approximately 1.9, which again corresponded to the fast acoustic disturbance. The lower receptivity coefficients from this study signify reduced boundary layer disturbance responses, and subsequently lower amplitude initial disturbances in the boundary layer. These require additional amplification before they reach the experimental breakdown amplitudes and trigger transition. This, in turn, pushes the expected transition location further downstream and increases the expected N-factor at transition, which explains the large overprediction of both transition location and transition N-factor demonstrated in the results here.

The question now remains, what is the source of this large disparity in the receptivity coefficients? This can be associated with a number of factors. The meanflow cases studied here were defined by Marineau as having significant nose bluntnesses. In particular, the 9.525 mm nose radius cone in Case B was shown experimentally to have significantly weakened transition delaying effect relative to its nose bluntness, though it did not fully demonstrate the transition reversal phenomenon that was observed in some even blunter cones[7]. Additionally, while the second mode was found to still be significant in this case, it was significantly weakened by the large nose bluntness. This reduced dominance of the second mode instability may allow for other potential sources of instability, such as transient growth effects or roughness caused by surface imperfections, that were not accounted for in our receptivity simulations to impact the boundary layer instabilities in the experimental case. Additionally, Marineau's receptivity coefficients were not calculated directly from individual case data and were instead found using correlations of his experimental data. As such, they may not accurately reflect the true receptivity response of the flow field for each of the cases considered here.

Additionally, uncertainties exist with the general freestream profile which can be critical to correclty determining the receptivity response of the flow. The freestream noise profile, presented as normalized pitot tube measurements in Fig. 5.4, was not directly measured for the investigated cases and were instead based upon measurements for similar freestream Reynolds numbers cases from prior experiments[38, 110], which leads to some uncertainty in the actual freestream conditions of the experiment. Furthermore it was shown in the receptivity investigation of Case B and Case I that the type of the incident disturbances can have dramatic differences on the overall receptivity behavior, both in terms of the peak magnitudes of the boundary layer disturbances as well as the disturbance bands that are excited. While the data provided here gives a distribution of environmental pressure disturbance amplitudes, it does not depict the types of disturbances present in the experimental environment. Previous work has shown that acoustic radiation from turbulent wall boundary layers likely dominates these flow fields[89, 68], though more thorough characterization of the environment through both experimental measurements and simmulations is critical to the correct application of the receptivity coefficient data presented here. The phase coherence of the incident pulse disturbances used to generate the receptivity coefficients may also play a significant role. As discussed in the introduction recent work by Egorov, et al[76] has shown that the receptivity response over flat plates can be highly dependent on the coherence of the forcing. In particular, they showed that incoherent forcing with randomized disturbance phases can result in much stronger disturbance growth in the boundary layer due to the lack of interference effects. This may partially explain the reduced receptivity coefficient found in the axisymmetric analysis for Case B and Case I, as the noise present in the experimental environment is likely highly incoherent in nature. However, these findings are fairly novel and have not been confirmed over a wide range of conditions, and as such require additional study to confirm. This is especially true in the more complex flow environment present over a blunt cone.

CHAPTER 6

Receptivity Analysis of Azimuthally Varying Acoustic Pulse Disturbances in Case S

The prior receptivity analysis for the 9.525 mm nose radius cone in Case B and the 5.08 mm nose radius cone in Case I were focused on the excitation of the second mode disturbance, which has been shown to be dominant in a variety of hypersonic flight conditions. The second mode is a simple two-dimensional disturbance, and as such the prior analysis is not concerned with the presence of azimuthally varying, oblique disturbances. However, due to the nature of flight and tunnel conditions, external flow conditions are often not confined to be perfectly two-dimensional. For example, the freestream noise present in a conventional hypersonic or supersonic windtunnel primarily consists of acoustic radiation emanating from the walls of the windtunnel. Depending on the flow conditions, this acoustic noise can radiate from the walls at angles of incidence, generating obique wavefronts that impact the body of interest[111, 89]. Thus, even in experimental environments without explicitly imposed obilque perturbations or angle of attack, natural oblique disturbances can exist. Particulate impacts from atmospheric dust or other detritus can also induce highly localized perturbations with inherent oblique mode content[107, 46]. Additionally, the actual nonlinear breakdown of a boundary layer into turbulence can be highly dependent on excited oblique mode disturbances as well[77, 5, 85]. As such future considerations of oblique instabilities will be necessary to complete the characterization of the receptivity processes in hypersonic flows.

The following analysis presents preliminary results investigating the receptivity of a small bluntness 1.0 mm nose radius cone, labelled as Case S in Table 1.1, to planar acoustic pulses with added azimuthal variation. This azimuthal variation ensures the excitation a number of oblique modes with non-zero azimuthal wavenumbers in the boundary layer. Due to the exceptional computational cost associated with simulating the 3D flow environments necessary to capture these oblique modes, the total flow domain has been dramatically shortened to a length of 0.5 m. The unsteady cases consist of freestream fast acoustic and slow acoustic pulses. To start with, planar axisymmetric pulses are studied order to compare directly to similar data for Case B and Case I. What follows afterwards are unsteady DNS using azimuthally varying pulses described in Section 3.3.2 which were tuned to primarily excite a small number of lower azimuthal modes.

6.1 Case S Meanflow Results

The axisymmetric Case S meanflow is calculated in the same manner as the Case B and Case I meanflows, utilizing the same shock fitting algorithm as discussed in Section 3.1. Again, the streamwise grid density was chosen from prior experience to ensure sufficient resolution to capture the disturbance modes of interest in both LST and unsteady DNS analysis. This ranged from a streamwise grid distribution of approximately 30 points per mm upstream on the cone to 5 points per mm near the end of the domain. In total, this resulted in 3188 points in the streamwise direction to resolve the cone up to a length of 0.5 m. In order to resolve the boundary layer and general shock layer, 240 points were utilized for the wall normal direction. Exponential grid stretching was again used to concentrate points near the surface of the cone to ensure sufficient resolution for the boundary layer. The meanflow is initially converged using $K = 4$ total points in the azimuthal direction, though only two are ever directly calculated, as symmetry conditions and a spectral method are utilized in the azimuthal direction. After the base axisymmetric/2-D meanflow is converged it can be easily refined in the azimuthal direction using symmetry. The 2-D meanflow contours for both temperature and pressure are shown in Fig. 6.1 both near the nose region of the cone as well as throughout the downstream domain.

Similar to previous results for Case B in Fig. 4.1 and Case I in Fig. 4.4 the most extensive gradients for both temperature and pressure are concentrated near the nose region of the

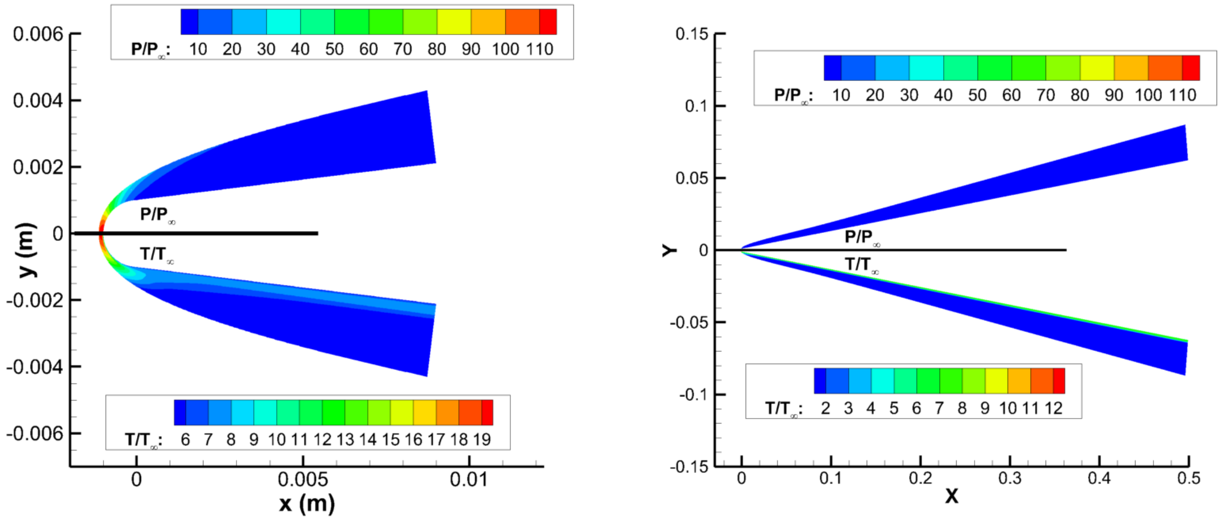

(a) (b)

Figure 6.1: Meanflow pressure (top) and temperature (bot) contours for Case S: (a) near the nose and early frustum of the cone (b) total streamwise length.

cone. This is due to the strong bow shock that forms off the surface of the cone in this region. We also see a more extensive temperature gradient emerging from the nose and propagating downstream along the cone, which is representative of the formation of an entropy layer that forms due to the changing curvature of the local bow shock. Due to the significantly reduced bluntness of the cone in Case S, this entropy layer is swallowed much further upstream on the cone. This can be observed in the boundary layer profiles of both velocity and temperature at different streamwise locations shown in Fig. 6.2.

Again, the boundary layer profiles demonstrate the same general behaviors as expected from prior meanflow data. While the boundary layer does experience growth as the sampling position moves further and further downstream, this variation is extremely weak. Additionally the temperature profile, which is representative of the entropy layer, demonstrates a thicker profile at the most upstream sampled positions on the cone. The thickness of the entropy layer is seen to converge towards and become ”swallowed” by the boundary layer at approximately $s^* = 0.0338m$, approximately 30 nose radii downstream on the cone. This is significantly farther upstream than both Case B and Case I and reflects the weakened nose

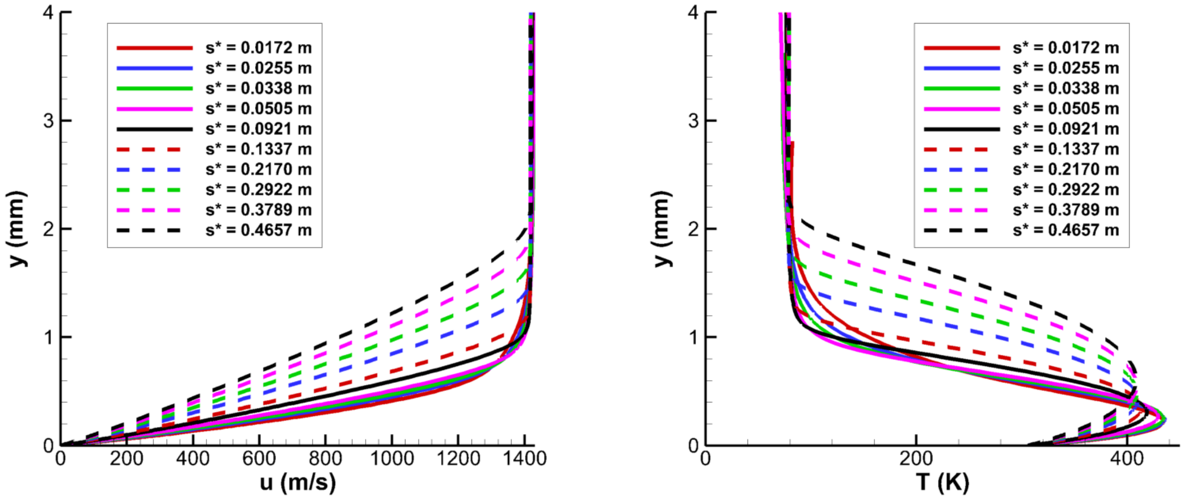

(a) (b)

Figure 6.2: Case S boundary layer profiles at different streamwise positions for (a) streamwise velocity and (b) temperature.

bluntness effects through the flow.

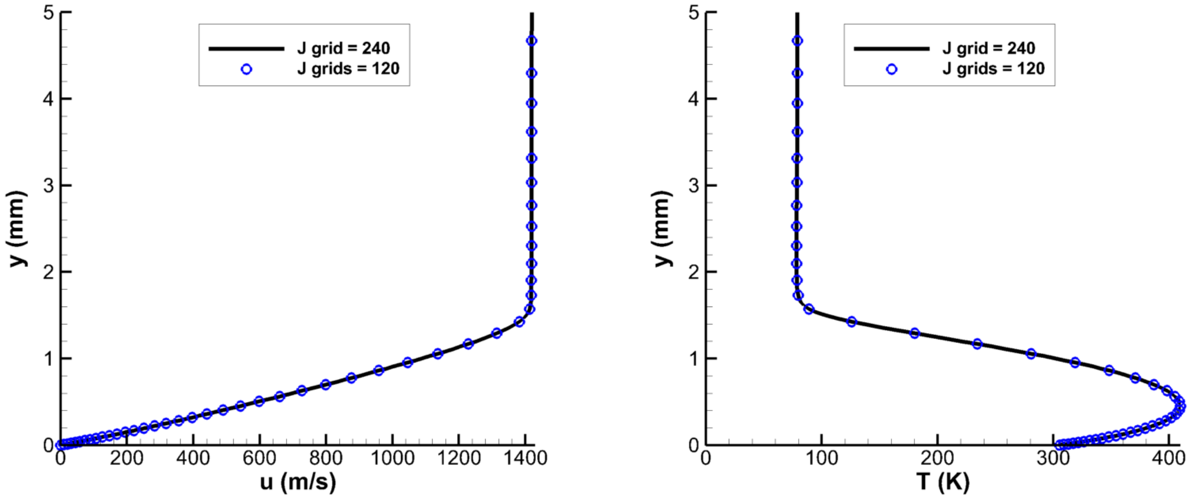

(a) (b)

Figure 6.3: Case S grid convergence comparison of wall normal (a) U velocity and (b) T temperature profiles at $\mathbf{s^* = 0.248}$ m.

The grid convergence of the basic Case S meanflow is confirmed using the sample profiles shown in Fig. 6.3, where the velocity and temperature profiles at a streamwise position of $s^* = 0.248$ m are plotted for the basic 240 point and a halved wall normal grid are shown. The excellent agreement between the two results indicates sufficient meanflow convergence.

6.2 Case S LST Results

LST analysis was performed to identify the primary second mode instability, which is used to compare to prior results in Case B and Case I. The phase speed and growthrate of a discrete 300 kHz disturbance are presented in Fig. 6.4. The phase speed results demonstrate that the mode F disturbance becomes supersonic far upstream on the cone at this streamwise location. The growthrates show that after synchronization the discete mode S is expected to destabilize into the primary second mode instability. The synchronization location is denoted in the data near a streamwise position of $s^* = 0.15m$ by localized crossings of the mode F and mode S disturbances in the phase speed plot. This is also reflected in the rapid destabilization of the mode S growthrate, as well as fluctuations in the stable mode F disturbance. Noticeable oscillations in the phase speed plot and growth rate plots near $s^* = 0.11$ m are indicative of the local synchronization of the discrete mode F disturbance with the continuous entropy and vorticity spectrum.

The LST growth rate contours as well as the neutral stability curve for Case S are plotted in Fig. 6.5 at two different contour levels. The contour levels in Fig. 6.5b are equalized with the growth rates for Case B in Fig. 4.7 and Case I in Fig. 4.10 for comparison. The average dimensional growth rates for Case S are found to significantly exceed those of Case I and Case B, with the peak growth rate being approximately 100% higher in Case S than in Case B. Additionally, second mode destabilization is observed to occur much further upstream in Case S. This further corroborates the stabilizing nature of nose bluntness on the second mode instability.

One thing of note is the location of the peak dimensional growth rates in the neutral stability contour. In general, and also as seen in Case B and Case I, the growth rates are expected to peak at the lowest second mode frequencies near the end of the domain.

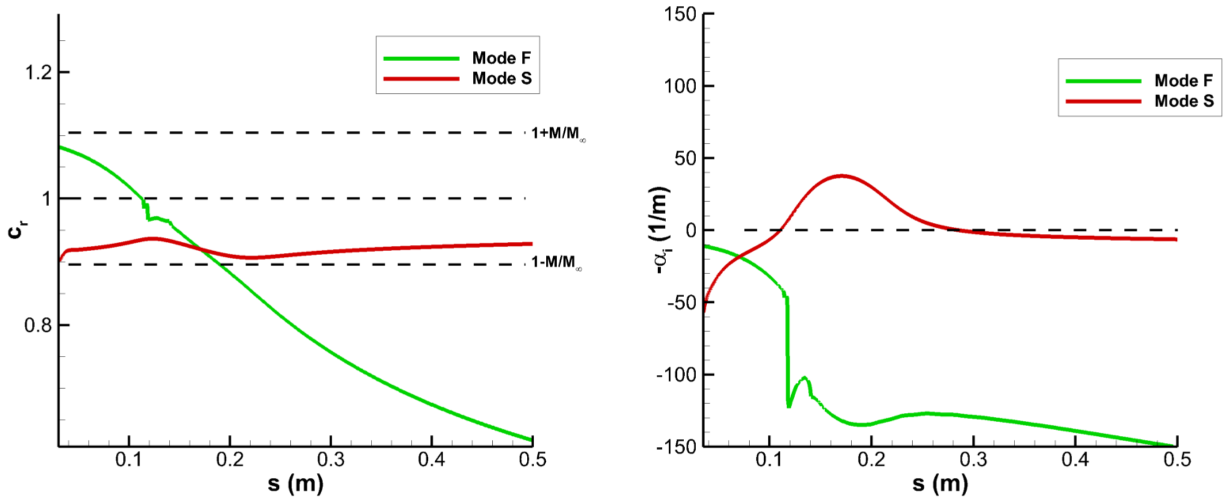

(a)

(b)

Figure 6.4: (a) LST phase speed and (b) LST growth rates for Case S discrete mode F and mode S disturbances at 300 kHz.

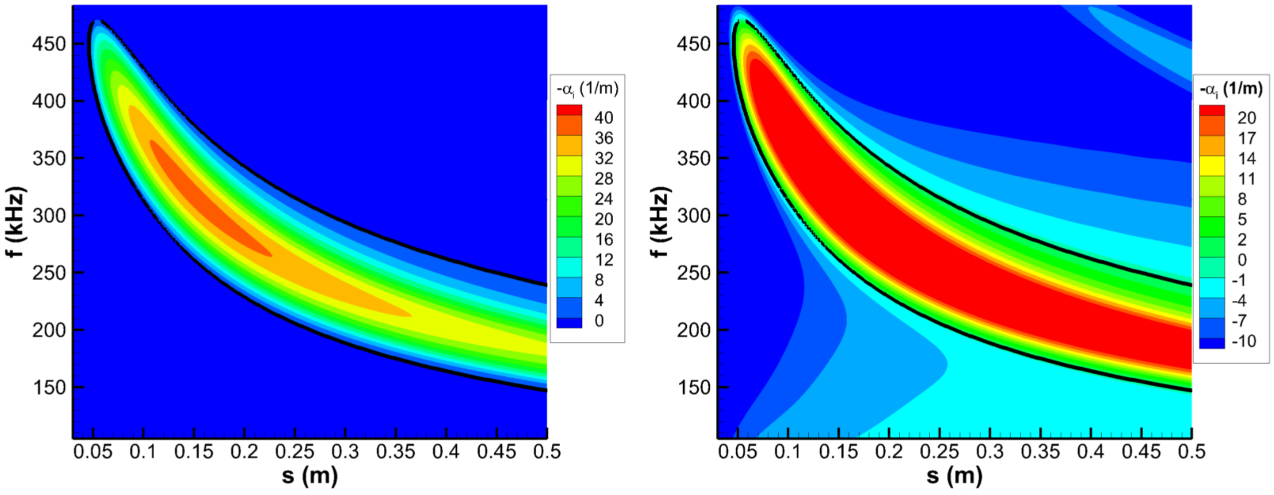

(a)

(b)

Figure 6.5: LST growthrate contours with neutral stability curves outlined in black for (a) dimensional growthrate showing peak growthrate and (b) dimensional growth rate at contour levels to compare with Case B and Case I.

In fig. 6.5a however, the dimensional growth rate is shown to peak upstream near the highest frequencies. This is only observed in the dimensionalized growth rates though, as the nondimensional contour in Fig. 6.6 demonstrates the expected profile. This is because the boundary layer lengthscale parameter used to dimensionalize the growthrate L^*, as defined in Eqn. 3.23, for Case S increases more quickly than the nondimensional growthrate itself. This may be due to the lower unit Reynolds number of the flow somewhat weakening the development of the second mode.

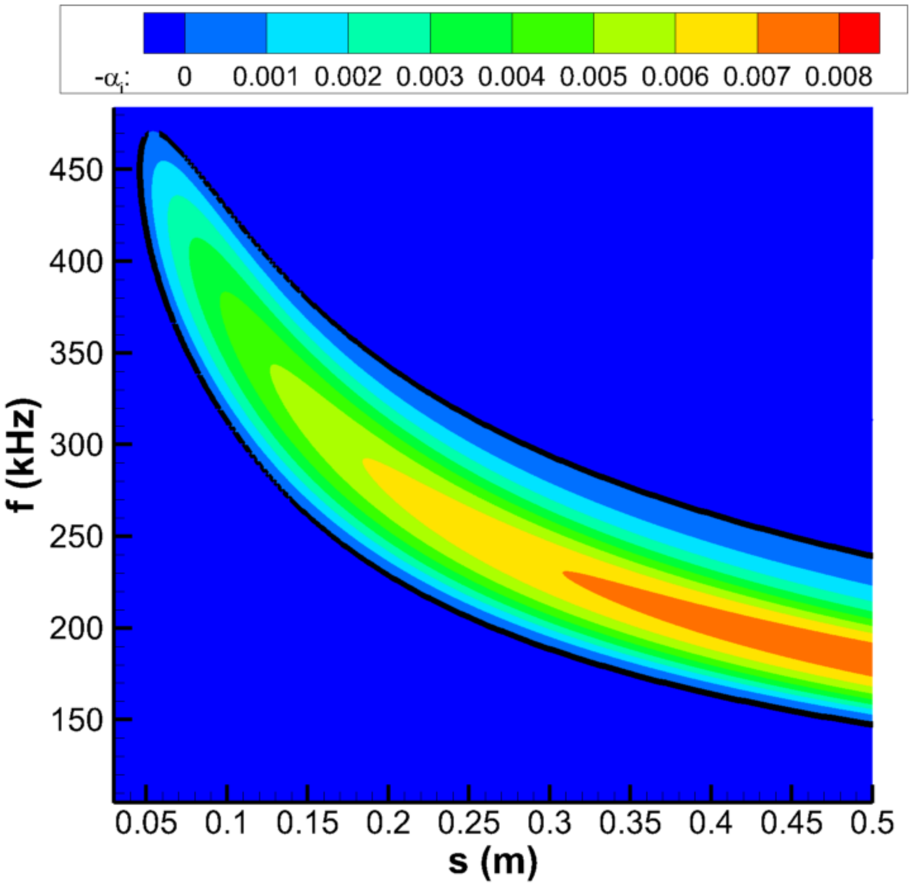

Figure 6.6: Nondimensional growthrate contour with neutral stability curve outlined in black.

A selection of discrete frequency N-factor curves are plotted in Fig. 6.7, along with the total N-factor profile in black. The N-factor is shown to peak at approximately 5.7 at the end of the cone, which is significantly lower than the peak downstream values for both Case B and Case I which peaked at N-factors of approximately 9.3 and 14.6 respectively in Fig. 5.5. This is again likely due to the lower freestream unit Reynolds number as well as the reduced streamwise domain length hindering the development of more readily amplified lower frequency disturbances.

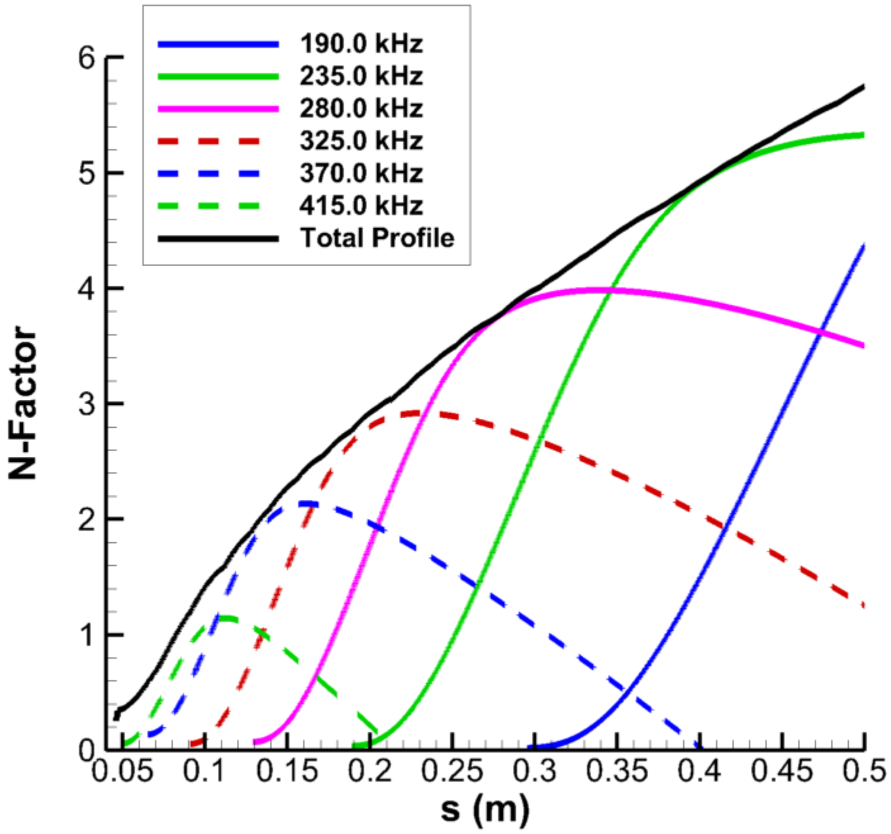

Figure 6.7: Case S total N-factor profile and N-factor curves for a selection of disturbance frequencies.

In general, while the peak growth rates are shown to be significantly stronger for Case S than the other cases, the limited streamwise domain length prevents the development of more readily amplified lower frequency disturbances. This, along with the weakening effect of the lower freestream unit Reynolds number, reduces the maximum estimated N-factor profile of the flow. Additionally, the lower nose bluntness is observed to shift the second mode mode to higher frequencies. This is because the reduced nose bluntness results in thinner boundary layers which are more conducive to higher frequency disturbances.

6.3 Case S Unsteady Results

The results of the unsteady DNS analysis are presented in the following sections. The Case S meanflow is perturbed utilizing a selection of fast and slow acoustic disturbances, including both axisymmetric planar disturbances in the vein of Section 3.3 as well as the azimuthally varying 3-D pulses described in Section 3.3.2. Similar to Case I, the planar pulse disturbances in the freestream were fixed with a maximum non-dimensional amplitude of $\epsilon M_\infty = 1.0E-8$ in order to ensure the linear development of boundary layer disturbances. The azimuthal disturbances are defined using the conditions prescribed in Table. 3.2. It was elected to focus only on the acoustic pulse disturbances due to the significant broadband content observed for the planar fast acoustic pulse cases in both Case B5 and Case I5, and the fact that the temperature and vorticity pulses demonstrated close qualititative similarities to the slow acoustic pulse in the majority of prior cases.

6.3.1 Receptivity to Axisymmetric Pulses

The receptivity response to the axisymmetric planar fast and slow acoustic disturbances are investigated in order to directly compare the baseline receptivity response of Case S to the prior two cone meanflows. Beginning in Fig. 6.8 are pressure snapshots of the shock layer near the end of the cone for the planar fast acoustic pulse. Fig. 6.8a again demonstrates the particular local pressure disturbance front that results from shock-disturbance interactions of the planar pulse with the shock. This can be seen at $x = 0.44$ m, and is very similar to what was observed in Case I. Namely, a significant pulse front is excited at the local intersection of the planar fast acoustic pulse and the shock, but the induced disturbances aren't as strong or widely distributed throughout the shock layer as they are in Case B5. This is likely because the second mode disturbances have been sufficiently amplified to overshadow weaker perturbations in the rest of the shock layer.

The trailing second mode wavepacket is also depicted in Fig. 6.8b showing the expected banded structure. It should be noted that the characteristic acoustic radiation of the supersonic mode is also just barely visible here, but its extreme weakness and the destabilized

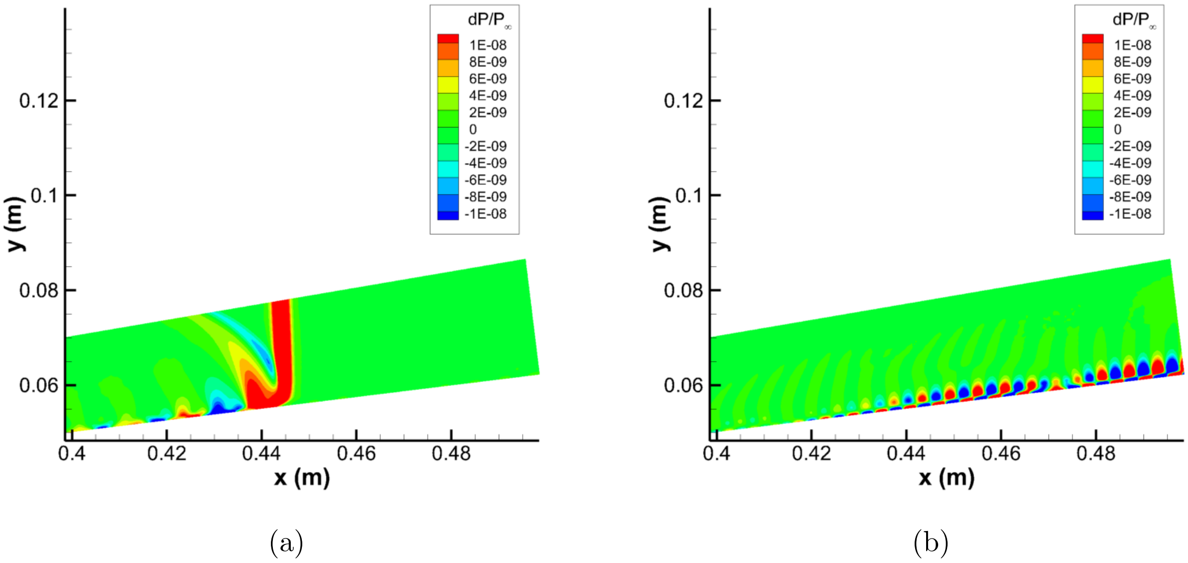

Figure 6.8: Time snapshots of pressure disturbances near the end of the domain for the planar fast acoustic pulse in Case S: (a) pulse front from local shock-disturbance interaction and (b) primary second mode wavepacket.

discrete mode F suggest that this is merely transient excitation from the local unsteady pulse and not evidence of an amplifying supersonic mode. Also of note is the distinct dip in the boundary layer perturbation amplitude observed at $x = 0.475$ m in Fig. 6.8b which is indicative of strong wavepacket interference. This interference occurs due to wave dispersion effects causing disturbances of differing frequencies to propagate at different phase speeds, which may lead to local constructive amplification or destructive dampening as seen here[102].

Similar temperature snapshots for the fast acoustic disturbance in Case S are shown in Fig. 6.9. The pulse front depicted in Fig. 6.9a demonstrates temperature disturbances propagating throughout the shock layer in a similar manner to the acoustic perturbations in Fig. 6.8a, though the relative amplitude of the temperature disturbances are much weaker. This shows that the planar fast acoustic pulse also introduces a wide variety of forcing waves, including acoustic as well as entropy disturbances, into the shock layer as it propagates. However, the excited acoustic front is much stronger relative to the boundary layer modes.

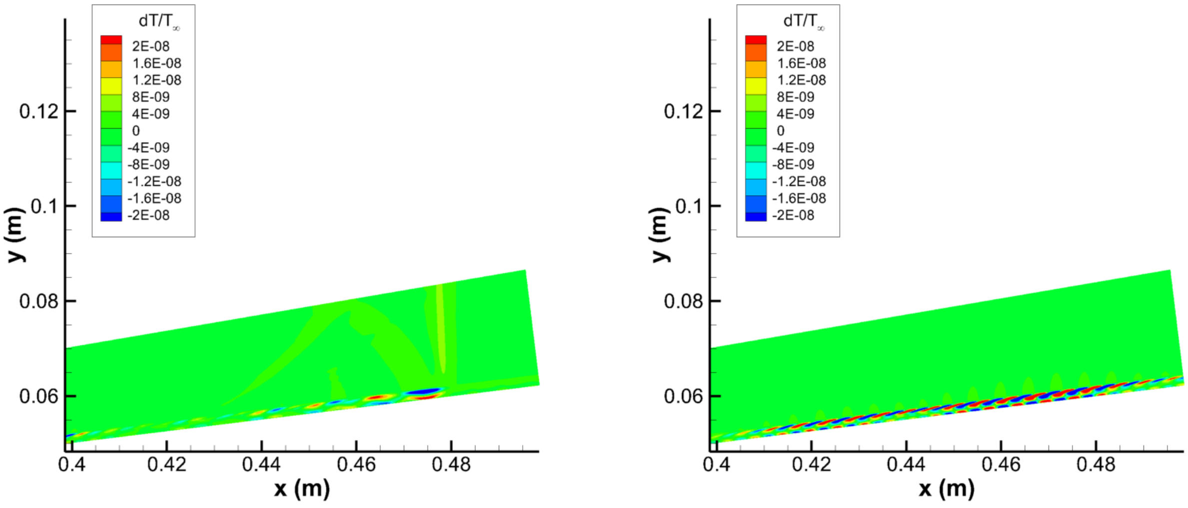

(a) (b)

Figure 6.9: Time snapshots of temperature disturbances near the end of the domain for the planar fast acoustic pulse in Case S: (a) pulse front from local shock-disturbance interaction and (b) primary second mode wavepacket.

The characteristic ropelike patterns in Fig. 6.9b further corroborate the dominance of the second mode instability. Furthermore, localized decreases in the temperature perturbation amplitudes near $x = 0.44$ m and $x = 0.49$ m also demonstrate the localized interference effects discussed previously.

A set of similar unsteady pressure and temperature snapshots are presented for the planar slow acoustic pulse case in Fig. 6.10. Contrary to the fast acoustic pulse, the planar slow acoustic pulse front appears near the trailing primary wavepacket in Fig. 6.10a near $x = 0.48$ m. This is due to the slower propagation speed of the slow acoustic pulse in the freestream. Additionally, while the pulse front here is visible near the local shock-disturbance interaction it does not propagate as strongly towards the wallbound disturbance wavepacket, seemingly interfering only with these modes slightly at the edge of the boundary layer. The temperature disturbances also demonstrate the same ropelike structures as the planar fast acoustic pulse, albeit at a higher amplitude. This indicates the stronger second mode receptivity to the slow acoustic disturbance for the planar pulse that was also found for Case B and Case I.

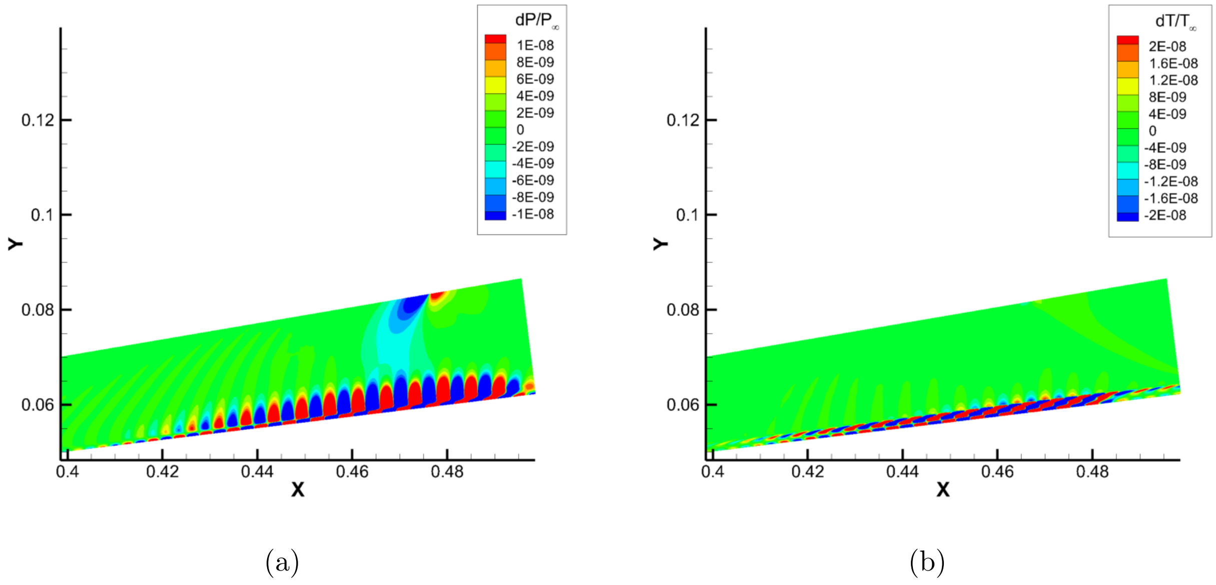

(a) (b)

Figure 6.10: Time snapshots of (a) pressure and (b) temperature disturbances near the end of the domain for planar slow acoustic pulse in Case S.

The acoustic pulse front in Fig. 6.10 is somewhat unexpected here, as similar fronts were not strongly exhibited for the other planar slow acoustic cases in Case B6 or Case I6, though this may be due to the instability conditions of the meanflow. Previous LST analysis showed weakened total amplification of the second mode disturbances in spite of the the higher peak growth rates due to the shorter amplification length and narrower instability band. This is due to the reduced unit Reynolds number of Case S. As such, the developed boundary layer disturbances are relatively weak when compared to corresponding slow acoustic results in Case B6 and Case I6, allowing for the weak pulse front to be more readily observable in the contour levels here.

The spectral surface pressure amplitude contours for both acoustic cases are presented in Fig. 6.11 and Fig. 6.12 at two contour levels. Fig. 6.11 shows scaled contour levels that allow for better observation of the peak disturbance amplitudes near the end of the cone. For both acoustic pulses good agreement is observed between LST and DNS results, with the primary second mode bands centering about the branch II neutral point as expected. The slow acoustic pulse data in Fig. 6.11b in particular demosntrates the expected amplification

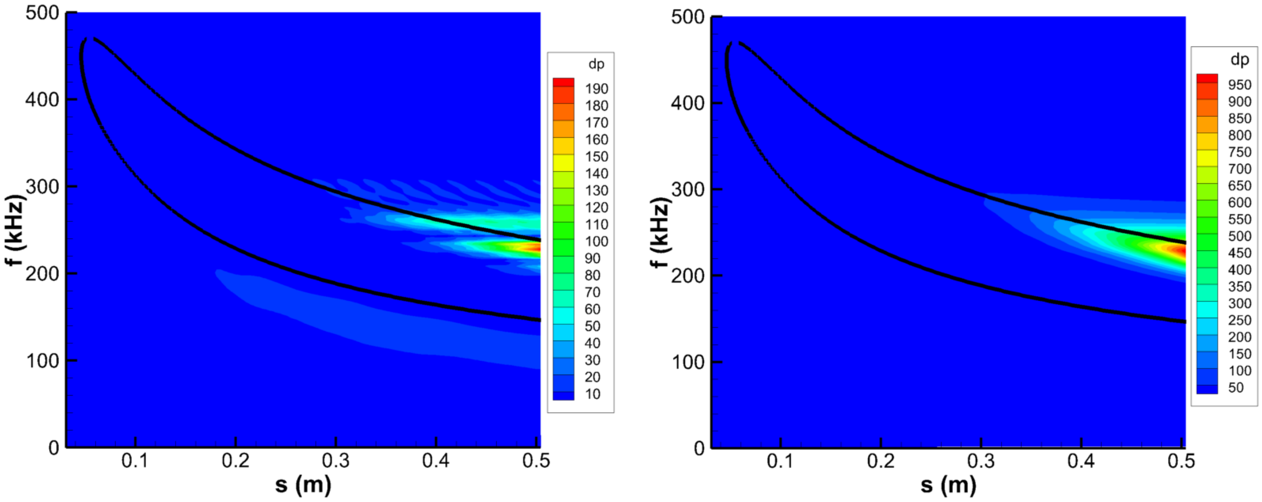

(a)

(b)

Figure 6.11: FFT decomposed surface pressure contours for Case S: (a) after planar fast acoustic pulse and (b) after planar slow acoustic pulse.

pattern of a second mode dominated boundary layer, with minimal secondary excitation from other modal or nonmodal noise. Similar to the prior axisymmetric pulse results for Case B and Case I, the planar fast acoustic pulse in Fig. 6.11a depicts a more complex disturbance profile. Namely, significant valleys in the disturbance amplitude are observed in the primary second mode amplification band near 250 kHz and 210 kHz, which are associated with the wavepacket interference discussed previously[102]. A prominent band of weakly amplified disturbances is also seen directly below the second mode band, between frequencies of 100 kHz and 300 kHz. The proximity of this lower frequency band to the second mode as well as the consistent modal shape indicates that this band is most likely associated with a weakly amplified first mode. While downstream LST analysis demonstrated weak excitation of a higher mack mode instability, the first mode was not captured. As such, this additional band is likely a result of the high level of additional broadband forcing from the fast acoustic pulse and not due to an innate instability of the first mode itself.

Rescaled contours for direct comparison to Case B and Case I planar pulse results are shown in Fig. 6.12. These figures corroborate previous observations, with the primary second

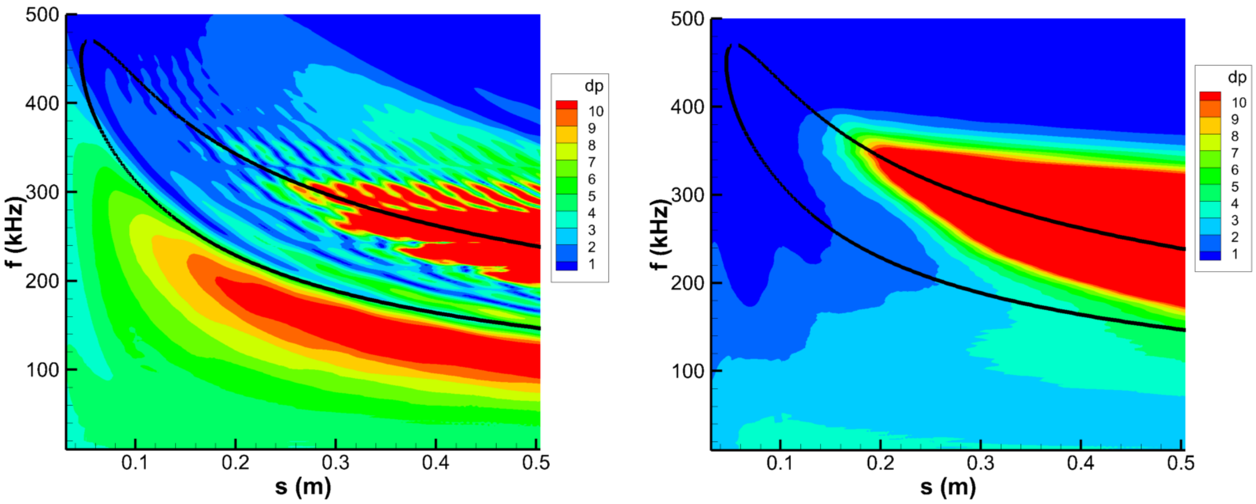

(a)

(b)

Figure 6.12: FFT decomposed surface pressure contours for Case S: (a) after planar fast acoustic pulse and (b) after planar slow acoustic pulse. Contour levels adjusted for comparison to previous cases' results.

mode bands observed to continue extending further upstream than in the Case B5, B6, I5, and I6 results. The rescaled slow acosutic data demonstrates weak low frequency forcing from upstream on the cone, while the fast acoustic contours show much more significant "feathering" that is associated with the broadband amplification and interference expected of the fast acoustic pulse.

The FFT decomposed pressure perturbation spectra throughout the shock layer is presented for both the axisymmetric fast and slow acoustic pulses in Fig. 6.14 at a streamwise position of $x = 0.49$ m. The spectra are also highly reminiscient of similar results for the planar acoustic results in Case B and Case I. Namely, the axisymmetric slow acoustic pulse results in a much stronger second mode in the boundary layer, but has minimal noise excitation from the local pulse front. On the other hand, the fast acoustic pulse results in significant low amplitude disturbances across a wide range of frequencies in the shock layer. These are observed to interact with and modulate both the primary second mode frequencies, as well as the secondary frequency bands observed in the surface spectra.

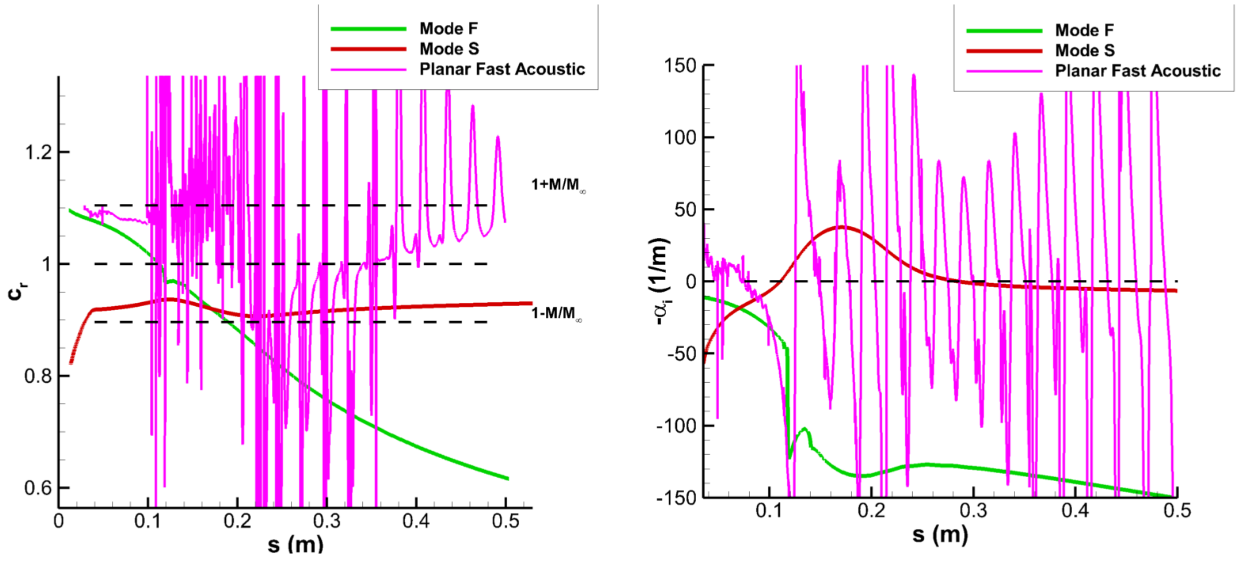

(a) (b)

Figure 6.13: Unsteady DNS vs LST results for 300 kHz disturbance after planar fast acoustic pulse disturbance for (a) phase speed and (b) growth rate.

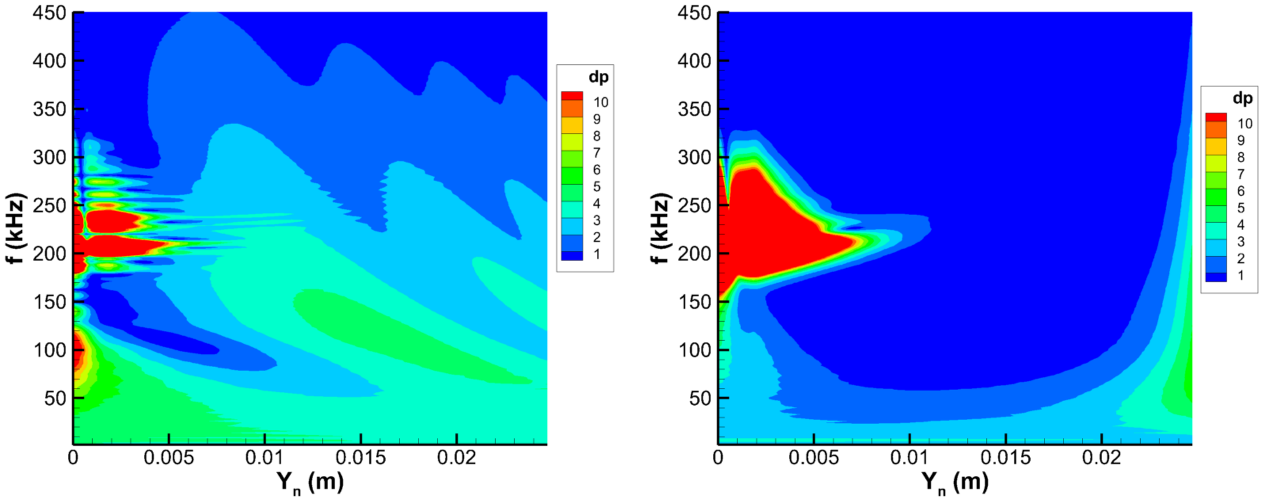

(a) (b)

Figure 6.14: Shock layer spectra at $x = 0.49$ m for Case S: (a) planar fast acoustic and (b) planar slow acoustic pulses.

The discrete frequency 300 kHz disturbance results are compared to LST for the planar fast acoustic pulse in Fig. 6.13 and for the planar slow acosutic pulse in Fig. 6.15. Again, the fast acoustic pulse is shown to excite a mix of continuous fast acoustic and discrete mode F disturbances upstream on the cone in the phase speed plot. The signal remains highly oscillatory throughout the domain, though the signal seems to center about the mode S phase speed after synchronization before slowly moving back to the continuous fast acoustic spectrum. The growth rate spectrum remains dominated by noise effects due to the strong broadband response observed for the planar fast acoustic pulse, similar to the prior cases.

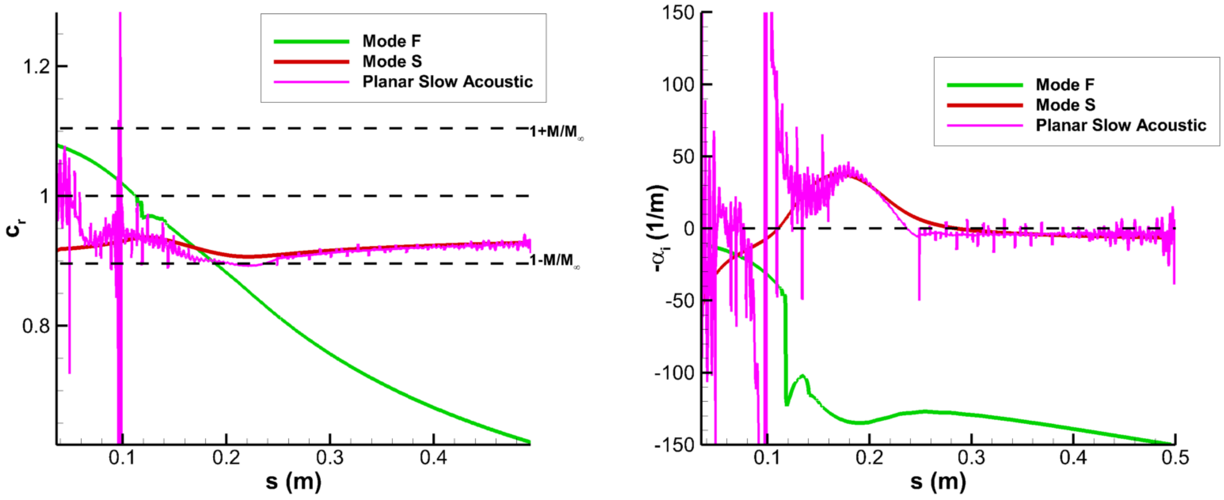

(a) (b)

Figure 6.15: Unsteady DNS vs LST results for 300 kHz disturbance after planar slow acoustic pulse disturbance for (a) phase speed and (b) growth rate.

The planar slow acoustic pulse results in Fig. 6.15 much more readily follow the expected LST profiles, which further indicates the stronger second mode receptivity response to broadband slow acoustic disturbances. The phase speed data shows highly oscillatory signals upstream on the cone centered between the entropy/vorticity spectrum and the continuous fast acoustic spectrum before the signal rapidly converges upon the discrete mode S LST curve. The growth rate figure also shows a highly oscillatory, but roughly neutral disturbance signal prior to synchronization. These are again indicative of locally induced continuous modes propagating to and interacting with the boundary layer upstream on the cone. The good agreement downstream on the cone indicates both a strong second mode receptivity response to the planar slow acoustic pulse, as well as relatively weak broadband excitation of continuous modes when compared to the planar fast acoustic pulse in Fig. 6.13. This behavior is in line with results from Case B6 and Case I6.

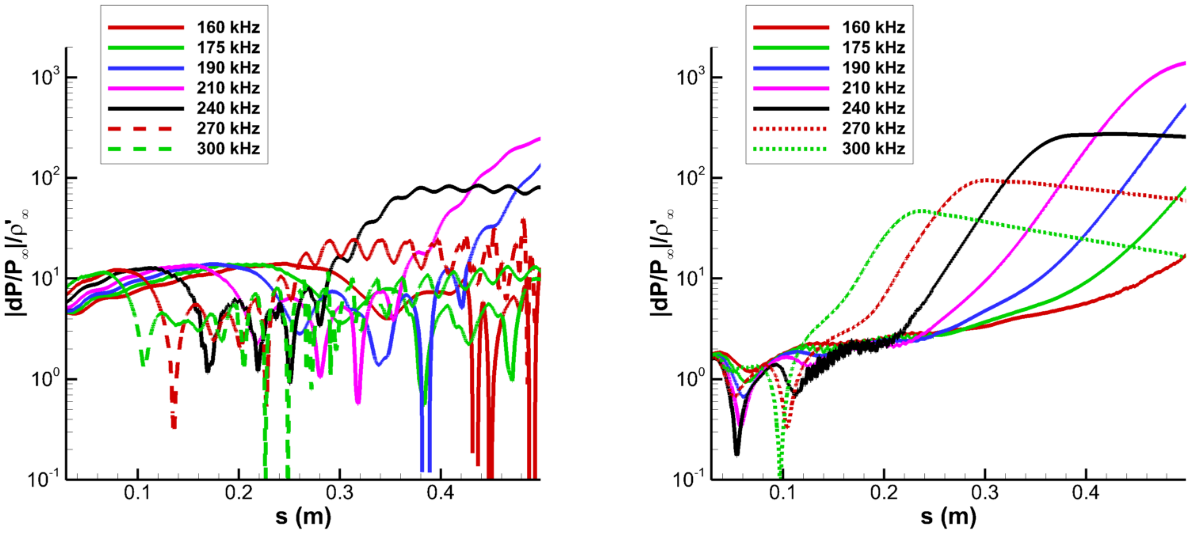

(a)

(b)

Figure 6.16: Streamwise development of selected discrete frequency disturbances for Case S (a) planar fast acoustic and (b) planar slow acoustic axisymmetric pulses.

The streamwise development of a selection of DNS disturbance frequencies is depicted in Fig. 6.16. The basic behaviors are similar to what was observed for Case B in Fig. 4.42 and for Case I in Fig. 4.53. Namely, relatively low amplitude disturbances are introduced upstream which experience gradual attenuation until the unstable second mode region. At this point, exponential growth in the disturbance amplitude is observed. The peak downstream amplitudes here are much lower (by up to one to two orders of magnitude) than the planar fast and slow acoustic results for Case B and Case I, which is again due to the reduced second mode amplification caused by the low unit Reynolds number of the Case S meanflow.

In terms of the acoustic receptivity response, the planar slow acoustic pulse results in significantly higher second mode amplitudes, as expected. For instance, the peak sampled frequency of 210 kHz was found to be approximately six times larger at the end of the cone for the slow acoustic case. However, the initial upstream response to the planar slow acoustic pulse is approximately four times weaker than that for the planar fast acoustic pulse. In fact, the upstream disturbances remain significantly higher in general for the planar fast acoustic pulse. This is caused by the strong local fast acoustic pulse front induced by the shock-disturbance interaction which is not sufficiently overshadowed until far downstream by the second mode. A similar effect was also observed for Case B5 and Case I5.

In general, the receptivity of Case S to axisymmetric, planar acoustic disturbances falls into the expected behaviors from prior observations. Namely, strong upstream continuous mode excitation is observed prior to second mode amplification. The planar slow acoustic pulse results in the highest peak amplitudes and also primarily excites the second mode disturbance in particular. While the planar fast acoustic pulse results in the lowest overall pressure disturbance amplitudes, it induces a significantly more complex broadband response in both the boundary layer and shock layer of the cone. Additionally, the effects of both nose bluntness and unit Reynolds number are further confirmed here. The reduced nose bluntness is shown to shift the unstable second mode band to a higher range of frequencies and push the second mode region further upstream on the cone. However, the reduced unit Reynolds number is shown to reduce the overall amplification rate of disturbances in both the LST and unsteady DNS results.

6.3.2 Receptivity to Azimuthally Varying Pulses

The receptivity to the azimuthally varying acoustic pulse disturbances are discussed in this section. Using the parameters listed in Table. 3.2, the incident acoustic pulses are designed to significantly excite disturbance frequencies of up to 500 kHz and azimuthal modes up to K = 5. Due to this relatively narrow band of excited azimuthal wavenumbers, a total of 32 points in the azimuthal direction are simulated. This allows for oblique modes with wavenumbers up to K = 16 to be calculated. The resulting 3-D boundary layer disturbances are further studied using two-dimensional FFT analysis. The 3-D pulses utilize a very similar freestream gaussian pulse formulation as the axisymmetric disturbances, allowing for continuous frequency and azimuthal wavenumber spectra disturbances in the freestream.

Similar to the planar pulse cases, while the 3-D disturbances are constrained in the azimuthal and streamwise directions they are otherwise infinite in the wall normal direction. This also allows the 3-D azimuthal acoustic pulses to continue forcing the flow downstream along the cone as they propagate, though the general noise profile is expected to be reduced due to the overall smaller extent of the incident disturbance. Additionally, a filtering scheme is utilized to dampen non-physical high wavenumber noise that in the spectral method utilized for fluxes in the azimuthal direction. The filtering scheme is based on the spectral "roll off" method described by Pruett and Chang[112] and originally proposed by Gottlieb et al.[113]. This spectral roll off method is meant to minimally damp the high wavenumber noise to avoid deleterious affects on the accuracy of the lower wavenumber modes.

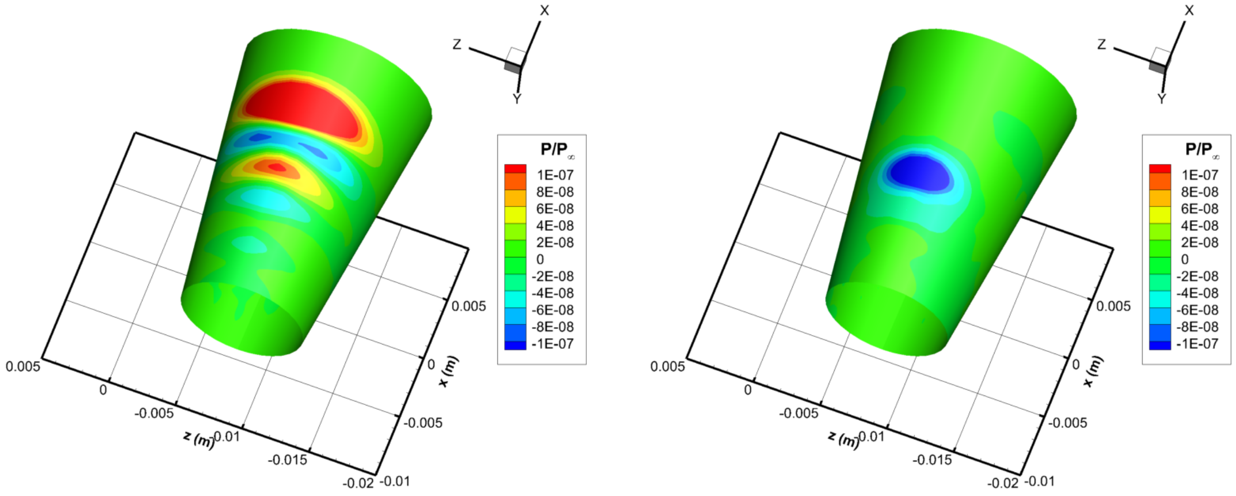

(a) (b)

Figure 6.17: Snapshot of upstream surface pressure perturbations at $t = 0.0336$ ms for (a) 3-D fast acoustic and (b) 3-D slow acoustic pulses.

First, the surface pressure disturbance contours at $t = 0.0336$ ms is plotted in Fig. 6.17 for both 3-D pulse cases at an upstream location. From the LST analysis this domain encompasses the region immediately prior to as well as some streamwise locations just beyond the initial onset of the highest frequency second mode disturbances (at about 450-480 kHz). At this point strong excitation of discrete mode disturbances is not expected. Even at this upstream location distinct differences are observable in the surface pressure perturbations. While the slow acoustic pulse induces a centralized pressure perturbation near $x = 0.02$ m in Fig. 6.17b the fast acoustic pulse induces a more oscillatory signal in Fig. 6.17a. This can be further examined using the FFT decomposed surface pressure amplitude spectra in Fig. 6.18, which is sampled at $x = 0.049$ m. The pressure amplitudes here and in similar plots are normalized by the spectral content of the incident freestream pulse to account for uneven disturbance distributions in both frequency and wavenumber.

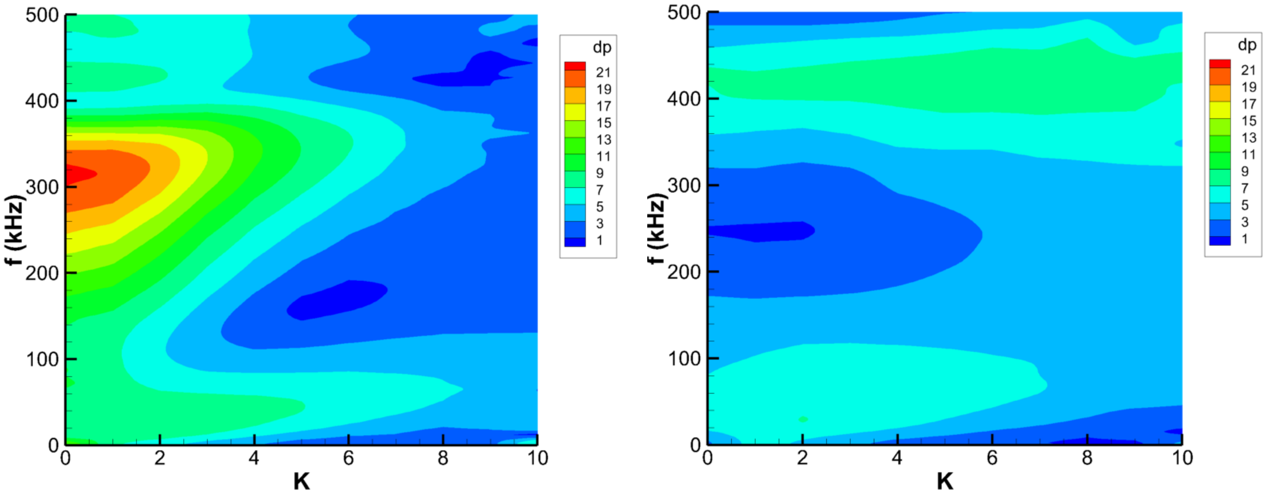

(a)

(b)

Figure 6.18: FFT decomposed surface pressure spectra at $x = 0.049$ m for (a) 3-D fast acoustic and (b) 3-D slow acoustic pulses.

While the fast acoustic pulse induces a small amount of excitation at low azimuthal wavenumbers near the expected second mode frequencies, the primary excitation is focused about 300 kHz and extends up to azimuthal wavenumbers of K = 7 in Fig. 6.18a. The slow acoustic pulse, on the other hand, generally demonstrates much weaker excitation across the board in Fig. 6.18b though the second mode frequencies are slightly more excited in this case at throughout the plotted wavenumber range. The coherent band of excited disturbances for the fast acoustic pulse is not centered about frequencies that are associated with a discrete mode instability, and as such are attributed to stronger excitation of continuous modes. This is similar to prior observations for axisymmetric fast acoustic disturbances.

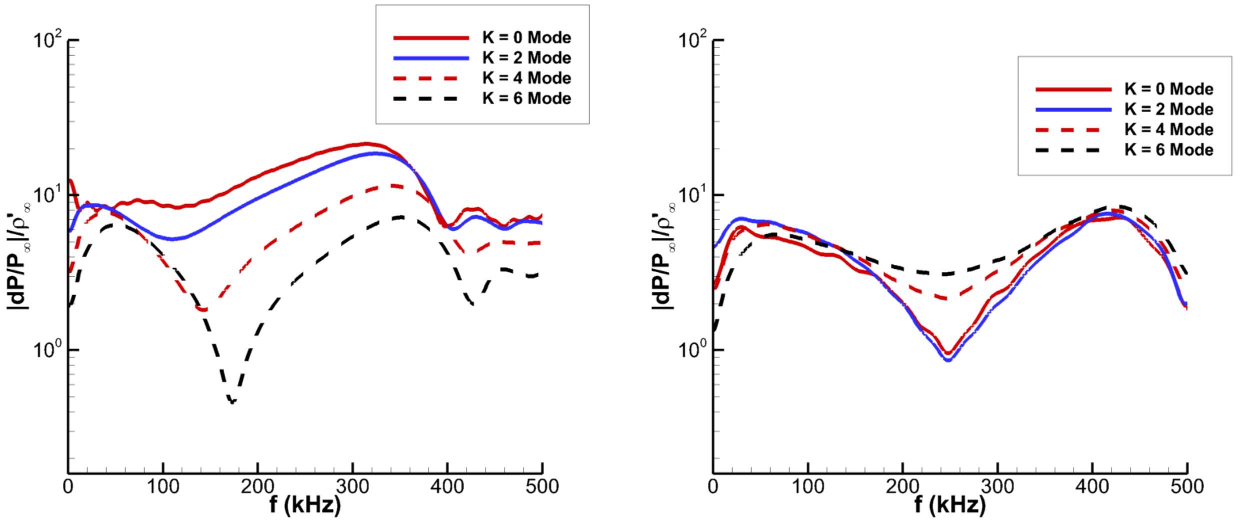

(a)

(b)

Figure 6.19: FFT decomposed surface pressure spectra for selected wavenumbers at $x = 0.049$ m for (a) 3-D fast acoustic and (b) 3-D slow acoustic pulses.

A selection of azimuthal wavenumbers are plotted for both 3-D acoustic pulse cases at $x = 0.049$ m in Fig. 6.19. Again, for the fast acoustic case the most significant amplification is observed near approximately 300 kHz, with smaller maxima near 40 kHz and 440 kHz. These smaller maxima are associated with low frequency entropy layer modes as well as the local second mode disturbances which are unstable but have not yet experienced significant amplification. The slow acoustic results demonstrate a significantly different spectral profile. Most obviously, the amplified forcing band near 300 kHz is absent, with a minimum instead being observed there. Instead, the peak disturbances are centered about the same lower frequency disturbance associated with upstream entropy layer modes and high frequency second mode. However, the peak disturbances here are only approximately 30% of that for the 300 kHz disturbance in the fast acoustic case. While the fast acoustic disturbance sees the forced surface pressure amplitudes fall significantly with increasing azimuthal wavenumber, the slow acoustic data demonstrates relatlively minimal variation in the given range. Thus, the fast acoustic disturbance is shown to induce significant continuous mode disturbances at the lowest wavenumbers while the slow acoustic pulse seems to excite weak boundary layer disturbances across a wide range of wavenumbers at this upstream location.

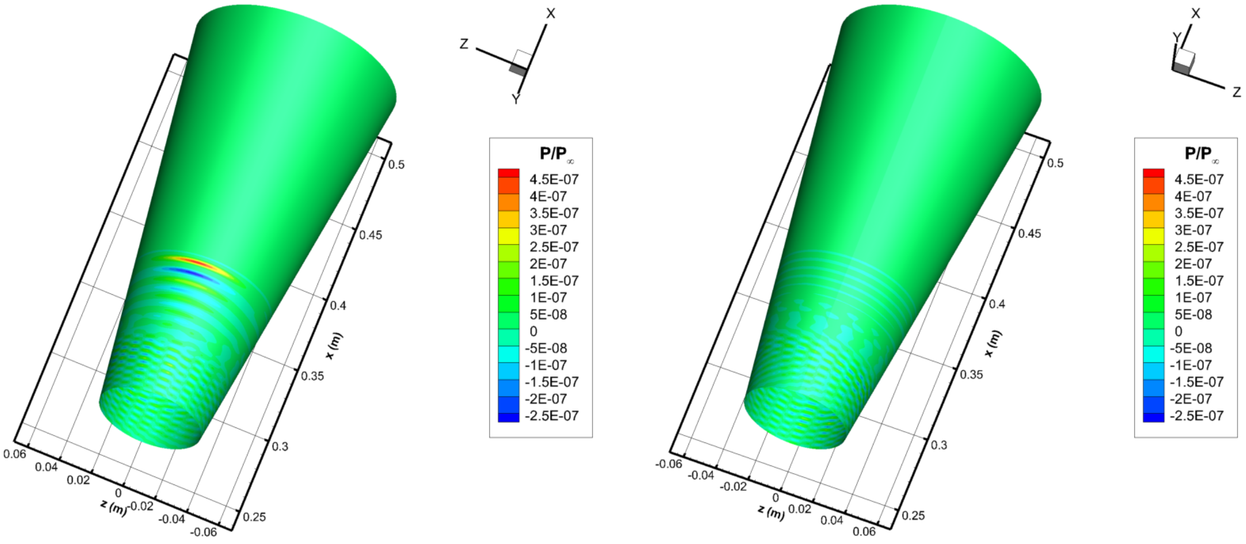

(a)

(b)

Figure 6.20: Snapshot of downstream surface pressure perturbations for a 3-D fast acoustic disturbance at $t = 0.2153$ ms at (a) windward of incident pulse and (b) leeward of incident pulse.

The disturbance development at several downstream positions is also plotted to demonstrate the develop of boundary layer instabilities. Fig. 6.20 depicts surface pressure perturbations at $t = 0.2153$ ms after perturbation by the 3-D fast acoustic pulse. The plotted domain ranges from $x = 0.25$ m to $x = 0.5$ m in the streamwise direction. At this time, the disturbance wavepacket has propagated to approximately $x = 0.35$ m. The contours both windward and leeward of the incident freestream pulse are shown to demonstrate the azimuthal distribution of surface disturbances. A similar strong alternating high and low pressure wavepacket is observed near $x = 0.35$ m on the windward side in Fig. 6.20a. This is the primary acoustic front induced by the local freestream pulse, similar to the pulse front observed in the axisymmetric contours in Fig. 6.8a, and as such is also expected to introduce strong continuous mode forcing to the flow. Trailing behind it at the beginning of the zone are a collection of much lower amplitude surface perturbations that are distributed evenly across the azimuthal direction. This trailing mode contains the primarily excited 2-D wave modes, as well as other disturbances excited by the pulse. The low relative amplitude of the trailing wavepacket indicates weak excitation of the second mode for the fast acoustic pulse at this given time.

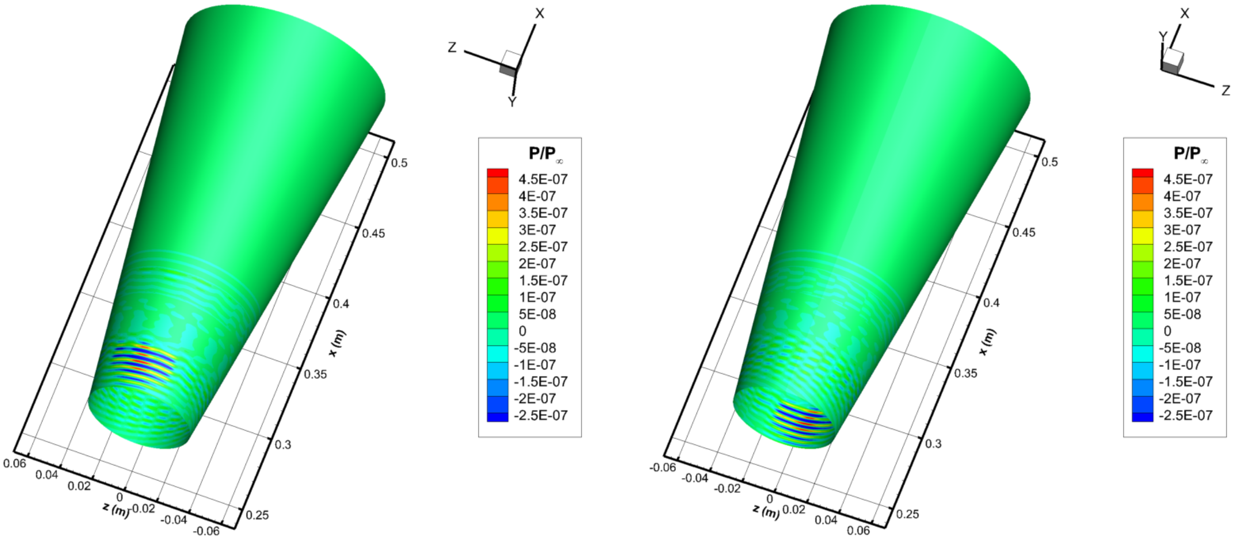

(a) (b)

Figure 6.21: Snapshot of downstream surface pressure perturbations for a 3-D slow acoustic disturbance at $t = 0.2153$ ms at (a) windward of incident pulse and (b) leeward of incident pulse.

Similarly, Fig. 6.21 depicts surface pressure perturbations at $t = 0.2153$ ms after perturbation by the 3-D slow acoustic pulse. Again, a primary packet of disturbances is observed near the entrance of the cone that is limited to only a small width in the azimuthal direction. This is again the direct influence of the local slow acoustic pulse, which was was also observed in the axisymmetric pulse case to more strongly interact with the shock layer in Case S. Due to the slower propagation speed of the slow acoustic disturbance, this pulse front lags behind its fast acoustic counterpart. The much more regular banded appearance of the wavepacket is reprsentative of a developing discrete mode disturbance, which is most likely the second mode here. This axisymmetric band of disturbances coincides with the local slow acosutic pulse forcing, and may lead to strong interactions in the modal wavepacket. The contours on the leeward plot in Fig. 6.21b are similarly weak relative to the local forcing modes, and indicate relatively weak second mode and oblique mode excitation outside of the local forcing at this time.

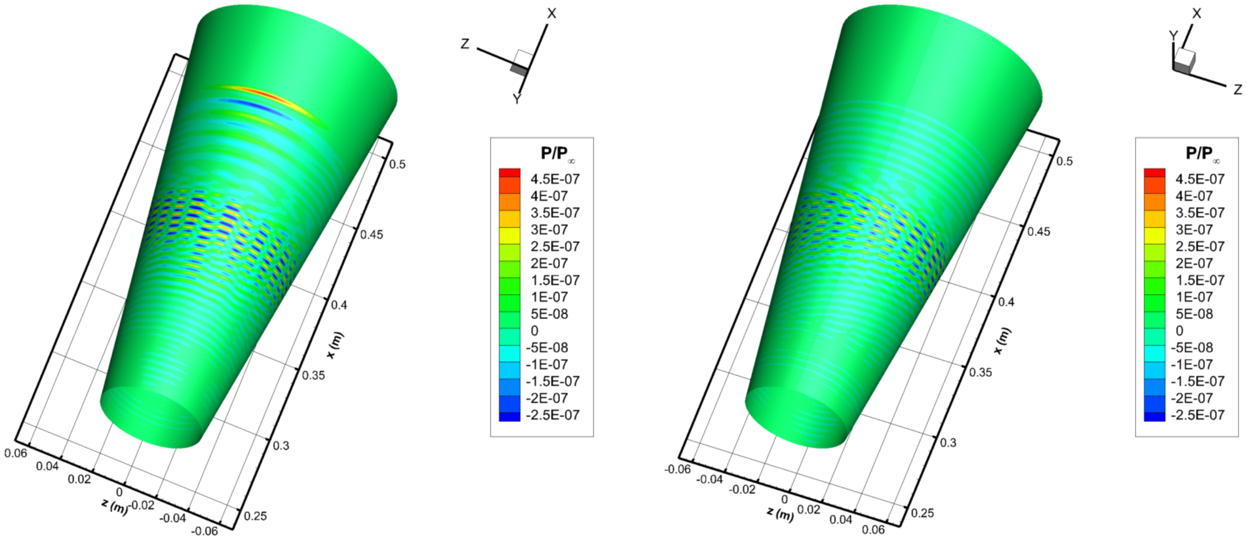

(a)

(b)

Figure 6.22: Snapshot of downstream surface pressure perturbations for a 3-D fast acoustic disturbance at $t = 0.2851$ ms at (a) windward of incident pulse and (b) leeward of incident pulse.

Similar surface pressure contours are shown for the 3-D fast acoustic pulse in Fig. 6.22 and for the 3-D slow acoustic pulse in Fig. 6.23 at a later time of $t = 0.2851$ ms. The shock-disturbance front component near $x = 0.45$ m in Fig. 6.22a on the windward side of the fast acoustic results demonstrate little variation from the earlier sampling location. This indicates minimal amplification or attenuation of the disturbance modes associated with this wavepacket. This is due to the local reintroduction of disturbances by the pulse, and the general stability of the continuous modes. The trailing wavepacket near $x = 0.38$ m in both the windward and leeward figures for the fast acoustic case demonstrate the rapid amplification of boundary layer modes. These contain the 2-D second mode disturbance, as well as other potentially oblique mack mode instabilities. While the leeward contours for the fast acoustic case demonstrate relatively consistent amplification patterns , the windward contours demonstrate some distortions in the amplification pattern behind the shock-disturbance front. Notably, immediately behind the shock-disturbance front some of the perturbations are out of phase azimuthally. This indicates strong excitation of higher waver number oblique modes along with the 2-D second mode, which is invariant in the azimuthal direction. The distortions at these positions is likely due to interference with the forcing front near $x = 0.45$ m.

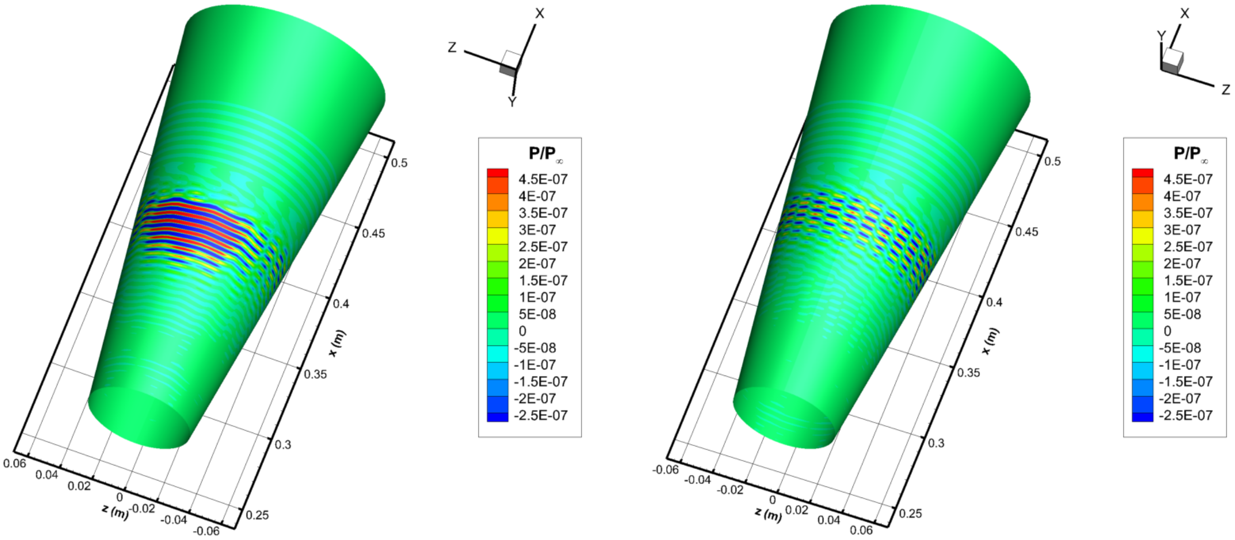

(a)

(b)

Figure 6.23: Snapshot of downstream surface pressure perturbations for a 3-D slow acoustic disturbance at $t = 0.2851$ ms at (a) windward of incident pulse and (b) leeward of incident pulse.

The contours at the same time are plotted for the slow acoustic case in Fig. 6.23. For the windward contour in Fig. 6.23athe slow acoustic pulse front is observed to still be coincident with the primary disturbance wavepacket. Additionally, the disturbance front demonstartes significant growth in both the amplitude and spanwise extent which suggests strong adherence to the amplification expected of the second mode. While a third mode instability was potentially identified in LST analysis, the disturbance band was located much further downstream. As such the amplification observed here is likely primarily associated with the second mode disturbances. The leeward results in Fig. 6.23b similarly demonstrate uniformly developed disturbances throughout the azimuth. This greater uniformity in the azimuthal direction further emphasizes the dominance of a 2-D second mode disturbance in the boundary layer, as higher wavenumber modes are expected to induce additional disturbance variation in this direction. Due to this pulse coincidence, the local slow acoustic front may interact constructively with the primary boundary layer disturbance modes. This may explain the much stronger second mode response observed to the slow acoustic disturbance.

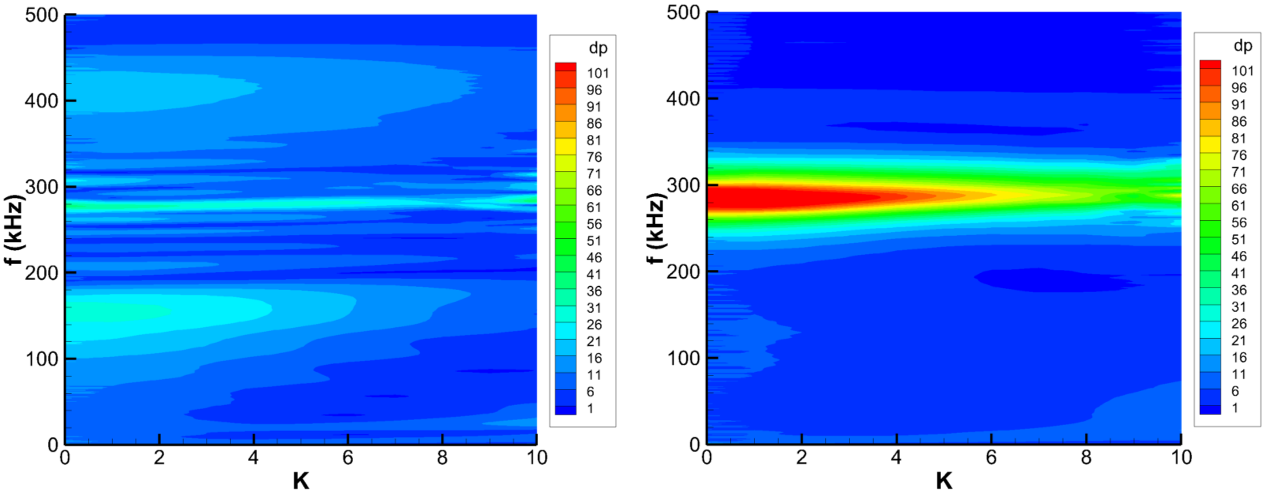

(a)

(b)

Figure 6.24: FFT decomposed surface pressure spectra at $x = 0.255$ m for (a) 3-D fast acoustic and (b) 3-D slow acoustic pulses.

The 2-D surface pressure amplitude spectra at the more downstream sampling position of $x = 0.255$ m are presented in Fig. 6.24. The contour levels are increased from those in Fig. 6.18 to properly show the amplitude gradients in the spectra, as significant amplification has occurred for the boundary layer disturbances. The amplitude contours are again normalized by the analytical spectrum of the freestream pulse to account for non-uniform frequency and wavenumber distributions in the incident disturbance. Contrary to the upstream point depicted in Fig. 6.18, both the fast and slow acosutic results here demonstrate significant amplification of the primary second mode frequencies for both zero and non-zero wavenumbers. The slow acoustic results in Fig. 6.24b demonstrate expected results, with the primary disturbance band being centered about the maximal local second mode frequency of approximately 280 kHz. The amplification is strongest for the 2-D zero wavenumber modes, which correspond to the primary second mode disturbance while the higher wavenumber modes see are comparatively less amplified. The fast acoustic results in Fig. 6.24a also demonstrate the strongest band of pressure disturbances near 280 kHz, though the spectrum is not nearly as regular. Similar to the axisymmetric planar pulse cases, a much more broadband frequency and wavenumber distribution is observed for the 3-D fast acoustic pulse. The primary second mode band is highly oscillatory while secondary coherent bands between 300 and 450 kHz as well as between 100 and 200 kHz appear much more regular. These secondary bands are also attributed to the strong introduction of continuous mode and first mode disturbances by the local pulse front. The irregularity of the second mode band is likely due to strong interference effects between these additionally forced modes and the primary second mode wavepacket. Due to the significant phase lag observed between the fast acoustic pulse front and the primary disturbance wavepacket, a significant phase difference is intrinsically imposed upon the primary disturbance modes and the forced modes. This likely results in strong interference, and the highly oscillatory signal seen for the fast acoustic case.

A selection of different wavenumbers are at $x = 0.255$ m for both acoustic pulse cases are plotted in Fig. 6.25. These reflect prior observations, as both the fast and slow acoustic results demonstrate peak amplitudes at the primary second mode frequencies. Additionally, at this sampling position the second mode response for the fast acoustic pulse is an order of magnitude weaker than that of the slow acoustic pulse and further reflects the weak second mode receptivity to fast acoustic disturbances. At the central second mode frequency minimal decreases are observed as the disturbance wavenumber increases in both cases, indicating strong high wavenumber excitation at this upstream position. For the fast acoustic case, the 150 kHz band and the 400 kHz demonstrate much more drastic decreases in the higher wavenumber disturbance content. This implies minimal amplification of the secondary forced modes.

A final disturbance sampling point at the end of the cone is also considered. The surface pressure spectra at $x = 0.499$ m for the acoustic pulses is shown in Fig. 6.26. The fast

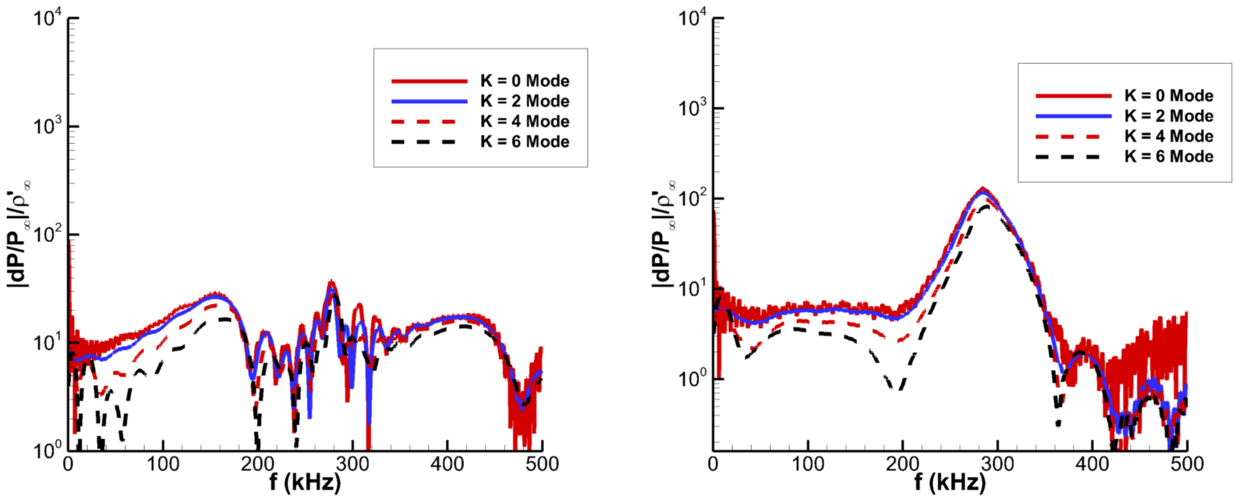

(a)

(b)

Figure 6.25: FFT decomposed surface pressure spectra for selected wavenumbers at $x = 0.255$ m for (a) 3-D fast acoustic and (b) 3-D slow acoustic pulses.

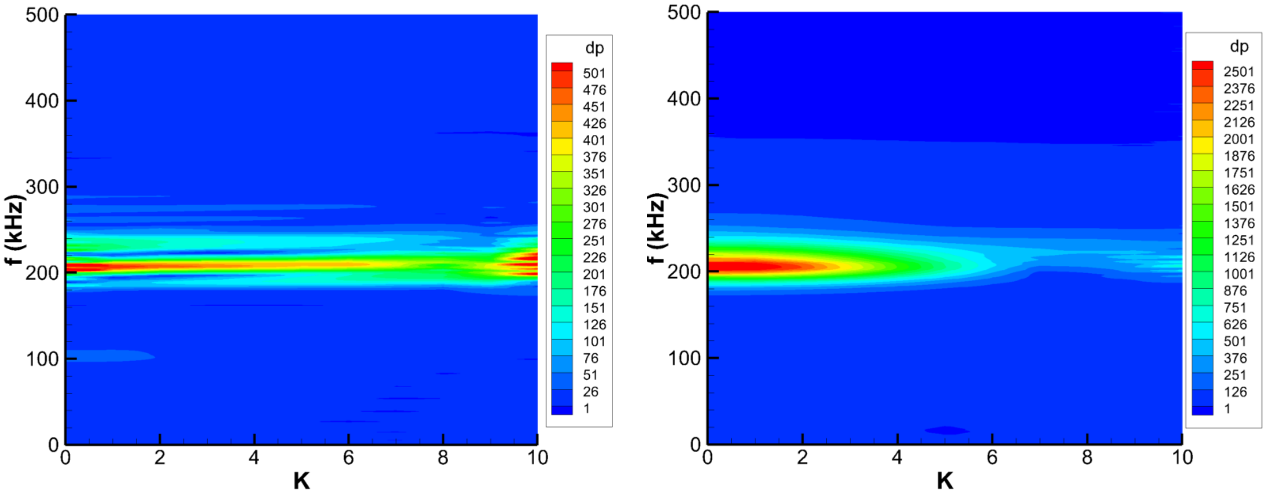

(a)

(b)

Figure 6.26: FFT decomposed surface pressure spectra at $x = 0.499$ m for (a) 3-D fast acoustic and (b) 3-D slow acoustic pulses.

acoustic pulse results in Fig. 6.26a share similar structures to the data sampled at $x = 0.255$ m. Namely, the peak disturbance amplitudes occur at the zero wavenumber with a highly erratic disturbance band. Strong high azimuthal wavenumber excitation is also observed at this final sampling location, though the secondary maxima near K = 10 is likely due to interference effects from numerical noise that the spectral filtering was not able to fully damp out. Furthermore, some evidence of secondary frequency disturbance bands near 100 kHz and 280 kHz can be seen, though they are orders of magnitude weaker than the primary disturbance frequencies. In order to more easily see these bands the fast acoustic contours are rescaled in Fig. 6.27. These secondary bands are consistent with previously observed results at the prior streamwise sampling points. However, the higher frequency component seems to be much more affected by modal interference affects at this point. In general, the amplified disturbances have shifted to lower frequencies here due to the slowly increasing boundary layer thickness. However, this shift seems to have unevenly affected the second mode and the other forced modes, causing significant overlap between the second mode band and the higher frequency continuous mode forcing in particular. This is reflected by the much stronger oscillations observed for both bands, and is indicative of enhanced interference effects.

The slow acoustic spectrum in Fig. 6.26b is much cleaner, further denoting the strong primary modal excitation in this case. In comparison to the fast acoustic results, the high wavenumber content past K = 6 is over an order of magnitude weaker than the 2-D zero wavenumber disturbances. The higher K = 8 through K = 10 wavenumber content is also likely associated with numerical noise, though unlike the fast acoustic case the weaker broadband azimuthal wavenumber receptivity to the slow acoustic pulse prevents the extraneous amplification of these spurious modes.

The frequency spectra for a selection of wavenumbers is plotted at $x = 0.499$ m in FIg. 6.28 for both acoustic pulse cases. The fast acoustic pulse again demonstrates minimal variation in peak amplitudes between 200 and 300 kHz as the azimuthal wavenumber increases, while the secondary low frequency band near 100 kHz does weaken significantly at higher wavenumbers. This further emphasizes the broadband frequency and wavenumber response to a 3-D fast acoustic pulse. The slow acoustic pulse, on the other hand, continues to demonstrate a very clean spectrum with rapid broadband decay as the wavenumber increases. In

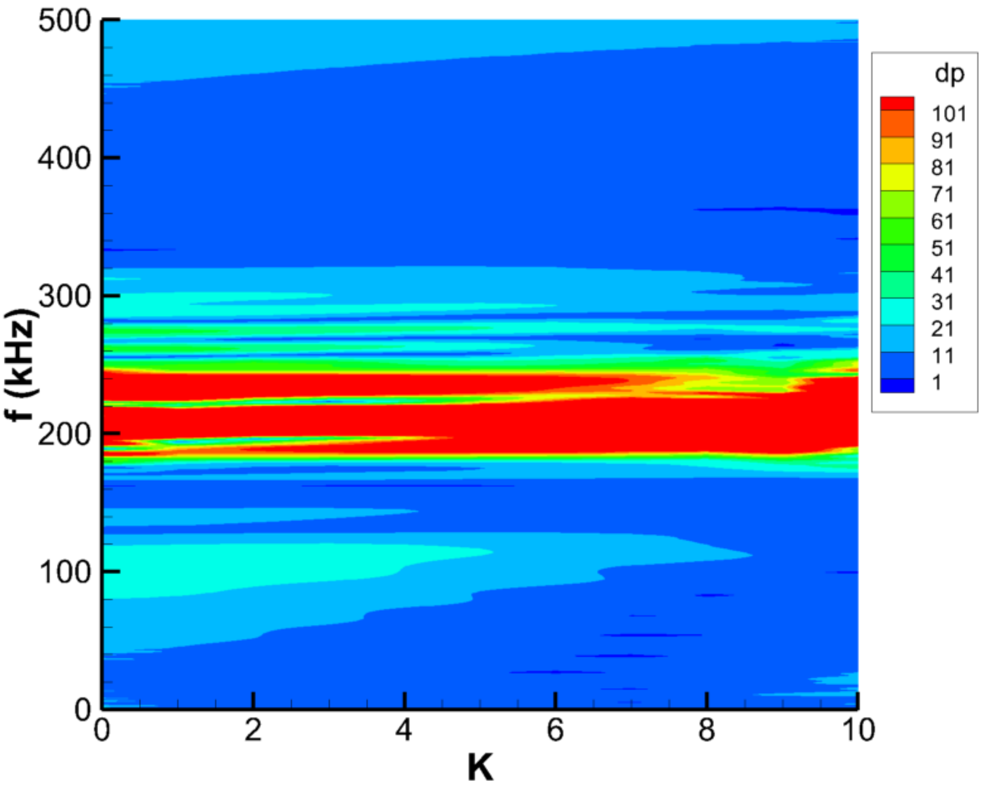

Figure 6.27: FFT decomposed surface pressure spectra at $x = 0.499$ m for a 3-D fast acoustic pulse rescaled to show disturbance bands outside of second mode .

particular, the K = 6 mode is an order of magnitude lower in amplitude than the primary K = 0 second mode. This further reinforces the strong receptivity response of the primary second mode to the slow acoustic disturbance.

As mentioned previously, the primary second mode is a two-dimensional disturbance. This means it experiences no significant variation along the azimuthal direction of a cone, resulting in an azimuthal wavenumber of K = 0. To confirm this, the prior axisymmetric planar acoustic pulse results are compared to the K = 0 spectral results at $x = 0.499$ m in Fig. 6.29. The amplitudes are corrected to account for differences in the peak disturbance amplitudes of the freestream pulses. In both cases excellent agreement is observed between the zero wavenumber and the axisymmetric disturbances, particularly for the slow acoustic results. The same is true for the fast acoustic results, though the noisier oscillatory nature

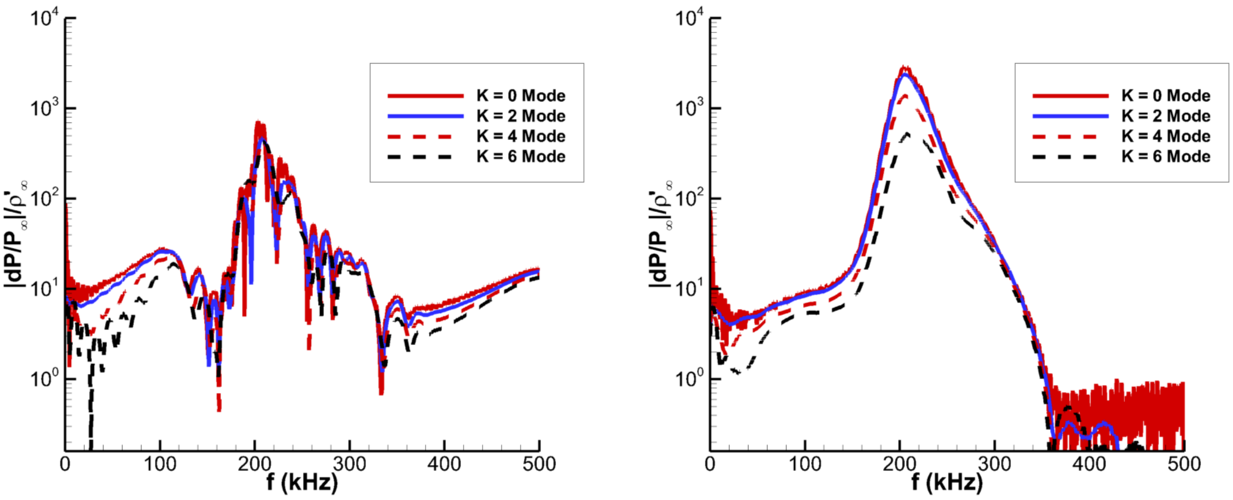

(a)

(b)

Figure 6.28: FFT decomposed surface pressure spectra for selected wavenumbers at x = 0.499 m for (a) 3-D fast acoustic and (b) 3-D slow acoustic pulses.

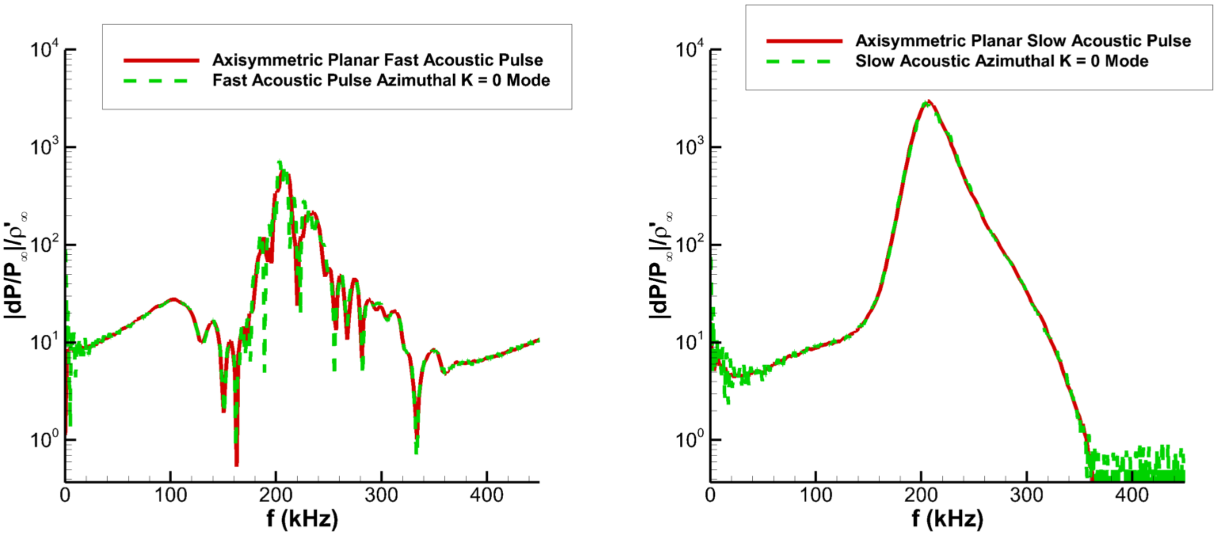

(a)

(b)

Figure 6.29: Comparison of FFT decomposed surface pressure spectra at x = 0.499 m between axisymmetric planar and 3-D pulses for K = 0 wavenumber disturbances for (a) fast acoustic and (b) slow acoustic cases.

of the spectra demonstrates some minor disagreement. In general, these results further reconfirm the strong excitation of second mode perturbations in the flow, even for the fast acoustic pulse.

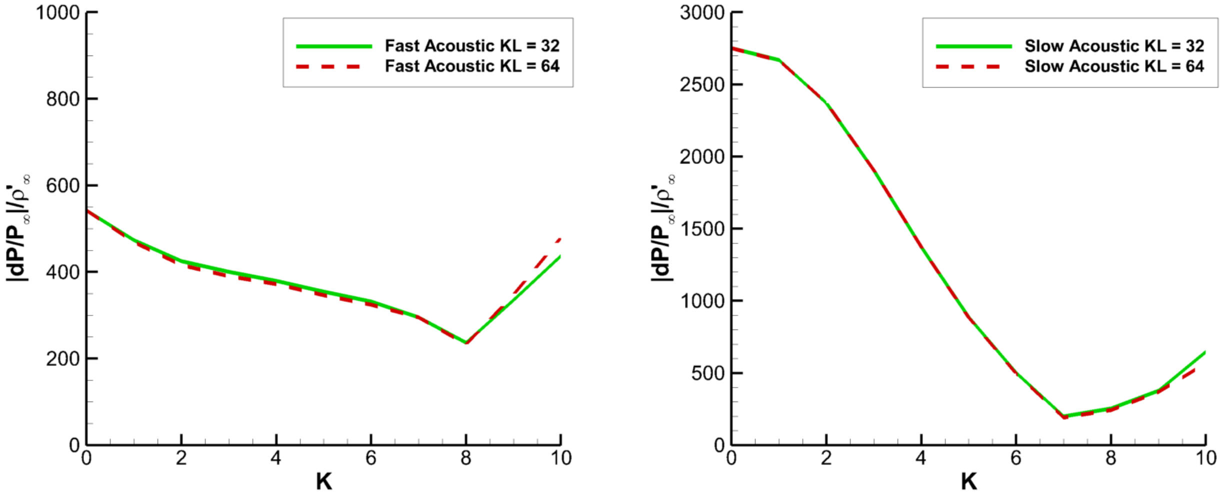

(a) (b)

Figure 6.30: Comparison of KL = 32 vs KL = 64 grid density data for a 205 kHz disturbance at $x = 0.499$ m for (a) 3-D fast acoustic and (b) 3-D slow acoustic pulses.

The parameters of the freestream acoustic pulses were chosen to both excite the primary second mode frequencies as well as a limited number of azimuthal modes. This is to ensure that significant azimuthal resolution would not be required to fully resolve the oblique modes of interest. To ensure this, the unsteady results at $x = 0.499$ m were also calculated using a redoubled grid in the azimuthal direction with 64 points. The results for the 205 kHz disturbance are plotted in Fig. 6.30 for both the fast acoustic and slow acoustic 3-D pulses. In both cases, variation between the KL = 32 grid density and the Kl = 64 grid density results were minimal, averaging below 0.5% except for the highest plotted azimuthal wavenumber which saw errors of approximately 3%. However, the noise at this highest wavenumber is not directly associated with the boundary layer modes excited by the freestream pulse. Instead, the filtering scheme applied in the azimuthal direction is found to unable to totally dampen all of the high wavenumber noise in the flow. This results in the slight increase in disturbance ampitudes at K = 10 observed in both acoustic pulses. As such, the KL = 32 grid is confirmed to be appropriate for the small band of azimuthal wavenumbers that were of interest.

6.4 Case S Summary

The Case S meanflow was converged up to a streamwise length of 0.5 m. Stability analysis was performed using LST, and the receptivity of the meanflow to 2-D and 3-D broadband acoustic disturbances was investigated using unsteady DNS simulations. LST results confirm the behaviors expected from the reduced nose bluntness and reduced freestream unit Reynolds number effects when compared to Cases B and I. Namely, the reduced nose bluntness causes the unstable second mode region to shift both upstream and to higher frequencies. The sharper nose causes the developed entropy layer to become swallowed earlier, allowing for second mode development to begin earlier on the cone. The smaller nose radius also results in a thinner boundary layer, which amplifies higher frequency disturbances. Both contribute to increased second mode sensitivity. However this effect is counterbalanced by the reduced freestream unit Reynolds number which causes lower overall amplification, which is reduced in the lower maximum N-factors at the end of the cone.

In terms of the unsteady results the 2-D/axisymmetric acoustic disturbances demonstrate very similar general behaviors to what was observed for in previous cases. The planar fast acoustic pulse induced a relatively weak receptivity response for the primary second mode, but excited a much broader band of boundary layer disturbances. This is attributed to the strong introduction of continuous modes by the propagating pulse. The slow acoustic pulse showed consistent, strong excitation of the second mode without any of the broadband effects and reflects conventional findings of acoustic receptivity.

The 3-D pulse receptivity results demonstrate much of the same behaviors as the axisymmetric cases. Namely, the fast acoustic pulse induces a weaker second mode but stronger broadband frequency response. For the 3-D disturbances, however, this also extends to the azimuthal wavenumber content. While the 3-D slow acoustic disturbance excited a clean second mode disturbance spectrum that saw primary amplification of the low wavenumbers, the 3-D fast acoustic pulse instead induced significant noise across the sampled wavenumber range. In particular, the higher wavenumbers remained relatively equal in amplitude to the low wavenumber second mode disturbances at the primary instability frequencies. The zero wavenumber disturbances were also found to agree well with the axisymmetric results, and show similar second mode excitation from both the 3-D and axisymmetric pulses. In general, broadband fast acoustic disturbances are confirmed to induce strong multimodal responses in both axisymmetric and 3-D boundary layers.

CHAPTER 7

Conclusion and Summary

7.1 Achievements

In this work a detailed examination of the receptivity behavior of several blunt cone geometries to broadband freestream disturbances has been made and a framework for the application of broadband receptivity data to transition prediction has been established. While the receptivity of hypersonic cones has been widely studied in the past, a large majority of historical studies have focused on highly unrealistic discrete frequency freestream waves which are not representative of the distributed broadband nature of both freestream noise and the actual boundary layer disturbance response[62]. More contemporary receptivity studies, such as aforementioned works by Huang and Zhong[4], Chuvakhov, et al.[46], and Goparaju, et al.[59], have begun to consider more realistic sources of broadband perturbation in the freestream. However, these prior studies have remained limited in their considered scope of disturbances and in the direct applicability of their receptivity data.

Over the course of this study a broad range of freestream forcing conditions including broadband freestream fast acoustic, slow acoustic, temperature (entropy), and vorticity disturbances were studied. This wide consideration of multiple distinct broadband disturbance types allows for a more generalized view of the receptivity mechanism in hypersonic flows to the complex disturbance environments that may be present in flight. While similar considerations of multiple disturbance types have been made in some other receptivity studies in the past, these prior studies utilized unrealistic discrete frequency freestream waves that are incapable of inducing the broadband disturbance responses observed here. This is particularly the case for the observed resposnes to the planar fast acoustic pulses, which demonstrated significant excitation outside of the primary second mode that has not been previously observed in literature. Similar results were observed in the preliminary study of the receptivity to 3-D broadband pulse disturbances, in which the fast acoustic disturbance was found to induce highly broadband disturbances in both the frequency and spanwise wavenumber spectra. These results indicate that the effects of broadband perturbations can be highly distinct from prior discrete frequency receptivity results, and necessitate more careful consideration in future work.

The derived receptivity coefficients for Case B and Case I are also novel as a large portion of contemporary broadband receptivity studies neglect to produce comprehensive data that is directly applicable to more advanced transition prediction schemes, like the amplitude method. The spectral receptivity coefficients derived in this work represent the expected linear receptivity response to arbitrary broadband freestream disturbances of the four canonical types, and can represent a broad range of forcing conditions. As such, the receptivity coefficients derived here can be used to estimate the initial second mode disturbance amplitudes that result from arbitrary broadband freestream forcing. When used in combination with an amplitude method approximation like the iterative method based on Marineau[6], they can be used to provide preliminary estimates of the onset of transition over a hypersonic vehicle. While there still remains room for improvement in terms of the accuracy of the amplitude method procedure utilized here, it has still presented significant accuracy gains in some cases compared to the conventional e^N method. Utilizing the amplitude method framework and receptivity data presented in this work preliminary estimates of the onset of transition can be made, which can in turn prevent the overdesigning of thermal protection systems. This can lead to significant gains in terms of overall weight and payload efficiencies for the vehicle.

7.2 Axisymmetric Pulse Receptivity and the Nose Bluntness Effect

In the first portion of this work both the receptivity of blunt cones to broadband freestream pulse disturbances, as well as the effects of nose bluntness on broadband receptivity were investigated. The investigated pulses consist of acoustic, temperature, and vorticity disturbances which are advected by the freestream velocity. Two pulse geometries were utilized: a finite pulse which forces the cones only near the leading edge, and a planar geometry which also introduces forcing downstream along the cones as it propagates through the domain. Using a combination of the unsteady DNS results and stability profiles derived from LST analysis, the spectral second mode receptivity coefficients and the corresponding disturbance phase angles of the two cones were calculated and compared.

While this study is primarily concerned with the receptivity of the second mode instability, some observations were made about the impact of nose bluntness on the development of the supersonic mode instability. Recent investigations of the supersonic mode have primarily focused on high enthalpy flows[114, 3, 24, 25]. However, it has been shown that supersonic modes can also exist in low enthalpy flows with warm walls. Though, the supersonic modes in these cases can be very weak and easily damped out[102]. Excited supersonic modes were observed in all of the axisymmetric unsteady cases here. The supersonic modes are shown to be stronger relative to the second mode for the blunter cone in Case B, as illustrated by the larger extent of the characteristic acoustic radiation emanating from the boundary layer disturbances in Fig. 4.14a and Fig. 4.36b. This is attributed to the destabilized discrete mode F for Case B which is more likely than the discrete mode S to have its phase speed cross that of the continuous slow acoustic spectrum and become supersonic relative to the meanflow. Thus, an unstable mode F can potentially allow for stronger, unstable supersonic modes which can destabilize independently of the second mode. A variety of flow conditions govern which one of the discrete modes eventually destabilizes into the second mode, but the relatively uniform freestream and boundary conditions between these cases indicates some dependence on nose bluntness[81].

For the finite spherical disturbances in Case B it is found that the fast acoustic pulse generates the largest receptivity coefficients followed by the temperature, slow acoustic, and vorticity pulses respectively. For the planar disturbances in Case B the strongest response was observed for the slow acoustic, fast acoustic, temperature, and vorticity pulses in that order. Results for Case I show that finite temperature disturbances generate the strongest second mode receptivity coefficients, followed by the fast acoustic, slow acoustic, and vorticity pulses. For the planar Case I disturbances the slow acoustic pulse generated the strongest receptivity coefficients, followed by the temperature, fast acoustic, and vorticity pulses in that order.

For the finite pulse cases, the receptivity to fast acoustic disturbances appears to be relatively agnostic to nose radius while slow acoustic disturbances experience noticeable amplification with sharper nose geometries. Specifically, Case I2 is shown to have a 60% larger peak receptivity coefficient when compared to Case B2. More significant variations are observed for the finite temperature and vorticity pulses. The receptivity coefficients for the finite temperature pulse Case I3 was observed to be approximately three times that of it's counterpart in Case B3, while the finite vorticity pulse in Case I4 was an order of magnitude larger than its counterpart in Case B4.

In terms of the planar results, the planar fast and slow acoustic pulses were shown to induce the strongest modal responses in Case B and Case I. However, the planar fast acoustic pulse was found to also induce a highly broadband boundary layer response while the slow acoustic pulse primarily forced the second mode. The receptivity spectra for the planar fast acoustic pulses had very similar profiles between the cones, with low amplitude receptivity coefficients at the lower second mode frequencies followed by gradually increasing higher frequency disturbances. However, the peak values for the planar fast acoustic disturbance were 50% higher for Case B5 compared to Case I5. This is due to the weaker second mode amplification predicted by LST for Case B while similar excitation was found in the instabilities outside of the second mode. The decomposition method utilized in this study filters out less of the high frequency extramodal contribution due to the weaker second mode growth in Case B. Additionally, for the planar slow acoustic pulses the peak receptivity coefficients for Case B6 were almost twice as high as for Case I6. This is somewhat counterintuitive considering the higher second mode amplification predicted for the sharper Case I, but can be explained through the stronger excitation of lower frequency extramodal disturbances observed in the unsteady DNS for Case B6 when compared to Case I6. These extramodal perturbations originate upstream on the cone and are not dampened before second mode amplification begins in the planar slow acoustic cases. Additionally, even though second mode amplification gradually dominates in the appropriate frequency band and streamwise locations, this lower frequency noise is continuously introduced by local shock-pulse interactions.

The planar temperature and vorticity pulses in Case I followed a similar trend to their finite pulse counterparts. Namely, Cases I7 and I8 induced significantly higher receptivity coefficients and general second mode amplitudes than Case B7 and B8. The planar temperature pulse was also shown to induce a much noisier broadband spectral response in Case I7 than in Case B7, and demonstrated disturbance content that was somewhat similar to what was observed for the planar fast acoustic cases. This contributes to the highly modulated, multimodal receptivity spectra predicted for this case. The temperature disturbances were also observed to be more capable of agitating low frequency disturbances associated with entropy layer modes in Case I, which recent work by Wan, Su, and Chen[64] and Chen, et al.[67] have shown to be important in exciting primary disturbances downstream along the cone. This may be responsible for the much stronger temperature pulse receptivity response in Case I. These entropy layer modes may also be important in the transition reversal phenomenon observed in much blunter geometries, as seen in work by Goparaju, Unnikrishnan, and Gaitonde[59] and Paredes, et al. [80]. The planar vorticity pulse is shown again to be an order of magnitude larger in Case I, with little variation from the behavior shown by the finite vorticity pulse case other than the increased amplitudes associated with the planar pulse cases in general.

Overall, nose bluntness was observed to have significant effects on the receptivity behavior of the studied blunt cones to freestream pulse disturbances. The degree of this variation is dependent on the incident pulse geometry and disturbance type. Similar to prior studies, LST shows that larger bluntness attenuates the primary second mode instability by reducing the growth rate and pushing the unstable second mode region further downstream. Additionally, the larger nose bluntness in Case B is seen to shift both the unstable second mode band and the frequency of the peak receptivity coefficients to lower frequencies. This is due to the thicker boundary layer that forms over the blunter geometry, which in turn amplifies higher wavelength and lower frequency disturbances. Differences in extramodal disturbance content were also observed. For one, supersonic modes characterized by acoustic radiation emanating from the boundary layer are shown to be more prevalent in Case B due to the destabilized discrete mode F. Case B also generally demonstrated higher upstream forcing amplitudes prior to the second mode region which consist of stronger continuous mode as well as potential non-modal instabilities. The impact of these extramodal disturbances is reflected in the spectral receptivity coefficient and phase angle profiles. Though acoustic disturbances still resulted in the strongest receptivity response for both cones, the temperature and vorticity pulses saw a much greater relative increase in Case I. This may be influenced by the stronger low frequency entropy layer disturbances observed in Case I, which have been linked to second mode excitation. The acoustic disturbance coefficients, however, were generally much less sensitive relative to the changes in nose bluntness.

7.3 Application of 2-D Receptivity Spectra to Transition Prediction

One of the most direct applications of specctral receptivity coefficient data is to the amplitude method, which requires receptivity correlations to estimate initial disturbance amplitudes in the flow. The spectral receptivity coefficients for the planar pulse cases found in the prior receptivity analysis were applied to an iterative approximation of the amplitude method based on Marineau[6]. This approximation was based on amplitude method relations originally proposed by Mack[90]. The amplitude method itself utilizes data from directly measured or simulated flow fields along with amplification factors from stability theory to estimate the absolute amplitudes of boundary layer disturbances. This is in contrast to more simple, traditional transition estimation methods which primarily utilize disturbance amplification ratios. These are unable to account for the highly variable freestream noise environments that can be present in experimental windtunnels and in flight. Marineau's[6] approximation of the amplitude method simplifies the governing integral using experimentally derived correlations for second mode breakdown amplitudes, transition threshold amplitudes, and the freestream noise spectra. Since the DNS cases in this study are based on experimental cases Marineau investigated, it was elected to attempt to apply the receptivity coefficients for Case B and Case I to this iterative method.

Using the iterative method Case B results saw errors of between 60% to 30% using the branch I sampling point coefficients, with the fast acoustic pulse demonstrating the best agreement to the reported experimental transition location. This error is similar in magnitude to conventional e^N predictions using threshold N-factors of 5.5 to 6[6]. However, the error observed here lies far outside of the experimental uncertainty reported by Marineau. The results for Case I show errors of between 21% for the vorticity pulse to 12% for the fast acoustic pulse using the same branch I sampling data. This is well within the experimental uncertainty and demonstrates a distinct improvement in accuracy over conventional $e^N methodology$. However, this result is significantly worse than Marineau's own reported result using his receptivity calculations.

The disagreement here can be traced to differences in the receptivity coefficients utilized to solve for the initial second mode amplitudes. Marineau's coefficients were found to be significantly larger than any of those calculated for the pulses in Case B or Case I. Marineau's larger coefficients result in higher overall boundary layer amplitudes, which cause the iterative method to converge on a more upstream transition location. This disparity in the receptivity coefficient can be associated with a number of factors, such as increased sensitivity to non-modal noise from the large nose bluntnesses of the investigated cases. Additionally, Marineau's receptivity coefficients were not directly calculated from the full spectrally decomposed disturbance content as the coefficients in this study were. Instead, he utilized his correlated expression for the transition N-factor as well as experimental correlations for breakdown amplitudes to estimate the receptivity coefficients. The large reliance on correlations for the generation of key receptivity data, the estimation of boundary layer breakdown amplitudes, and the freestream noise profile may have caused the significant divergence found here. On another note, recent results by Egorov, et al[76] have shown that the strong coherence of the incident freestream disturbance may result in reduced boundary layer disturbance amplitudes due to interference effects. However, this has not been investigated extensively and requires additional verification. There remains significant room for improvement in this implementation of the amplitude method, and in the correlations necessary for its efficient application in engineering design processes.

7.4 Receptivity Analysis of Azimuthally Varying Acoustic Pulse Disturbances in Case S

While the previous sections of this work have focused primarily on 2-D/axisymmetric disturbances, which have been found to dominate for a large range of conditions, true flight conditions are expected to contain oblique disturbances as well due to more complex vehicle geometries and environmental forcing. As such, a preliminary analysis the receptivity of a sharper nose case to both 2-D planar pulses as well as 3-D azimuthally varying pulses was also investigated. The freestream parameters for Case S were also based on tunnel conditions reported by Marineau, et al.[7] for higher atmospheric conditions. However, unlike Case B and Case I, Case S does not directly reflect an experimental study done by Marineau. This reduced Reynolds number case was chosen to better accomodate stability constraints for the unsteady DNS code. Analysis focused on the receptivity to acoustic disturbances, as these were found to induce the most significant modal responses in Case B and Case S. The 1.0 mm nose radius for Case S was found to impact the second mode stability profile in the expected manner. That is, it destabilized the flow by pushing the unstable second mode region further upstream and also increased the frequency of the amplified disturbances due to the thinner boundary layer found in sharper cones. However, the reduction in freestream unit Reynolds number counteracted this effect, leading to reduced overall disturbance amplification. This resulted in lower overall disturbance N-factors.

The receptivity of the sharper Case S was investigated to axisymmetric planar fast and slow acoustic pulses to mirror the results found in Cases B5, B6, I5, and I6. Very similar general behaviors are observed in the spectral receptivity response of Case S to prior 2-D/axisymmetric pulse results. Namely, the slow acoustic pulse much more readily excites the primary second mode disturbance and minimally forces anything outside of the second mode. One difference of note is the stronger pulse front observed for the slow acoustic disturbance, which was observed in the time history snapshots to introduce much more significant shock layer perturbations relative to the boundary layer modes when compared to Case B6 and Case I6. While some interference effects were observed near the edge of the boundary layer, the spectral profiles in Case S don't demonstrate significant interactions with the primary surface modes. The planar fast acoustic pulse was again seen to induce highly complicated broadband spectra in the boundary layer disturbances that are associated with the downstream introduction of continuous mode disturbances by the local shock-disturbance front. While the second mode amplitudes were significantly lower than the slow acoustic case, the disturbance frequencies outside of the primary second mode band were observed to be over an order of magnitude larger in the planar fast acoustic case, further emphasizing the strong broadband response expected of broadband fast acoustic forcing.

The receptivity to azimuthally varying acoustic disturbances was also investigated using unsteady DNS to extend our understanding of broadband receptivity to more complex forcing environments. The pulse geometry was utilized again, and further tailored to excite only a small selection of azimuthal wavenumbers so as to reduce grid resolution requirements. The general results broadly reflect observations for the 2-D pulse cases. Results sampled near $x = 0.0490$ m, near the second mode branch I neutral position for the highest frequency second mode disturbances, demonstrate distinct differences in the induced boundary layer disturbance profile between the two acoustic pulse cases. The 3-D slow acoustic pulse induced a weak, isolated packet of disturbances that experienced minimal excitation or attenuation. The azimuthal fast acoustic pulse on the other hand demonstrated the presence of significant modal disturbances, which due to the upstream position are assumed to be composed of locally excited continuous modes. More downstream sampling positions near $x = 0.255$ m and $x = 0.499$ m demonstrate significant discrete mode excitation in both the fast and slow acoustic cases. The 3-D slow acoustic pulse was seen to primarily amplify the 2-D second mode disturbance as well as a selection of lower wavenumber disturbances. Higher wavenumbers up the K = 8 also were also excited, though to a much weaker degree. In general, the high wavenumber modes were not efficiently forced by the 3-D slow acoustic disturbance. The 3-D fast acoustic pulse also shows significant broadband responses in both the frequency and wavenumber spectra. Similar to the axisymmetric planar fast acoustic pulse, continuous mode excitation was observed over a broad range of disturbance frequencies. Though, these secondary amplified frequency bands were isolated primarily to lower wavenumbers. This is likely due to the limited extent of the induced shock-disturbance interactions. Amplification at the primary second mode frequencies is also observed, but is over an order of magnitude lower in magnitude than the slow acoustic case. Higher wavenumbers were also significantly stronger in the fast acoustic case, remaining near the peak amplitude of the 2-D second mode. These findings confirm the complex response to broadband freestream forcing, particularly in the case of freestream fast acoustic waves.

7.5 Suggestions for Continued Research

While this work has rigorously studied the impact of broadband freestream disturbances on hypersonic flows in cone geometries, the results are not yet adequate to fully characterize the stability behaviors for a general hypersonic vehicle. Additionally, some improvements can be made to better prepare the data for direct application in more advanced transition prediction methodologies like Mack's amplitude method.

First of all, while an effort was made to generalize the freestream disturbance pulses to encompass a wide range of possible forcing, this work and other work in the field of linear receptivity have not exhaustively studied the many factors and variations on freestream noise that may be present in experimental or flight conditions. Historically, receptivity studies have primarily focused on the response to discrete frequency waves, which is highly unrealistic considering the broadband nature of physical disturbances. Recent studies such as this work, and other works like those by Goparaju, et al.[59], Egorov, et al.[76], and Balakumar and Chou[62] have begun to focus more on broadband receptivity. However, there remains relatively little work in this field. Preliminary findings show that the coherence of the freestream disturbance may play a significant role in the final amplitude of excited boundary layer disturbances due to interference effects. This is partially supported by findings in this study, which show that wavepacket interference can lead to a series of highly damped frequencies in the primary disturbance wavepacket. Freestream noise environments are also unlikely to be as sterile as many computational receptivity studies assume, as multiple perturbation sources of different types may be present and simultaneously interact with the vehicle body. Additionally, the combined effect of both 2-D and oblique disturbances to broadband freestream forcing has not been fully studied. True hypersonic vehicles will require more complex geometries and fly in a wider range of conditions that will likely result in the existence of not only significant second mode disturbances, but also oblique crossflow modes which may respond differently to freestream perturbations. Thermochemical non-equilibrium effects must also be accounted for to accomodate much higher enthalpy flight conditions that can occur in the lower atmosphere. Such considerations necessitate further, more complex study to fully elucidate the nature of hypersonic boundary layer receptivity.

Current transition prediction tools also require additional development to further improve their accuracy and general applicability for engineering design. The conventional e^N method's detriments have been well documented, but its ease of usability and corrections with correlations has ensured its continued application. While the amplitude method is able to directly estimate disturbance amplitudes and thus provide more accurate estimates of transition, it requires many more data inputs that can possibly introduce additional sources of error as well. For instance, simplifications of the governing amplitude method relation, like those suggested by Mack[90] and Marineau[6], often require estimates of spectral bandwidth parameters, freestream noise profiles, and breakdown threshold amplitudes that need to be correlated experimentally. This can leave a significant margin for error without careful consideration. The receptivity spectra itself can also be an issue as well, as sufficiently noisy boundary layer disturbance profiles like those for the planar fast acoustic pulse cases here can induce highly noisy spectra. In order to better isolate disturbance modes of interest, more advanced modal decomposition methods such as the biorthogonal decomposition discussed by Tumin[115, 83] can be utilized to further separate the coupled modes present in the boundary layer disturbance profile. These could provide more clear depictions of the modal response of hypersonic boundary layers and further clarify the receptivity coefficients necessary for application in the amplitude method. These are just a few avenues of further research in this line that may prove to be of interest to other researchers.

REFERENCES

[1] Zhong, X. and Wang, X., "Direct Numerical Simulation on the Receptivity, Instability, and Transition of Hypersonic Boundary Layers," *Annual Review of Fluid Mechanics*, Vol. 44, No. 1, 2012, pp. 527–561.

[2] Ma, Y. and Zhong, X., "Receptivity of a supersonic boundary layer over a flat plate. Part 1. Wave structures and interactions," *Journal of Fluid Mechanics*, Vol. 488, July 2003, pp. 31–78.

[3] Knisely, C. P. and Zhong, X., "Significant Supersonic Modes and the Wall Temperature Effect in Hypersonic Boundary Layers," *AIAA Journal*, Vol. 57, No. 4, 2019, pp. 1552–1566.

[4] Huang, Y. and Zhong, X., "Numerical Study of Hypersonic Boundary-Layer Receptivity and Stability with Freestream Hotspot Perturbations," *AIAA Journal*, Vol. 52, No. 12, 2014, pp. 2652–2672.

[5] Hader, C. and Fasel, H. F., "Direct numerical simulations of hypersonic boundary-layer transition for a flared cone: fundamental breakdown," *Journal of Fluid Mechanics*, Vol. 869, 2019, pp. 341–384.

[6] Marineau, E., "Prediction Methodology for Second-Mode dominated Boundary-Layer Transition in Wind Tunnels," *AIAA Journal*, Vol. 55, No. 2, 2017, pp. 484–499.

[7] Marineau, E., Moraru, C., Lewis, D., Norris, J., and Lafferty, J., "Mach 10 Boundary-Layer Transition Experiments on Sharp and Blunted Cones," *19th AIAA International Space Planes and Hypersonic Systems and Technologies Conference*, No. AIAA Paper 2014-3108, 2014.

[8] Paredes, P., Choudhari, M. M., Li, F., Jewell, J. S., Kimmel, R. L., Marineau, E. C., and Grossir, G., "Nose-Tip Bluntness Effects on Transition at Hypersonic Speeds," *Journal of Spacecraft and Rockets*, Vol. 56, No. 2, 2019, pp. 369–387.

[9] Fedorov, A., "Transition and Stability of High-Speed Boundary Layers," *Annual Review of Fluid Mechanics*, Vol. 43, No. 1, 2011, pp. 79–95.

[10] Reshotko, E., "Hypersonic Stability and Transition," *Hypersonic flows for reentry problems*, Vol. 1, No. A93-42576 17-02, 1991, pp. 18–34.

[11] Schneider, S. P., "Summary of Hypersonic Boundary-Layer Transition Experiments on Blunt Bodies with Roughness," *Journal of Spacecraft and Rockets*, Vol. 45, No. 6, 2008, pp. 1090–1105.

[12] Ma, Y. and Zhong, X., "Receptivity of a Supersonic Boundary Layer over a Flat Plate. Part 3. Effects of Different Types of Free-stream Disturbances," *Journal of Fluid Mechanics*, Vol. 532, June 2005, pp. 63–109.

[13] Reshotko, E. and Tumin, A., "Application of Transient Growth Theory to Bypass Transition," *IUTAM Symposium on One Hundred Years of Boundary Layer Research*, edited by G. Meier and K. Sreenivasan, Springer, 2006, pp. 83–93.

[14] Reshotko, E. and Tumin, A., "Role of Transient Growth in Roughness-Induced Transition," *AIAA Journal*, Vol. 42, No. 4, 2004, pp. 766–774.

[15] Reshotko, E., "Paths to Transition in Wall Layers," Tech. Rep. RTO-EN-AVT-151, NATO OTAN, 2008.

[16] Reshotko, E., "Transition Issues for Atmospheric Entry," *Journal of Spacecraft and Rockets*, 2008.

[17] Rayleigh, J. W. S., "On the stability, or instability, of certain fluid motions." *Proceedings of the London Mathematical Society*, Vol. 11, 1880, pp. 57–70.

[18] Tollmien, W., "Ueber die entstehung der turbulenz," *Nachr. Ges. Wiss. Goettingen, Math.-Phys. Kl.*, 1929, pp. 21–44.

[19] Schlichting, H., "Zur entstehung der turbulenz bei der plattenstroemung," *Nachr. Ges. Wiss. Goettingen, Math.-Phys. Kl.*, 1933, pp. 181–208.

[20] Lees, L. and Lin, C. C., "Investigation of the stability of the laminar boundary layer in a compressible fluid." Tech. Rep. TN-1115, NACA, 1946.

[21] Dunn, D. W. and Lin, C. C., "On the stability of the laminar boundary layer in a compressible fluid." *Journal of the Aeronautical Sciences*, Vol. 22, 1955, pp. 455–477.

[22] Mack, L. M., "Boundary layer stability theory," Tech. Rep. 900-277, Jet Propulsion Labt, 1969.

[23] Mack, L. M., "Boundary Layer Linear Stability Theory," Tech. rep., AGARD report No. 709 Neuilly-sur-Seine, France, 1984.

[24] Knisely, C. P. and Zhong, X., "Sound radiation by supersonic unstable modes in hypersonic blunt cone boundary layers. I. Linear stability theory," *Physics of Fluids*, Vol. 31, No. 2, 2019, pp. 024103.

[25] Knisely, C. P. and X., Z., "Sound radiation by supersonic unstable modes in hypersonic blunt cone boundary layers. II. Direct numerical simulation," *Physics of Fluids*, Vol. 31, No. 2, 2019, pp. 024104.

[26] Grosch, C. E. and Salwen, H., "The continuous spectrum of the Orr-Sommerfeld equation. Part 1. The spectrum and the eigenfunctions," *Journal of Fluid Mechanics*, Vol. 87, No. 1, July 1978, pp. 33–54.

[27] Fedorov, A. and Tumin, A., "High-Speed Boundary-Layer Instability: Old Terminology and a New Framework," *AIAA Journal*, Vol. 49, No. 8, 2011, pp. 1647–1657.

[28] Knisely, C. P. and Zhong, X., "The Supersonic Mode and the Role of Wall Temperature in Hypersonic Boundary Layers with Thermochemical Nonequilibrium Effects," *2018 Fluid Dynamics Conference*, No. AIAA Paper 2018-3218, 2018.

[29] Softley, E., Graber, B. C., and Zempel, R. E., "Transition of the Hypersonic Boundary Layer on a Cone Part II: Experiments at M = 10 and More on Blunt Cone Transition," Tech. Rep. R68SD14, Space Sciences Laboratory, 1968.

[30] Stetson, K. and Rushton, G., "Shock Tunnel Investigation of Boundary-Layer Transition at M = 5.5," *AIAA Journal*, Vol. 5, No. 5, 1967, pp. 899–906.

[31] Stetson, K., Thompson, E., Donaldson, J., and Siler, L., "Laminar Boundary Layer Stability Expierments on a Cone at Mach 8, Part 1: Sharp Cone," *16th Fluid and Plasmadynamics Conference*, No. AIAA Paper 83-1761, 1983.

[32] Stetson, K., Thompson, E., Donaldson, J., and Siler, L., "Laminar Boundary Layer Stability Experiments on a Cone at Mach 8, Part 2: Blunt Cone," *22nd Aerospace Sciences Meeting*, No. AIAA Paper 84-0006, 1984.

[33] Kara, K., Balakumar, P., and Kandil, O., "Effects of Nose Bluntness on Hypersonic Boundary-Layer Receptivity and Stability over Cones," *AIAA Journal*, Vol. 55, No. 12, 2011, pp. 2593–2606.

[34] Lei, J. and Zhong, X., "Linear Stability Analysis of Nose Bluntness Effects on Hypersonic Boundary Layer Transition," *Journal of Spacecraft and Rockets*, Vol. 49, No. 1, 2012, pp. 24–37.

[35] Paredes, P., Choudhari, M. M., Li, F., Jewell, J. S., and Kimmel, R. L., "Nonmodal Growth of Traveling Waves on Blunt Cones at Hypersonic Speeds," *AIAA Journal*, Vol. 57, No. 11, 2019, pp. 4738–4749.

[36] Reshotko, E., "Transient growth: A factor in bypass transition," *Physics of Fluids*, Vol. 13, 2001, pp. 1067–1075.

[37] Jewell, J. S., Kennedy, R. E., Laurence, S. J., and Kimmel, R. L., "Transition on a Variable Bluntness 7-Degree Cone at High Reynolds Number," *2018 AIAA Aerospace Sciences Meeting*, No. AIAA Paper 2018-1822, 2018.

[38] Marineau, E., Moraru, C., Lewis, D., Norris, J., and Lafferty, J., "Investigation of Mach 10 Boundary Layer Stability of Sharp Cones at Angle-of-Attack, Part 1: Experiments," *53rd AIAA Aerospace Sciences Meeting*, No. AIAA Paper 2015-1737, 2015.

[39] Marineau, E., Guillaume, G., Wagner, A., Leinemann, M., Radespiel, R., Tanno, H., Chynoweth, B. C., Schneider, S. P., Wagnild, R. M., and Casper, K. M., "Compilation and Analysis of Second-Mode Amplitudes on Sharp Cones in Hypersonic Wind Tunnels," *Journal of Spacecraft and Rockets*, Vol. 56, No. 2, 2018.

[40] Juliano, T. J., Borg, M. P., and Schneider, S. P., "Quiet Tunnel Measurements of HiFiRE-5 Boundary-Layer Transition," *AIAA Journal*, Vol. 53, No. 4, 2015, pp. 832–846.

[41] Schneider, S., "Effects of High-Speed Tunnel Noise on Laminar-Turbulent Transition," *Journal of Spacecraft and Rockets*, Vol. 38, No. 3, 2001, pp. 323–333.

[42] Reed, H. L. and Saric, W. S., "Stability of Three-Dimensional Boundary Layers," *Annual Review of Fluid Mechanics*, Vol. 21, 1989, pp. 235–284.

[43] Reed, H. L., Saric, W. S., and Arnal, D., "Linear Stability Theory Applied to Boundary Layers," *Annual Review of Fluid Mechanics*, Vol. 28, No. 1, 1996, pp. 389–428.

[44] Balakumar, P. and Kegerise, M., "Receptivity of Hypersonic Boundary Layers to Acoustic and Vortical Disturbances," *49th AIAA Aerospace Sciences Meeting including the New Horizons Forum and Aerospace Exposition*, No. AIAA Paper 2011-371, 2011.

[45] Chou, A., *Characterization of Laser-Generated Perturbations and Instability Measurements on a Flared Cone*, Master's thesis, Purdue University, West Lafayette, IN, 2010.

[46] Chuvakhov, P. V., Fedorov, A. V., and Obraz, A., "Numerical modelling of supersonic boundary-layer receptivity to solid particulates," *Journal of Fluid Mechanics*, Vol. 859, January 2019, pp. 949–971.

[47] Wang, X. and Zhong, X., "Effect of wall perturbations on the receptivity of a hypersonic boundary layer," *Physics of Fluids*, Vol. 21, 2009, pp. 044101–1–19.

[48] Mortensen, C. H. and Zhong, X., "Real-Gas and Surface-Ablation Effects on Hypersonic Boundary-Layer Instability over a Blunt Cone," *AIAA Journal*, Vol. 54, No. 3, 2016, pp. 976–994.

[49] Wang, X. and Zhong, X., "Receptivity of a Hypersonic Flat-Plate Boundary Layer to Three-Dimensional Surface Roughness," *Journal of Spacecraft and Rockets*, Vol. 45, No. 6, 2008, pp. 1165–1174.

[50] Fong, K. and Zhong, X., "Numerical simulation of roughness effect on the stability of a hypersonic boundary layer," *Computers and Fluids*, Vol. 96, 2014, pp. 350–367.

[51] Haley, C. L., Casper, K., and Zhong, X., "Joint Numerical and Experimental Investigation of Roughness Effect on Hypersonic 2nd Mode Instability and Transition," *AIAA Scitech 2019 Forum*, No. AIAA Paper 2019-0873, 2019.

[52] Kovasznay, L. S. G., "Turbulence in Supersonic Flow," *Journal of the Aeronautical Sciences*, Vol. 20, No. 10, 1953, pp. 657–682.

[53] McKenzie, J. F. and Westphal, K. O., "Interaction of Linear Waves with Oblique Shock Waves," *Physics of Fluids*, Vol. 11, No. 11, 1968, pp. 2350–2362.

[54] Balakumar, P. and Malik, M., "Discrete modes and continuous spectra in supersonic boundary layers," *Journal of Fluid Mechanics*, Vol. 239, June 1992, pp. 631–656.

[55] Ma, Y. and Zhong, X., "Receptivity of a supersonic boundary layer over a flat plate. Part 2. Receptivity to freestream sound," *Journal of Fluid Mechanics*, Vol. 488, July 2003, pp. 79–121.

[56] Malik, M. and Balakumar, P., “Receptivity of Supersonic Boundary Layers to Acoustic Disturbances,” *35th AIAA Fluid Dynamics Conference and Exhibit*, No. AIAA Paper 2005-5027, 2005.

[57] Fedorov, A. V., “Receptivity of a High-Speed Boundary Layer to Acoustic Disturbances,” *Journal of Fluid Mechanics*, Vol. 491, September 2003, pp. 101–129.

[58] Fedorov, A. V., Ryzhov, A. A., Soudakov, V. G., and Utyuzhnikov, S. V., “Receptivity of a high-speed boundary layer to temperature spottiness,” *Journal of Fluid Mechanics*, Vol. 722, May 2013, pp. 533–553.

[59] Goparaju, H., Unnikrishnan, S., and Gaitonde, D. V., “Effects of nose bluntness on hypersonic boundary layer receptivity and stability,” *Journal of Spacecraft and Rockets*, Vol. 58, No. 3, 2021, pp. 668–684.

[60] Zhong, X. and Ma, Y., “Boundary-Layer Receptivity of Mach 7.99 Flow over a Blunt Cone to Free-Stream Acoustic Waves,” *Journal of Fluid Mechanics*, Vol. 556, June 2006, pp. 55–103.

[61] Balakumar, P. and Kegerise, M., “Receptivity of Hypersonic Boundary Layers over Straight and Flared Cones,” *48th AIAA Aerospace Sciences Meeting Including the New Horizons Forum and Aerospace Exposition*, No. AIAA Paper 2010-1065, 2010.

[62] Balakumar, P. and Chou, A., “Transition Prediction in Hypersonic Boundary Layers Using Receptivity and Freestream Spectra,” *AIAA Journal*, Vol. 56, No. 1, 2018, pp. 2593–2606.

[63] Lei, J. and Zhong, X., “Numerical Simulation of Freestream Waves Receptivity and Breakdown in Mach 6 Flow over Cone,” *43rd Fluid Dynamics Conference*, No. AIAA Paper 2013-2741, 2013.

[64] Wan, B., Su, C., and Chen, J., “Receptivity of a Hypersonic Blunt Cone: Role of Disturbances in Entropy Layer,” *AIAA Journal*, Vol. 58, No. 9, 2020, pp. 4047–4054.

[65] He, S. and Zhong, X., “Hypersonic Boundary-Layer Receptivity over a Blunt Cone to Freestream Pulse Disturbances,” *AIAA Journal*, Vol. 59, No. 9, 2021, pp. 3546–3565.

[66] Jewell, J. S. and Kimmel, R. L., “Boundary-Layer Stabiity Analysis for Stetson’s Mach 6 Blunt-Cone Experiments,” *Journal of Spacecraft and Rockets*, Vol. 54, No. 1, 2017.

[67] Chen, Y., Tu, G., Wan, B., Su, C., Yuan, X., and Chen, J., “Receptivity of a hypersonic flow over a blunt wedge to a slow acoustic wave,” *Physics of Fluids*, Vol. 33, 2021, pp. 084114.

[68] Duan, L., Choudhari, M. M., Chou, A., Munoz, F., Radespeil, R., Schilden, T., Schroder, W., Marineau, E., Casper, K., Chaudhry, R., Candler, G., Gray, K., and Schneider, S., “Characterization of Freestream Disturbances in Conventional Hypersonic Wind Tunnels,” *Journal of Spacecraft and Rockets*, Vol. 56, No. 2, 2016, pp. 578–607.

[69] Zhong, X., "Effect of Nose Bluntness on Hypersonic Boundary Layer Receptivity over a Blunt Cone," *35th AIAA Fluid Dynamics Conference and Exhibit*, No. AIAA Paper 2005-5022, June 2005.

[70] Wheaton, B., Juliano, T., Berridge, D., Chou, A., Gilbert, P., Casper, K., Steen, L., and Schneider, S., "Instability and Transition Measurements in the Mach-6 Quiet Tunnel," *39th AIAA Fluid Dynamics Conference*, No. AIAA Paper 2009-3559, 2009.

[71] Chou, A., Wheaton, B., Ward, C., Gilbert, P., Steen, L., and Schneider, S., "Instability and Transition Reserach in a Mach-6 Quiet Tunnel," *49th AIAA Aerospace Sciences Meeting*, No. AIAA Paper 2011-0283, 2011.

[72] Huang, Y., *Numerical Study of Hypersonic Boundary-Layer Receptivity and Stability with Freestream Hotspot Perturbations*, Ph.D. thesis, University of California, Los Angeles, 2016.

[73] Schneider, S. P., "Developing Mechanism-Based Methods for Estimating Hypersonic Boundary-Layer Transition in Flight: The Role of Quiet Tunnels," *Progress in Aerospace Sciences*, Vol. 72, January 2015, pp. 17–29.

[74] Koontz, R., Buck, G., and Kimmel, R., "Experimental Study of Spark-Induced Impulsive Acoustic Disturbances in Supersonic Flow," *40th AIAA Aerospace Sciences Meeting and Exhibit*, No. AIAA Paper 2002-0141, 2002.

[75] Browne, O., Al Hasnine, S., and Brehm, C., "Numerical Method for Particulate-Induced High-Speed Boundary Layer Transition Simulations," *AIAA Journal*, Vol. 59, No. 4, 2021, pp. 1196–1213.

[76] Egorov, I. V., Fedorov, A. V., Novikov, A. V., and Chuvakhov, P. V., "The Role of Receptivity in Prediction of High-Speed Laminar-Turbulent Transition," *IUTAM Laminar-Turbulent Transition*, edited by S. Sherwin, P. Schmid, and X. Wu, Springer International Publishing, Cham, 2022, pp. 541–552.

[77] Hader, C. and Fasel, H. F., "Towards simulating natural transition in hypersonic boundary layers via random inflow disturbances," *Journal of Fluid Mechanics Rapids*, Vol. 847, 2018, pp. R3–1–14.

[78] Aleksandrova, E., Novikov, A., Utyuzhnikov, S., and Fedorov, A., "Experimental Study of the Laminar-Turbulent Transition on a Blunt Cone," *Journal of Applied Mechanics and Technical Physics*, Vol. 55, No. 3, 2014, pp. 375–385.

[79] Tumin, A., "Multimode decomposition of spatially growing perturbations in a two-dimensional boundary layer," *Physics of Fluids*, Vol. 15, 2003, pp. 2525–2540.

[80] Paredes, P., Choudhari, M. M., and Li, F., "Mechanism for frustum transition over blunt cones at hypersonic speeds," *Journal of Fluid Mechanics*, Vol. 894, July 2020, pp. A22.

[81] Fedorov, A. and Khokhlov, A., “Prehistory of Instability in a Hypersonic Boundary Layer,” *Theoretical Computational Fluid Dynamics*, Vol. 14, 2001, pp. 359–375.

[82] Gaydos, P. and Tumin, A., “Multimode Decomposition in Compressible Boundary Layers,” *AIAA Journal*, Vol. 42, No. 6, June 2004, pp. 1115–1121.

[83] Tumin, A., “Three-Dimensional Spatial Normal Modes in Compressible Boundary Layers,” *Journal of Fluid Mechanics*, Vol. 586, September 2007, pp. 295–322.

[84] Miselis, M., Huang, Y., and Zhong, X., “Modal Analysis of Receptivity Mechanisms for a Freestream Hot-Spot Perturbation on a Blunt Compression-Cone Boundary Layer,” *46th AIAA Fluid Dynamics Conference*, No. AIAA Paper 2016-3345, 2016.

[85] Sivasubramanian, J. and Fasel, H. F., “Direct numerical simulation of transition in a sharp cone boundary layer at Mach 6: fundamental breakdown,” *Journal of Fluid Mechanics*, Vol. 768, April 2015, pp. 175–218.

[86] Lei, J. and Zhong, X., “Numerical Study of Freestream Waves Induced Breakdown in Hypersonic Boundary Layer Transition,” *42nd AIAA Fluid Dynamics Conference and Exhibit*, No. AIAA Paper 2012-2692, 2012.

[87] Chang, C., Malik, M., Erlebacher, G., and Hussaini, M., “Compressible stability of growing boundary layers using parabolized stability equations,” *22nd Fluid Dynamics, Plasma Dynamics and Lasers Conference*, 1991.

[88] Crouch, J. and Ng, L., “Variable N-Factor Method for Transition Prediction in Three-Dimensional Boundary Layers,” *AIAA Journal*, Vol. 38, No. 2, 2000, pp. 211–216.

[89] Duan, L., Choudhari, M. M., and Zhang, C., “Pressure fluctuations induced by a hypersonic turbulent boundary layer,” *Journal of Fluid Mechanics*, Vol. 804, 2016, pp. 357–368.

[90] Mack, L. M., “Transition and laminar instability,” Tech. Rep. NASA CP-153203, Jet Propulsion Laboratory, 1977.

[91] Ustinov, M. V., “Amplitude method of prediction of laminar-turbulent transition on a swept-wing,” *Fluid Dynamics*, Vol. 52, No. 1, Jan 2017, pp. 71–87.

[92] Fedorov, A. and Tumin, A., “The Mack’s amplitude method revisited,” *Theoretical Computational Fluid Dynamics*, Vol. 36, 2021, pp. 9–24.

[93] Mack, L. M., “Transition Prediction and Linear Stability Theory,” Tech. rep., AGARD CP-224, 1977.

[94] Mortensen, C. H., “Toward an understanding of supersonic modes in boundary-layer transition for hypersonic flow over blunt cones,” *Journal of Fluid Mechanics*, Vol. 846, July 2018, pp. 789–814.

[95] Prakash, A., Parsons, N., Wang, X., and Zhong, X., "High-order shock-fitting methods for direct numerical simulation of hypersonic flow with chemical and thermal nonequilibrium," *Journal of Computational Physics*, Vol. 230, No. 23, 2011, pp. 8474–8507.

[96] Williamson, J., "Low-Storage Runge-Kutta Schemes," *Journal of Computational Physics*, Vol. 35, No. 1, 1980, pp. 48–56.

[97] Zhong, X., "High-Order Finite-Difference Schemes for Numerical Simulation of Hypersonic Boundary-Layer Transition," *Journal of Computational Physics*, Vol. 144, No. 2, 1998, pp. 662–709.

[98] Malik, M. R., "Numerical Methods for Hypersonic Boundary Layer Stability," *Journal of Computational Physics*, Vol. 86, No. 2, February 1990, pp. 376–413.

[99] Press, W., Teukolsky, S., Vetterling, W., and Flannery, B., *Numerical Recipes in Fortran 77 - The Art of Scientific Computing*, Press Syndicate of the University of Cambridge, 2nd ed., 1992.

[100] Lei, J. and Zhong, X., "Linear Stability Analysis of Nose Bluntness Effects on Hypersonic Boundary Layer Transition," *48th AIAA Aerospace Sciences Meeting Including the New Horizons Forum and Aerospace Exposition*, No. AIAA Paper 2010-898, 2010.

[101] He, S. and Zhong, X., "Numerical Study of the Receptivity of a Blunt Cone to Freestream Pulse Disturbances in Hypersonic Flow," *AIAA Aviation 2021 Forum*, No. AIAA Paper 2021-2887, 2021.

[102] Haley, C. and Zhong, X., "Supersonic mode in a low-enthalpy hypersonic flow over a cone and wave packet interference," *Physics of Fluids*, Vol. 33, No. 5, 2021, pp. 054104.

[103] Balakumar, P. and Kegerise, M. A., "Receptivity of Hypersonic Boundary Layers over Straight and Flared Cones," *AIAA Journal*, Vol. 53, No. 8, 2015, pp. 2097–2109.

[104] Zhong, X., "Leading-Edge Receptivity to Free Stream Disturbance Wave for Hypersonic Flow Over a Parabola," *Journal of Fluid Mechanics*, Vol. 441, August 2001, pp. 315–367.

[105] He, S. and Zhong, X., "Hypersonic Boundary Layer Receptivity over a Blunt Cone to Freestream Pulse Disturbances," *AIAA Scitech 2020 Forum*, No. AIAA Paper 2020-2057, 2020.

[106] Knisely, C., Haley, C. L., and Zhong, X., "Impact of Conical Hypersonic Boundary Layer Transition on Skin Drag and Heating," *AIAA Scitech 2019 Forum*, No. AIAA Paper 2019-1134, 2019.

[107] Fedorov, A. and Kozlov, M., "Receptivity of high-speed boundary layer to solid particulates," *6th AIAA Theoretical Fluid Mechanics Conference*, No. AIAA Paper 2011-3925, 2011.

[108] Casper, K., Beresh, S., and Schneider, S., “Comparison of Methods for Determining Boundary Layer Edge Conditions for Transition Correlations,” *33rd AIAA Fluid Dynamics Conference and Exhibit*, No. AIAA Paper 2003-3590, 2003.

[109] Liechty, D., Berry, S., Hollis, B., and Horvath, T., “Pressure Fluctuations Beneath Turbulent Spots and Instability Wave Packets in a Hypersonic Boundary Layer,” *49th AIAA Aerospace Sciences Meeting including the New Horizons Forum and Aerospace Exposition*, No. AIAA Paper 2011-372, 2011.

[110] Marineau, E., Lewis, D., Michael, S., John, L., White, M., and Amar, A., “Investigation of Hypersonic Laminar Heating Augmentation in the Stagnation Region,” *51st AIAA Aerospace Sciences Meeting*, No. AIAA Paper 2013-0308, 2013.

[111] Duan, L., Choudhari, M. M., and Wu, M., “Numerical study of acoustic radiation due to a supersonic turbulent boundary layer,” *Journal of Fluid Mechanics*, Vol. 746, May 2014, pp. 165–192.

[112] Pruett, C. and Chang, C., “Spatial Direct Numerical Simulation of High-Speed Boundary-Layer Flows Part II: Transition on a Cone in Mach 8 Flow,” *Theoretical and Computational Fluid Dynamics*, Vol. 7, 1994, pp. 397–424.

[113] Gottlieb, D., Hussaini, M., and Orszag, S., “Introduction: Theory and applications of spectral methods,” *Spectral Methods for Partial Differential Equations*, edited by R. Voigt, D. Gottlieb, and M. Hussaini, SIAM, Philadelphia, PA, 1984, pp. 1–54.

[114] Bitter, N. P. and Shepherd, J. E., “Stability of highly cooled hypervelocity boundary layers,” *Journal of Fluid Mechanics*, Vol. 778, September 2015, pp. 533–553.

[115] Tumin, A. and Reshotko, E., “Spatial theory of optimal disturbances in boundary layers,” *Physics of Fluids*, Vol. 13, 2001, pp. 2097–2104.